IN-SITU DETECTION OF AIRBORNE FIBRES BY LIGHT SCATTERING

A thesis submitted for the degree
of Doctor of Philosophy
of the University of London

by

SATINDER SINGH PUREWAL B.SC.,M.Sc.,A.R.C.S.,D.I.C.

Department of Chemical Engineering
and Chemical Technology,
Imperial College of Science and Technology,
Prince Consort Road,
London SW7.

February 1982

ACKNOWLEDGEMENT

My sincerest thanks go to my supervisor, Dr.A.R.Jones without whose assistance and constant encouragement this work would not have been possible. His infectious wit and boundless enthusiasm were a welcome spur for awakening latent research talent on some dull unproductive days past.

The technical assistance of Mr.E.Barnes, Mr.A.Harrup, Mr.T.Stephenson and his crew is deeply appreciated. Their co-operation at every crucial stage of the project has not gone unnoticed.

The glass-blowers Mr.C.Smith and Mr.K.Grose afforded appreciable help whenever required and their marked priority for my work helped to save precious time. I am also grateful to Mr.M.Dix and Mr.D.Wood who gave valuable advice on electronics.

Occasional assistance from Mr.L.Moulder with photography is acknowledged. Thanks are due to Mr.N.A.H.Salpadoron who helped to prepare the fibre samples for electron microscopy.

The expertise available at the H.S.E. laboratories in Cricklewood was an invaluable asset for bringing this project to a successful conclusion and special thanks must go to Mr.N.Vaughn, Dr.Rood and Dr.LeGuen. I would also like to thank H.S.E. for providing the necessary financial support for the project.

Last, but not least the ultra fast typing of Suzanne is gratefully acknowledged.

ABSTRACT

The carcinogenic nature of airborne asbestos dust has been well documented in the past couple of decades. In order to minimise health hazards associated with inhalation of various types of fibres, regulatory laws exist. To date, enforcement of these laws has entailed the use of time consuming and unreliable sampling methods using phase contrast or electron microscopy. Light scattering methods have been used to monitor fibres with limited success. An in-situ light scattering system is required so that continuous monitoring of any hazardous environment is feasible.

Our investigations showed that the use of circularly polarised light,in a modified laser doppler anemometer,is successful for detecting form anisotropy (shape). The method is based on the fact that cylindrical particles scatter light differently when polarised parallel and perpendicular to their axes, whereas isometric particles such as spheres do not. The scattered light is analysed using two orthogonal polarisation directions. The relative strength of the signals for fibres and ballotini has been found to be an excellent parameter for distinguishing between cylindrical and spherical particles.

The particles used in our experiments were fibrous quartz, ballotini, water spray and laboratory dust. Experimental results correlate well with theoretical results for scattering from an infinite cylinder. If errors in the circular polarisation generating optical elements and variability of fibre orientation are taken into account then excellent agreement between experimental results and theoretical predictions is

achieved both for the forward and backward scattering directions.

Further developmental work should include localisation of the test space and on-line data analysis. Theoretical calculations indicate that it would be advantageous to use long wavelength light sources. Not only are they eye-safe, but also enhance the distinguishability between fibres and spheres.

"Logical consequences are the
scarecrows of fools and the
beacons of wise men."

"Irrationally held truths may be
more harmful than reasoned errors".

T.H.Huxley 1825-1895

CONTENTS

CHAPTER ONE OPTICAL METHODS OF FIBRE DETECTION-A REVIEW

LIST OF FIGURES

CHAPTER THREE

CHAPTER FOUR

CHAPTER FIVE

APPENDICES

LIST OF TABLES

LIST OF PLATES

NOTATION

A	total scattered field due to a_n^s
B	total scattered field due to b_n^s
D_{ij}	particle separation
$\underline{E}$	electric field
E_0	field amplitude to $t=0$
$\underline{H}$	magnetic field
$H_n^{(1)}$	Hankel function of first kind
I	intensity. $I_{\parallel}$ represents polarisation parallel to scattering plane while $I_{\perp}$ is perpendicular to it
J_n	Bessel function of first kind
$\underline{L}$	Vector for solution of wave equation
L	fibre length
$\underline{M}$	Vector for solution of wave equation
N	number of particles in a chain
$\underline{N}$	vector for solution of wave equation
P	Power
$P_2(\cos\chi)$	Legendre polynomial
Q	efficiency factor
$R=\left\|\frac{A+B}{A-B}\right\|^2$	observed polarisation ratio
R_j	radius of j^{th} Rayleigh sphere
R^1	ratio of two orthogonal intensities
$\underline{S}$	Poynting vector
S	scattering Matrix
V	visibility of scattered signal
V_c	fringe contrast
$Z_n(x)$	Bessel function of any kind
a	radius of cylinder
a_n, b_n	expansion coefficients
c	speed of light in Vacuo
f	frequency

$h_n^{(i)}(x)$	spherical Hankel functions
$i = \sqrt{-1}$	
$j_n(x)$	spherical Bessel functions of first kind
$k = \frac{2\pi}{\lambda}$	wavenumber
$k_0 = \frac{2\pi}{\lambda}$	wavenumber in vacno
$m = m_0 + im_e$	refractive index
$\hat{n}$	unit vector normal to surface
p	polarisation
r	radial co-ordinate
r_j, θ_j, ϕ_j	spherical co-ordinates of j^{th} Rayleigh sphere
t	time
v	velocity
$x = \frac{2\pi a}{\lambda}$	particle size parameter
x, y, z	Cartesian co-ordinates
$y_n(x)$	spherical Bessel functions of second kind
z_1	cylindrical co-ordinate
Z_R	Rayleigh distance
Ψ	scalar wave amplitude
α	cylindrical co-ordinate
β	phase
γ	half angle of interference
δ	error in phase plate
ε	permittivity
ε_0	permittivity of free space
θ	scattering angle (polar angle)
θ_b	half angle of convergence
λ	wavelength
λ_0	wavelength in vacuo
μ	permeability
μ_0	permeability of free space

ρ	cylindrical co-ordinate
σ_o	beam radius (at $1/e^2$ points)
ϕ	spherical azimuthal angle
χ	spherical polar angle of orientation
ψ	spherical azimuthal angle of orientation
$\omega = 2\pi f$	angular frequency

CHAPTER ONE

OPTICAL METHODS OF FIBRE DETECTION - A REVIEW

1.1 Introduction

The adverse heath effects of asbestos have been known since shortly after the turn of the century (Murray, 1907; Cooke, 1924; Selikoff et.al. 1965). Airborne asbestos dust has been found to result in serious human respiratory ailments, among which asbestosis and lung cancer are prominent, as reported by Smith (1955), Becklake (1976) and Bruckman et.al. (1977). Also fibres of other substances such as glass, talc, textiles and, more recently, zeolite are suspected of being causatory agents of similar pulmonary problems. Consequently, the detection and measurement of concentration of airborne fibre is mandatory if the enforcement of regulatory laws is to be realised. However, progress in techniques for determining the in-situ concentration of these minerals has been minimal.

The word asbestos describes a crystal habit and is a broad term embracing a number of fibrous mineral silicates that differ in chemical composition. Selikoff (1972) has reported that there appears to be no basis for distinguishing the health effects of one type of asbestos over another. The physiological response seems more dependent on crystal structure than chemical composition.

There is no unique chemical property of asbestos that can be used as the basis for its measurement. Thus in order to detect asbestos we have to base our measurements on physical characteristics such as size, shape and optical properties. To date the available measurement techniques vary widely in type and capability. Essentially, the methods entail obtaining a sample by means of extraction and subsequently examining by an appropriate technique. This poses problems related to obtaining a representative sample, the possibility that the sample can alter during its preparation and the problem of relating the measured concentration of the sample back to the original environment. Sampling is also a time-consuming process entailing unnecessary time delays during which concentration of fibres in the environment might change.

Light scattering techniques have been successfully applied to obtain size distributions of samples obtained from the environment (Powers and Somerford, 1978; Gadsden et.al.,1970). However, what is required is an in-situ light scattering technique which can provide on-line information about fibre concentration.

1.2 Light Scattering - an Introduction.

When a beam of electromagnetic radiation is directed on a particulate cloud, three processes of interest can occur: scattering, absorption and transmission. By observing the scattered light it is possible to obtain information relating to the size, shape and optical properties of the particle cloud. Thus light scattering is a very powerful diagnostic tool.

In order to understand light scattering we have to consider the propagation of waves in media. A plane wave travelling in the Z direction can be written in the form:

$$\Psi = \Psi_0 \exp \{i (kz - \omega t)\} \qquad (1\text{-}2\text{-}1)$$

where Ψ_0 is the amplitude at time t=0 and spatial co-ordinate z=0, $k(=2\pi/\lambda)$ is the wave number for wavelength λ and $\omega(=2\pi f)$ is the angular freqency for frequency f.

The energy carried by the wave is proportional to the square of the amplitude. Thus,

$$\overline{\Psi^2} = \Psi\Psi^* = |\Psi_0|^2 \qquad (1\text{-}2\text{-}2)$$

where Ψ^* is the complex conjugate of Ψ and $\overline{\Psi^2}$ is the average intensity over many cycles.

The refractive index (m) of a medium is defined by

$$m = \frac{c}{v} \qquad (1\text{-}2\text{-}3)$$

where c is the speed of light in free space and v the velocity in the medium. In general, m is complex and is related to the permeability (μ) and the permittivity (ε) of the medium. The imaginary component gives rise to conduction which, in turn, is responsible for absorption.

The wave represented in Equation (1-2-1) is scalar. The energy in visible radiation is transported in the form of oscillating electric and magnetic vector fields. If the associated vectors are orthogonal to each other and to the direction of propagation, then the wave is said to be plane polarised. If the vectors oscillate in random fashion, then the wave is unpolarised. The vectors may rotate with change in amplitude in which case it represents elliptical polarisation; however, if constant amplitude is maintained then it is circular polarisation.

For electromagnatic waves the electric ($\underline{E}$) and magnetic ($\underline{H}$) field vectors are related through Maxwells equations (Stratton, 1941). From these field equations we obtain the wave equation for homogeneous isotropic media,

$$\nabla^2\underline{E} + \omega^2\mu\varepsilon\underline{E} = 0 \qquad (1\text{-}2\text{-}4)$$

A similar equation can be derived for the magnetic field $\underline{H}$.

The solution of the one-dimensional form of Equation (1-2-4) in Cartesian co-ordinates is,

$$\underline{E} = \underline{E}_0 \exp\left(i\ \omega \sqrt{\varepsilon\mu}\ z\right) \qquad (1\text{-}2\text{-}5)$$

This is equivalent to $\Psi_0 \exp(ikz)$ of equation (1-2-1).

For a periodic field, such as Ψ, the power crossing unit area per unit time is given by the Poynting Vector

$$\underline{S} = \underline{E} \wedge \underline{H} \qquad (1\text{-}2\text{-}6)$$

This is usually refered to as the intensity of the wave.

However, for real photon detectors it is more correct to describe the intensity by

$$I \propto |\underline{E}|^2 \qquad (1\text{-}2\text{-}7)$$

The most common method of solving any scattering problem is to solve the wave equation in the co-ordinate system relevent to the particle geometry, and relating the internal and external waves through the electromagnetic boundary conditions.

Analytic solutions of the vector wave equation are obtained from the scalar Helmholtz equation

$$\nabla^2\Psi + k^2\varepsilon\Psi = 0 \qquad (1\text{-}2\text{-}8)$$

using the vector relationships

$$\underline{L} = \underline{\nabla}\Psi \ ; \ \underline{M} = \underline{\nabla}\wedge\hat{a}\Psi \ ; \ \underline{N} = \frac{1}{k}\underline{\nabla}\wedge\underline{M} \qquad (1\text{-}2\text{-}9)$$

where $\hat{a}$ is a constant vector of unit length.

The method of separation of variables gives the solutions, however the number of geometries or co-ordinate systems for which the wave-equation is separable, is restricted to six: Cartesian; circular; elliptic and parabolic cylindrical; spherical; conical.

The fields are given by

$$\underline{E} = -\sum_n (a_n\underline{M}_n + b_n\underline{N}_n)$$

$$\underline{H} = -\frac{i}{\omega\mu_0}\sum_n (a_n\underline{N}_n + b_n\underline{M}_n) \qquad (1\text{-}2\text{-}10)$$

where a_n and b_n are coefficients of the expansion.

These are solved using the electromagnetic boundary conditions which require that the components of the electric and magnetic fields which are tangential to the surface be continuous across the boundary. Thus,

$$\hat{n}\wedge(\underline{E}_e-\underline{E}_t) = 0 \ ; \ \hat{n}\wedge(\underline{H}_e-\underline{H}_t) = 0 \qquad (1\text{-}2\text{-}11)$$

where $\hat{n}$ is a unit vector normal to the surface. The subscripts e and t refer to the external and transmitted waves respectively.

The polarisation of the scattered light is of prime significance in determining the physical characteristics of the scatterer. It is normal practice to define the plane of measurement as the plane containing the incident and the scattered waves as shown in Figure (1-2-a). The incident and scattered electric fields can be resolved into two orthogonal components as indicated. The relationship between these components can be written in the form

$$\begin{pmatrix} E_{\parallel,s} \\ E_{\perp,s} \end{pmatrix} = \frac{e^{ikr}}{r} \begin{pmatrix} S_2 & S_3 \\ S_4 & S_1 \end{pmatrix} \begin{pmatrix} E_{\parallel,i} \\ E_{\perp,i} \end{pmatrix} \qquad (1\text{-}2\text{-}12)$$

For isotropic particles such as spheres, there is no coupling between orthogonal vectors and $S_3 = S_4 = 0$.

Lorentz (1890) and Mie (1908) developed independently the so-called 'Mie Theory' which gives analytic solutions to the wave equation for spheres. The coefficients a_n and b_n (Equation (1-2-10)) are functions of the refractive index m and the size parameter x $(=\frac{2\pi a}{\lambda})$ where a is the radius of the sphere, and can be found in several textbooks including Van de Hulst (1957), Born and Wolf (1975), Kerker (1969), Stratton (1941) and Bayvel and Jones (1981). Lord Rayleigh (1881) obtained the solution for an infinite cylinder at perpendicular incidence. A general solution for infinite cylindrical symmetry was first presented by Wait (1955,1959).

Saxon (1974) gives an integral formulation for solving the vector wave equation in terms of the Green's function to find the scattered field. Several approximate theories for light scattering exist and some important ones are summarised in Table (T-1-2-a) with their domains of validity.

A more comprehensive study of light scattering can be

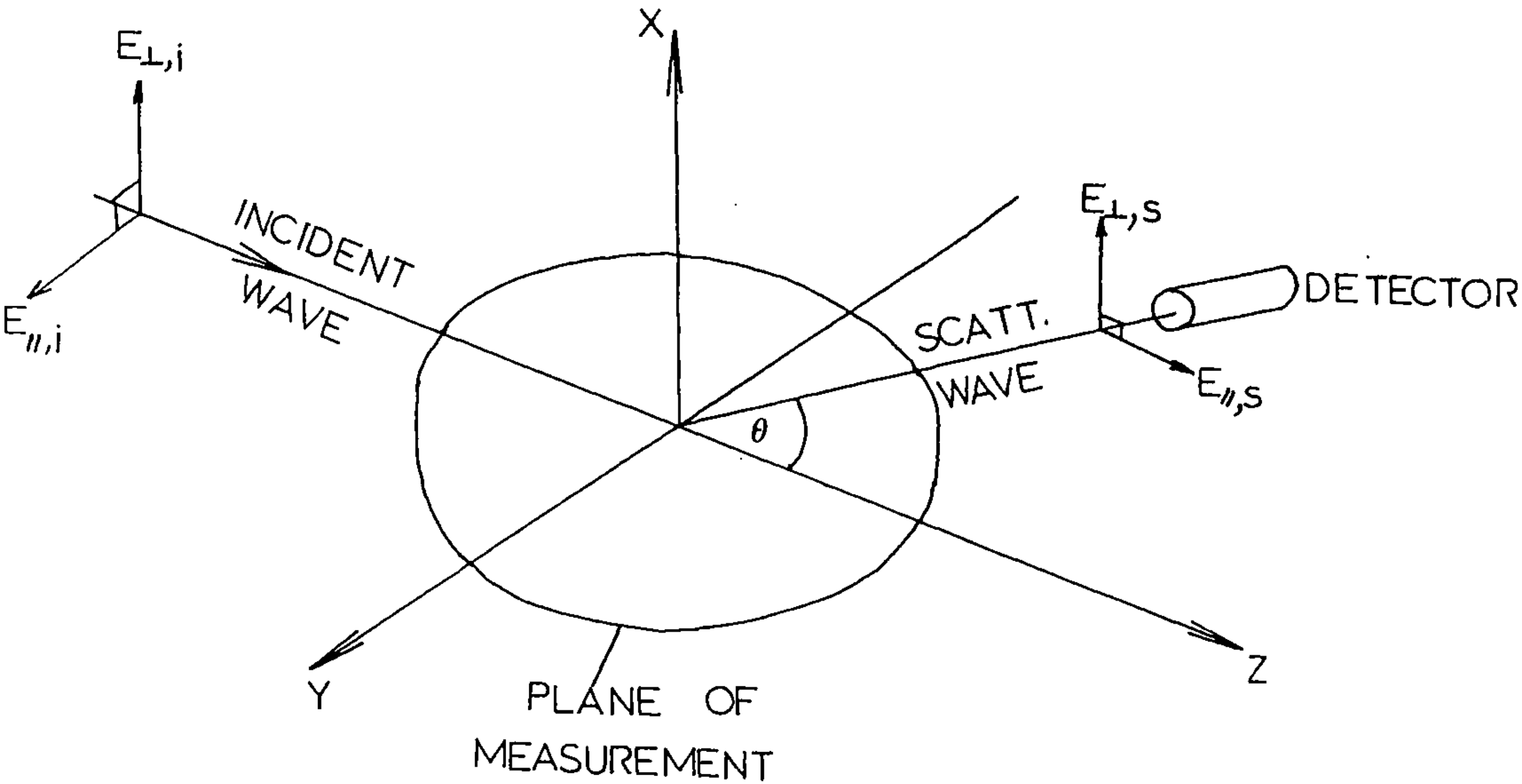

Fig.(1-2-a) Definition of the plane of measurement containing the incident and scattered waves with scattered angle θ

Table (T-1-2-a) Comparison of Various Domains of Scattering

Region	Approximation	Scattered Intensity	Comments
Rayleigh Scattering	$x << 1$ $x \mid m-1 \mid << 1$	$I_{\parallel}=(I_o k_o^4 \mid \alpha \mid^2)\cos^2\Theta/r^2$ $I_{\perp}=(I_o k_o^4 \mid \alpha \mid^2)/r^2$	Polarisation of particle is proportional to incident field α = polarisability e.g. for a sphere $\alpha = \frac{3V}{4}\left(\frac{m^2-1}{m^2+2}\right)$ where V is the volume Valid to within 10% for $x \mid m \mid < 0.6$ Valid to within 1% for $x \mid m \mid < 0.2$
Rayleigh-Gans-Debye Scattering (RGD)	$\mid m-1 \mid << 1$ $x \mid m-1 \mid << 1$	$I_{\parallel}=\frac{(I_o k_o^2 V)}{r^2}\left\|\frac{m-1}{2\pi}\right\|^2 \mid R(\Theta,\phi) \mid^2 \cos^2\Theta$ $I_{\perp}=\frac{(I_o k_o^2 V)}{r^2}\left\|\frac{m-1}{2\pi}\right\|^2 \mid R(\Theta,\phi) \mid^2$	$R(\Theta,\phi)=\frac{1}{V}\int_v \exp(i\delta)dv$ where δ is the relative phase of ray scattered by dv. Scatterers are weak i.e. no reflection Also no added phase shift or absorption
Large Particles	$x >> 1$ $x \mid m-1 \mid >> 1$	$I \propto \left[\frac{2J_1(k_o a \sin\Theta)}{k_o a \sin\Theta}\right]^2 \mid K(\Theta) \mid^2$	$K(\Theta)$ = inclination factor $K(\Theta)$ 1 for far field (Θ small) It can be shown that $\mid K(\Theta) \mid^2 = \frac{1}{2}(1 + \cos^2\Theta)$ for large Θ* Use geometrical optics and diffraction theory
Anomalous Diffraction	$x >> 1$ $\mid m-1 \mid << 1$	$I(\Theta)=k^2a^4 \mid A(\rho,z) \mid^2 I_o/r^2$ $A(\rho,z)=\int_0^{\pi/2} (1-\exp(-i\rho\sin\zeta))$ $\times J_o(z\cos\zeta)\cos\zeta\sin\zeta d\zeta$	$\rho=2x(m-1)$, $z = x\,\Theta$ The wave is mainly transmitted and interferes with the diffracted wave.
Total Reflection	$m \to \infty$	$I_{\parallel}= x^6 (1-\frac{1}{2}\cos\Theta)^2$ $I_{\perp}= x^6 (\cos\Theta - \frac{1}{2})^2$	$m = n_1-n_2$ $m \to \pm\infty$ i.e. $n_1 \to \infty$ or $n_2 \to \infty$

* see (Hodkinson, 1966)

found in Kerker (1969) and Van de Hulst (1957). For a mathematical study see, for example, Saxon (1974), Bates (1975), Stratton (1941) and Bayvel and Jones (1981).

1.3 Detection of fibres.

(i) Sampling methods.

The method normally accepted for ascertaining the concentration of airborne fibres consists of manual counting and sizing by phase contrast microscopy as reported by Edwards and Lynch (1968) and Addingley (1966). The sample is collected by filtration on a nucleopore filter and subsequently examined with an electron microscope (Spurny et.al.,1976; Henry et.al., 1972).

Gadsden et.al. (1970) used an infra-red technique to detect chrysotile which has a sharp infra-red absorption band at 2.72μm. However, this method is unsuitable for amphibole asbestos minerals (e.g.amosite, crocidolite, etc.), because the absorption is considerably weaker.

Goodhead and Martindale (1969) describe an X-ray diffraction method for determining amosite and chrysotile concentrations in the atmosphere. The disadvantage of this technique is that detection is only possible if a sample of 30mg or more is collected.

These methods are relatively imprecise due to human errors in sample preparation and interpretation of results. In addition, significant time delays occur during which the concentration of fibres in the environment under test can change considerably.

Up to date reviews of sampling methods have been carried out by Cadle (1975) and Allen (1975).

(ii) Advantages of using Light Scattering

Due to the non-intrusive nature of light, scattering is a very powerful diagnostic tool. It has many interdisciplinary applications including pollution measurement (Eiden, 1966), astrophysics (Wickramsinghe, 1967) and biological scattering systems (Wyatt,1968). Here we are only concerned with scattering by macroscopic particles, thus any quantum mechanical effects are neglected.

The angular distribution of scattered light is related to the physical properties of the scatterer such as shape, size and refractive index. Also for non-spherical particles the scattered light contains information about the orientation of the particle. Thus it is possible to ascertain the physical characteristics of particles by measuring the scattered light.

A notable distinguishing feature of asbestos dust is that it has cylindrical shape (see P-1-3-1-2). Since different particle shapes exhibit different light scattering characteristics it should be possible to extract the form anisotropy (shape) of the scatterer. A significant advantage of using light scattering is that in-situ monitoring is carried out and with a mini-computer real time monitoring of potentially hazardous environments is possible.

(iii) Light Scattering Techniques for Particle Sizing

Optical sizing can be broadly divided into imaging and non-imaging types. The former include flash photography (Beer and Chigier,1972) and holography (Bexon et.al.,1973). Non-imaging methods can be sub-divided into two classes: those which measure sizes of a large number of particles simultaneously, and those which count and size individual particles one at a time. Optical light scattering methods

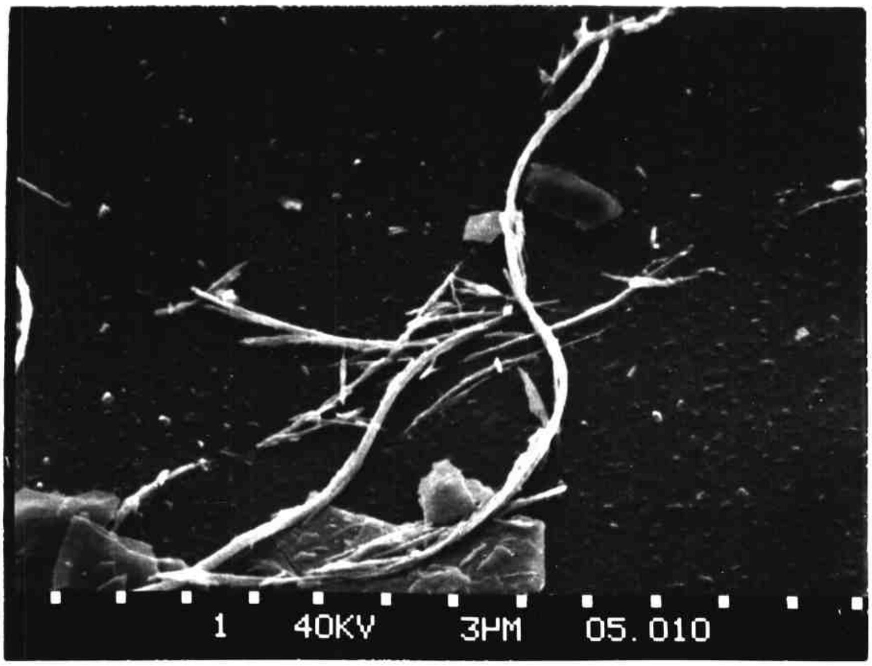

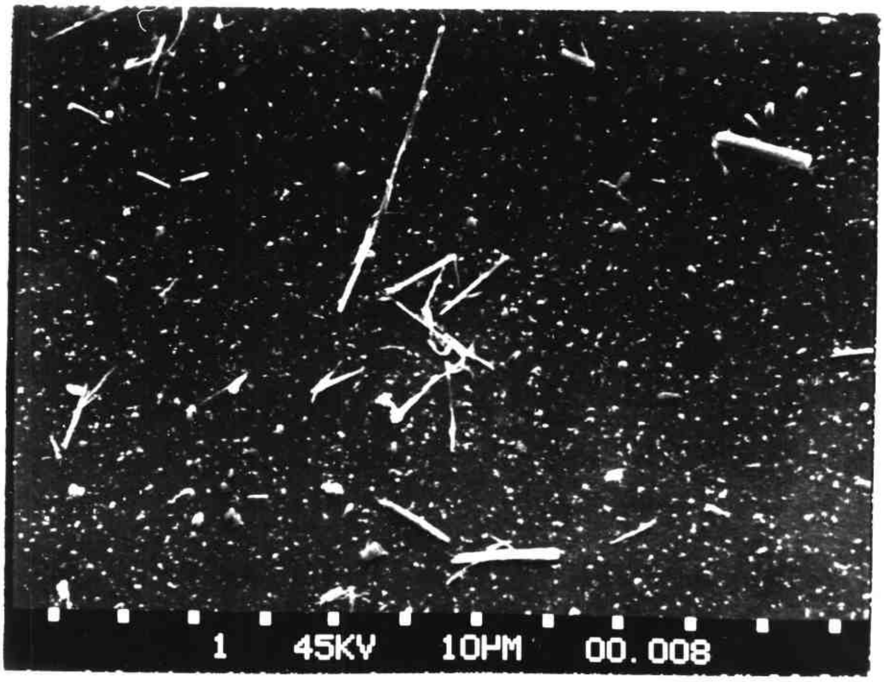

(ii)

P-1-3-1 (i) Sample of Chrysotile; each division 3μm
(ii) Sample of Amosite; each division 10μm

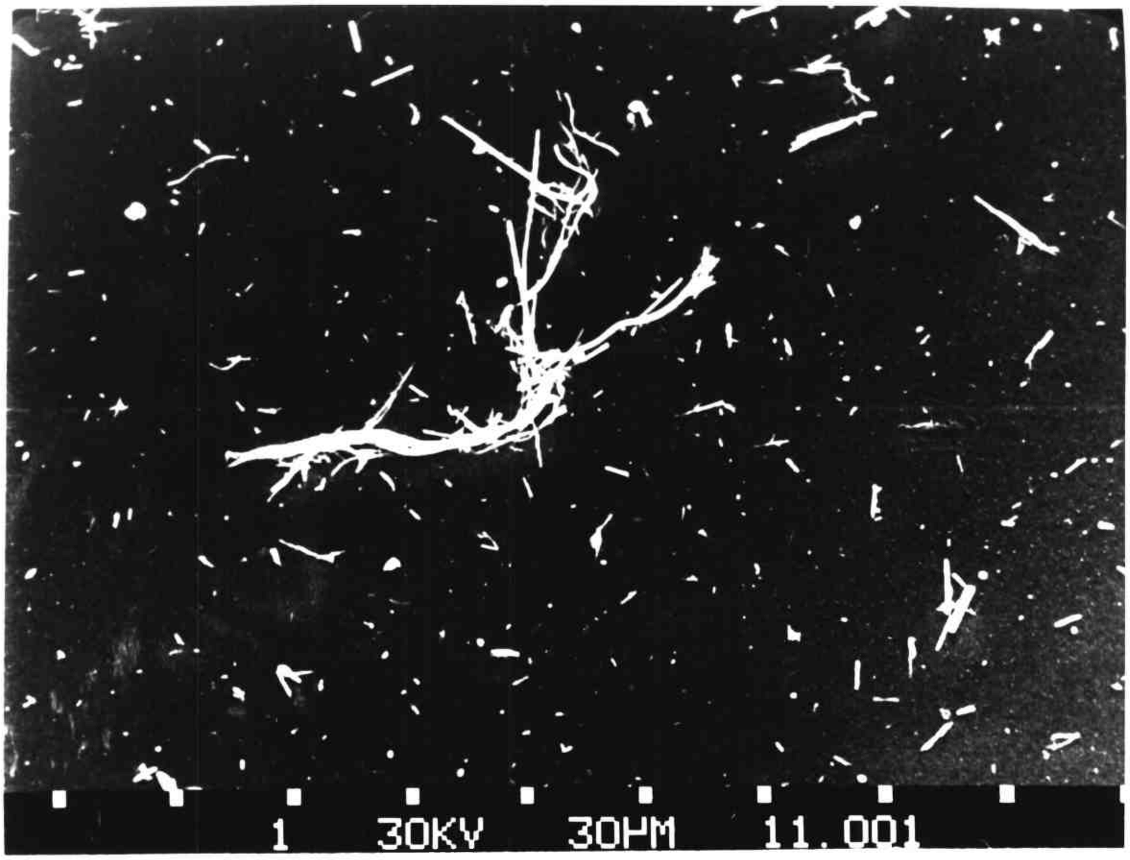

(i)

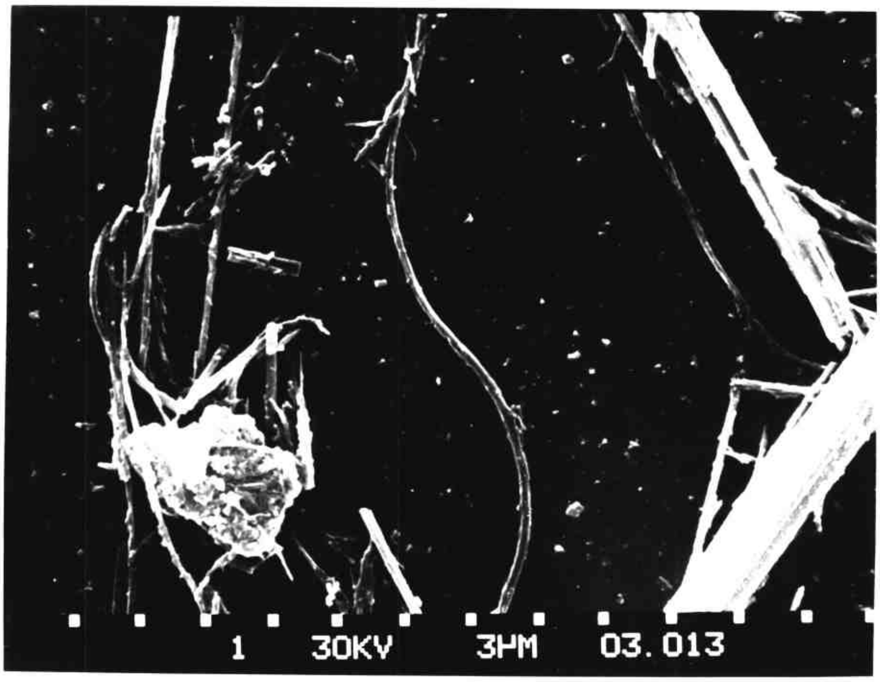

(ii)

P-1-3-2 (i) Chrysotile and Amosite; each division 30µm

(ii) Chrysotile, Amosite and Crocidolite; each division 3µm have been used to size spheres: forward diffraction technique by Hodkinson (1966), Swithenbank et.al.(1976); and fringe scattering by Hong and Jones (1976). An instrument based on the forward diffraction integration technique was developed by Swithenbank (1976) and later reported by Wenner (1979). It is currently marketed by Malvern Instruments Ltd., of Malvern.

The diffraction method is insensitive to refractive index since the forward lobe is due primarily to Fraunhofer diffraction, which is independent of the optical properties of the particle and it arises from the light passing near the particle rather than from the rays undergoing reflection and refraction. It also lacks spatial resolution since it integrates along a beam of light. It has been successfully applied to sprays, though its use is limited.

Powers and Somerford (1978) used an inversion procedure to obtain a size distribution of asbestos fibres by illuminating electron micrographs of the fibres by a coherent source of light. For He-Ne wavelength illumination, a fibre of width >10μm is considered to act as a slit which allows the use of Fraunhofer diffraction. The inversion procedure is based on the Fourier transform of the scattering pattern to obtain the distribution of widths. Large fibres can be aligned in a magnetic field (Timbrell,1975) but for fibres of diameter <10μm, the same inversion procedure can be used by using an electron micrograph as the scattering object. By this method the form anisotropy is readily apparent. However, the sample of fibres had to be obtained from the atmosphere by some means. Inevitably it is a batch process and the sample extraction mechanism destroys the true correlation between the actual concentration and the one obtained by the inversion scheme.

Timbrell (1975) distingushed between different types of asbestos by measuring the light scattered from a large number of magnetically oriented fibres.

Naylor and Kaye (1971) used an optical spatial filtering technique to demonstrate that a particle of known shape and size can be detected among a background of other particles. The method requires the construction of a spatial filter and several microscope slides under test. It is of limited use and does not have any significant advantages over existing sampling methods.

(iv) Fibrous Aerosol Monitors

An instrument designed for the detection and counting of fibres in the workshop environment is currently being marketed by the GCA Corporation of Massachusetts. Its schematic layout is shown in Figure (1-3-a). The particles are drawn by an air-pump and then exposed to a rotating electric field which induces a dipole charge on the fibres. This aligns them with the rotating field which, in turn, imposes a rotational motion of several hundred revolutions per second. Concurrently, a CW He-Ne laser beam illuminates the fibres and the resulting signals are detected by a photo-multiplier located orthogonally to the axis of the laser beam.

As the fibre rotates it emits two sharp peaked pulses for each complete fibre rotation. The degree of pulse sharpness serves as the basis of the method of fibre length discrimination. For a cylinder which has a large but finite length, the scattering function for perpendicular incidence is given by Van de Hulst (1957) as

$$I = I_0 \frac{L^2}{\pi^2 r^2} \quad \frac{\mathrm{Sin}\,\pi L\Psi/\lambda}{\pi L\Psi/\lambda} \quad T^2(\theta) \qquad (1\text{-}3\text{-}1)$$

where $T(\theta)$ is a complex function of θ, m, λ and x; L is the fibre length; m the fibre refractive index at wavelength λ;

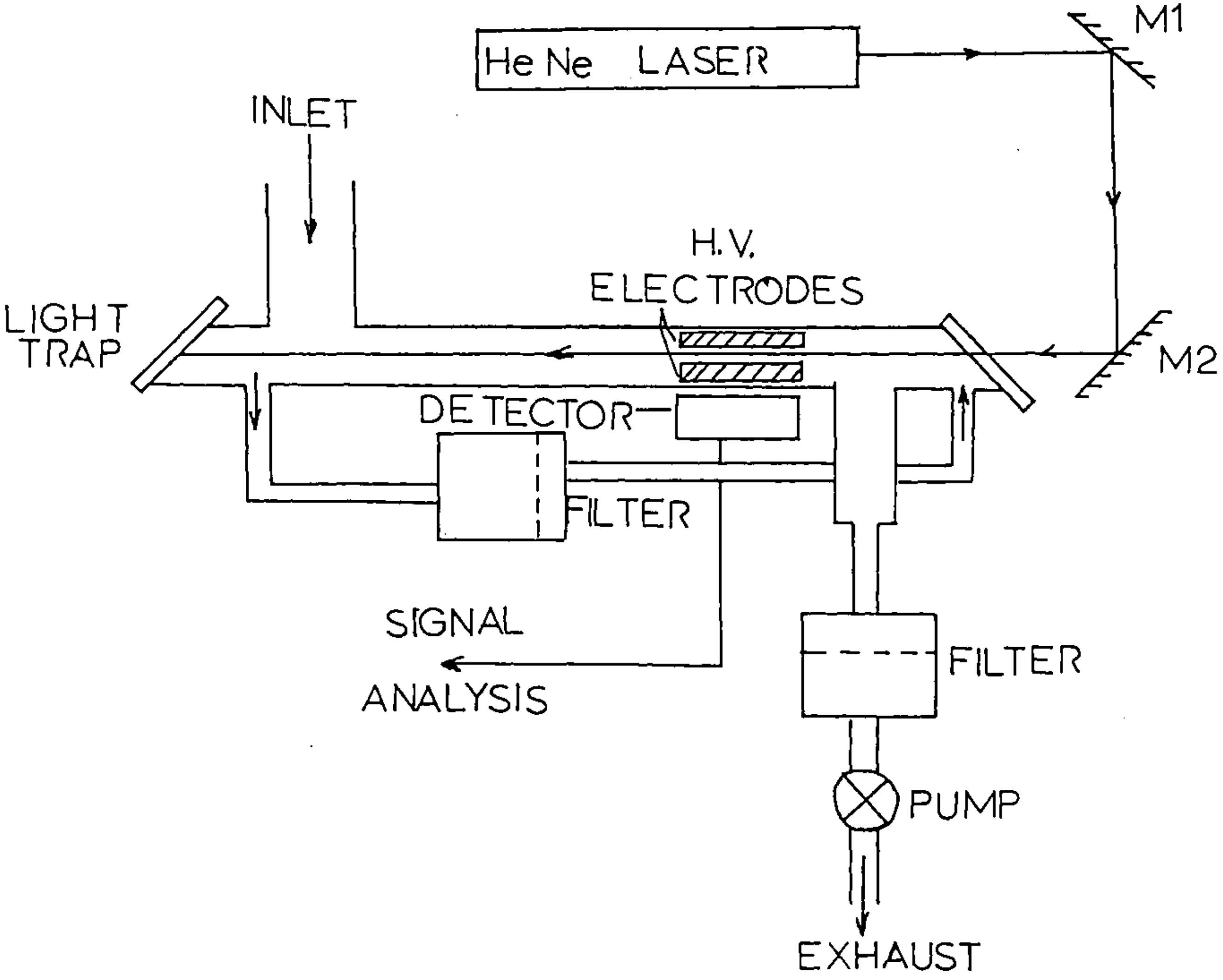

Fig.(1-3-a) Schematic lay-out of the fibrous Aerosol Monitor

ψ=fibre axis angle in the plane of rotation; θ the scattering angle (= 90° in this case) and r the distance between the fibre and the detector.

If we assume that all the parameters are constant apart from L, it turns out that as the fibre length increases pulse sharpness and amplitude increase concurrently. Thus the measurement of widths, or sharpness of these pulses uniquely characterises fibre length. Jones (1979) predicted the same phenomenon from chains assembled from Rayleigh spheres.

Using a similar principle, work has been carried out by Chubb (1977) to develop a prototype fibre monitor. The main difference being that two signals are detected using a pair of photo-multipliers and the field being applied, in turn, to a pair of cylindrical electrodes. However, results obtained did not establish a clear distinguishability between fibres and non-fibrous particles.

The methods outlined above are very elegant for monitoring fibres and building up a size distribution. Their advantages lie in the independence from electrical properties and the index of refraction of fibres, and the relative simplicity of signal processing is attractive. However, there are several disadvantages, as listed below:

(a) The measurement of the diameters of the fibres is not apparent. This is important for monitoring asbestos fibres since carcinogenicity depends primarily on fibre diameter as reported by Bogovski et.al.(1972).

(b) The fibres are drawn with an air-pump thus preventing an accurate correlation of the results with the original environment.

(c) The amount of light scattered by a non-spherical particle depends not only on the diameter of the particle but on its length to diameter ratio (aspect ratio) and on the orientation of the fibre with respect to the light source (Gentry and Spurny, 1978). Consequently, irregularly shaped dust particles present among the sampled fibres are likely to give ambiguous results.

(v) In-situ detection

In order to obtain a true concentration measurement of airborne fibres, in-situ detection is the ideal. This necessitates the use of an optical light scattering method in preference to readily available sampling methods whose reliability is questionable.

Holve and Self (1979) and Holve (1980) describe an optical method for in-situ measurement of particles. Essentially the method is a variation of the forward diffraction method with analysis for defining the test space. An elegent inversion technique is used to eliminate the dependence on particle trajectory. The system is automated to calculate particle size distributions. However, despite its on-line attraction of in-situ measurement the method does not provide information about particle shape.

1.4 Laser Doppler Anemometry (LDA)

Particle sizing using LDA was descibed by Farmer (1972), Fristrom et.al,(1973) and Eliasson et.al.(1974). LDA was originally used for velocity measurement as indicated by Yeh and Cummings (1964) and Durst and Whitelaw (1971,1976).

Two laser beams are made to cross at a point to form an interference pattern and a particle traversing these fringes generates an alternating signal, the frequency of which is proportional to the velocity. However, the amplitude of the signal is dependent upon the size and the optical properties of the particle. In general, an alternating signal can be written

$$I = A_1 + B_1 \cos \omega t \qquad (1\text{-}4\text{-}1)$$

where I is the intensity and ωt is the phase. Hong and Jones (1976) have developed a method for sizing particles by measuring the visibility given by

$$\text{Visibility} = \frac{B_1}{A_1} \quad . \qquad (1\text{-}4\text{-}2)$$

An alternative is to measure the mean intensity A_1 which in certain circumstances can be shown to be a linear function of size (Chigier,1976). Hong (1976) has made a comparison between the fringe scattering method and the foward diffraction scheme. A summary is presented in Table T(1-4-a). It is apparent that for counting individual particles the fringe scattering mode seems most appropriate. However, irregular particles transversing the test space would in general, be randomly aligned and the form anisotropy would have to be extracted by some other means.

1.5 Anisotropy

Two types of anisotropy can be defined: form anisotropy due to shape and optical anisotropy due to refractive index . For an isotropic homogeneous particle, such as a sphere, the two orthogonal components of the incident electric wave are scattered equally (i.e.$S_3 = S_4 = 0$ in the scattering Matrix equation (1-2-12)). Thus, there is no nett rotation of the field and the scattered vector retains the incident polarisation. This is not the case for a non-spherical anisometric particle such as a cylinder where scattering properties vary with the incident polarisation.

For anisotropic particles, in general, we have to retain

TABLE (1-4-a) Comparison of fringe scattering and forward diffraction scattering

System	Fringe Scattering	Forward Diffraction
Method	Double crossed laser beams. use Mie theory	Single laser beam use Diffraction theory
Measured Parameter	Visibility	Scattered light intensity near $\theta = 0^{\circ}$
Characteristics	(a) Not required to assume a particle size distribution (b) High spatial resolution (c) Best applied to tenuous clouds (for test volume of $1 mm^3$, the maximum particles density is $10^9 m^{-3}$)	(a) a size distribution is assumed (b) Light integrated along incident beam, hence low spatial resolution in forward direction. (c) Best applied to moderate dense particle clouds to ensure representative sample in beam. Multiple scattering limits upper concentration

the complete scattering matrix (Equation (1-2-12)). Thus in Figure (1-2-a) if $E_{\perp,i} = 0$ then both $E_{\perp,s}$ and $E_{\parallel,s}$ are non-zero.

One method of describing anisotropy is via the Stokes' Matrix.

$$\begin{pmatrix} I_{sca} \\ Q_{sca} \\ U_{sca} \\ V_{sca} \end{pmatrix} = \frac{S}{r^2} \begin{pmatrix} I_{c} \\ Q_{c} \\ U_{c} \\ V_{c} \end{pmatrix} \qquad (1\text{-}5\text{-}1)$$

where $I = I_{\parallel} + I_{\perp}$; $Q = I_{\parallel} - I_{\perp}$; $U = 2\sqrt{I_{\parallel} I_{\perp}} \text{Cos}(\phi_{\parallel} - \phi_{\perp})$; $V = 2\sqrt{I_{\parallel} I_{\perp}} \text{ Sin}(\phi_{\parallel} - \phi_{\perp})$ and ϕ represents the phase.

Form anisotropy is easily detectable if an external field is applied to a system of anisotropic particles. The deformation of particle shapes produces alignment with the field giving rise to optical anisotropy producing birefringence, (Kerker, 1969). Electric or magnetic fields have been used to align particles (Jennings and Morris, 1975; Morris et.al.,1975; Ravey and Mazeron, 1975).

A widely used method of studying colloidal and macromolecular systems has been the application of a hydrodynamic field where flow conditions produce an alignment. Figure (1-5-a) shows a rod subjected to a flow field and its tendency to align its axis with the stream lines. The balance produced between the Brownian motion and the applied force results in a distribution of orientations. Cerf and Scheraga (1952) have shown that the optical effect of double refraction produces birefringence. Jones and Wong (1975) used streaming birefringence to demonstrate the presence of anisotropic particles in a flame.

A general feature of anisotropy is to increase the scattering and absorption by particles (Chylek, 1977;

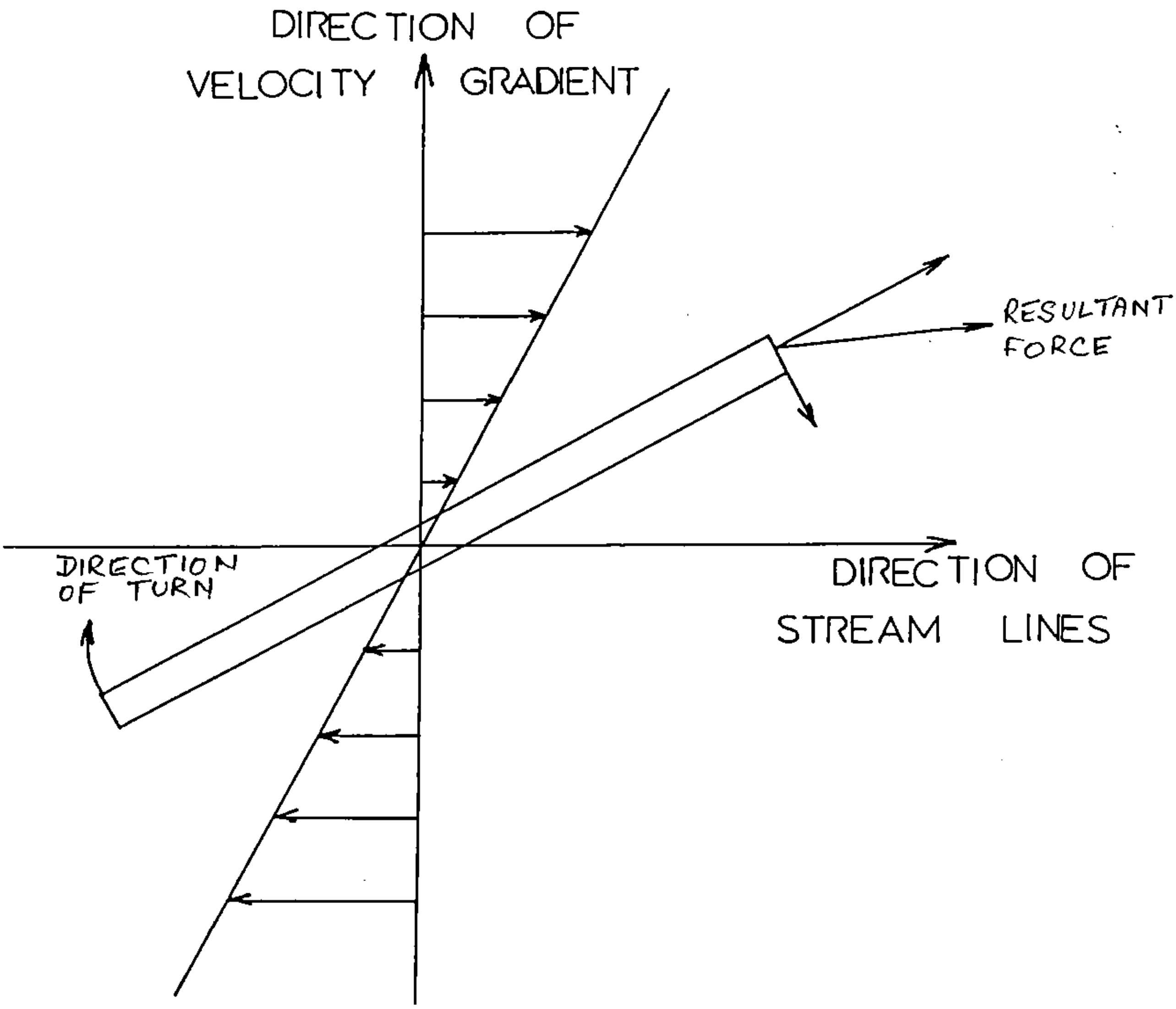

Fig.(1-5-a) Effect on a rod subjected to a hydrodynamic flow field

Kerker, 1969; Greenberg, 1972; Jones, 1972). Anisotropy of refractive index will not be treated here, but informative details can be found in Born and Wolf (1975) and Kerker (1969).

1.6 Aim of this work

The essence of the problem is to devise a system capable of distinguishing between fibrous and non-fibrous shapes. Anisotropy can be detected by several optical processes such as depolarisation and streaming birefringence as outlined by Kerker (1969). The first of these does not readily distinguish the effect of anisotropy. The second is shape sensitive and relies on fluid flow conditions to produce alignment of a sample of form anisotropic particles. In a light scattering system measurement in the forward direction is relatively independent of refractive index. Thus for $\theta = 0$, the form anisotropy should be apparent.

In order to develop a non-destructive technique for in-situ monitoring of airborne asbestos fibres the use of light scattering has many advantages as outlined earlier. Since the scattered light contains information about form anisotropy it is desirable to explore a light scattering technique which is sensitive to size and shape, but relatively insensitive to optical properties.

The detection and measurement of concentration of acicular shaped particles is the prime objective of this work bearing in mind that the ultimate objective is the production of an instrument which can make on-line and in-situ concentration measurements of asbestos fibres. The Health and Safety Executive (HSE) have stipulated that the fibres considered toxic and carcinogenic have the following specifications:

5μm < length < 10μm

Diameter > 0.5μm

or Aspect Ratio > 3 : 1

1.7 Concluding Remarks

To date there is no satisfactory system available for continuous monitoring of asbestos fibres in the air. Sampling methods contain inherent experiemtal errors and entail considerable time delays. Fibre monitors currently marketed in the U.S.A. are unreliable and, more importantly, their inability to measure fibre diameter is a severe handicap since this is related to carcinogenicity (Bogovsky et.al., 1972).

Light scattering methods have been used mainly for nearly spherical particle sizing such as atmospheric aerosols (Ferrara et.al.,1970), biological cells (Wyatt,1972), cement particles (Cornillaut,1972) and pollens (Wertheimer and Wilcock, 1976). The majority of the work with fibres has considered single fibres, for example, metal wires (Lundberg,1969) and glass filaments (Farone and Kerker,1966; Cooke and Kerker,1969).

The forward diffraction method (Hodkinson,1966; Swithenbank et.al.,1976) bases its analysis on Fraunhofer diffraction, although rigorous Mie theory is readily available for spheres (Kerker,1969). There is a lack of rigorous theory for irregularly shaped particles, but one could use the diffraction theory of a slit in the case of a fibre. Jones (1974) and Chou (1976) have examined the detailed theory of spheres in the fringe scattering system. It is apparent that for small collecting apertures near the forward direction, diffraction theory may be valid (Chu and Robinson,1977; Hong and Jones,1976; Chigier, 1976). It would appear that fringe scattering is the most appropriate technique for fibre determination since it works best in the particle counting mode.

In order to determine the form anisotropy of the scatterer, it is important to know the polarisation of the incident and scattered waves. In this way the size and shape of the fibre can be determined. However, analysis must incorporate the effect of the orientation of the particle on scattered light.

CHAPTER TWO

THEORETICAL INVESTIGATION OF LIGHT SCATTERING BY AN INFINITE CYLINDER AT OBLIQUE INCIDENCE.

2.1 Introduction

One of the co-ordinate systems for which the wave equation is separable is that of circular cylindrical symmetry. However, rigorous solutions have only been obtained for an infinite cylinder. Lord Rayleigh (1881) obtained the solution at perpendicular incidence well before Lorentz (1890), Mie (1908) and Debye (1909) obtained rigorous solutions for a sphere. Von Ignatowsky (1905), Seitz (1905,1906) and Von Schaeffer (1907) extensively studied scattering at perpendicular incidence from infinite cylinders. The study of scattering from cylindrical structures was continued by researchers interested in microwaves and radiowaves (Mentzner,1955; King and Wu, 1959; Wait,1959). The optical properties of infinite cylinders are of particular interest in calculating the transmission of thermal radiation through fibrous insulations (Larkin,1957; Larkin and Churchill, 1959).

The solution of the problem of scattering of a plane polarised electro-magnetic wave by an infinite cylinder at oblique incidence was first presented by Wait (1955,1959). Farone and Querfeld (1965) rederived the solution using Van de Hulst's (1957) notation in a form more suitable for machine computation. In this Chapter, the theory of scattering for oblique incidence for an infinite cylinder is derived using Stratton's (1941) field expansions. The approach is the same as outlined by Bayvel and Jones (1981). The solution is given in a more general form, not being divided into intensities representing different orthogonal polarisations.

2.2 Solution of the Wave Equation

In the last Chapter, a method was outlined for finding the solutions of the vector wave equation

$$\nabla^2\underline{E} + k_0^2 m^2 \underline{E} = 0 \qquad (2\text{-}2\text{-}1)$$

by solving the scalar wave equation

$$\nabla^2\Psi + k_0^2 m^2 \Psi = 0 \qquad (2\text{-}2\text{-}2)$$

and obtaining the vector solution using the appropriate vectors $\underline{M}$ and $\underline{N}$ (Stratton,1941). The general expansions of the electric and magnetic vectors are

$$\underline{E} = -\sum_{n=-\infty}^{\infty} (a_n \underline{M}_n + b_n \underline{N}_n)$$

$$\underline{H} = -\frac{k}{i\omega\mu\mu_0} \sum_{n=-\infty}^{\infty} (b_n \underline{M}_n + a_n \underline{N}_n) \qquad (2\text{-}2\text{-}3)$$

Consider an infinite homogeneous isotropic cylinder, as shown in Figure (2-2-a) of arbitrary orientation where the tilt is defined by χ and ψ, the spherical polar and azimuthal angles respectively. The incident wave is defined in the (x,y,z) co-ordinates system while the cylinder rests in the (x_1,y_1,z_1) system. The scalar wave equation in cylindrical co-ordinates (ρ,α,z_1) is

$$\frac{1}{\rho}\frac{\partial}{\partial\rho}\left(\rho\frac{\partial\Psi}{\partial\rho}\right) + \frac{1}{\rho^2}\frac{\partial^2\Psi}{\partial\alpha} + \frac{\partial^2\Psi}{\partial z^2} + k^2 m^2 \Psi = 0 \qquad (2\text{-}2\text{-}4)$$

and it is satisfied by

$$\Psi_n = e^{ihz_1} Z_n(\sqrt{k^2-h^2}\,\rho)\, e^{-in\alpha} \qquad (2\text{-}2\text{-}5)$$

where Z_n is a cylindrical Bessel function and $h = k\cos\chi$. The vector solution is found via $\underline{M}$ and $\underline{N}$ using

$$\underline{M} = \nabla\wedge\hat{z}_1\Psi \qquad \underline{N} = \frac{1}{k}\nabla\wedge\underline{M} \qquad (2\text{-}2\text{-}6)$$

where $\hat{z}_1$ is the unit vector along Z_1. Substituting $k^* = \sqrt{k^2-h^2}$ gives,

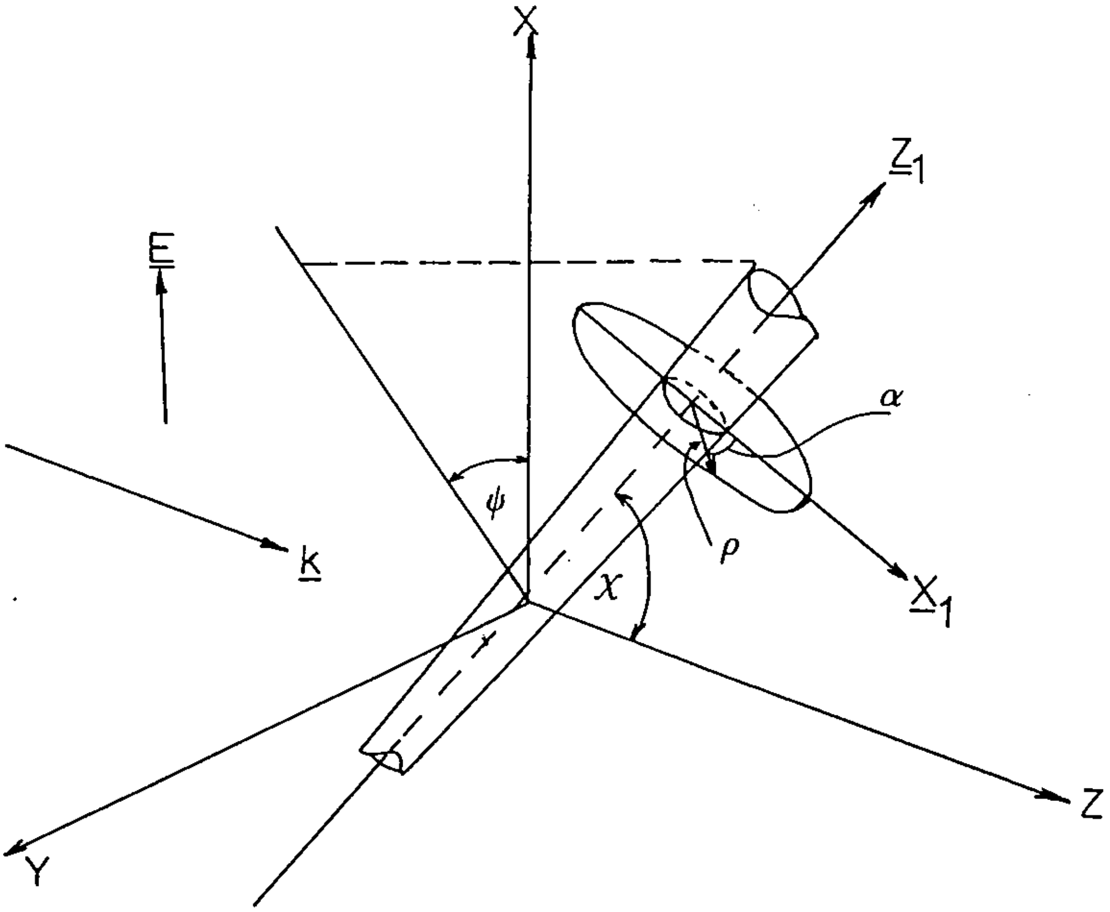

Fig.(2-2-a) Definition of co-ordinates for scattering by an infinite cylinder

$$\underline{M}_n = e^{i(hz_1-n\alpha)}\left(\frac{n}{\rho} Z_n(k^*\rho)\hat{\rho} - iK^*Z_n^{1}(k^*\rho)\hat{\alpha}\right)$$

$$\underline{N}_n = e^{i(hz_1-n\alpha)}\left(-\frac{hk^*}{k} Z_n^{1}(k^*\rho)\hat{\rho} + \frac{ihn}{k\rho} Z_n(k^*\rho)\hat{\alpha} + \frac{ik^*}{k} Z_n(k^*\rho)\hat{z}_1\right) \tag{2-2-7}$$

where Z_n is selected as follows:

(i) Incident Wave: $J_n(k_0^*\rho)$ is obtained from expansion of the plane wave in cylindrical co-ordinates.

(ii) Internal Wave: $J_n(k_m^*\rho)$ is chosen such that it is finite at $\rho = 0$

(iii) Scattered Wave: In the far field $\rho\to\infty$

$$H_n^{(1)}(k_0^*\rho) \simeq \frac{i^n(1-i)}{\sqrt{\pi k_0^*\rho}}\, e^{ik^*\rho}$$

This represents an outgoing cylindrical wave.

Here J_n are the Bessel functions of the first kind and $H_n^{(1)}$ are Hankel functions of the first kind (Abromowitz and Stegun, 1964).

The direction of the incident vector is arbitrary. The cylinder is oriented such that the azimuthal angle ψ is the angle between the cylinder axis and the incident wave. The incident electric field is given by

$$\underline{E}_{inc} = \hat{x}E_0\, e^{ik_0 z} \tag{2-2-8}$$

and it can be expanded in terms of $\underline{M}_n$ and $\underline{N}_n$ using Equation (2-2-3) giving

$$\underline{E}_{inc} = \frac{1}{k_0^*}\sum_{n=-\infty}^{\infty}(-i)^n\left(\sin\psi\underline{M}_n^{(i)} - i\cos\psi\underline{N}_n^{(i)}\right)$$

$$\underline{H}_{inc} = \frac{k}{i\omega\mu\mu_0}\sum_{n=-\infty}^{\infty}\frac{(-i)^n}{\lambda}\left(\sin\psi\underline{N}_n^{(i)} - i\cos\psi\underline{M}_n^{(i)}\right) \tag{2-2-9}$$

where $k_0^* = k_0 \sin\chi$

i.e. $a_n = -(-i)^n\dfrac{\sin\psi}{\lambda}$

$$b_n = i(-i)^n\frac{\cos\psi}{\lambda} \tag{2-2-10}$$

The expansions for the wave components for scattering from an infinite cylinder are expressed in simplified form if we define $h = k_o \sin \chi$ and $k_o^* = k_o \sin \chi$ and for the internal wave

$$k_m^* = k_o \sqrt{m^2 - \cos^2 \chi}$$

where χ is the tilt of the cylinder and m the refractive index.

By applying the electro-magnetic boundary conditions to E_z, E_α, H_z and H_α the forms of a_n^s and b_n^s are given by

$$a_n^s = \frac{A_1 B_3 + A_3 B_2}{A_1 B_1 - A_2 B_2} \qquad (2\text{-}2\text{-}11)$$

$$\hat{b}_n^s = \frac{A_3 B_1 + A_2 B_3}{A_1 B_1 - A_2 B_2} \qquad (2\text{-}2\text{-}12)$$

where

$$A_1 = \frac{k_0^*}{k_m^* J_n(k_m^* a)} \left(m^2 k_0^* J_n^1 (k_m^* a) \; H_n^{(1)} (k_o^* a) - k_m^* J_n' (k_m^* a) \; H_n^{(1)\prime} (k_o^* a) \right)$$

$$A_2 = \frac{hn}{k_0 a} \left(\frac{k_0^{*2}}{k_m^{*2}} - 1 \right) H_n^{(1)} (k_0^* a)$$

$$A_3 = (-i)^n \Bigg(\frac{\sin\psi}{k_0^*} \; \frac{hn}{k_0^* a} \left(1 - \frac{k_0^{*2}}{k_m^{*2}} \right) J_n(k_0^* a)$$

$$- \frac{i \cos \psi}{k_m^* J_n(k_m^* a)} \left(m^2 k_0^* J_n^1 (k_m^* a) J_n(k_0^* a) - k_m^* J_n(k_m^* a) J_n^1 (k_0^* a) \right) \Bigg)$$

$$B_1 = \frac{i\ k_0^*}{k_m^* J_n(k_m^* a)} \left(k_0^* J_n^1(k_m^* a)\ H_n^{(1)}\ (k_0^* a) - k_m^* J_n(k_m^* a) H_n^{(1)\prime}(k_0^* a) \right)$$

$$B_2 = \frac{ihn}{k_0 a} \left(\frac{k_0^{*2}}{k_m^{*2}} - 1 \right) H_n^{(1)}\ (k_0^* a)$$

$$B_3 = (-i)^n \left(\frac{\cos\psi}{k_0^*} \frac{hn}{k_0 a} \left(1 - \frac{k_0^*}{k_m^{*2}}\right) J_n\ (k_0^* a) \right.$$

$$\left. + \frac{i\ \sin\ \psi}{k_m^* J_n(k_m^* a)} \left(k_0^* J_n^\prime(k_m^* a) J_n(k_0^* a) - k_m^* J_n(k_m^* a) J_n^1(k_0^* a) \right) \right)$$

(2-2-13)

For normal incidence where $\chi = \pi/2$ and $h = 0$ and $k_0^* = k_0$ it is found that

$$a_n^s = (-i)^n \frac{\sin\ \psi}{k_0}\ \tilde{a}_n^s$$

$$b_n^s = -(-i)^n \frac{\cos\ \psi}{k_0}\ \tilde{b}_n^s \qquad (2\text{-}2\text{-}14)$$

where

$$\tilde{a}_n^s = \frac{J_n(k_0 a) J_n^1(mk_0 a) - mJ_n^1(k_0 a) J_n(mk_0 a)}{H_n^{(1)}(k_0 a) J_n^1(mk_0 a) - mH_n^{(1)1}(k_0 a) J_n(mk_0 a)}$$

$$\tilde{b}_n^s = \frac{mJ_n(k_0 a) J_n^1(mk_0 a) - J_n^1(k_0 a) J_n(mk_0 a)}{mH_n^{(1)}(k_0 a) J_n^1(mk_0 a) - H_n^{(1)1}(k_0 a) J_n(mk_0 a)}$$

(2-2-15)

are the original solutions of Rayleigh (1881) and Von Ignatowsky (1905)

In the far field

$$\underline{M}_n \simeq \frac{(1-i)}{\sqrt{\pi k_0^* \rho}} e^{ik_0^*\rho} i^n k_0^* e^{i(hz_1 - n\alpha)} \hat{\alpha}$$

$$\underline{N}_n \simeq \frac{-(1-i)}{\sqrt{\pi k_0^* \rho}} e^{ik_0^*\rho} i^{(n+1)} \frac{k_0^*}{k_0} e^{i(hz_1 - n\alpha)} (h\hat{\rho} - k_0^* \hat{z}_1) \qquad (2\text{-}2\text{-}16)$$

Consequently the scattered electric field is found by substituting for $\underline{M}_n$ and $\underline{N}_n$ into Equation (2-2-3), giving

$$\underline{E}_{sca} = (1-i) \frac{k_0^*}{k_0} \frac{e^{ik_0^*\rho}}{k_0^*} \sum_{n=-\infty}^{\infty} e^{i(hz_1 - n\alpha)}$$

$$X(a_n^s i k_0 \hat{\alpha} + b_n^s (h\hat{\rho} - k_0^* \hat{Z}_1)) \qquad (2\text{-}2\text{-}17)$$

Two parameters of theoretical interest are the scattering and extinction efficiency factors. The ratio of scattered power (P_{sca}) to the incident power (P_{inc}) on a particle is

$$Q_{sca} = \frac{P_{sca}}{P_{inc}} \qquad (2\text{-}2\text{-}18)$$

where Q_{sca} is the scattering efficiency. Absorption and extinction efficiencies (Q_{abs} and Q_{ext} respectively) are defined in a similar way; thus

$$Q_{ext} = Q_{sca} + Q_{abs}$$

For an infinite cylinder, it can be shown that

$$Q_{sca} = \frac{2k_0^{*2}}{k_0 a} \sum_{n=-\infty}^{\infty} (|a_n^s|^2 + |b_n^s|^2) \qquad (2\text{-}2\text{-}19)$$

$$Q_{ext} = \frac{2k_0^{*2}}{k_0 a} \sum_{n=-\infty}^{\infty} \Phi_n \qquad (2\text{-}2\text{-}20)$$

where

$$\Phi_n = \left(\mathrm{Re}(a_n^s) \cos\frac{n\pi}{2} - \mathrm{Im}(a_n^s) \sin\frac{n\pi}{2} \right) \sin\psi$$

$$- \left(\mathrm{Re}(b_n^s) \sin\frac{n\pi}{2} + \mathrm{Im}(b_n^s) \cos\frac{n\pi}{2} \right) \cos\psi \qquad (2\text{-}2\text{-}21)$$

For the special case of normal incidence $\chi = \pi/2$ and $k_0^* = k_0$, then

$$Q_{sca} = \frac{2}{k_0 a} \sum_{n=-\infty}^{\infty} \left(|\tilde{a}_n^s|^2 \sin^2\psi + |\tilde{b}_n^s|^2 \cos^2\psi \right)$$

$$Q_{ext} = \frac{2}{k_0 a} \sum_{n=-\infty}^{\infty} \left(\mathrm{Re}(\tilde{a}_n^s) \sin^2\psi + \mathrm{Re}(\tilde{b}_n^s) \cos^2\psi \right) \qquad (2\text{-}2\text{-}22)$$

At $\psi = 0$ and $\pi/2$ these an be reduced further to give the scattering and extinction efficiencies at normal incidence with cylinder axis parallel or perpendicular to the incident electric vector.

2.3 Influence of various parameters on scattering by a cylinder.

In order to establish a theoretical basis for studying the light scattered from an infinite cylinder, we have to choose which parameters are measureable and have physical significance. It can be seen from Equations (2-2-13) that a_n^s and b_n^s are functions of the refractive index m and the size parameter x $(=k_0 a)$.

The refractive index of asbestos varies considerably with type (Rajhans and Sullivan, 1981). Thus the influence of this has to be investigated. The effect of size on scattering has to be examined since $\underline{E}_{sca}$ is a function of x. Equations (2-2-15) show that at $\psi = 0$ only b_n^s is finite and at $\psi = \pi/2$ only a_n^s is finite. In order to explore the effect of orientation on scattering we can vary the polar angle χ

and investigate the behaviour of the ratio of $|E_{sca}|^2$ for the two values of $\psi = 0$ and $\pi/2$.

A computer program has been written to calculate the scattered radiation field from an infinite cylinder of arbitrary orientation. It has been tested against results quoted by several authors including Rayleigh (1918), Larkin and Churchill (1957), Van de Hulst (1957) and Kerker (1969). The first three give results for normal incidence and $\psi = 0$ and $\pi/2$ only. Kerker gives results for the general solution.

We need to study the ratio of two orthogonal intensities since this will be our subsequent basis of measurement (see Chapter 3). Thus, we define

$$R^1 = |\frac{A}{B}|^2 \qquad (2\text{-}3\text{-}1)$$

where $A = \sum_{n=-\infty}^{\infty} a_n^s$ and $B = \sum_{n=-\infty}^{\infty} b_n^s$

and explore its behaviour with increasing particle size. Here A and B are the scattered electric fields along two orthogonal directions. Figures (2-3-a-c) show R^1 plotted in forward scatter ($\theta=0$) for three values of the refractive index and for three values of χ equal to $90^\circ, 60^\circ$ and 30°. It is interesting to note that for $\chi=30^\circ$ a small change in x causes a large variation in R^1. Also it can be seen that the oscillations are damped out for a complex refractive index. Figure (2-3-d) shows R^1 plotted for the backward direction ($\theta=180^\circ$) for $m = 1.5$ and $\chi = 90^\circ$ where R^1 is very large. However at $\chi = 60^\circ$ (Figure (2-3-e)) its value is reduced considerably.

For a spherical particle orthogonal field components are scattered equally and A=B giving $R^1=1$. Theoretical plots of R^1 for an infinite cylinder (Figures (2-3-a-e)) indicate that $R^1>1$ for values of size up to $x = 10$. As stated in the

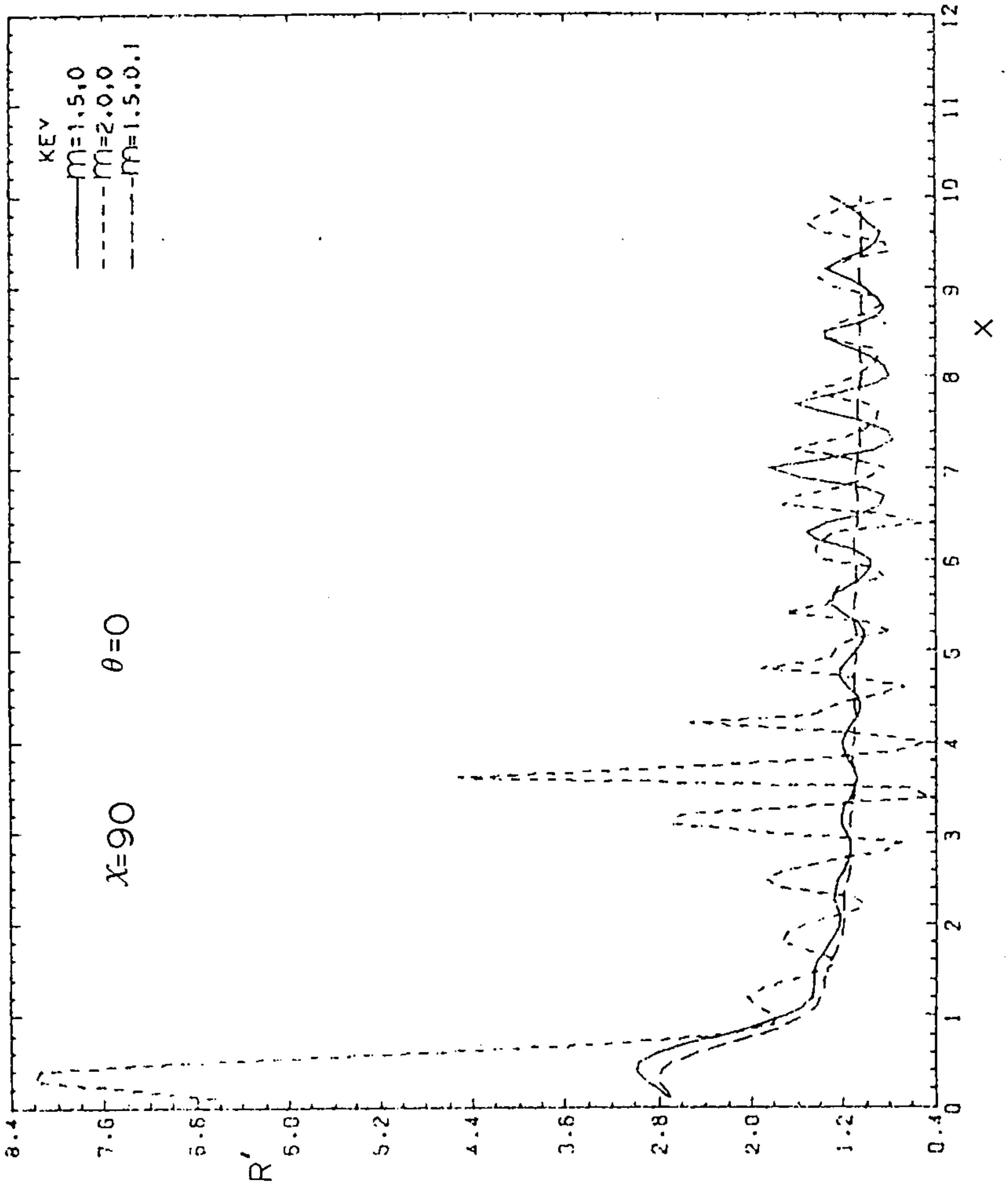

Fig.(2-3-a) Plot of R^1 against x for forward scattering $\chi = 90^{\circ}$

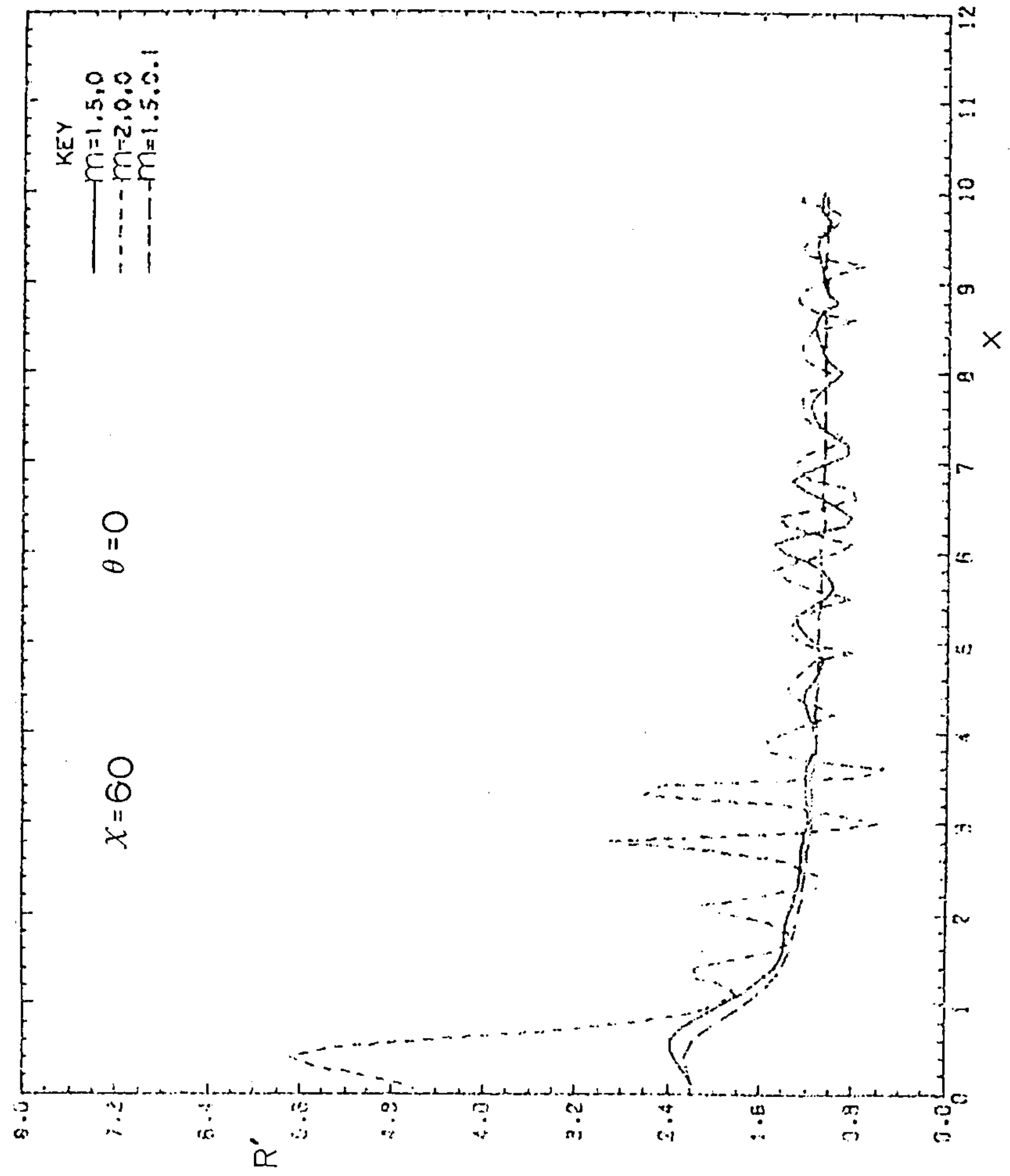

Fig.(2-3-b) Plot of R^1 against x for forward scattering $\chi=60^o$

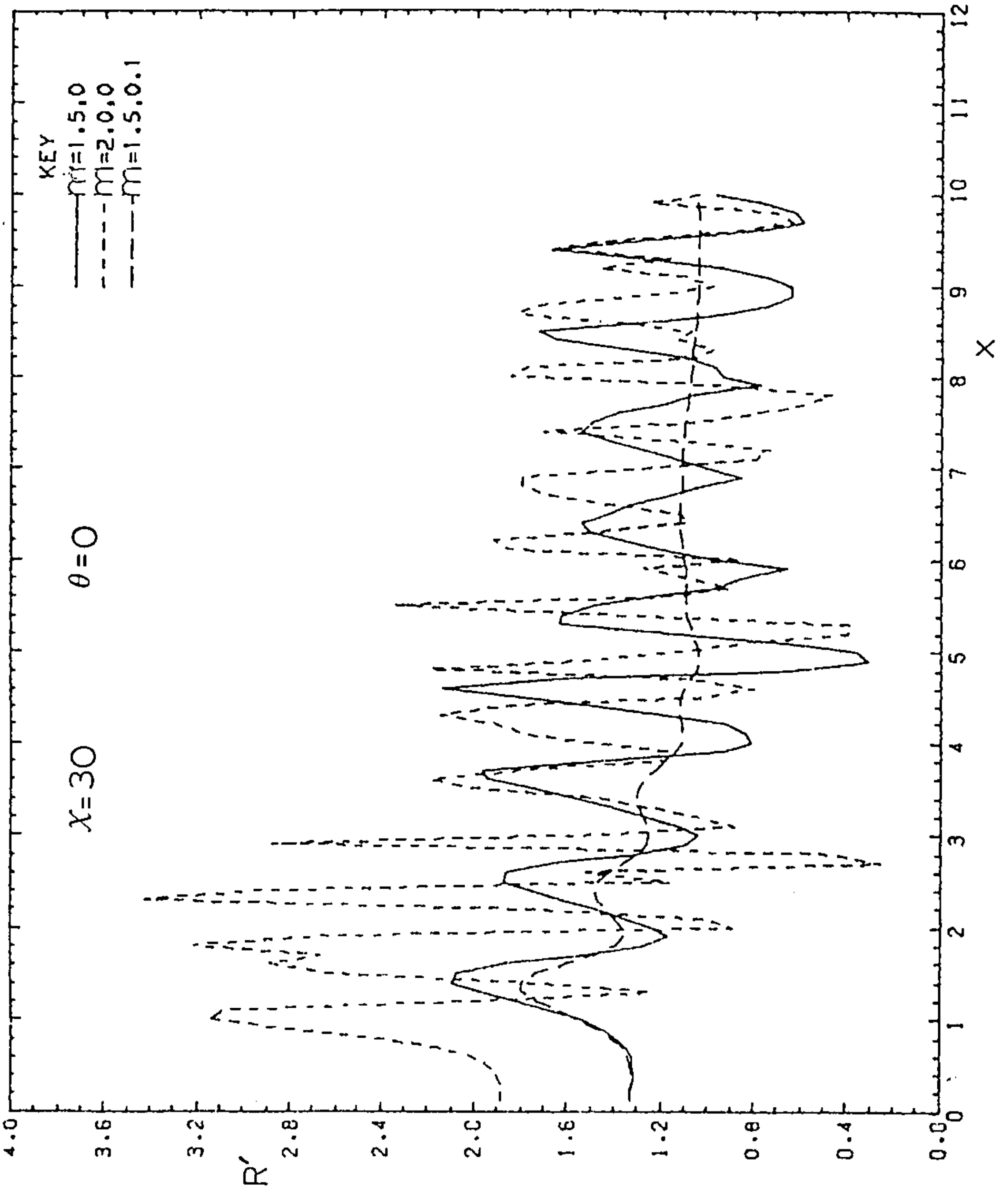

Fig.(2-3-c) Plot of R^1 against x for forward scattering $\chi=30^{\circ}$

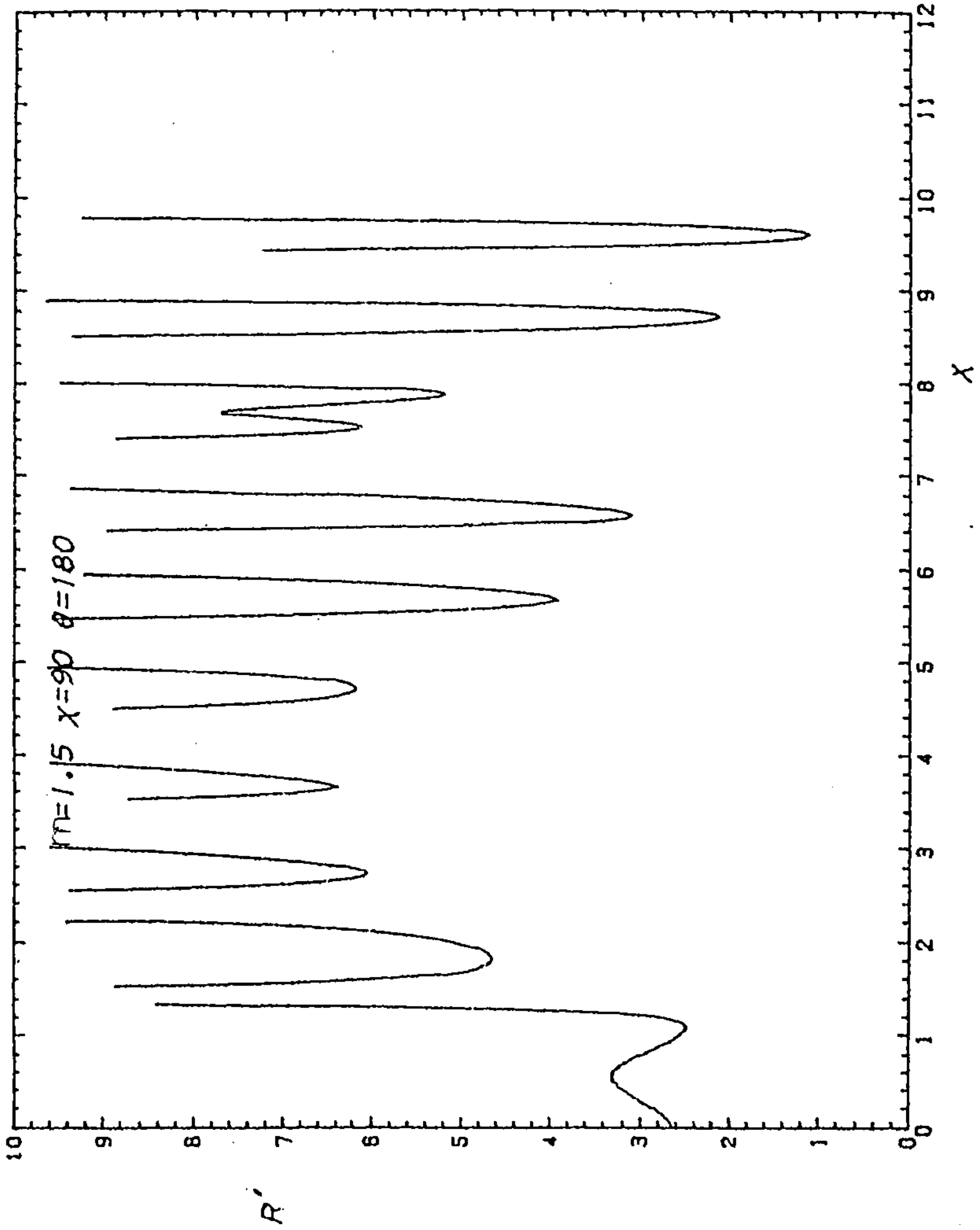

Fig.(2.3.d) Plot of R^1 against x for backward scattering χ=90°

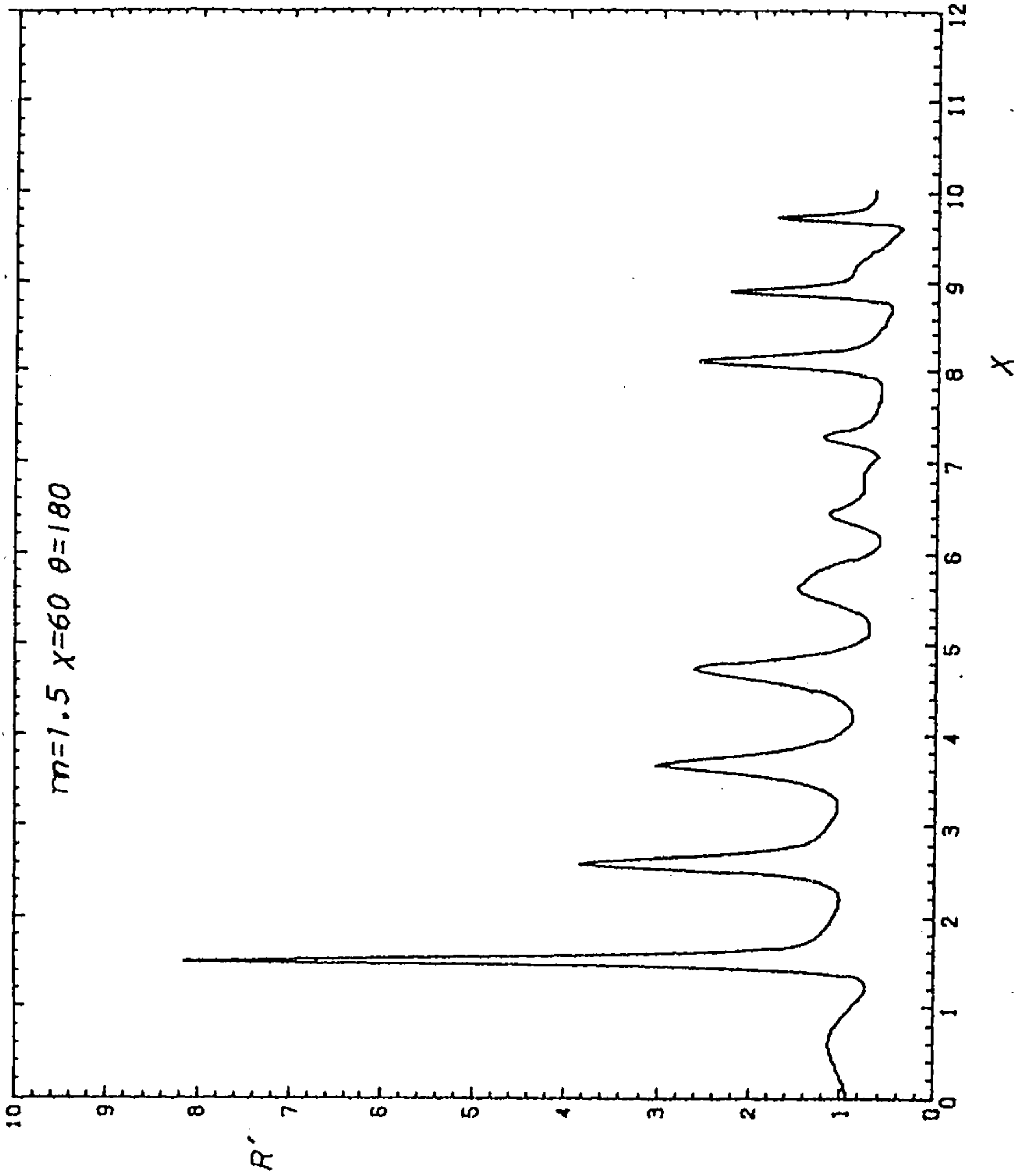

Fig.(2-3-e) Plot of R^1 against x for backward scattering χ=90°

last Chapter, we are only interested in fibres of diameter $\sim 0.5\mu m$. This gives a value for visible wavelengths of $x \sim 3$ and for this size we can see that at $\theta=0$, $R^1 \geqslant 1.2$. Thus in principle we can see this as a distinguishing parameter between spherical and cylindrical particles. These results indicate that fibres may be distinguishable even at very small values of x, almost end on incidence.

The total scattered intensity due to a_n^s and b_n^s is given by

$$I(a_n^s) = |a_n^s \cdot a_n^{s*}|$$

$$\text{and} \quad I(b_n^s) = |b_n^s \cdot b_n^{s*}| \qquad (2\text{-}3\text{-}2)$$

Figures (2-3-f-h) show $I(a_n^s)$ plotted against χ at $\theta=0$ for three values of refractive index with $\chi = 90^\circ$, 60° and 30°. Figures (2-3-i-k) show $I(b_n^s)$ plotted for the same three values of χ and in Figure (2-3-l) the variation of intensity with θ is explored for various values of χ and ψ. For back scatter, Figure (2-3-m) shows the intensity plotted against size. It can be noted that even though the ratios are higher in the backward direction, there is about twenty times reduction in the scattered intensity compared to the forward direction.

The scattering and extinction efficiencies (Q_{sca} and Q_{ext}) are plotted in Figures (2-3-n-s) over the range $x=0$ to 10. for various values of χ, ψ and m. For real refractive index the scattering efficiency oscillates about the value $Q=2$ and $Q_{ext} = Q_{sca}$. However for a complex refractive index both Q_{sca} and Q_{ext} reach a maximum value at $x = 1.0$ and maintain this value with increasing x.

2.3.2 Effect of optical anisotropy

Since we use quartz in our experiments (see Chapter 3)

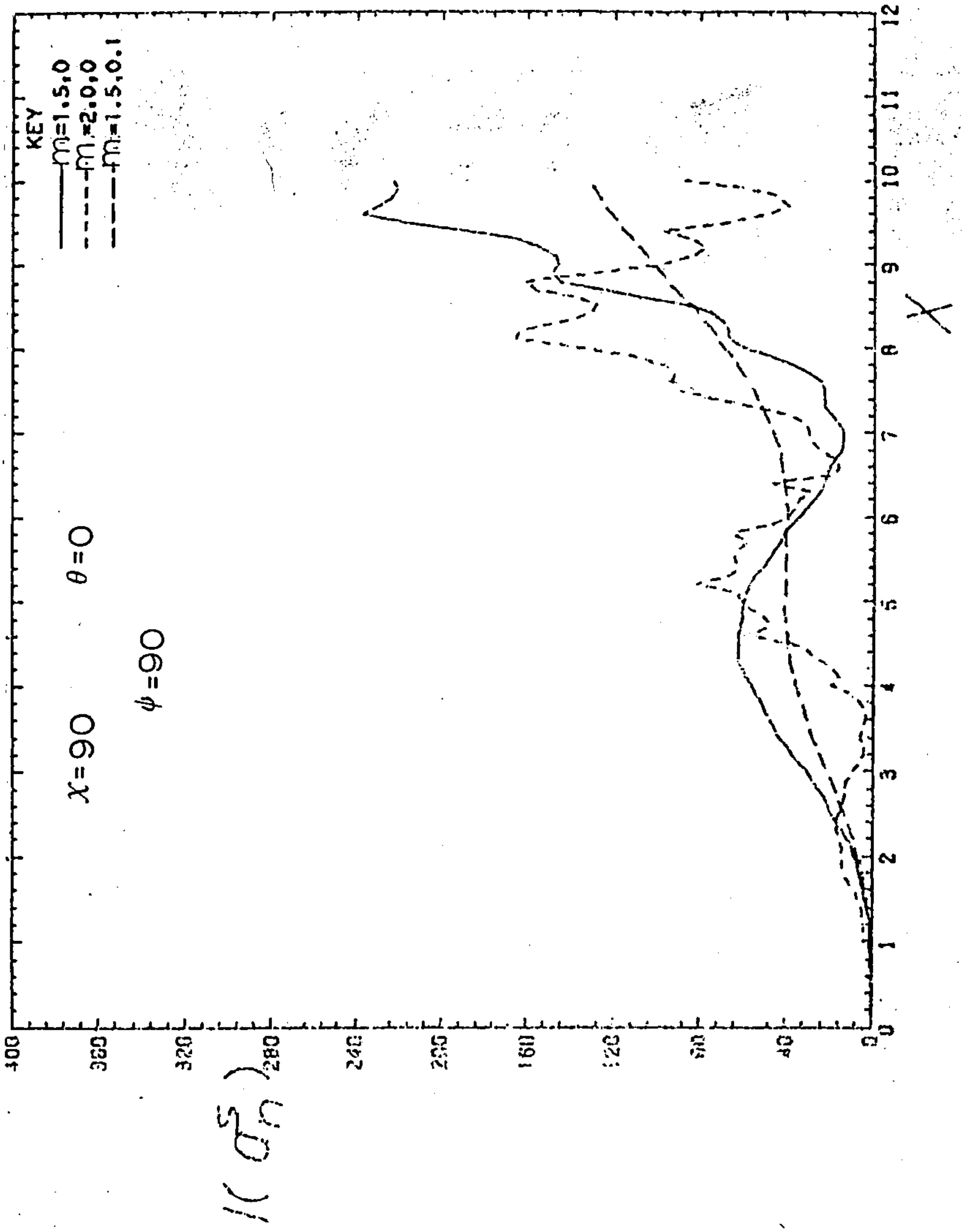

Fig.(2-3-f) Plot of intensity $I(a_n^s)$ against x for forward scattering χ=90

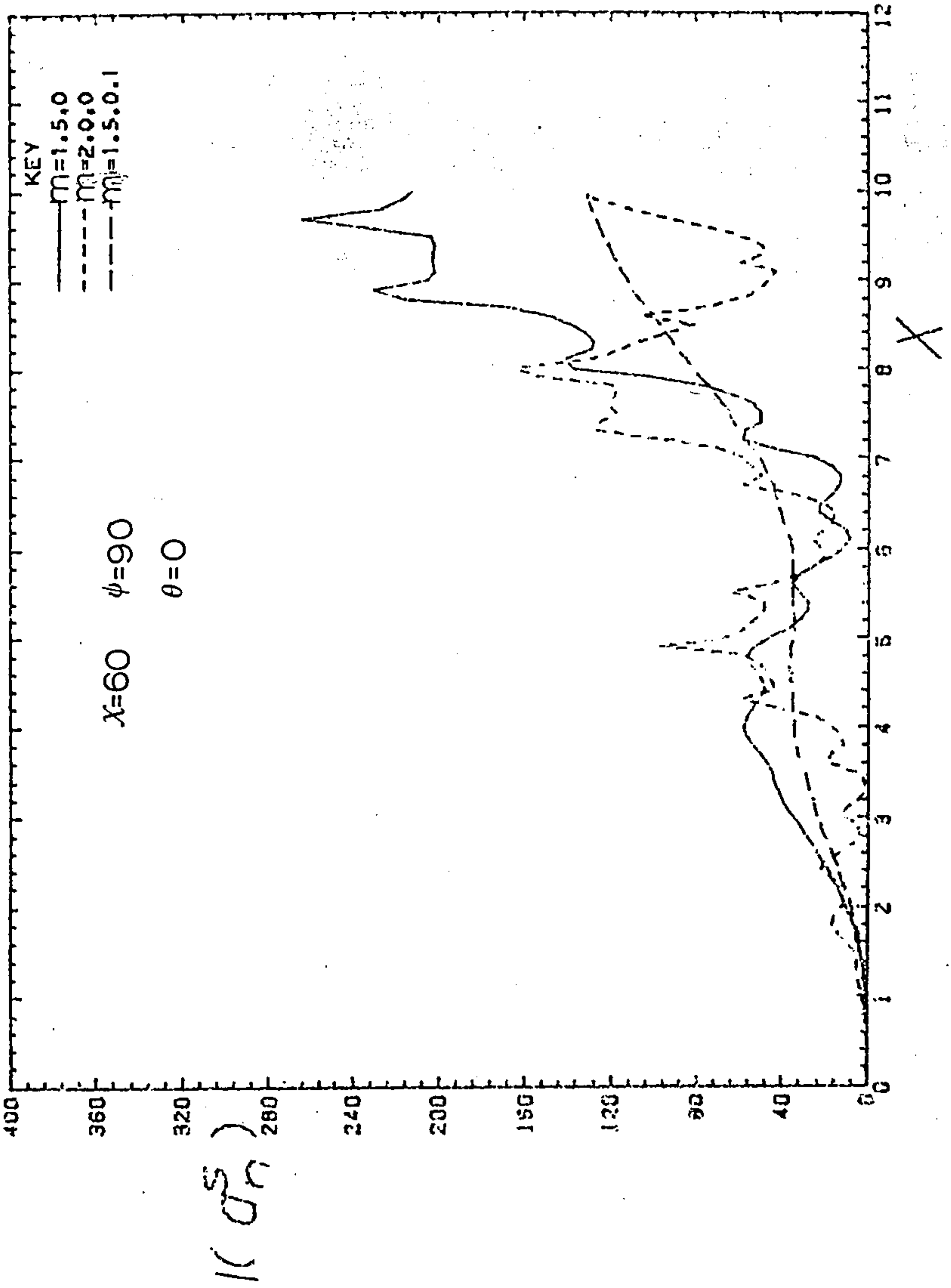

Fig.(2-3-g) Plot of intensity $I(a_n^s)$ against x for forward scattering $\chi=60$

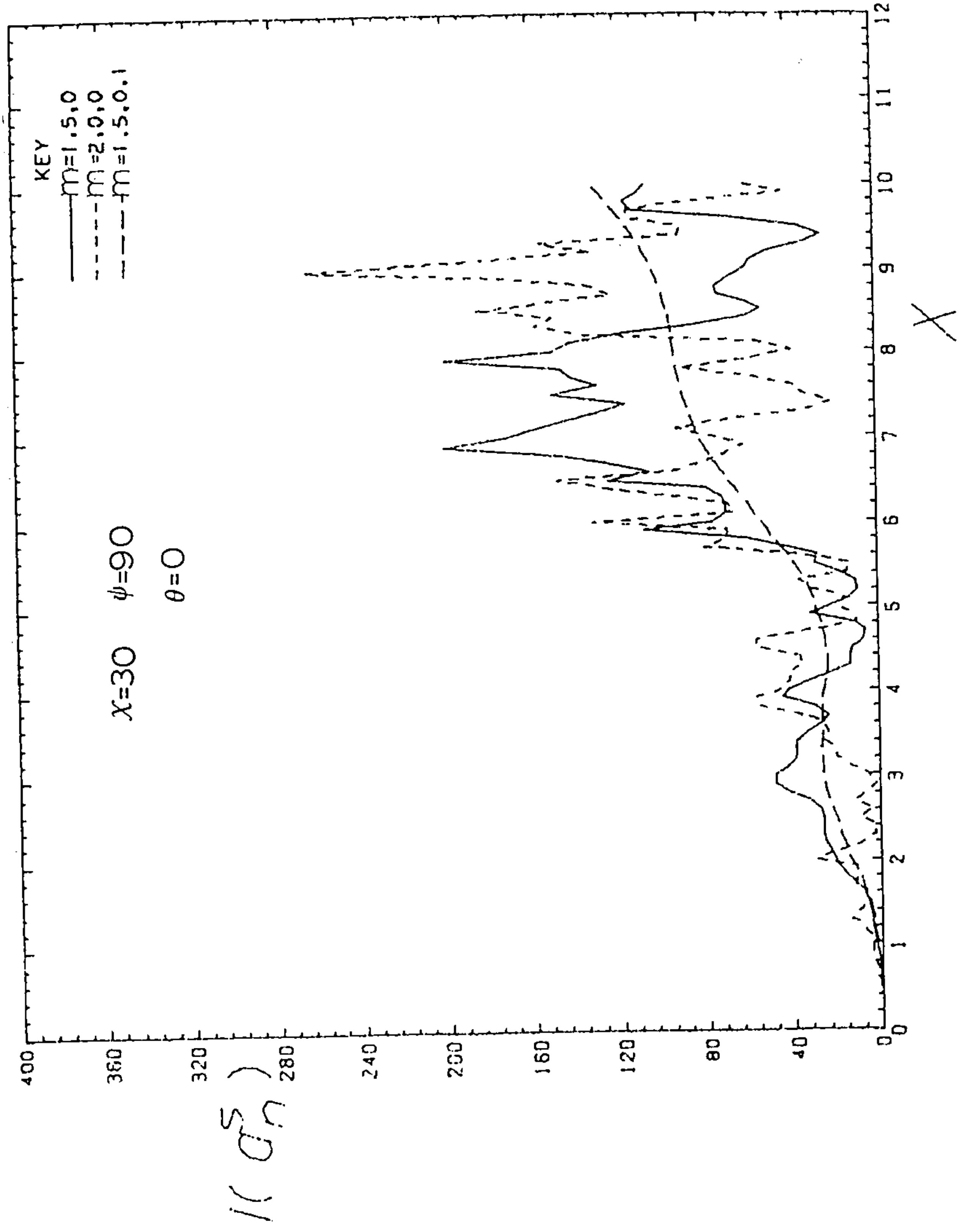

Fig.(2-3-h) Plot of intensity I(a_n^s) against x for forward scattering χ=30

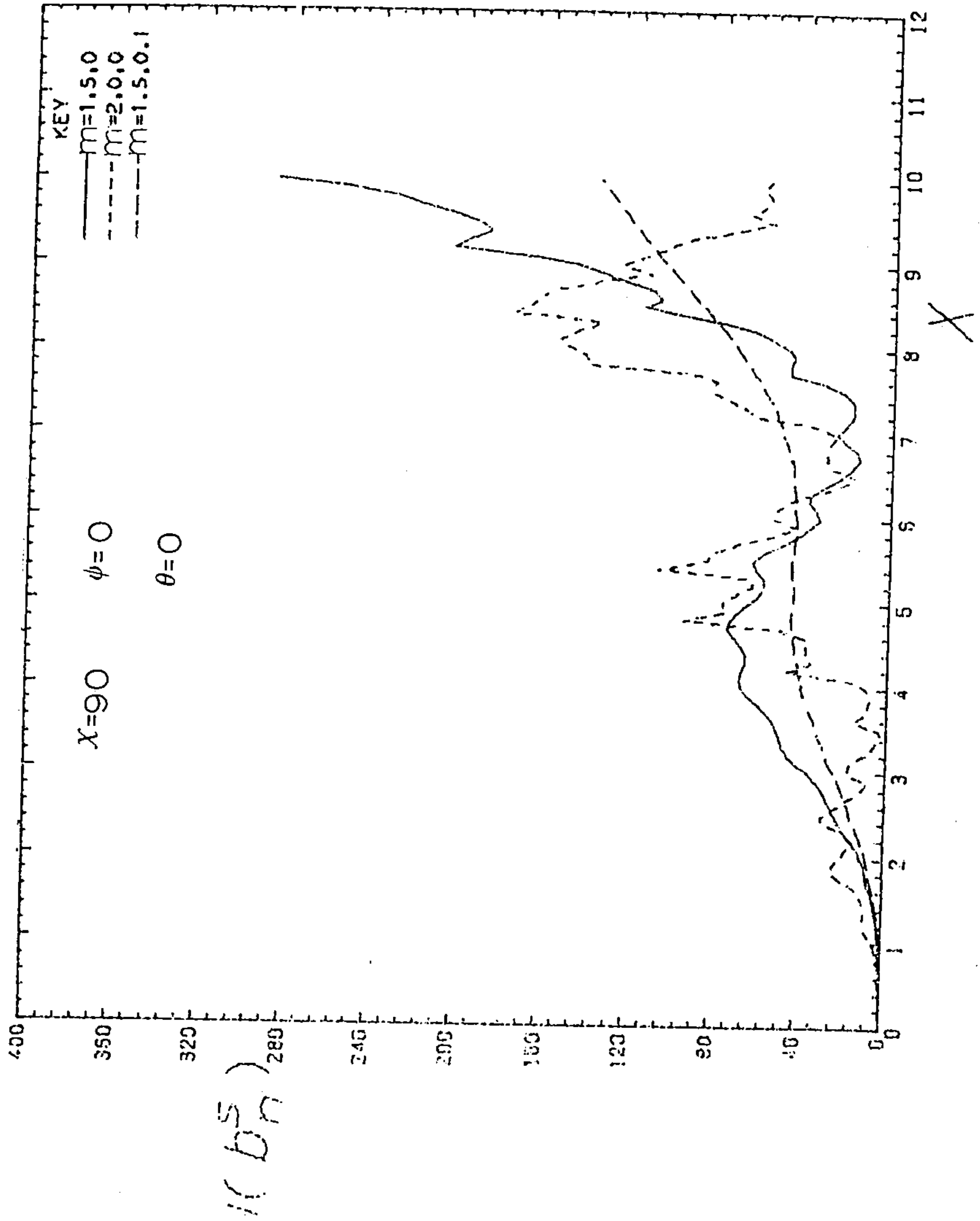

Fig.(2-3-i) Plot of intensity $I(b_n^s)$ against x for forward scattering $\chi=90$

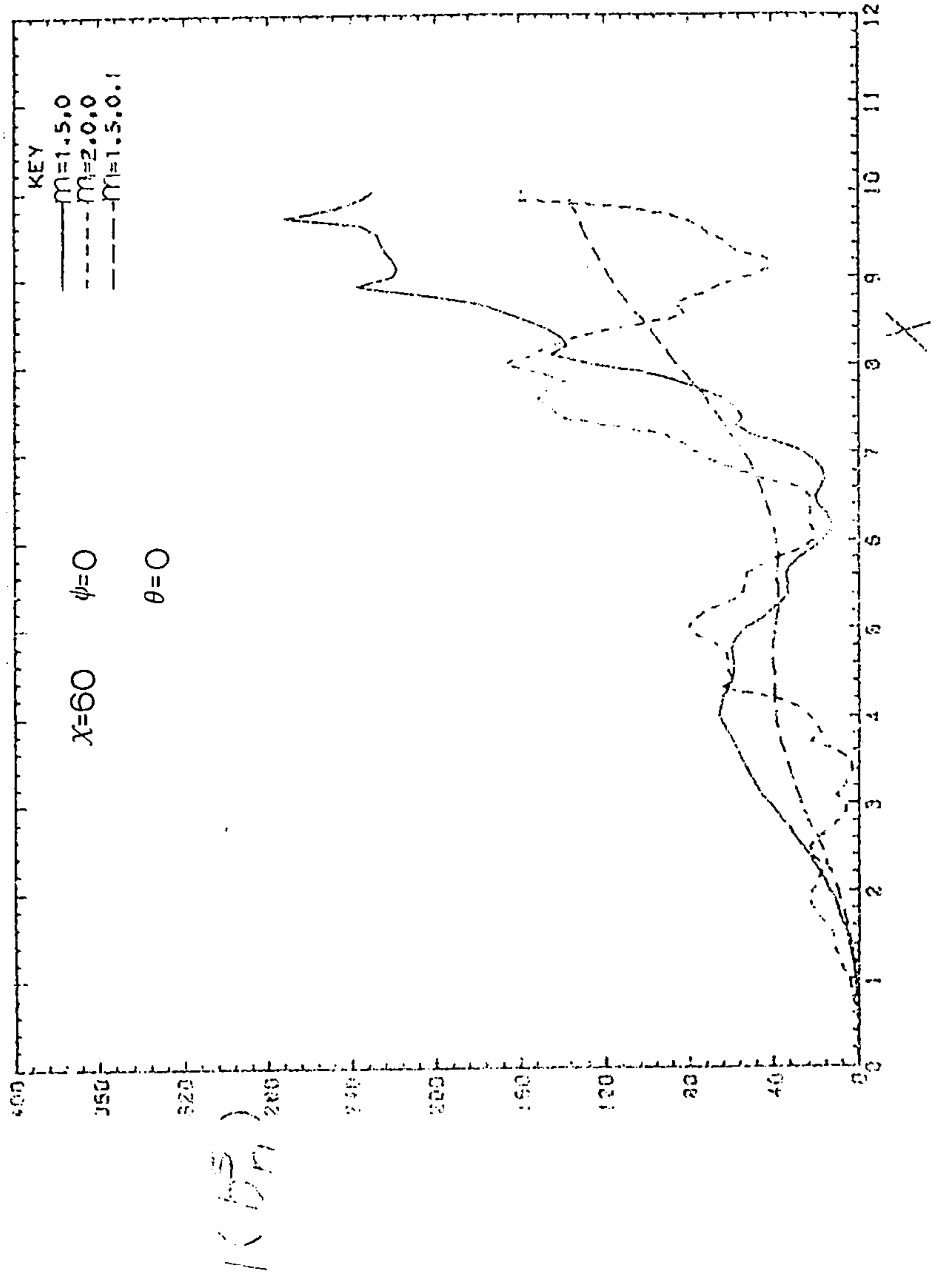

Fig.(2-3-j) Plot of intensity $I(b_n^s)$ against x for forward scattering $\chi=60$

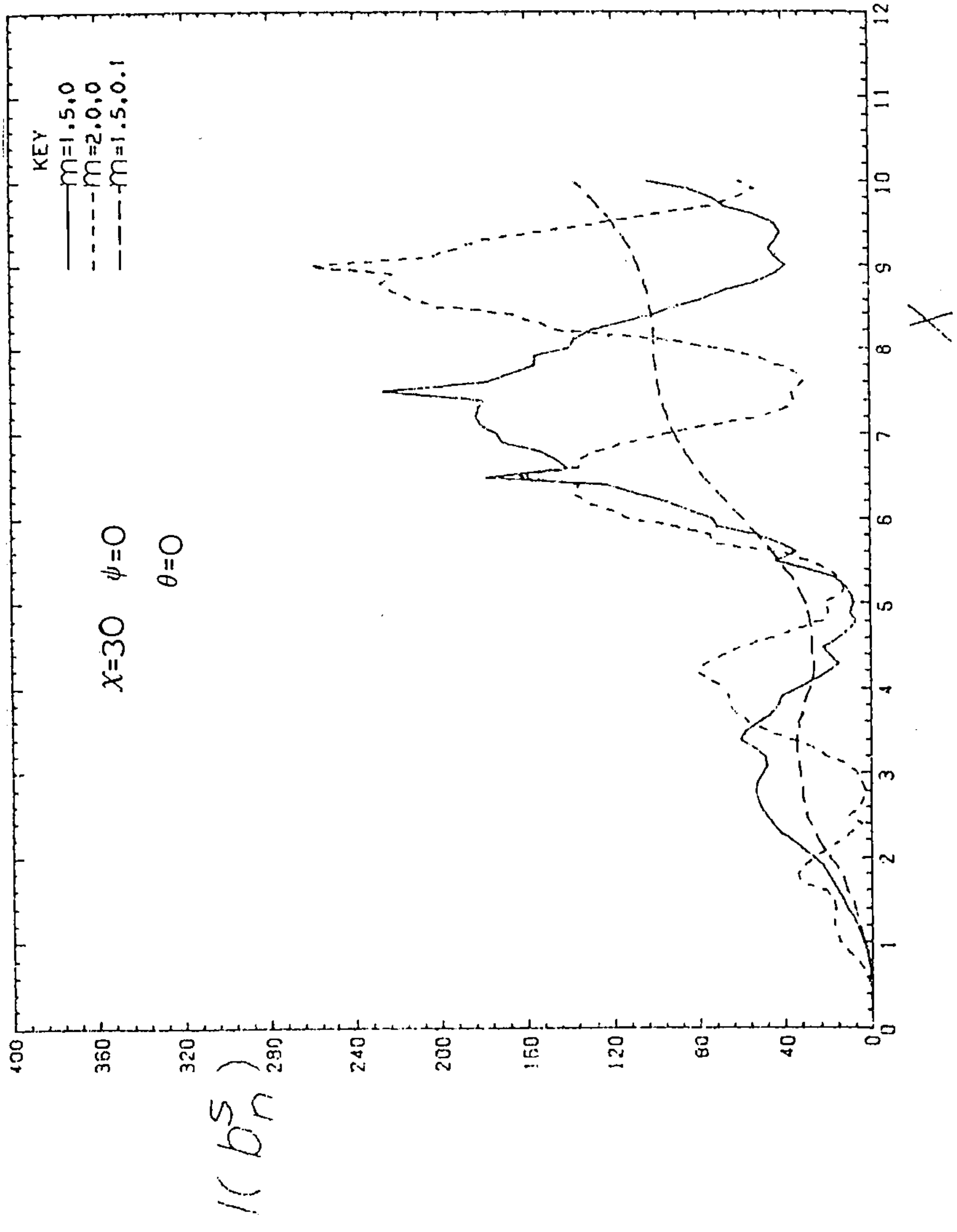

Fig.(2-3-k) Plot of intensity $I(b_n^s)$ against x for forward scattering χ=30

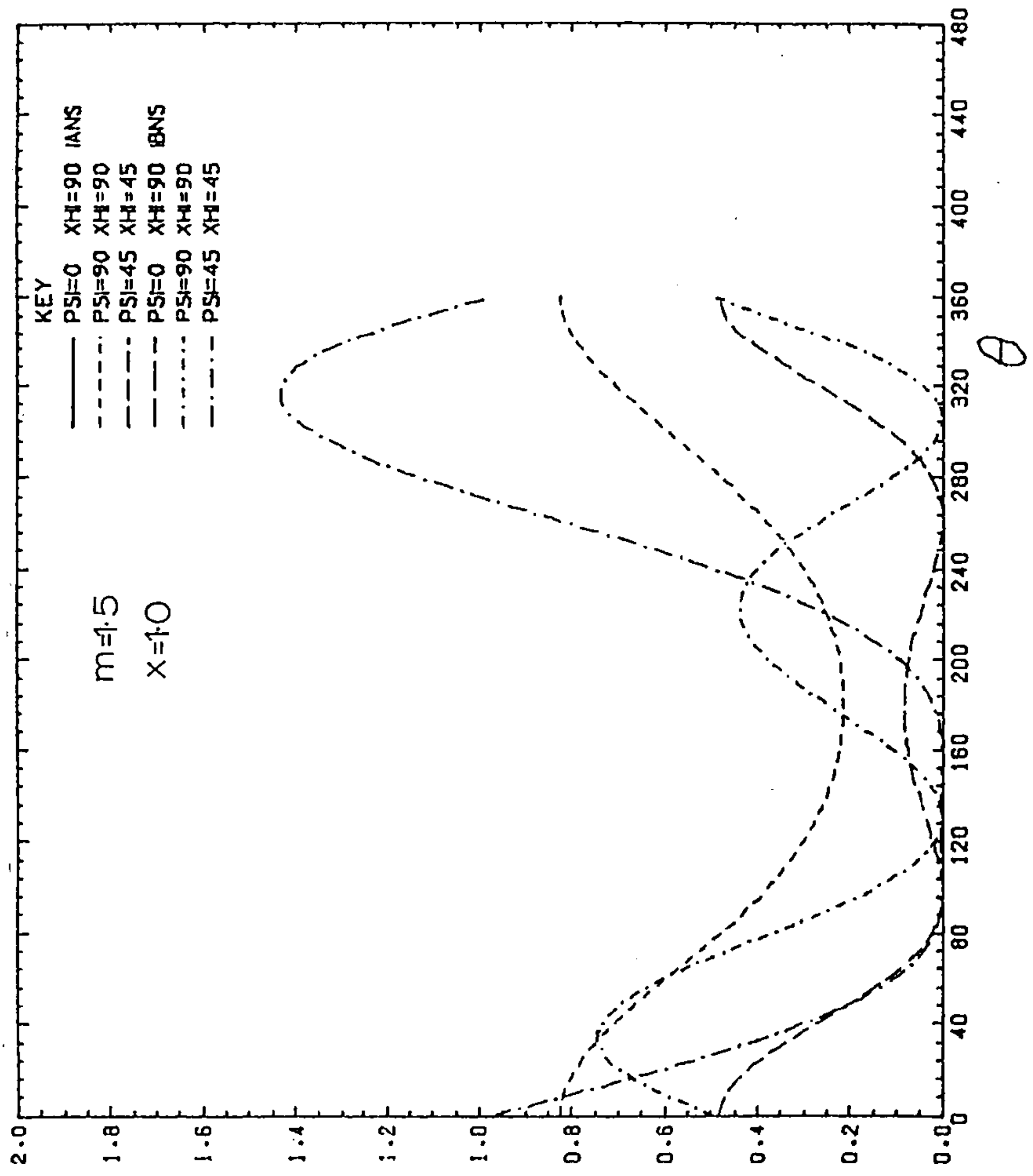

Fig.(2-3-1) Variation of intensity I with scattering angle θ with χ and ψ

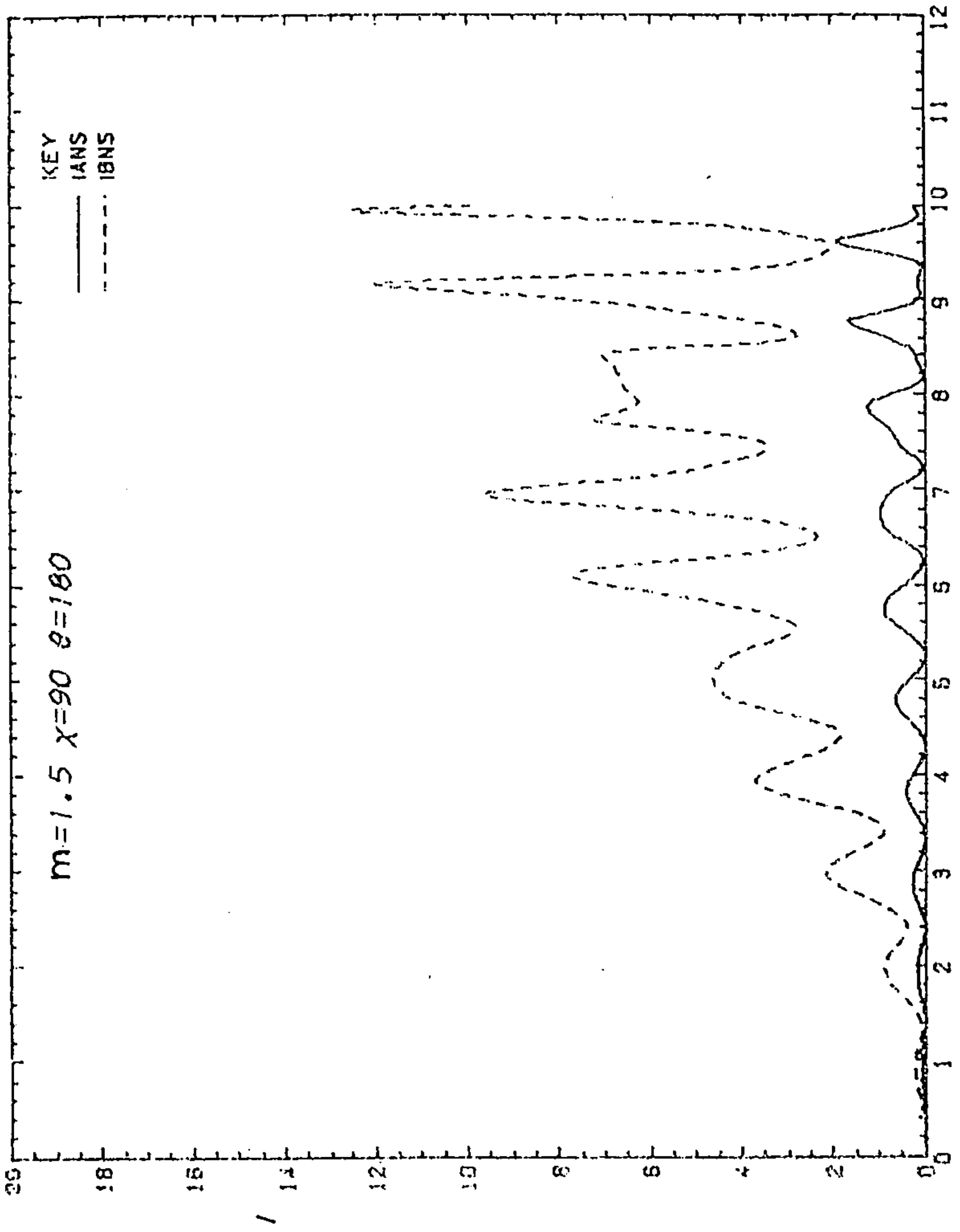

Fig.(2-3-m) Plot of intensity I against x
for back scattering at χ=90

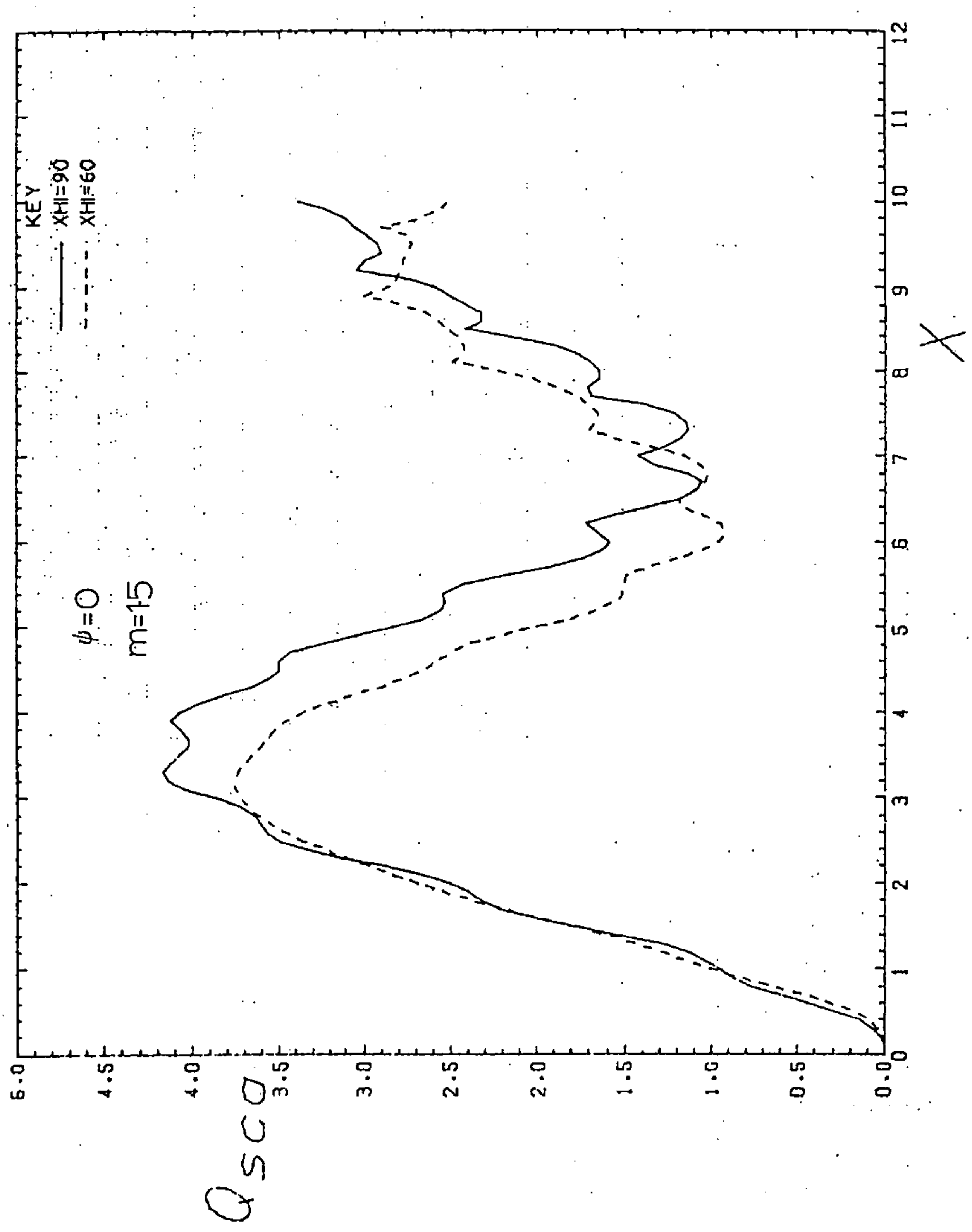

Fig.(2-3-n) Plot of scattering efficiency Q_{sca} against x for two values of χ

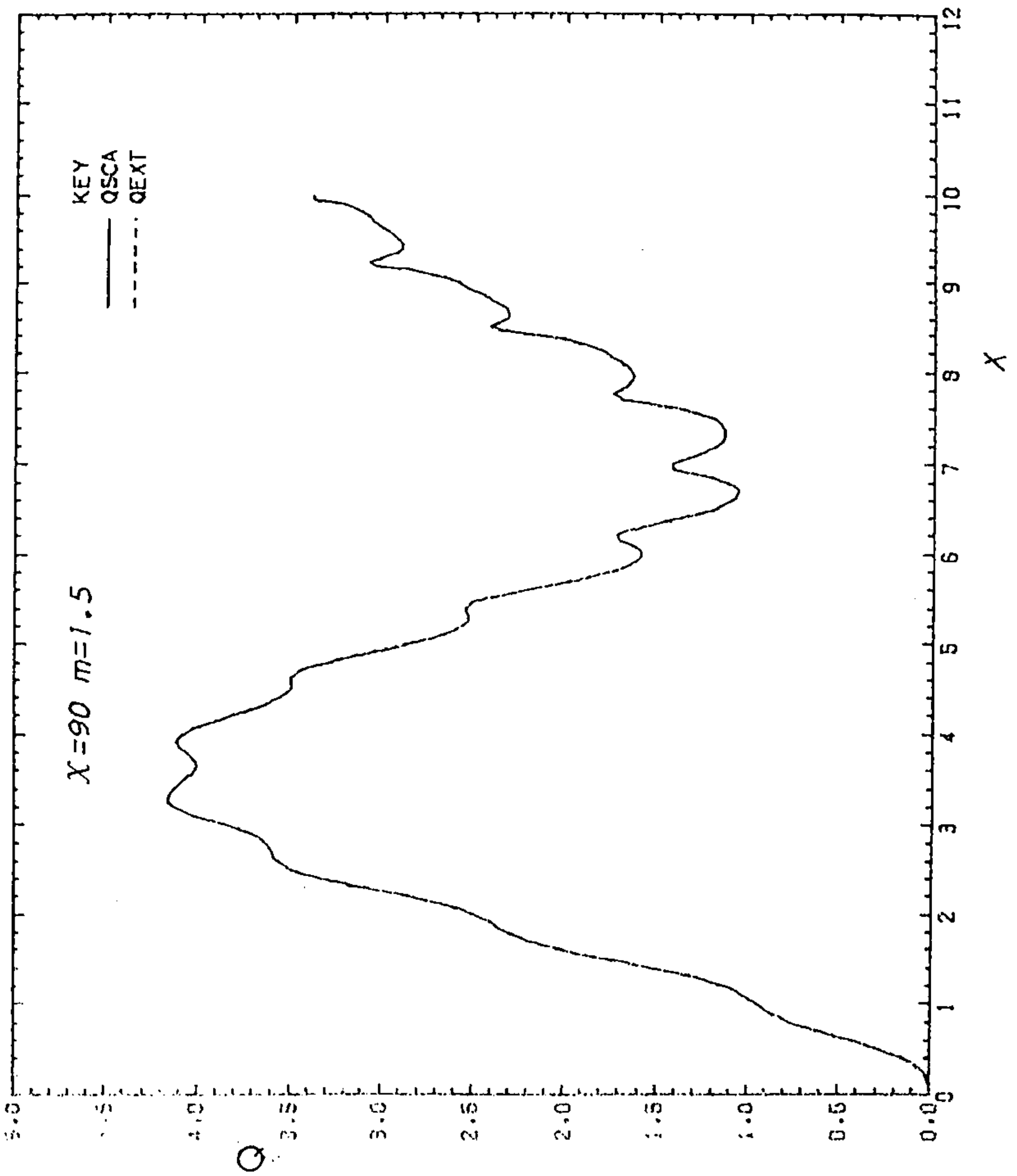

Fig.(2-3-o) Plot of scattering and extinction efficiencies against x for real refractive index χ=90

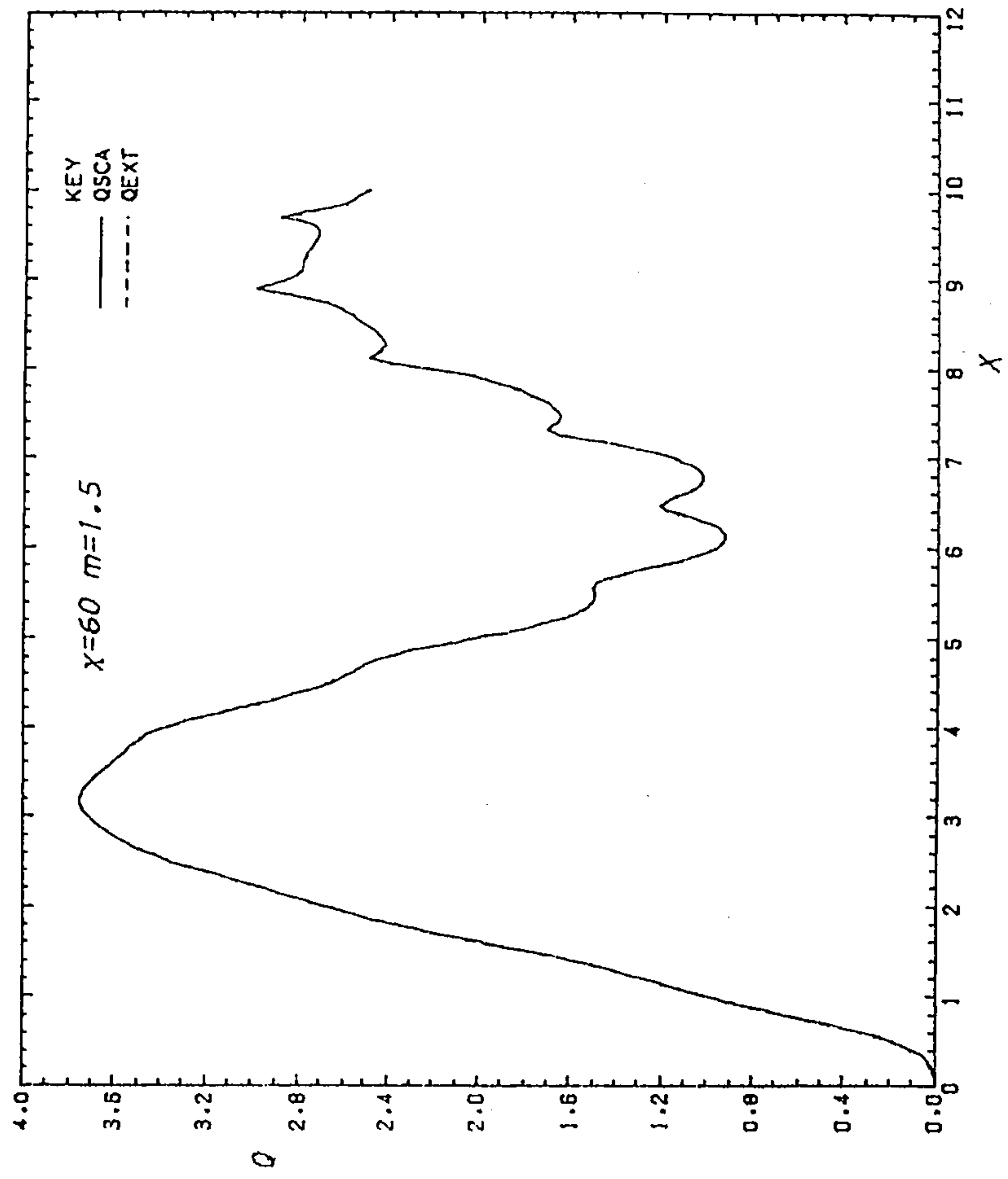

Fig.(2-3-p) Plot of scattering and extinction efficiencies against x for real refractive index χ=60

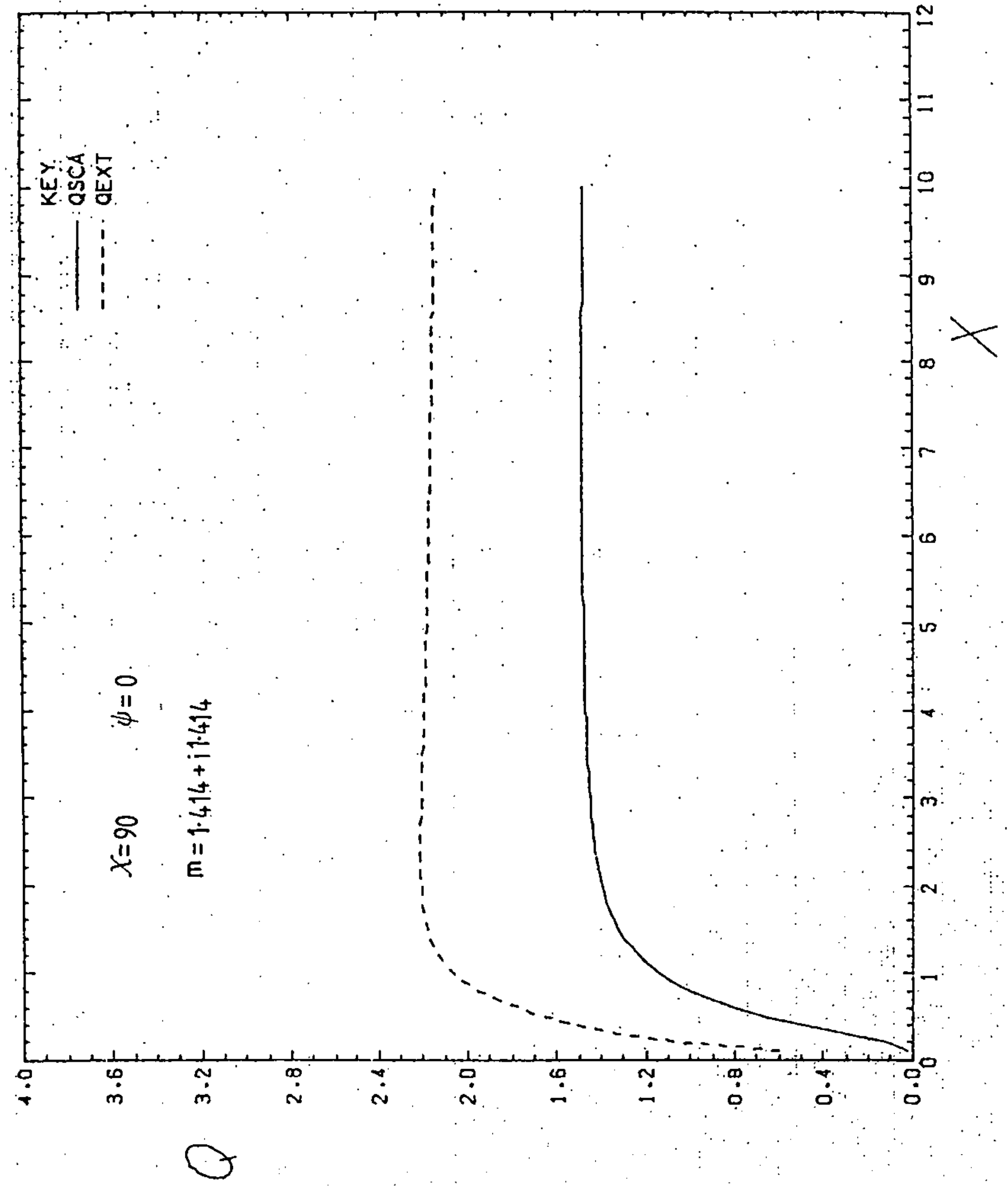

Fig.(2-3-q) Plot of Q_{sca} and Q_{ext} against x
for a complex refractive index ψ=0

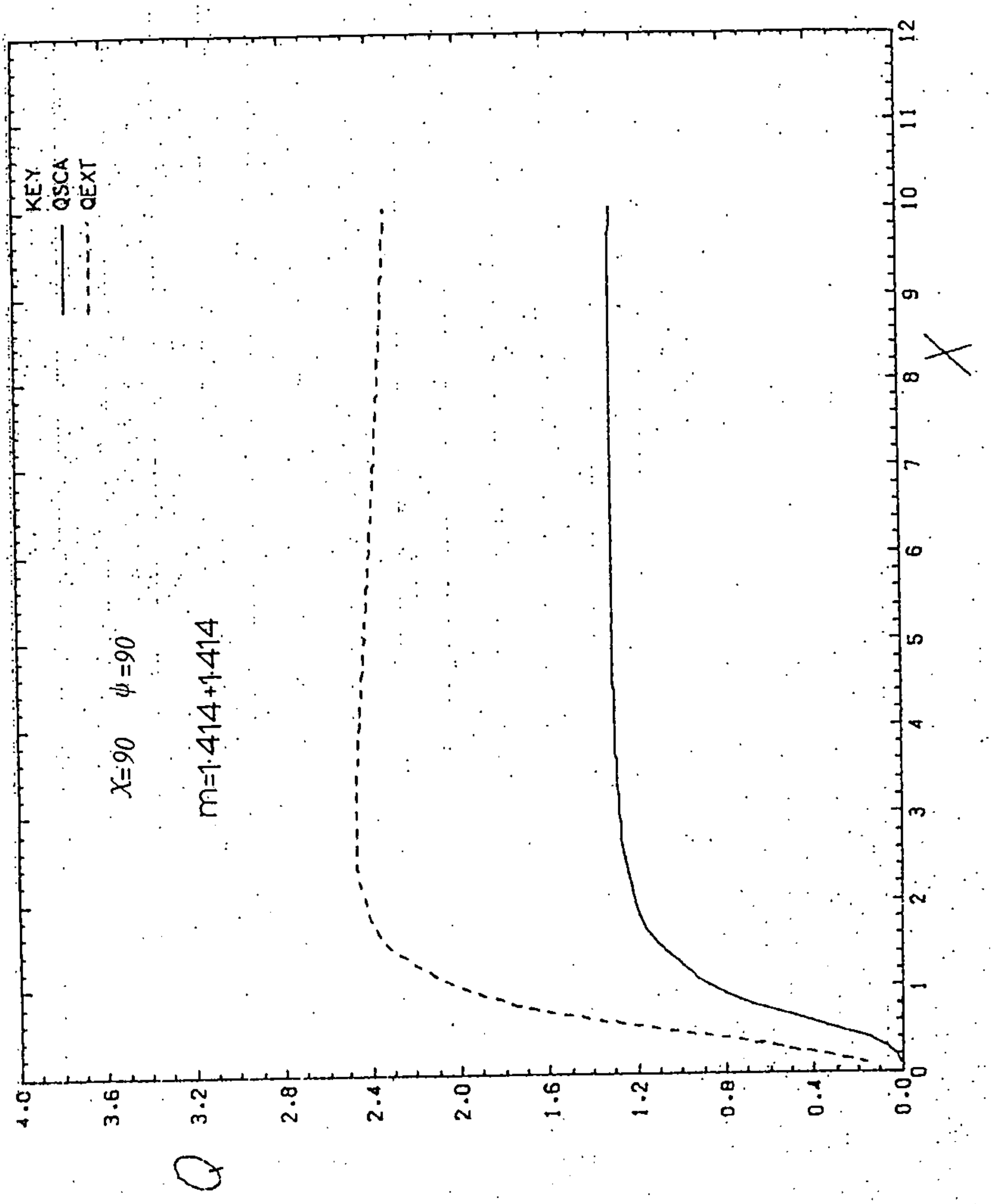

Fig.(2-3-r) Plot of Q_{sca} and Q_{ext} against x for a complex refractive index ψ=90

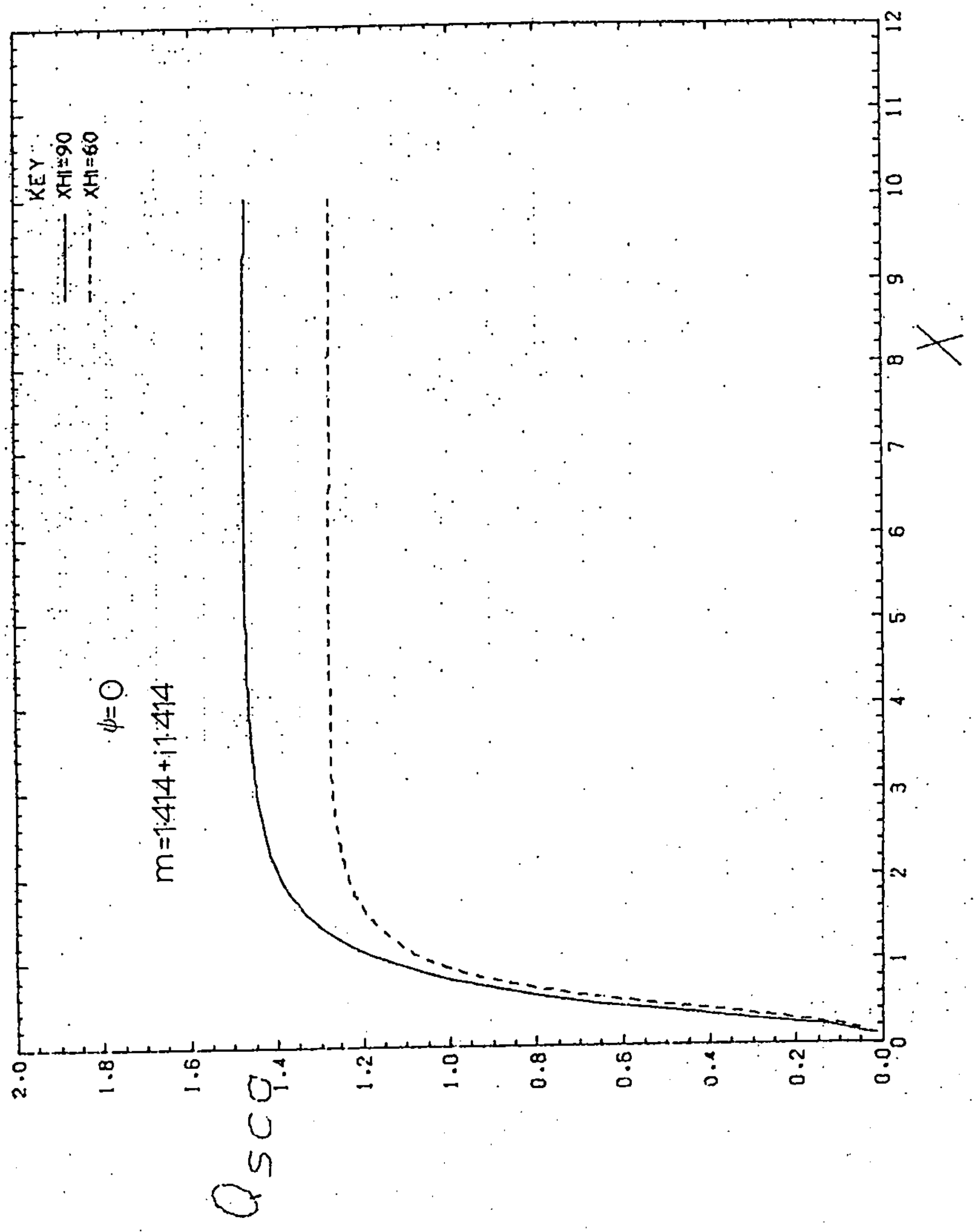

Fig.(2-3-s) Plot of Q_{sca} against x for a complex refractive index and two values of χ

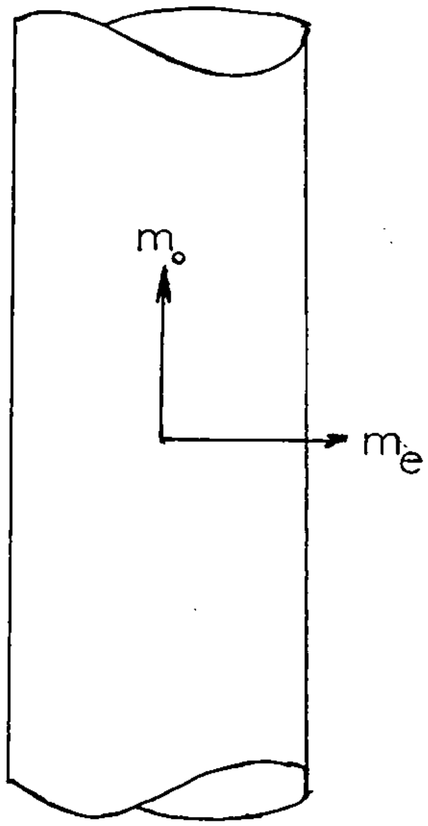

Fig.(2-3-t) The refractive index m consists of the ordinary (m_o) and the extraordinary components

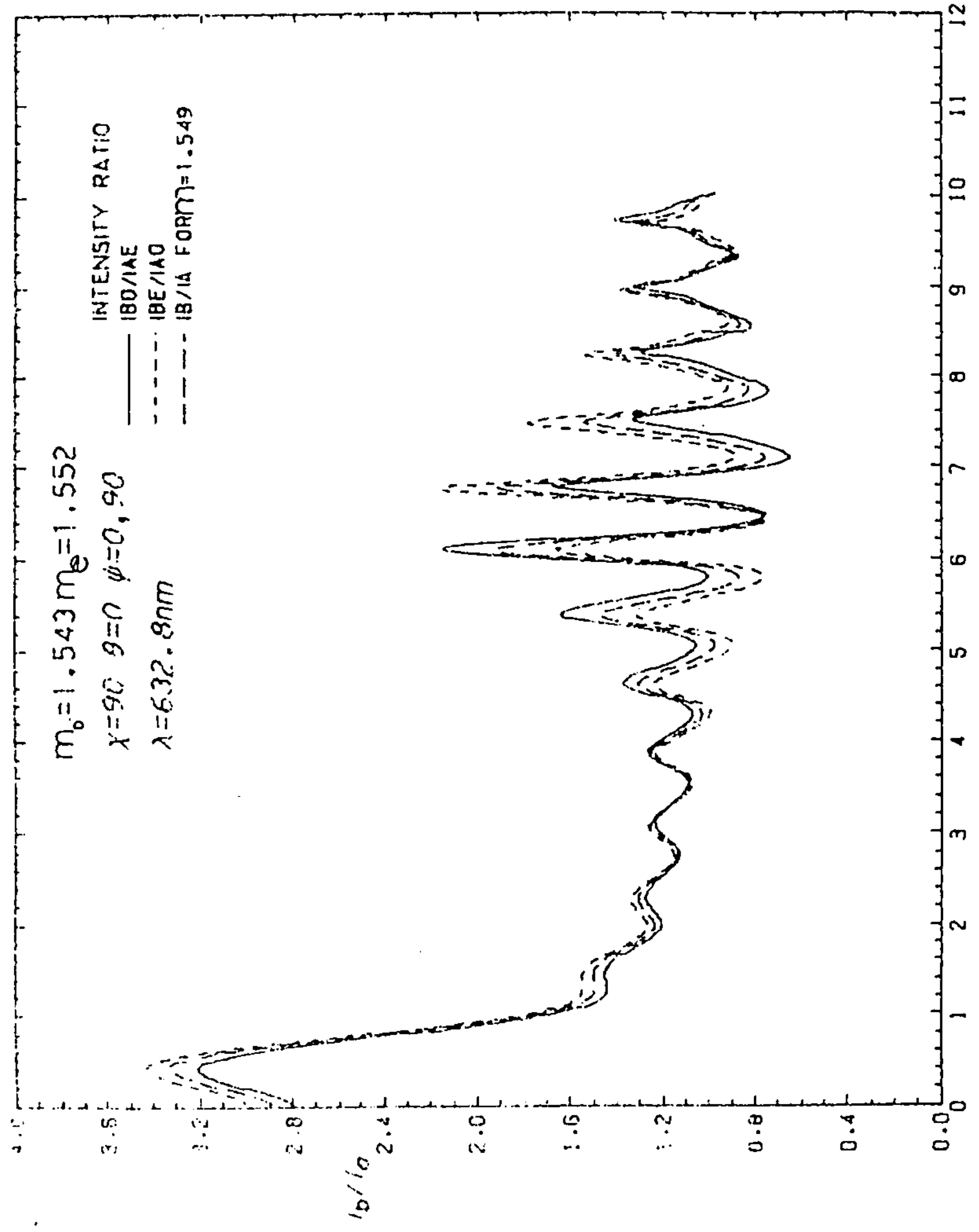

Fig.(2-3-u) Plot of the ratio I_b/I_a against x exploring the effect of optical anisotropy on scattering

—— m =1.543 m_e = 1.552

----m_o =1.552 m_e = 1.543

-- -- m_o = m_e = 1.549

we investigate scattering by microquartz fibres.

Quartz is generally anisotropic, there being two refractive indices as indicated in Figure (2-3-t), where m_o lies along the optic axis and m_e lies in a radial plane orthogonal to m_o. In order to estimate the significance of this, the intensities for polarisations along two orthogonal directions, $I_a s_n$ and $I_b s_n$, were calculated for m_o = 1.542 and m_e = 1.552 respectively for an upright cylinder irradiated with light of λ = 632.8nm. This was repeated for the values m_o = 1.552 and m_e = 1.542. The results are shown in Figure (2-3-u) with the case where the refractive index along the two orthogonal directions is the same i.e. $m_o = m_e = 1.549$. The ordinary (m_o) and extraordinary (m_e) refractive indices for He-Ne laser wavelength were interpolated using refractive indices for λ = 589nm and λ = 760nm as given by Weast (1980). Anisotropy gives rise to a change of 10% compared to the curve with refractive index m = 1.549. The maximum change is apparent near the peaks and the troughs of the oscillations. However, the polarisation ratio remains greater than unity.

2.4 Conclusion

The theoretical basis of light scattered from infinite cylinders has been outlined and results for the ratio R' against x indicate that its value could be used to distinguish between fibres and spherical particles. Furthermore, R' increases considerably for the backward direction which would be advantageous for the development of a measurement instrument such that all the optics and electronics could be enclosed in one box.

CHAPTER THREE

PRELIMINARY EXPERIMENTS

3.1 Introduction

The commercial fibrous monitor marketed by the GCA Corporation was reviewed in Chapter 1. It relies on physical rotation of sampled fibres while in the path of a linearly polarised laser beam. It is possible to apply the same principle to fibres in free space (i.e.in-situ) by not orienting the fibre in a particular fashion but to allow the electric vector of the light wave to rotate i.e. use circularly polarised light.

The fringe scattering method is based on laser doppler anemometry (Durst and Whitelaw,1971) in which two laser beams cross at a point to form a set of interference fringes. A particle traversing this pattern generates an attenuating signal the frequency of which is proportional to the velocity. However, the amplitude of the signal is dependent upon the light scattered by the particle and thus, upon its size and optical properties. A number of authors (e.g.Jones,1974 and Chou,1976) have looked at the detailed theory for spheres in this system, but there is no theoretical basis for irregular particles.

A modification of the fringe scattering technique (Hong and Jones, 1976; Hong,1977) using circularly polarised light was found to be of some success in distinguishing between fibres and spherical particles. Its apparent success was limited due to the majority of the fibres having a length greater than the fringe spacing.

3.2 Modified Fringe Scattering

(i) Theoretical

The GCA instrument (see Chapter 1) induces a dipole on a sampled fibre which is rotated at a very high speed by a varying electric field while the fibre is in the path of a linearly polarised laser beam. One could achieve the same result, in principle, by not sampling but allowing the electric vector of the light wave to vary with time, so that it is alternately parallel or orthogonal to the fibre. there are three ways of achieving this:

(a) physically rotating the electric vector,

(b) using two circular polarisations of different frequency and opposite sense,

(c) using two orthogonal linear polarisations of different frequency.

One comes up with problems on how to achieve (a) at sufficient speed, but (b) and (c) are easily implemented. The required speed of rotation (frequency) depends upon - and estimating requirements.

One could use two beams of circularly polarised light in the opposite sense to each other and of different frequency. This has the added advantage that the doppler signal will yield the direction of travel and the velocity of the particle to aid the determination of the sampled volume.

Jones (1979) obtained integral solutions for scattering by chains of small particles. In the Rayleigh approximation, the individual spheres are so small that the internal field may be considered to be constant (see Appendix A for details). Because the particles are small so is the chain length for reasonable aspect ratios.

For a fibre composed of Rayleigh spheres located in the plane Z=0 (Figure (3-2-a)), the scattered intensity due to each beam is given by

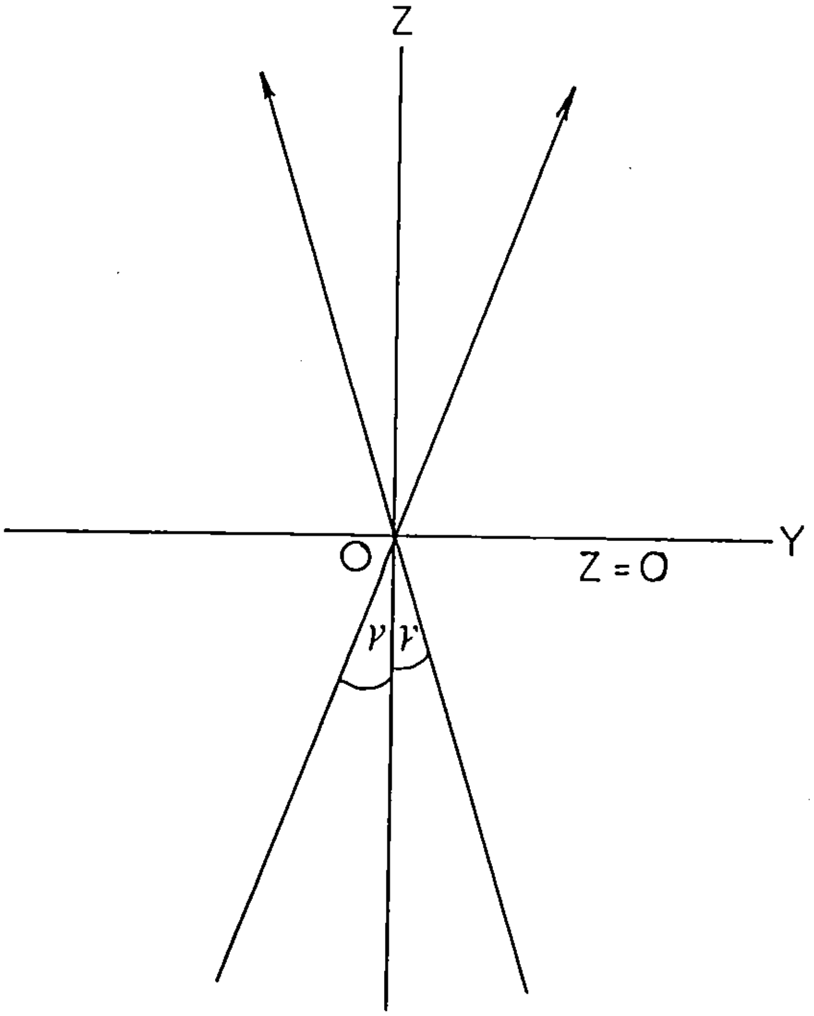

Fig.(3-2-a) Crossing of laser beams in the plane z=0

$$I^{(1)}_{sca} = |Z|^2 \sum_j \sum_{j_1} \Gamma^{(1)}_{1j} \Gamma^{(1)*}_{1j_1} e^{ik(y_{j_1}-y_j)(\sin\theta+\sin\gamma)}$$

$$I^{(2)}_{sca} = |Z|^2 \sum_j \sum_{j_1} \Gamma^{(2)}_{1j} \Gamma^{(2)*}_{1j_1} e^{ik(y_{j_1}-y_j)(\sin\theta-\sin\gamma)} \qquad (3\text{-}2\text{-}1)$$

where Z is a constant; Γ_{1j} is related to the incident wave (Appendix A); γ is the half angle between the interfering beams; θ is the scattering angle; y_{j_1} and y_j are the positions of the j_1 and j^{th} spheres.

The associated visibility V is given by

$$V = \frac{2\sqrt{|I^{(1)}_{sca}|.|I^{(2)}_{sca}|}}{|I^{(1)}_{sca}|+|I^{(2)}_{sca}|} \qquad (3\text{-}2\text{-}2)$$

A computer program was written to find the DC scattered intensity and the associated visibility for a fibre located in the plane Z=0. Two cases were examined; two opposite sense circularly polarised waves and two orthogonally linearly polarised waves parallel to the x and y directions. The computed visibilities at $\theta=0^{\circ}$ and 180° agreed with the results of Jones (1979) for either case of $\psi=0^{\circ}$ or 90° where ψ is the orientation of the fibre with respect to the x-axis.

It was found that for two orthogonal waves V is a function of ψ but for the case of circular polarisation V is independent of ψ. This is to be expected as this case corresponds to a rotating vector. Thus to eliminate the dependence on ψ circular polarisation is to be used in the experimental set-up.

Figure (3-2-b) shows V plotted against N, the number of particles in the chain, for two values of kR where R is the radius of the Rayleigh sphere. It can be seen that a significant increase in V occurs with an increase in refractive

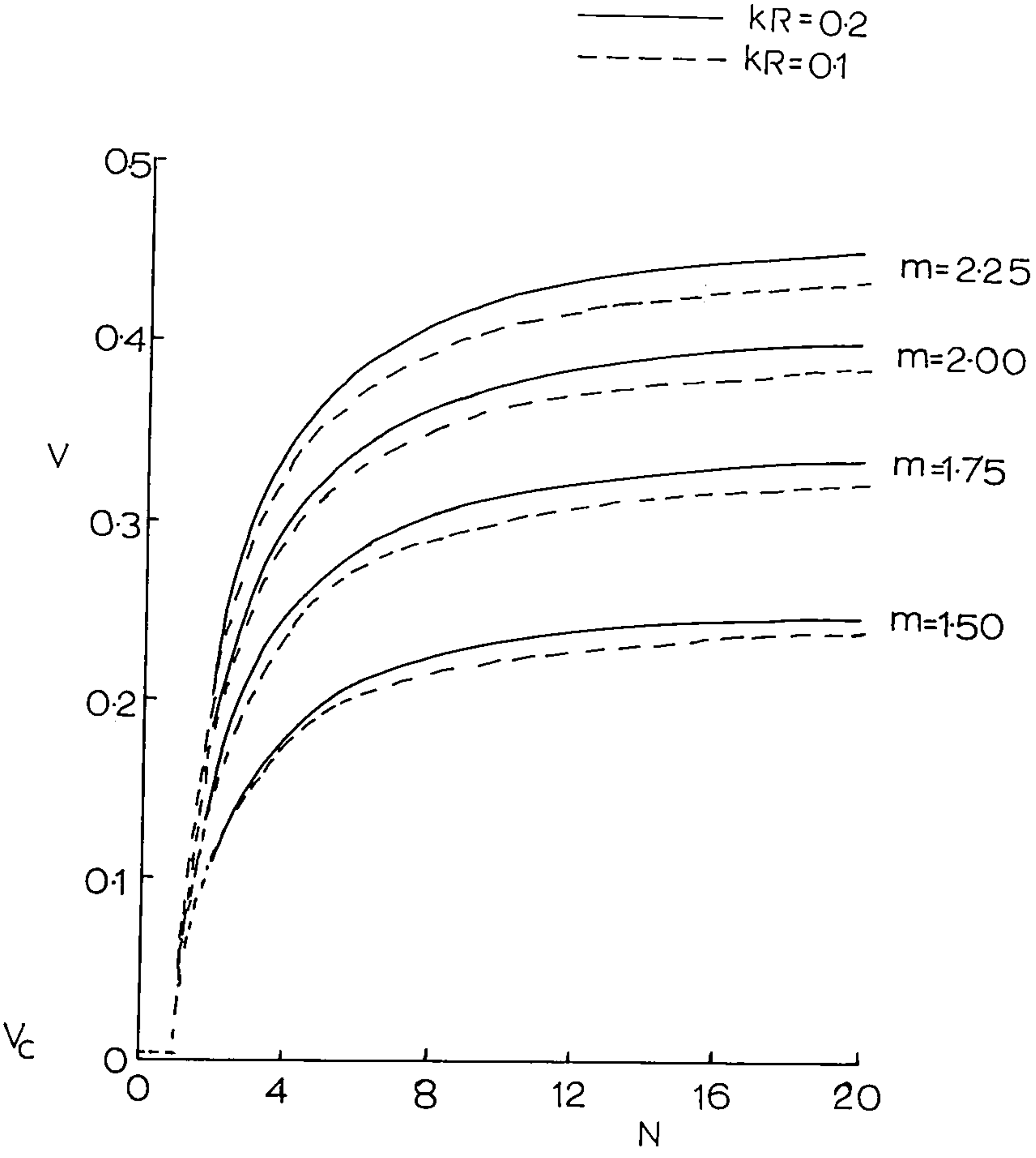

Fig.(3-2-b) Plot of visibility (V) against number of particles (N) for two values of refractive index (m)

Fig(3-2-c) Plot of DC scattered intensity (I_{DC}) against particle number (N) for various values of m and kR

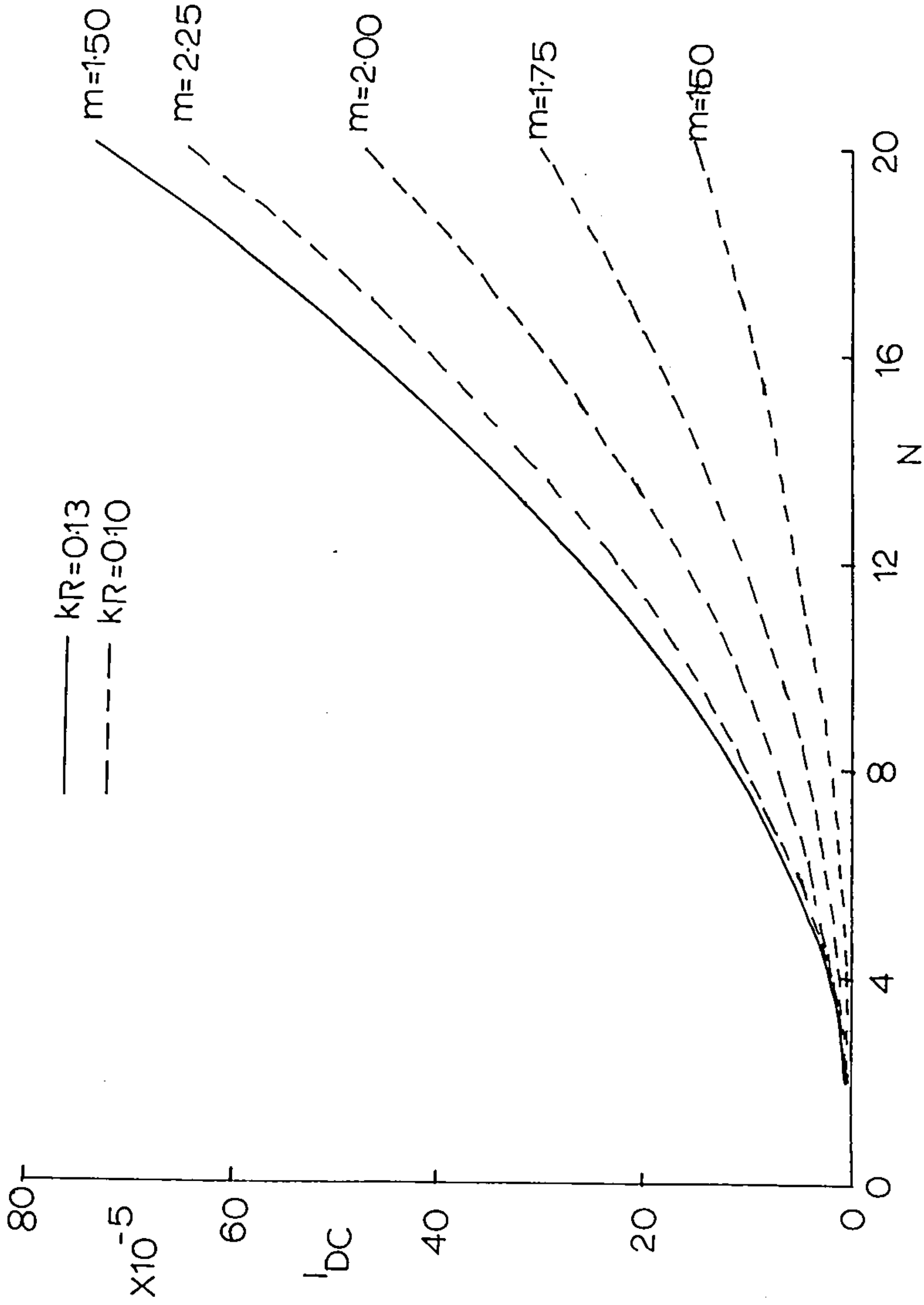

index (m) but the change in V with size is relatively insignificant. Thus the signal depends only on the aspect ratio (provided it is known). It can be easily shown that (Appendix B) the fringe contrast in the test space is given by

$$V_c = \tfrac{1}{2}(1 - \cos 2\gamma) \qquad (3\text{-}2\text{-}3)$$

For a single sphere of size small compared to the fringe spacing the visibility of the scattered light is $V=V_c$, but in the case of a fibre $V>V_c$ because the field components parallel and perpendicular to the fibre axis are scattered differently (Bayvel and Jones,1981). In Figure (3-2-c) is plotted the DC intensity $I_{DC} = |I_{sca}^{(1)}| + |I_{sca}^{(2)}|$ against N where a marked increase with size is noticeable. In principle, one could use this to find kR or the chain length when used in conjunction with Figure (3-2-b).

So far fibres lying in a plane Z=0 have been looked at. Fibres lying at an angle,not perpendicular to the direction of incidence, give rise to reduced visibility. When the axis of the fibres is parallel to the direction of incidence,the visibility is the same as that for a sphere of the same cross-section. This is to be expected since the cross-section seen by the incident light is spherical. However, we do not find this for an infinite cylinder which suggests that the Rayleigh sphere model may be inadequate for making predictions for real fibres.

(ii) Experimental

A system was devised to test the fringe method and its lay-out is shown in Figure (3-2-d). Light from a He-Ne laser source is reflected from a mirror and made to pass through a radial grating with spatial frequency of 10 lines per mm. Due to diffraction, several beams are produced. However, only

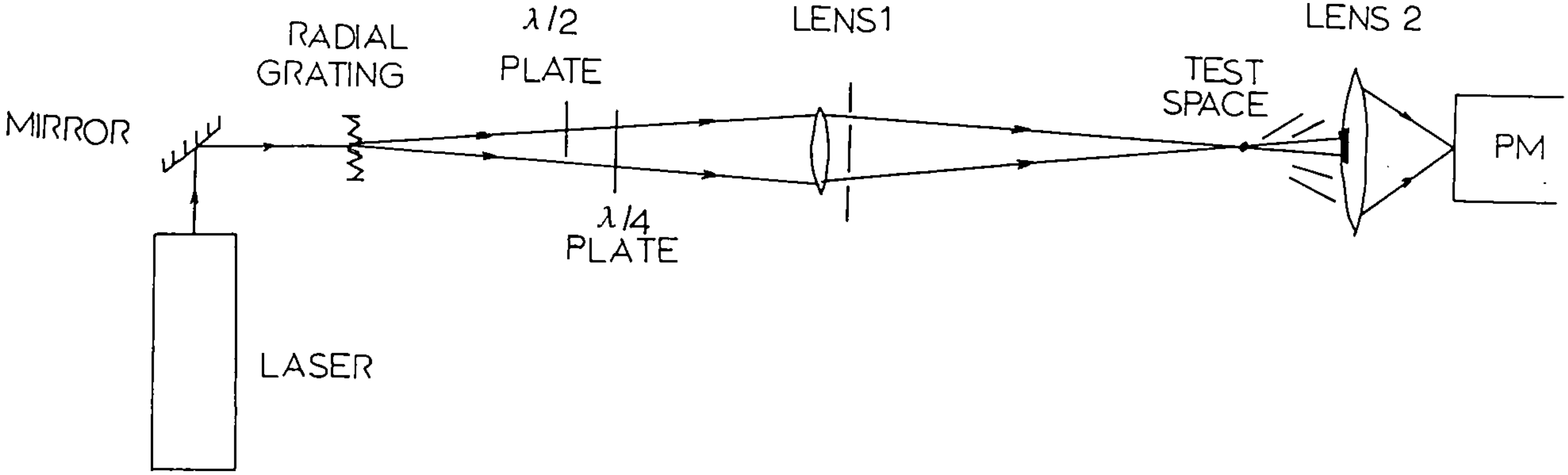

Fig.(3-2-d) OPtical lay-out of modified fringe scattering system the +1 and -1 orders are selectively passed through the phase plates, as shown, such that two circularly polarised beams in the opposite sense are produced. The zero order is effectively eliminated by placing a suitable stop on the lens. The radial grating is in the form of a disc (as shown below) with lines emanating radially from the centre.

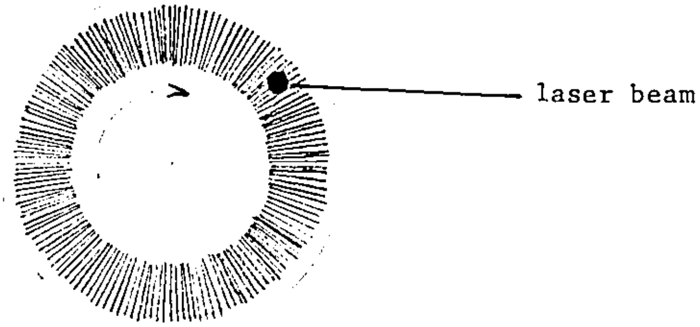

The two diffracted orders are focussed by the lens to form phase fringes (See Appendix B) of spacing ∿ 70μm in the test space. These can be made visible by inserting a polariser in front of the photomultiplier (PM) in which case the system reverts to an ordinary laser doppler anemometer (LDA).

The scattered light is focussed on a pin-hole located in front of the photomultiplier. For this method to work the fringe spacing should always be very much greater than the dimension of the biggest particle. The radial grating is made to rotate at ∿ 300 rpm orthogonal to the incident beam. This produces a doppler shift in the two diffracted beams resulting in a beat frequency in the test space which makes the fringes move (See Appendix B). In this way a significant number of fringes cross the moving particle and the scattered signal contains information about the sense of its velocity.

Plate P-3-2-1 (i) shows a signal from a dust particle when the polaroid was placed in front of the PM. It can be seen that the visibility (as defined, in Figure (3-2-e)) is almost unity. When the polariser was removed the signal shown in P-3-2-1 (ii) was obtained.

Here the fringe contrast is very small ($V \sim 1/600$). In fact we expect zero visibility with spherical particles and tests carried out with water spray and glass ballotini confirmed this. Fibres should, however, give $V>0$. Using this visibility difference to differentiate between fibres and other particles was not very successful because the system was designed to detect fibres of length $\leqslant 10\mu m$. The fibres we used were microquartz fibres with lengths more than $400\mu m$. For example, P-3-2-2-4 show electron micrographs of typical fibres used in the experiment. For detecting fibres of this size a very large (ideally infinite) fringe spacing is required. With this set-up signals of good visibility were obtained.

Figure (3-2-f) shows a slightly modified system where the diffracted orders are made to pass through the phase plate.

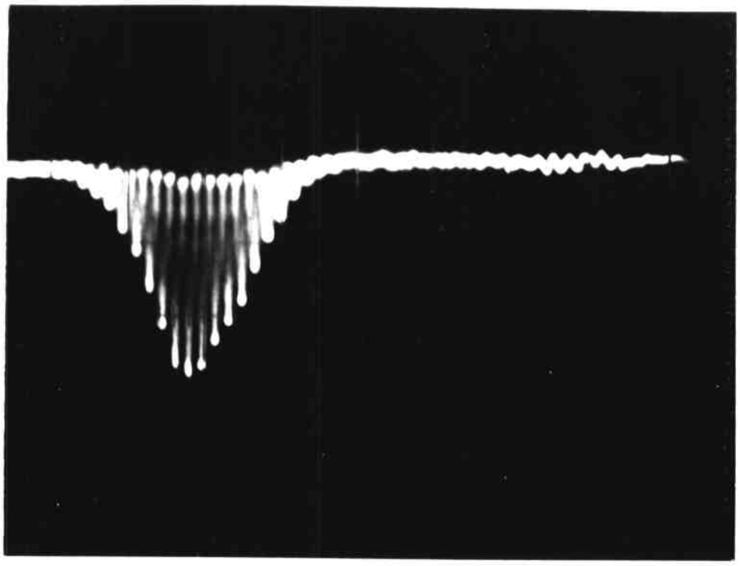

(i)

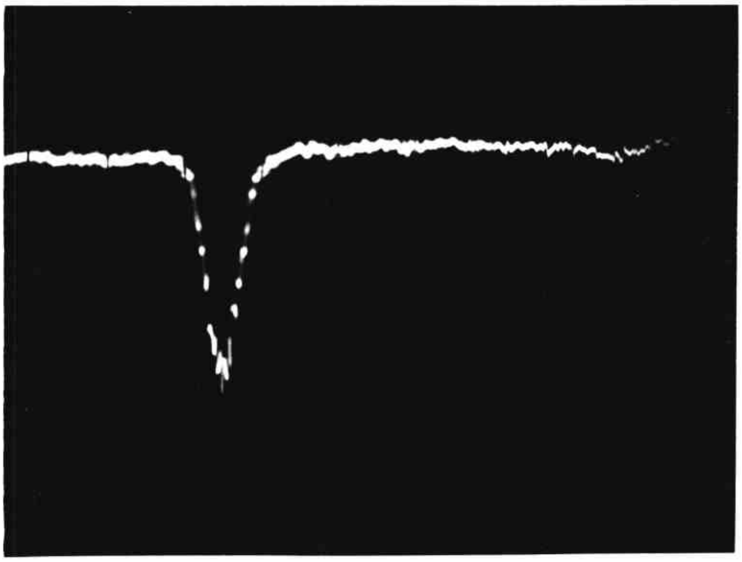

(ii)

P-3-2-1 (i) Signal from a dust particle with polariser in from of PM.

(ii) Signal from a dust particle without polariser in front of PM.

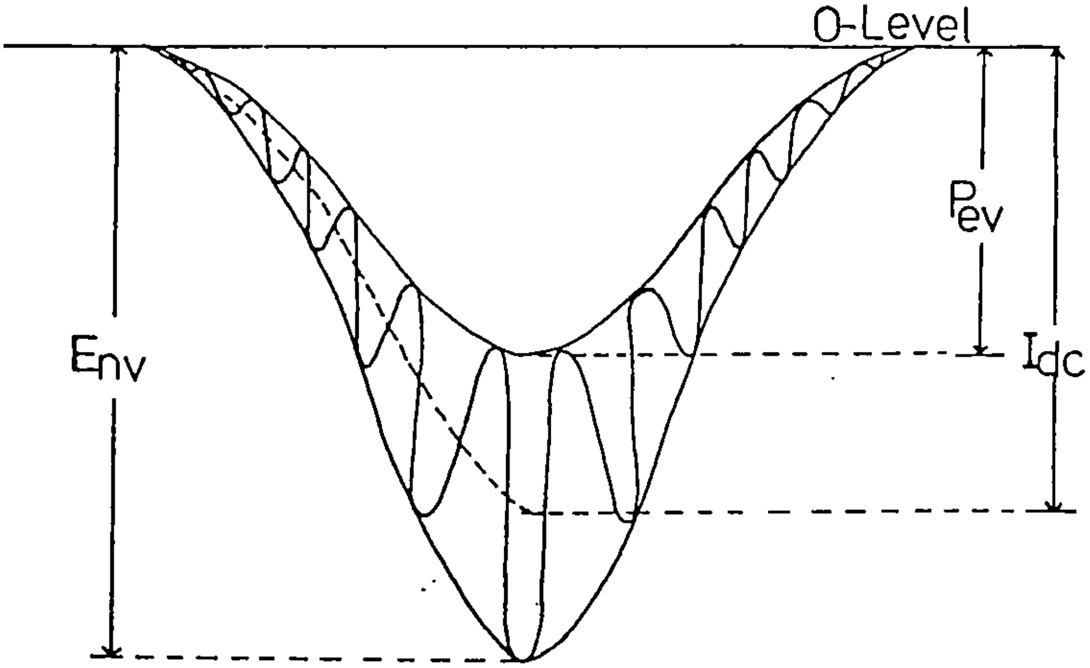

$$V_{sca} = (E_{nv} - P_{ev})/(2 \cdot I_{dc})$$

Fig.(3-2-e) Definition of visibility of a signal

P-3-2-2 Electron micrographs of quartz fibres
magnification = 3.0 k

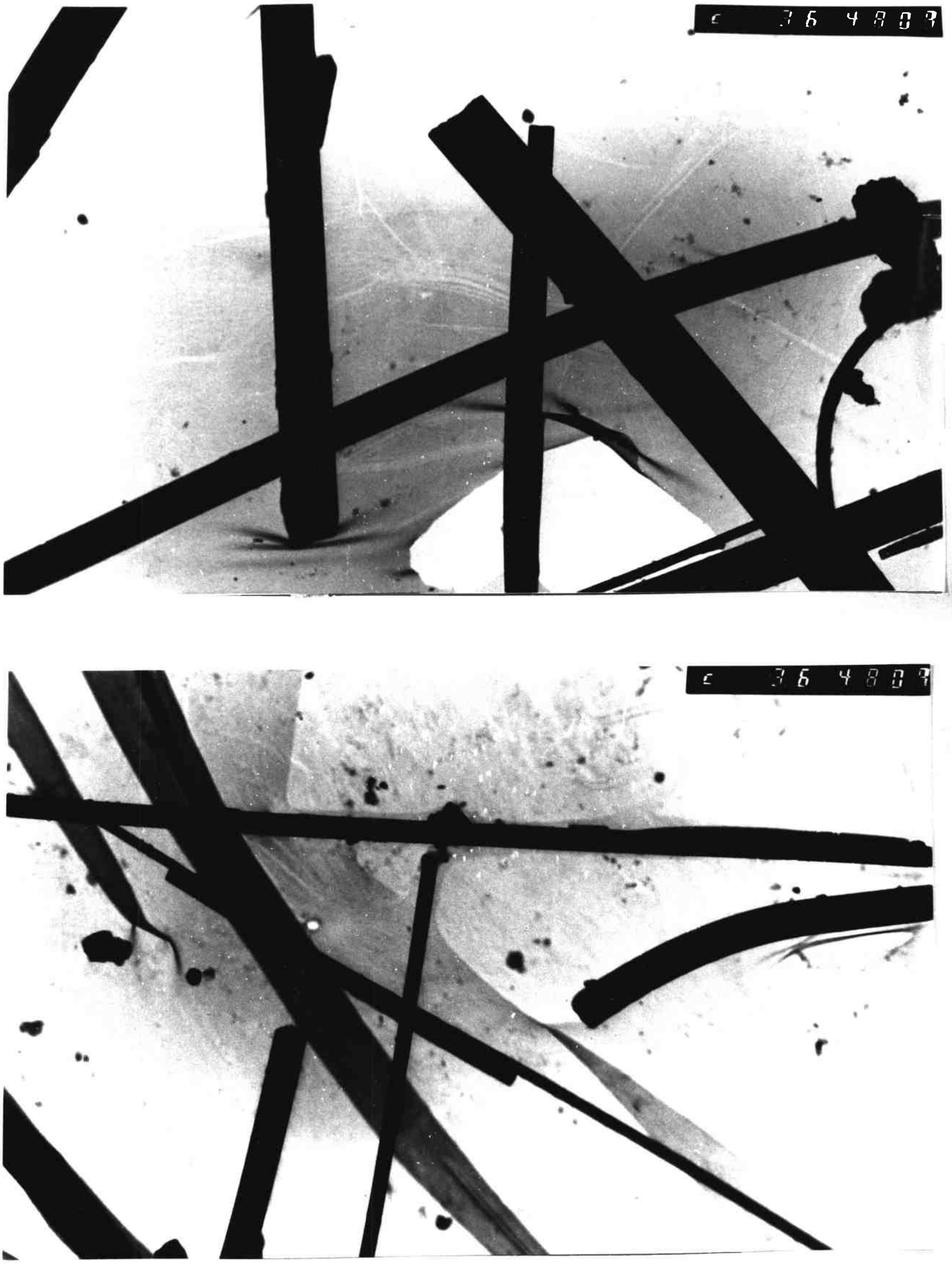

P-3-2-3 Electron micrographs of quartz fibres.
magnification = 3.6 k

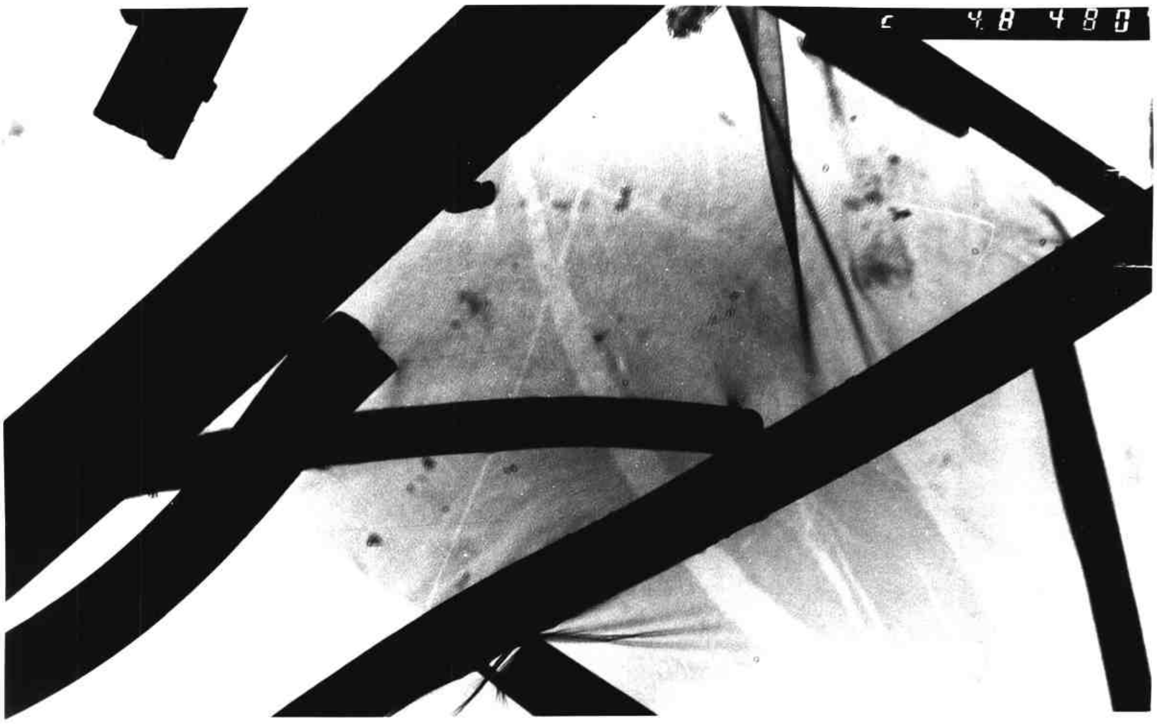

P-3-2-4 Electron micrograph of quartz fibres
magnification = 4.8 k

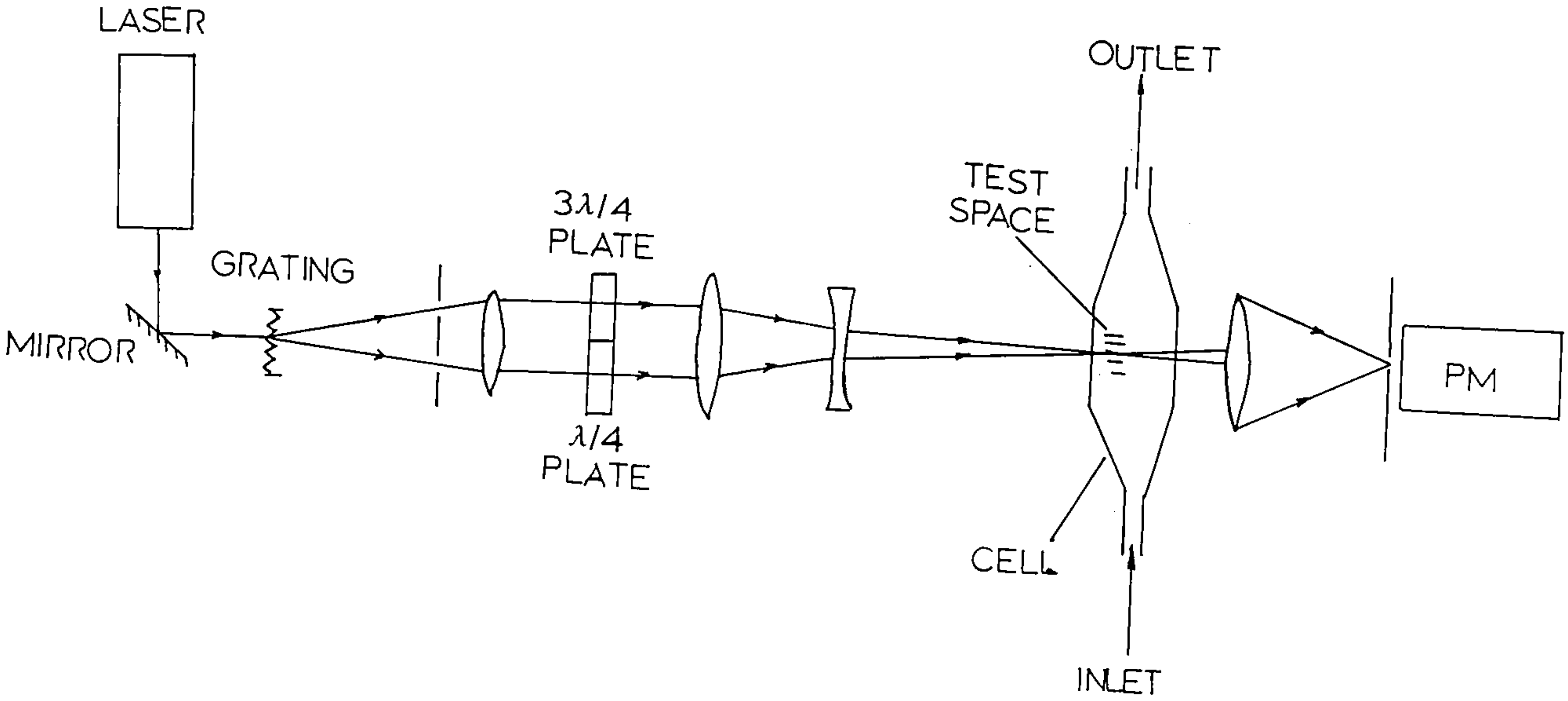

Fig.(3-2-f) Optical lay-out of ±1 diffracted orders forming the fringes in the test space one half of which is a quarter wave plate and the other half is a three quarter wave plate. A lens combination produces the required fringes in a test cell, with optically flat windows, through which fibres are passed. For observing signals from water spray or ballotini the optical cell was removed from the test space. The fringe spacing in this set-up is ~500μm and since, as indicated above, the fibres were of comparable size, it was not possible to obtain signals with high modulation.

To observe the signals we used a spectrum analysis unit attached to a Tektronix oscilloscope to select signals of 9.8kHz centre frequency with a band with of ± 1 hKz.

Signals obtained did not give a sufficient indication of distinguishability between fibres and ballotini. Part of the problem was that there could have been residual linear polarisation present in the beams which would have corrupted the results. Also there is light scattered from the optical elements which contributes to the overall noise level in the signal. From the theoretical analysis (Section (i)), we expect a visibility of ~0.1 for finite rods of Rayleigh scatterers thus the residual noise level is significant enough to bury the a.c. signal for weak scatterers such as fibres.

3.3 Sample Generation

Spherical drops are generated by forcing water through a narrow nozzle as shown in Figure (3-3-a). The diameters of the particles are dependent on the size of the opening and the flow rate of air. The particles emerge in a narrow stream which is directed to the test space.

Glass ballotini is commercially available in the size

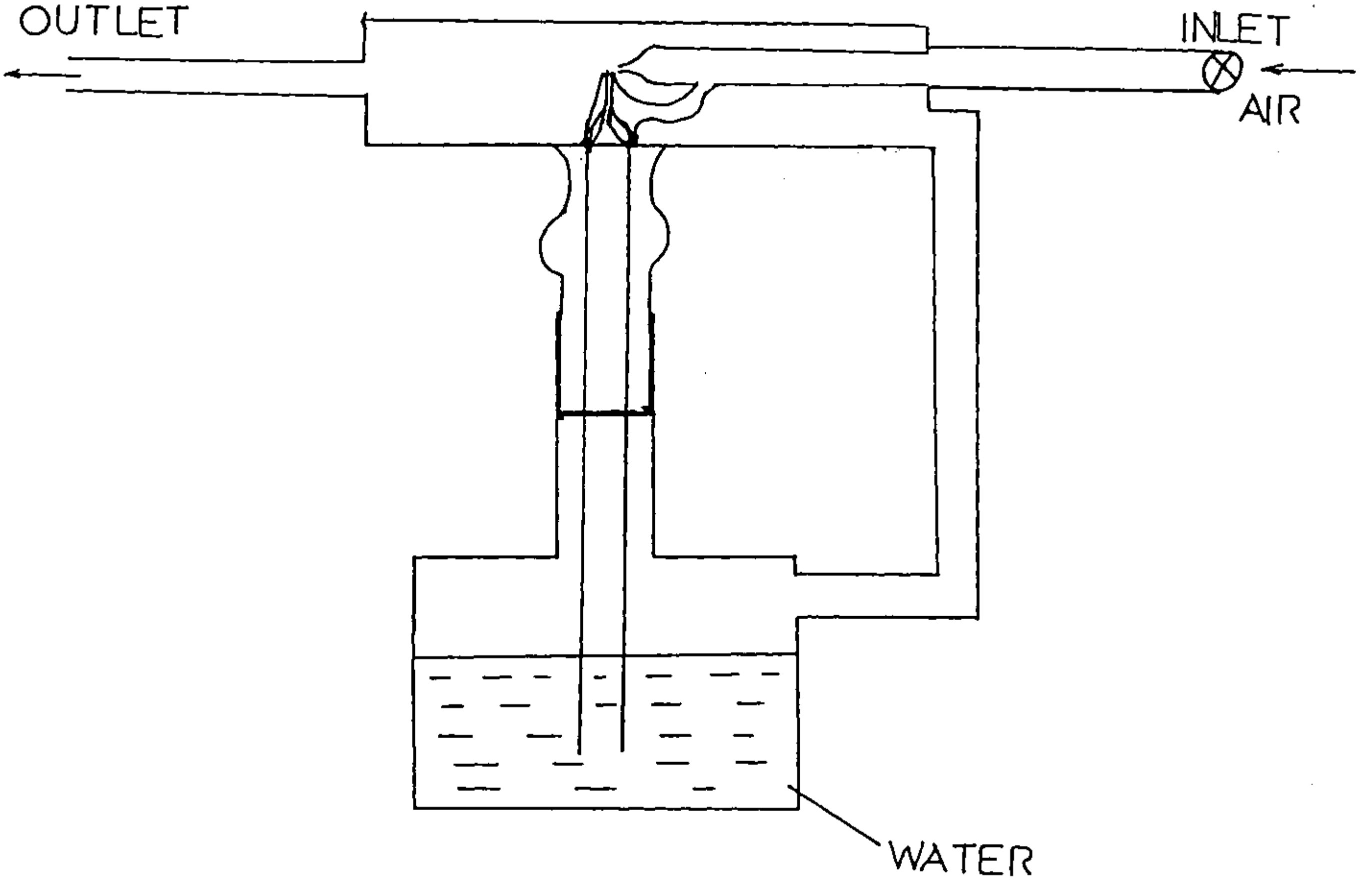

Fig.(3-3-a) Diagram of vessel used for producing water spray

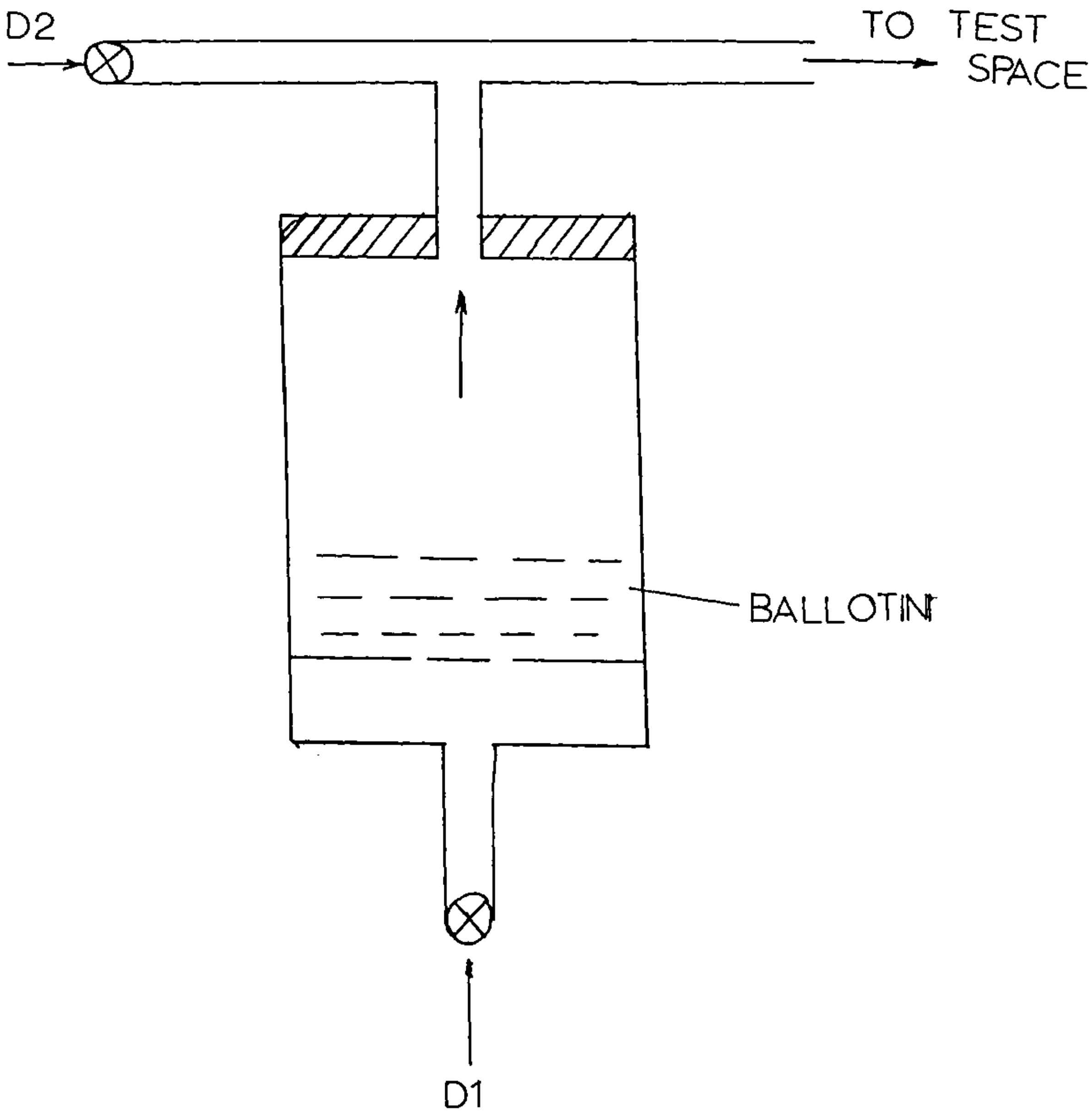

Fig.(3-3-b) Diagram of fluidised bed for ballotini with air inlets D1 and D2 range 0-60μm. Physically it is hard and spherical and is easily carried on an air stream by fluidising it in a bed. The flow rate effectively controls the size range of particles elutriated by the air. For example, only small sizes are picked up by the air stream at lower flow rates. Increasing the flow increases the size of particles carried over. (Hong,1977). The fluidising air passes through the inlet D1 (Figure (3-3-b)). Inlet D2 provides extra air flow to carry the particles to the test space.

Ground quartz fibres were obtained from HSE (Health and Safety Exectutive) and place in a Timbrell dust generator - a diagram of which is shown in Figure (3-3-c) and a picture in Plate P-3-3-1. It is a modified version of the dust disperser described by Timbrell et.al.(1968), with two synchronous drive motors and a set of two drive gears which allows a wide rate of sample feeds into the disperser bowl where a set of rotor blades disperses the sample.

It is possible to generate a required fibre concentration by the regulation of the rates of fibre feed and air flow. However, this was considered very unreliable due to inhomogeneity of the sample texture, variations in packing density, compaction during injection and changes in rates of piston drive or air flow.

For our experimental purposes we required well dispersed particles without agglomeration. To ensure this the fibres and air should be dry.

3.4 Split-Beam Expanded System.

Because of the problem of fibre length relative to fringe spacing, the system shown in Figure (3-4-a) was set up. Here half of the beam is polarised vertically and the other half

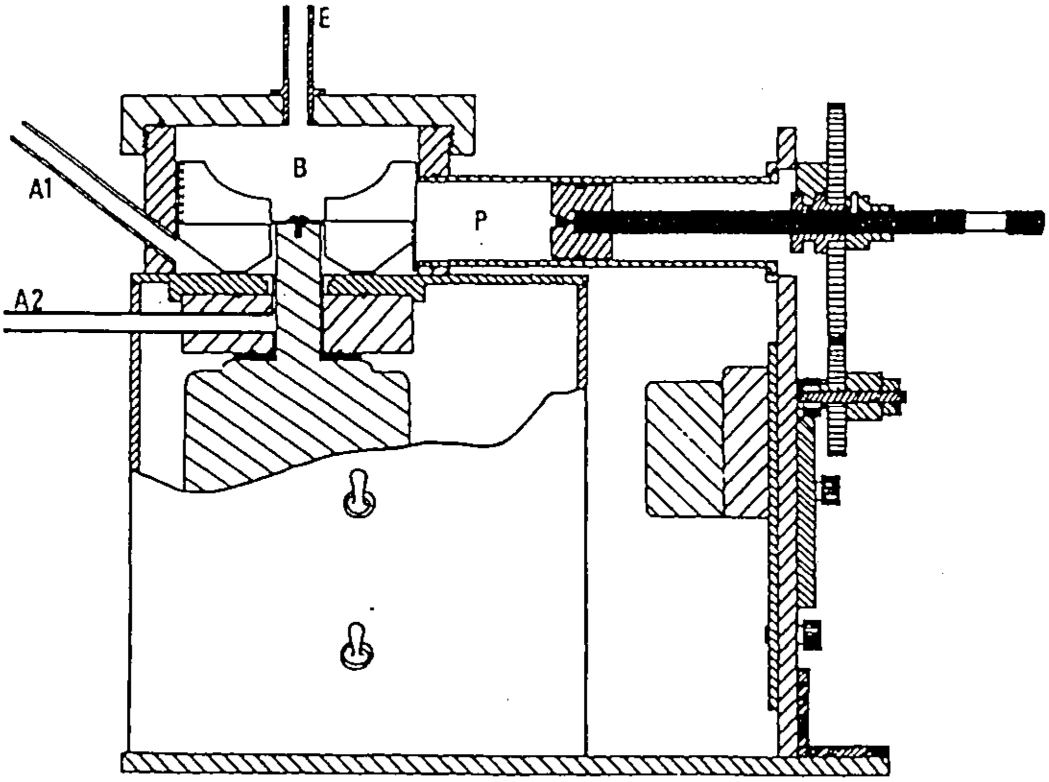

Fig.(3-3-c) Diagram of dust generator showing the piston drive (P), air inlets (A1 and A2), rotor blades (B) and the dust tube exit (E)

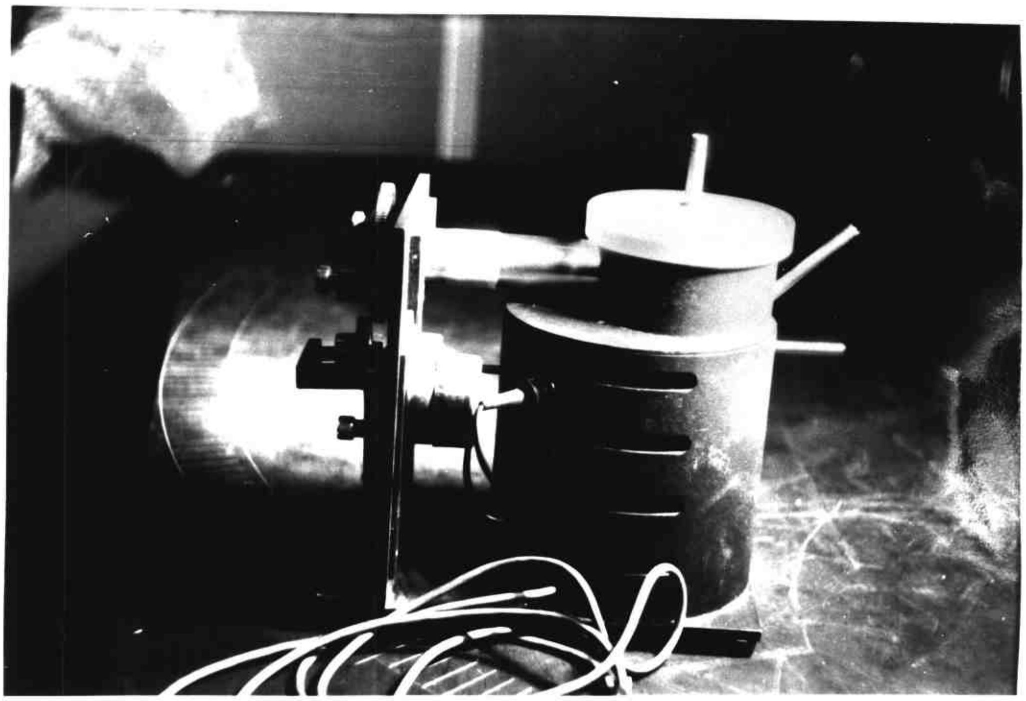

P-3-3-1 Photograph of Timbrell dust generator

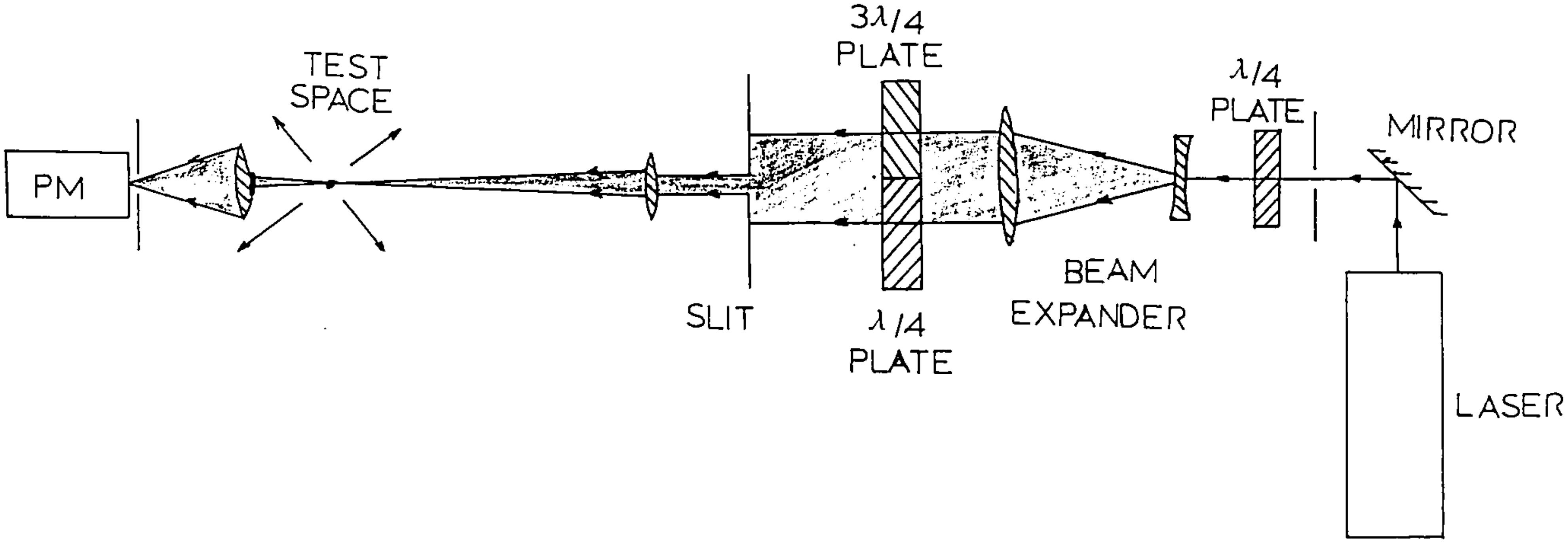

Fig.(3-4-a) Split-beam expanded system lay-out

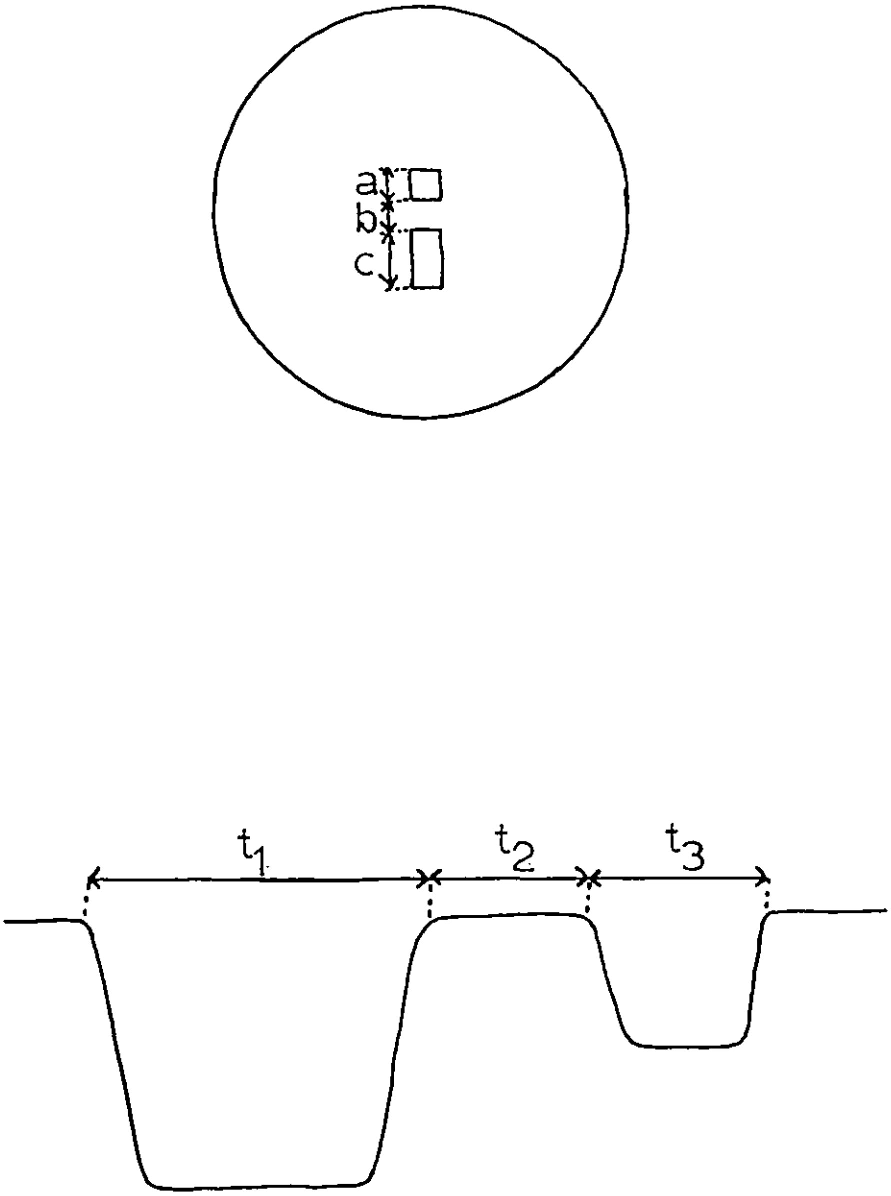

Fig.(3-4-b) (i) Aperture in front of photomultiplier

(ii) Definition of particle times t_1, t_2 and t_3 to cross a,b and c respectively horizontally. The slit is imaged at the test space by a lens such that the top half of the image is vertically polarised and the bottom half is horizontally polarised. The test space is then imaged onto the mask in front of the photomultiplier. A particle passing through the test space scatters each polarisation in turn, thus allowing the ratio of the two scattered intensities (R) to be determined. This system has the advantage that it uses all the light, there being no losses as at the grating in Figure (3-2-c).

In order to distinguish between a signal arising from a single or two or more particles passing through the test space together, two apertures of different size were placed in front of the photomultiplier. Light scattered from the vertically polarised part of the beam falls on the longer of the two of these apertures, and that scattered from the horizontally polarised part falls on the shorter one. This is due to the way the pin holes are arranged in front of the photomultiplier and the way the particles are injected. This arrangement leads to a characteristic signal when one particle alone passes through the test space as shown in Figure (3-4-b). The ratios $t_1 : t_2 : t_3$ are then the same as c : b : a. In practice this is chosen to be approximately 2 : 1 : 1.

With this set-up we consistently obtained for ballotini R=1 on average as expected, since both polarisations are scattered equally strongly by a spherical particle. With quartz fibres however, we obtained R=1.8 on average. This was a very promising result, but this method suffered the inherent disadvantage of being sensitive to orientation of the fibres. This problem was overcome using the optical system described in the next section, which used circular polarisation in the test space. The scattering is then independent of the orientation in the plane perpendicular to the direction of propagation.

3.5 Single-Beam Circularly Polarised Set-Up.

Figure (3-5-a)shows a set-up where the light from the

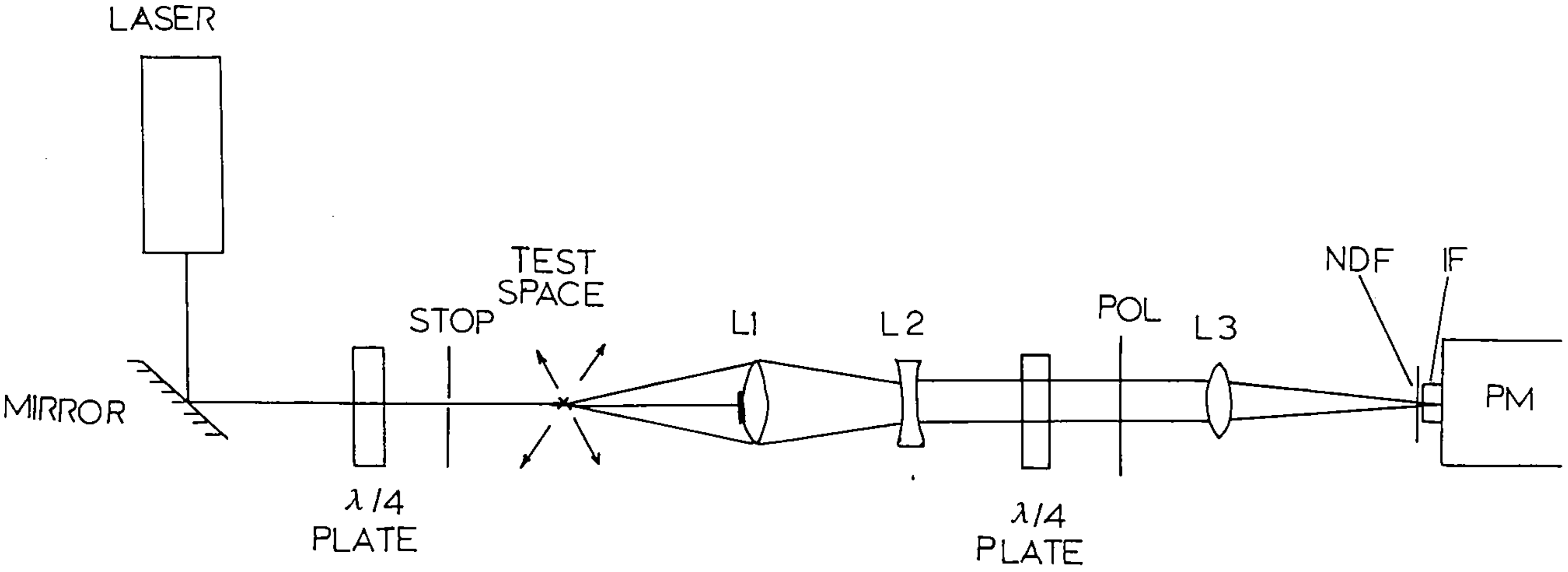

Fig.(3-5-a) Single-beam optics using circular polarisation laser is circularly polarised by a quarter wave plate and after passing through the test space, the beam hits a stop on lens L1, which ensures that very little unscattered light is collected. The scattered light is collected by L1 and converted into a parallel beam by L2. This then passes through another quarter wave plate which converts it back to linear polarisation. The polariser is used to select either the maximum or minimum signal (the effect on the scattered light by the angle of the polaroid axis is explored in Appendix C). Convex lens L3 focusses the light onto the pinhole in front of the photomultiplier (PM). A neutral density filter (NDF) is placed in front of the pinhole to prevent PM saturation. An interference filter (IF) ensures selective transmittance of light of He-Ne wavelength.

The optical system was lined up by placing a hair stretched across an optical holder in the test space such that the image formed by the optics coincided with the pinhole.

The hair was replaced by a source of ground quartz fibres. With the polaroid set to obtain maximum signal the magnitudes of the signals were recorded. Similarly, a set of readings was obtained with the polariser set at minimum. These results were plotted in the form of histograms as shown in Figure (3-4-b(i)). The ratio R of the maximum to the minimum signal comes but to be about 15 : 1. This experiment was repeated for glass ballotini particles and water spray and the results are shown in Figures (3-5-b(ii)) and (3-5-b(iii)) respectively. For ballotini R is around 100 : 1 and for water spray R is greater that 100 : 1. This experiment was repeated several times and similar results were obtained. This established a consistently

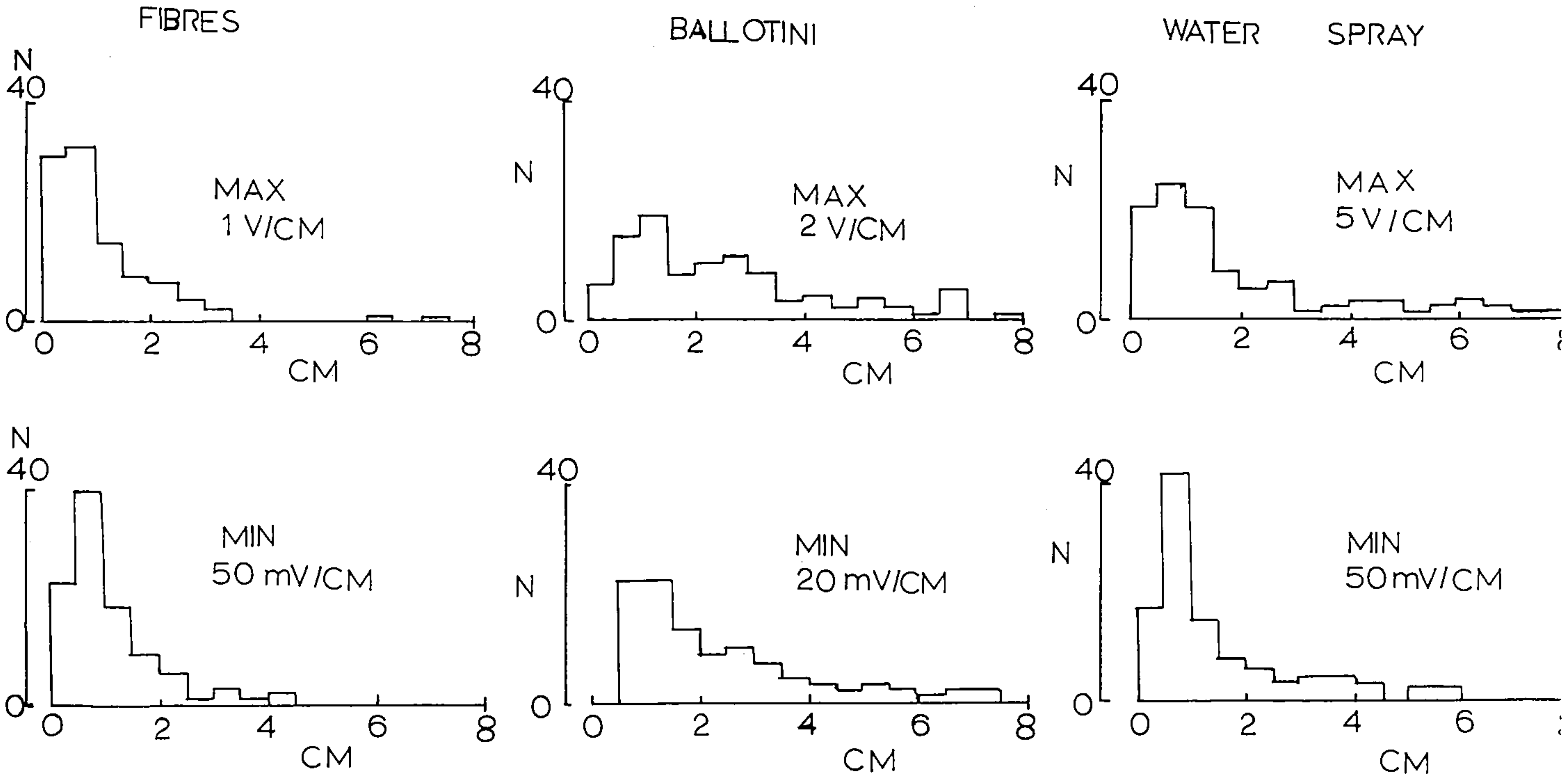

Fig.(3-5-b) MAX=Polariser set to give maximum signal. MIN=Polariser set to give minimum signal
Also quoted are the voltage scales on which the readings were taken.
(i)Plot of number/signal size in cm.for fibres (ii)same for ballotini (iii)same for water spray

different R for cylindrical and spherical particles, which could form the basis for anisotropic discrimination.

Consider a plane wave of the form

$$\underline{E}_{inc} = \hat{x}\, E_o\, e^{i\omega t} \qquad (3\text{-}5\text{-}1)$$

incident on a quarter wave whose fast axis lies along $\hat{y}'$ as shown below,

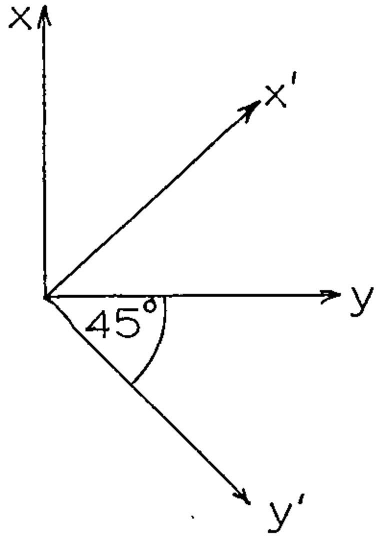

using the co-ordinate transformations (see Appendix C), the field emerging is

$$\underline{E}_1 = \tfrac{1}{2}\big((1-i)\hat{x} + (1+i)\hat{y}\big)\; E_o e^{i\omega t} \qquad (3\text{-}5\text{-}2)$$

Now if $\underline{E}_1$ is incident on a scatterer whose axis lies at angle ψ_s to the x-axis then it can be written as

$$\underline{E}_1 = \tfrac{1}{2}(1-i)(\hat{x}_s + i\hat{y}_s)\, E_o e^{i(\omega t+\psi_s)} \qquad (3\text{-}5\text{-}3)$$

where $\hat{x}_s$ and $\hat{y}_s$ are Cartesian axes of the scatterer. If A and B represent scattering factors in two orthogonal directions then the scattered field is

$$\underline{E}_s = \tfrac{1}{2}(1-i)\big(\hat{x}(A\cos\psi_s - iB\sin\psi_s)$$
$$+ \hat{y}(A\sin\psi_s + iB\cos\psi_s)\big)\, E_o e^{i(\omega t+\psi_s)} \qquad (3\text{-}5\text{-}4)$$

This field passes through the second quarter wave plate whose optic axis makes an angle of 90° to $\hat{x}$. The field emerging from the plate simplifies to

$$\underline{E}_2 = \frac{1}{2\sqrt{2}} (1-i) \left(\hat{x}(A+B)e^{i(\frac{\pi}{4} - \psi_s)} + \hat{y}(A+B)e^{-i(\frac{\pi}{4} - \psi_s)} \right) \times . E_o e^{i(\omega t+\psi_s)} \qquad (3\text{-}5\text{-}5)$$

Thus the polarisation ratio along two orthogonal directions is

$$R = \frac{|\underline{E}_x|^2}{|\underline{E}_y|^2} = \left| \frac{A + B}{A - B} \right|^2 \qquad (3\text{-}5\text{-}6)$$

This will be the basis for our measurements in the next Chapter.

Theoretically for a homogeneous isotropic sphere A=B and $R=\infty$. In order to obtain a rough distinguishability figure, we can assume Re $(AB^*)=0$, then since experimentally spherical patterns give $R=100$ we have

$$\left|\frac{A}{B}\right|^2 \leqslant 1.5 \qquad (3\text{-}5\text{-}7)$$

For fibres R comes out to be approximately 16, thus giving

$$\left|\frac{A}{B}\right|^2 \leqslant 3 \qquad (3\text{-}5\text{-}8)$$

This establishes a distinct difference which can be used for distinguishing between fibres and spherical particles.

3. 6 Conclusion

The apparent lack of success of the modified fringe system was due to:

(i) size of particles >> λ_f (fringe spacing)

(ii) the noise due to light scattered from optical elements was large compared to the depth of modulation of the signals.

This led to the use of a single beam where a circularly polarised beam of light eliminated the dependence on random orientation of the fibres. The results obtained with this system indicate the feasibility of this scheme for discriminating between different shaped particles. In order to extend this to individual particles we need to look at both polarisations simultaneously. This can be done with a beam splitter and two photomultipliers (see Chapter 4).

CHAPTER FOUR

MODIFICATION OF A LASER DOPPLER ANEMOMETER FOR FIBRE DETECTION.

4.1 Introduction

Various optical configurations for distinguishing between fibres and spheres were investigated in Chapter 3.

In this Chapter the lay-out of optics for looking at forward and backward scattering is described. An alignment procedure is described and the importance of the size of the test space is explored.

In order to test the feasibility of the system sample generators for spherical and cylindrical particles are described.

4.2 Optical System

(i) Components.

The main components of the system are

(a) A Helium-Neon laser source $\lambda = 632.8\mu m$ operating in the TEM_{00} mode, rated at a peak power of 26mW. Scientifica and Cook Ltd., Model SLH/20

(b) A Gould OS4000 digital storage oscilloscope

(c) Two mica quarter wave plates

(d) A beam splitter supplied by Barr & Stroud, Type BC 6P

(e) Two EMI photomultiplier tubes, Type 9658B
Two EMI photomultiplier housings, Type PR 1400RS
One EMI photomultiplier power supply, Type PM 28B

(ii) Alignment

In order to achieve the best results alignment of all optical elements is critical. For for [illegible] scattering, the initial alignment is carried out by placing a scatterer, such as a pin, in the test space and adjusting the relative distance between L1 and L2 such that a sharp image is formed at infinity. The photomultipliers PM1 amd PM2 are placed at the foci of L3 and L4 respectively. By removing the stop on L1 and observing the passage of the direct laser beam through the optics lateral adjustments to the optical components are made such that the beam passes through the elements centrally. The pinholes in front of PM1 and PM2 are adjusted so that they lie in the centre of the lightspots produced by L3 and L4. It was observed that no matter how accurate the alignment the images were indistinct. This must have a significant effect on the definition of the test space.

Alignment of the prism is carried out by adjusting three screws located on the table mount on which the prism is held. In this way the emerging beams from the two faces of the prism are made orthogonal to each other.

Alignment of the pinholes located in front of PM1 and PM2 is critical for obtaining good signals. By illuminating each pinhole in turn with a lamp, the holes are adjusted such that their images formed in the test space coincide when viewed through a microscope looking directly into the optical arrangement. By simultaneously viewing the pinholes and a pin located in the test space a condition of no parallex is achieved.

(iii) Optical lay-outs

The system shown in Figure (3-4-a) of Chapter 3 suffered the disadvantage of looking at one polarisation at a time. The drawback was overcome with the inclusion of a prism such that both polarisations could be observed simultaneously. This set-up is shown in Figure (4-2-a) and P-4-2-1-2.

The basic lay-out is the same as before with the exception of the prism which diverts one polarisation to PM1 and the other to PM2. Adjustment of the prism and the second quarter

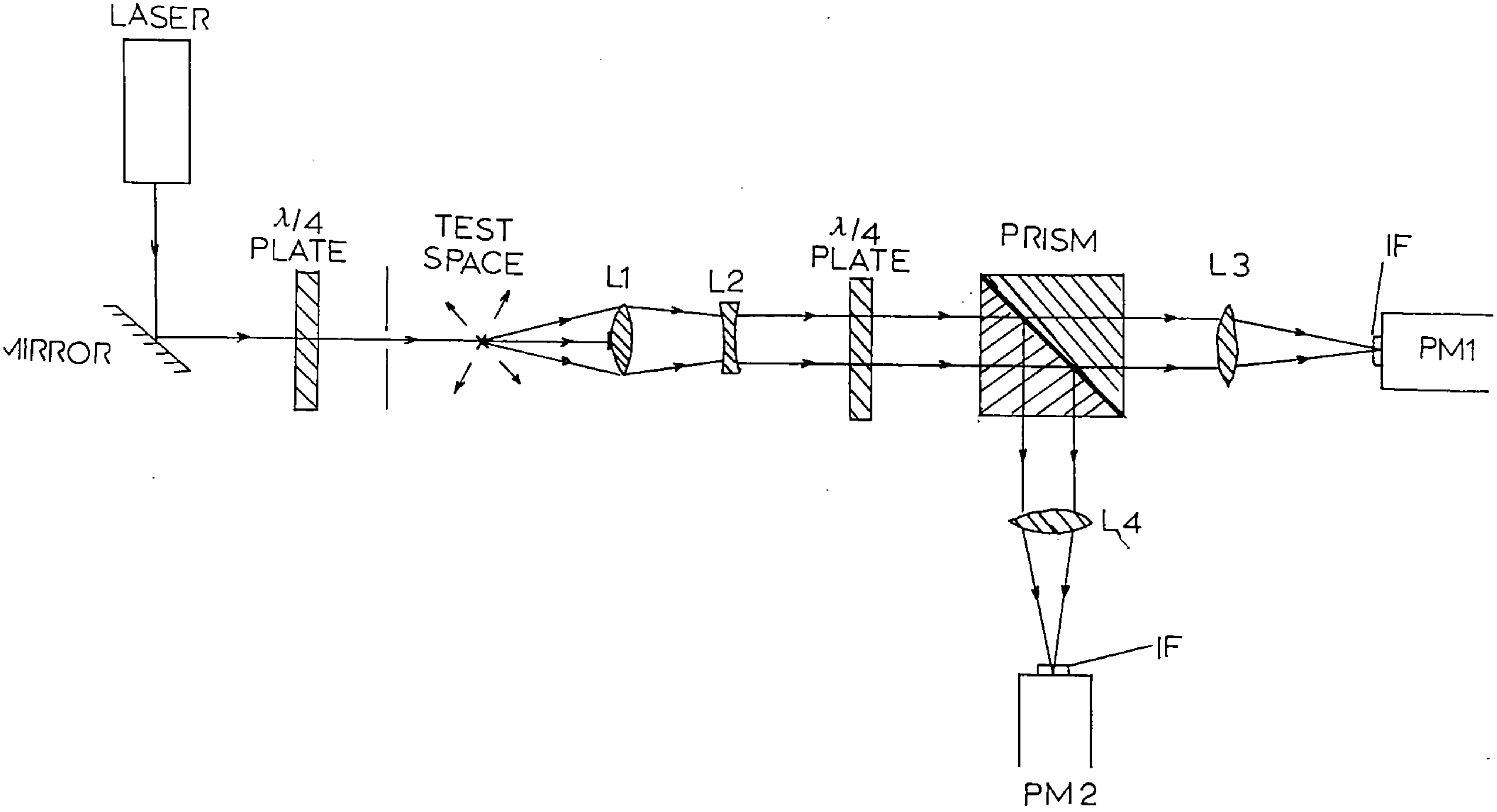

Fig.(4.2.a) Optical lay-out for observing the two orthogonal polarisations simultaneously in the forward direction using a polarising prism

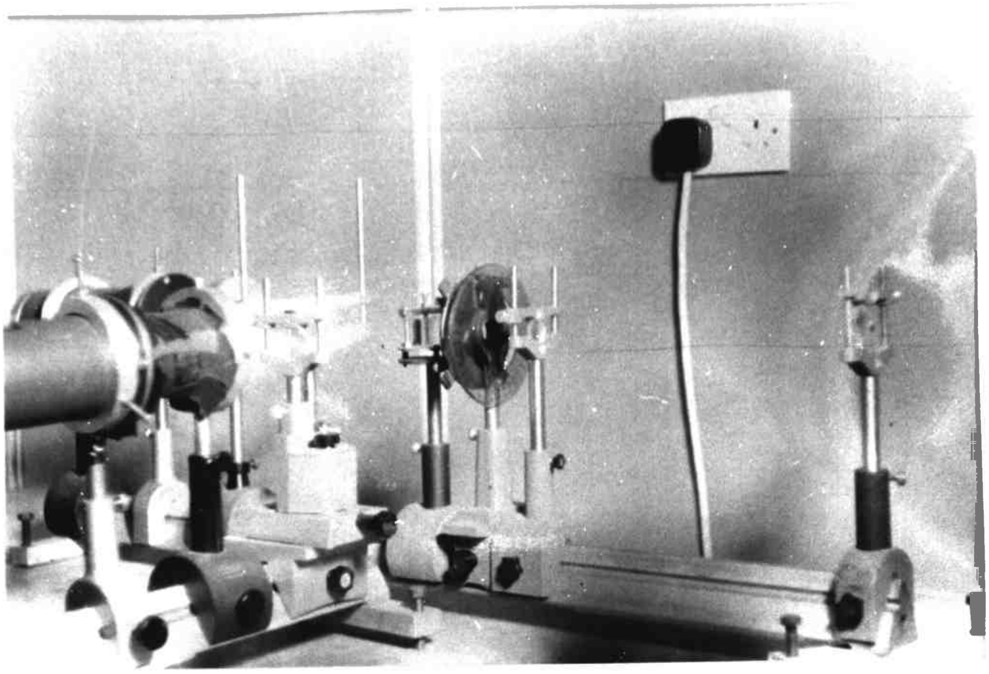

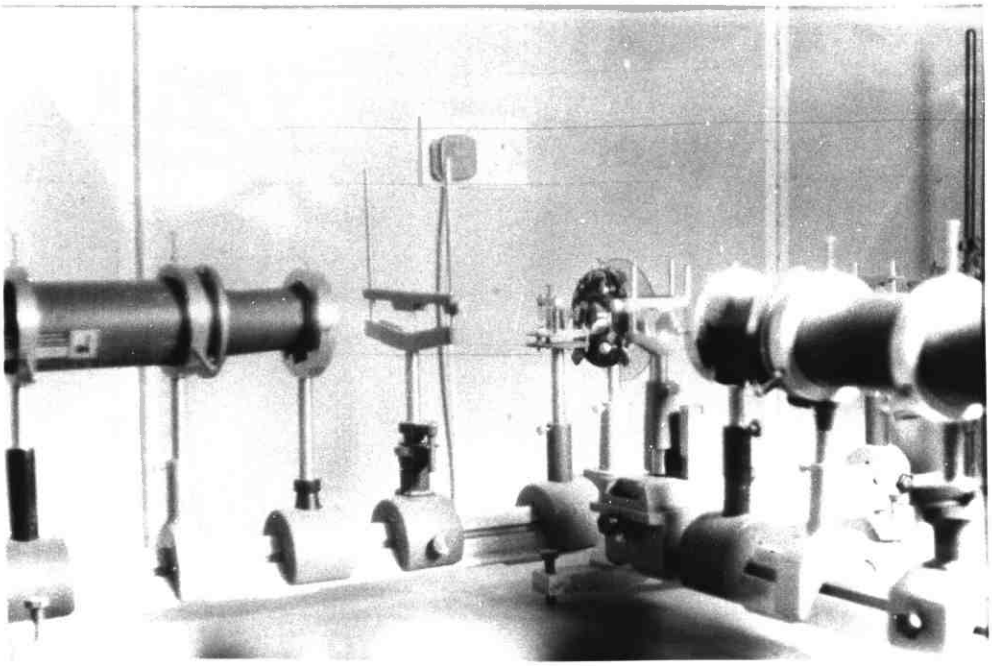

P-4-2-1 Photographs showing optics for light collection and signal detection.

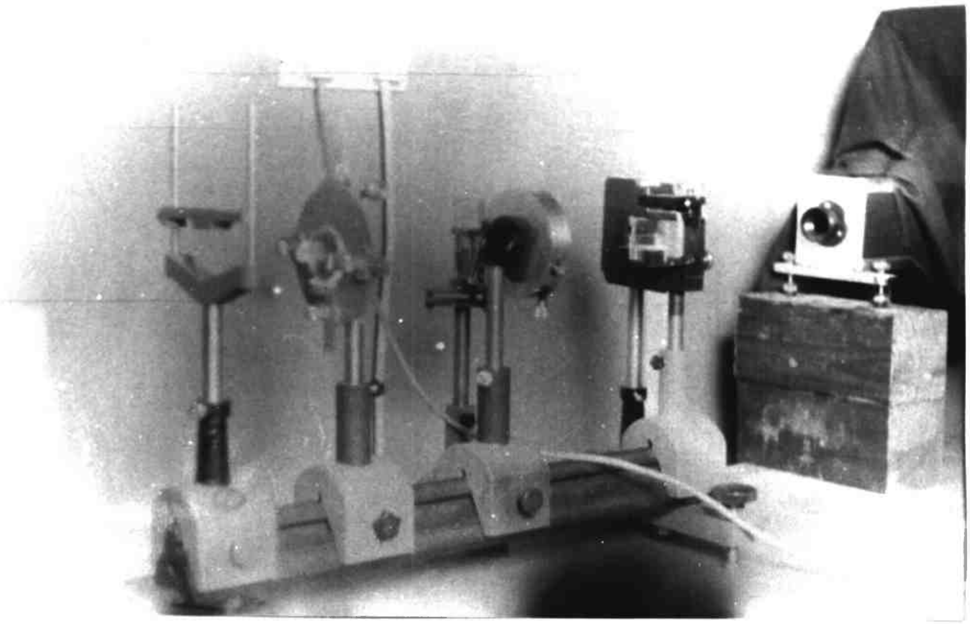

(i)

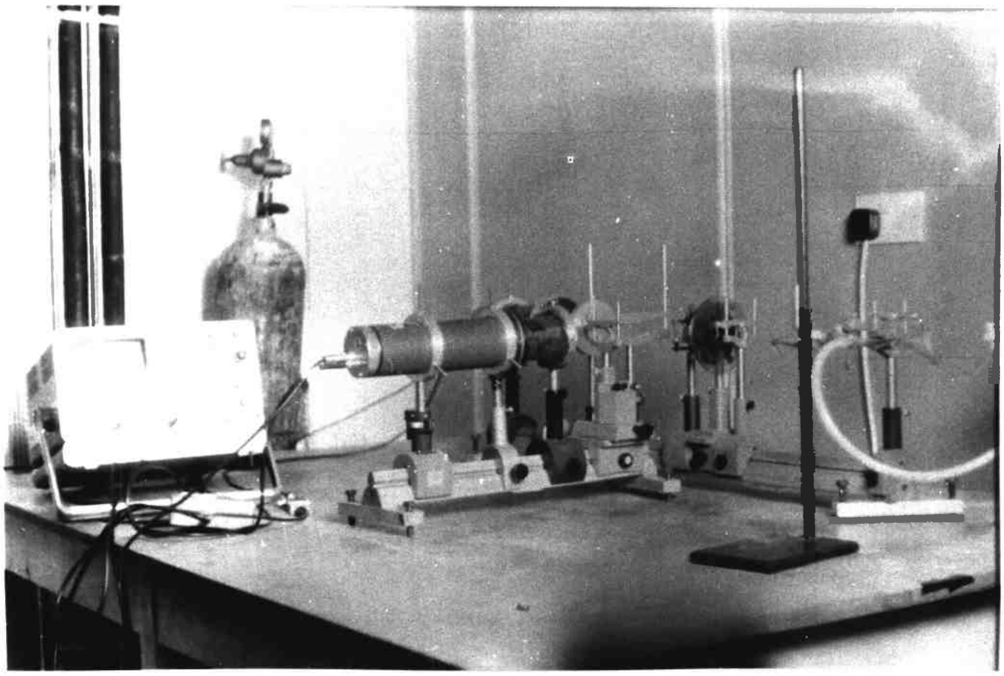

(ii)

P-4-2-2 (i) Plate showing arrangement for producing circularly polarised fringes.

(ii) Light collection and detection optics.

wave plate is carried out by observing the signal obtained from a 5μm precision pinhole placed in the test space while the laser beam is modulated by a rotating chopper. The signal obtained on PM2 is made to be a maximum and that on PM1 a minimum. The suppliers of the prism claim a maximum possible polarisation ratio of 500 : 1.

The magnitudes of the signals scattered by quartz fibres were recorded. This was repeated for water spray. However, in this case a neutral density filter was placed in front of PM2 to avoid the non-linear response part of the curve and the signals were correctly approximated. The results were plotted in histogram form and are shown in Figures (4-2-b(i)) and (4-2-b(ii)). It can be seen that there are very distinct peaks in each of the plots. One notable aspect of the plots is a distinct spread of the fibres over a range of $R^1(=|\frac{A}{B}|^2)$ which can be attributed to the fact that fibres can take arbitrary orientation.

Ideally the plot for water spray should be centred on $R^1=1.0$. However, from the histogram we obtain $R^1=1.07$, which is reasonable if we take into consideration the problem of alignment.

The result is also plotted on the same graph shown in Figure (4-2-c) where it is evident that the two shapes can be easily distinguished. In this case we may be able to specify a limit, say of $R^1=1.25$, such that any particle with $R^1>1.25$ will be fibre and any particle with $R^1<1.25$ will not. A separate identifying factor may be the intensity, since fibres tend to be small and produce only weak signals. This also leads to an indication of size. However, data analysis using R^1 was not pursued further since the experiment measures R defined by

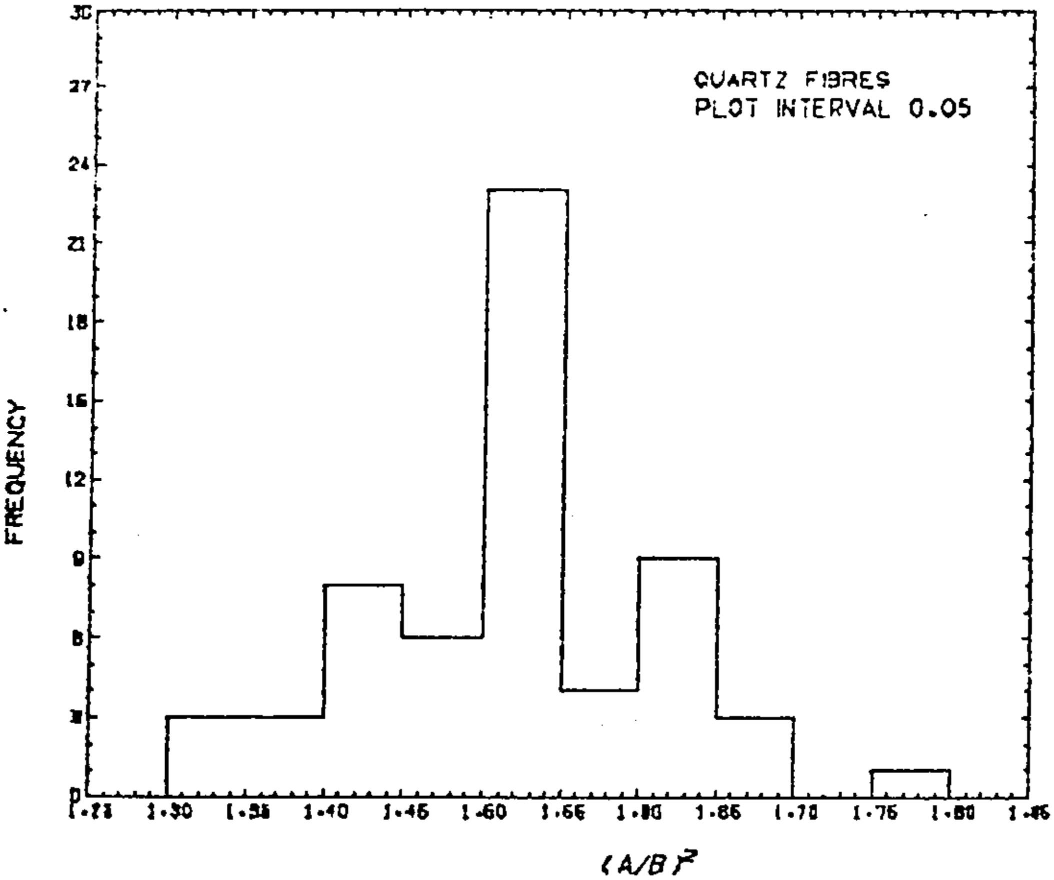

Fig.(4-2-b)(i) Experimental results for quartz fibres

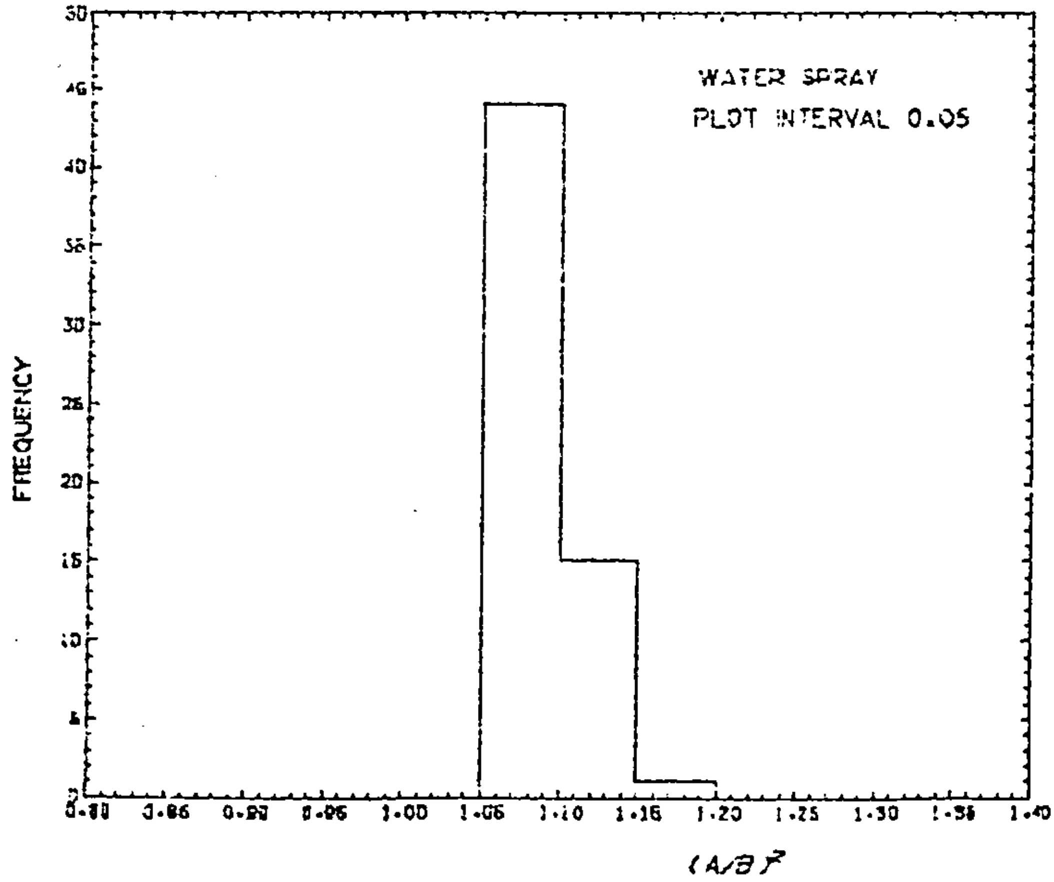

Fig.(4-2-b)(ii) Results of water spray

$(\underline{A})^2$ is the olarisation ratio

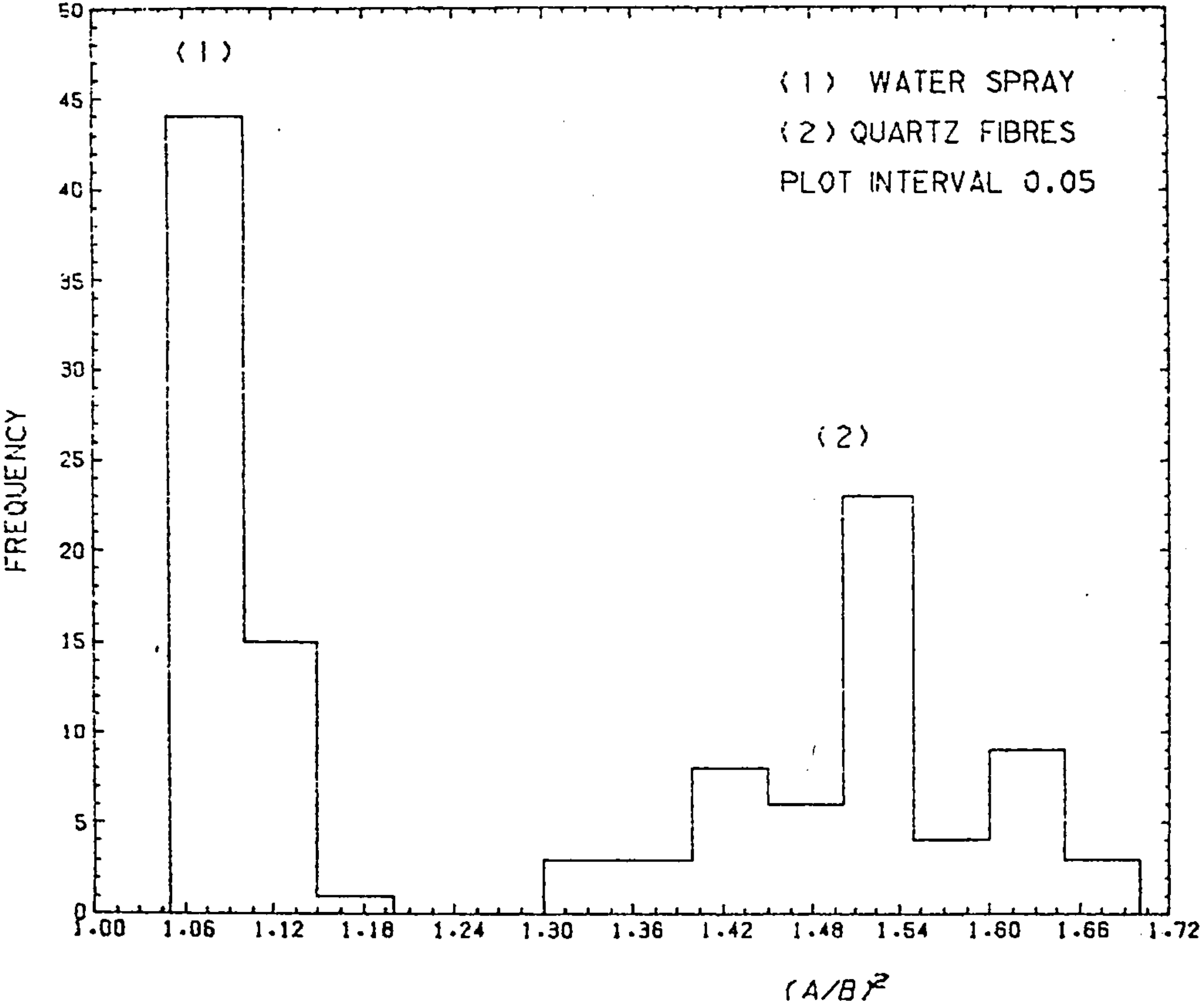

Fig.(4-2-c) Experimental results for fibres and water spray plotted on the same axis (see Chapter 3).

$$R = \left|\frac{A + B}{A - B}\right|^2 \qquad (4\text{-}2\text{-}1)$$

A comprehensive set of results using R is presented in the next Chapter.

Figure (4-2-d) shows the optical lay-out used for studying light scattering in the backward direction. The apparatus is essentially the same as for forward scattering except that a converging lens L focusses on the laser beam to a narrow waist in the test space and a near perfect mirror with a hole in the centre is used to collect the scattered light. The high intensity of light is required in this case since back scattered light is almost twenty times less than forward scattered light (see Chapter 2). L1 and L2 convert the scattered light into a parallel beam before it passed through the second quarter wave plate (QWP2). A light trap inhibits any stray light from the laser beam being reflected back into the optics (see Chapter 5 for results and discussion).

4.3 Test Space Considerations

In any optical system where light scattering measurements are made the size and shape of the test space are of paramount importance. The effective measurement value is determined in part by the intensity distribution by the illuminating beam, and in part by the geometry of the collection optics, including stops and apertures. Ideally, the test space should be roughly spherical or cubical shaped (Holve,1979) with a uniform illumination intensity and light collection efficiency.

For forward scatter measurements where the light is collected in the forward direction, the test space is confined by injecting particles at the point where the two images

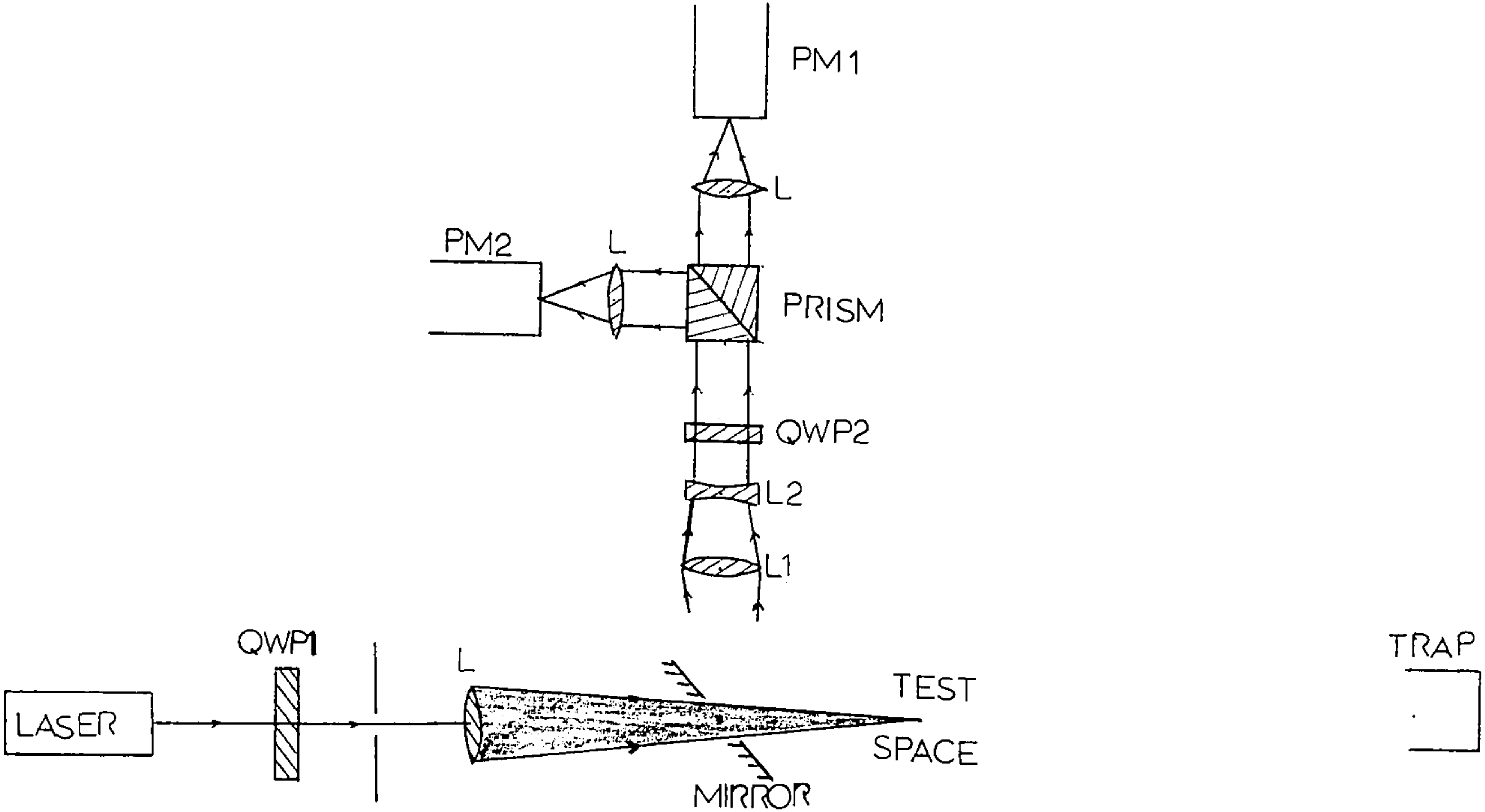

Fig.(4-2-d) Optical lay-out for studying scattering in the backward direction of the pinholes coincide as indicated in the alignment procedure. In the case of back scattering, the beam is focussed dowm to a waist of 500µm. Here again the alignment effectively locates the test space where the beam is at its narrowest. The particles are injected through a narrow opening such that they cross the test space where the beam is at this point.

In exploring the spatial variation of the polarisation ratio in the test space, several experiments were performed. One set-up used to do this is shown in Figure (4-3-a). The optical elements are the same as in Figure (4-2-a) except for the inclusion of a half wave plate instead of two quarter wave plates. The half wave plate rotates the plane of polarisation of the incident light by twice the angle of incidence to the optic axis. The plate is rotated to minimise the signal on PM2 and maximise the signal on PM1, or vice versa. The 5µm pinhole acts as a scatter and it is scanned in turn, horizontally and vertically to the optical bench, taking measurements of the sizes of the signals on PM1 and PM2. This experiment was repeated with the half wave plate replaced by a quarter wave plate.

The results obtained indicate that with horizontal scanning there is ~10% variation in the polarisation ratio, while vertical scanning gives ~40% variation in the ratio as the pinhole is moved away from the Gaussian maximum. This may be due to the overall aberrations of the optical system.

In both systems, however, the overall length of the test space is long and depends on the collection optics. The distribution of intensity of the illuminating beam, for operation in the TEM_{oo} mode, is Gaussian and given by

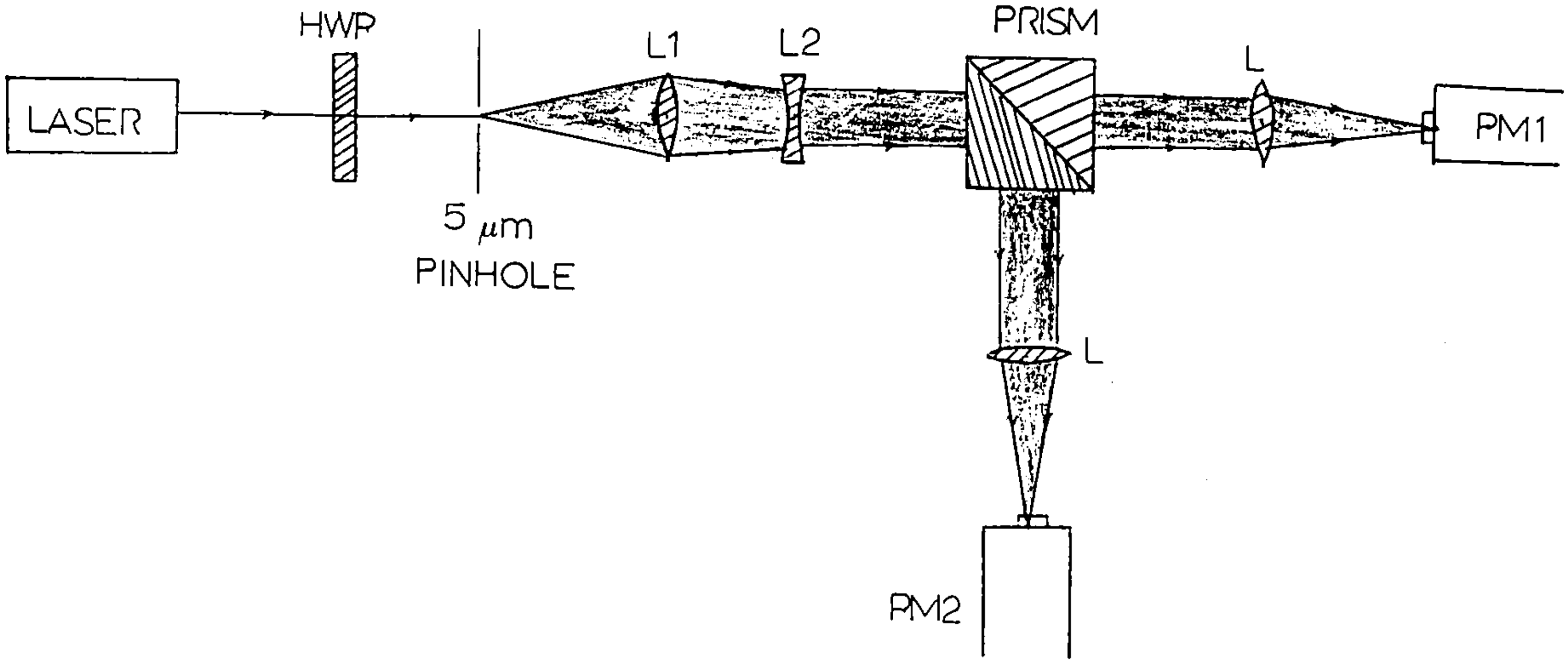

Fig.(4-3-a) Lay-out for characterising the test space incorporating a half wave plate

$$I(r,z) = (2p/\pi\sigma^2) \exp -2(r/\sigma)^2 \quad (4.3.1)$$

where P is the beam power and the radius (to $^1/e^2$ points intensity) is

$$\sigma(Z) = \sigma_0\left(1+(\lambda z/\pi\sigma_0^2)^2\right)^{\frac{1}{2}} \quad (4\text{-}3\text{-}2)$$

Here σ_0 is the beam radius at the waist (z=0) and is given in terms of the far field half angle of convergence θ_b by

$$\sigma_0 = \lambda/\pi\theta_b \quad (4\text{-}3\text{-}3)$$

The intensity distribution along the Z direction is Lorentzian and falls off much more slowly than the radius. The Rayleigh distance Z_R, where the intensity on axis falls to half the central waist intensity, is

$$Z_R = \pi\sigma_0^2/\lambda \quad (4\text{-}3\text{-}4)$$

For waist diameter of $2\sigma_0 \sim 0.5$mm and laser wavelength $\sim 0.5\mu$m, $Z_R \sim 19.6$cm. Thus the illumination volume is long compared with its width.

It is necessary and advantageous to limit the effective operating test volume. One method of achieving this is to use a lens on an axis close to the forward direction (Holve,1979). However, to fulfil the requirements of a monotonic signal response with least sensitivity to refractive index, a coaxial forward scatter (θ=0) geometry is most desirable.

Hong (1977) and Hong and Jones (1978), characterised the test space of a laser doppler anemometer (LDA) system by the fringe contrast. After obtaining successful results using the systems shown in Figures (4-2-a) and (4-2-d), a modified LDA was devised, as shown in Figure (4-3-b). The collection optics is the same as before, but a mirror-beam splitter combination produces a pair of parallel beams which are circularly polarised before focussed by lens L1 to form the

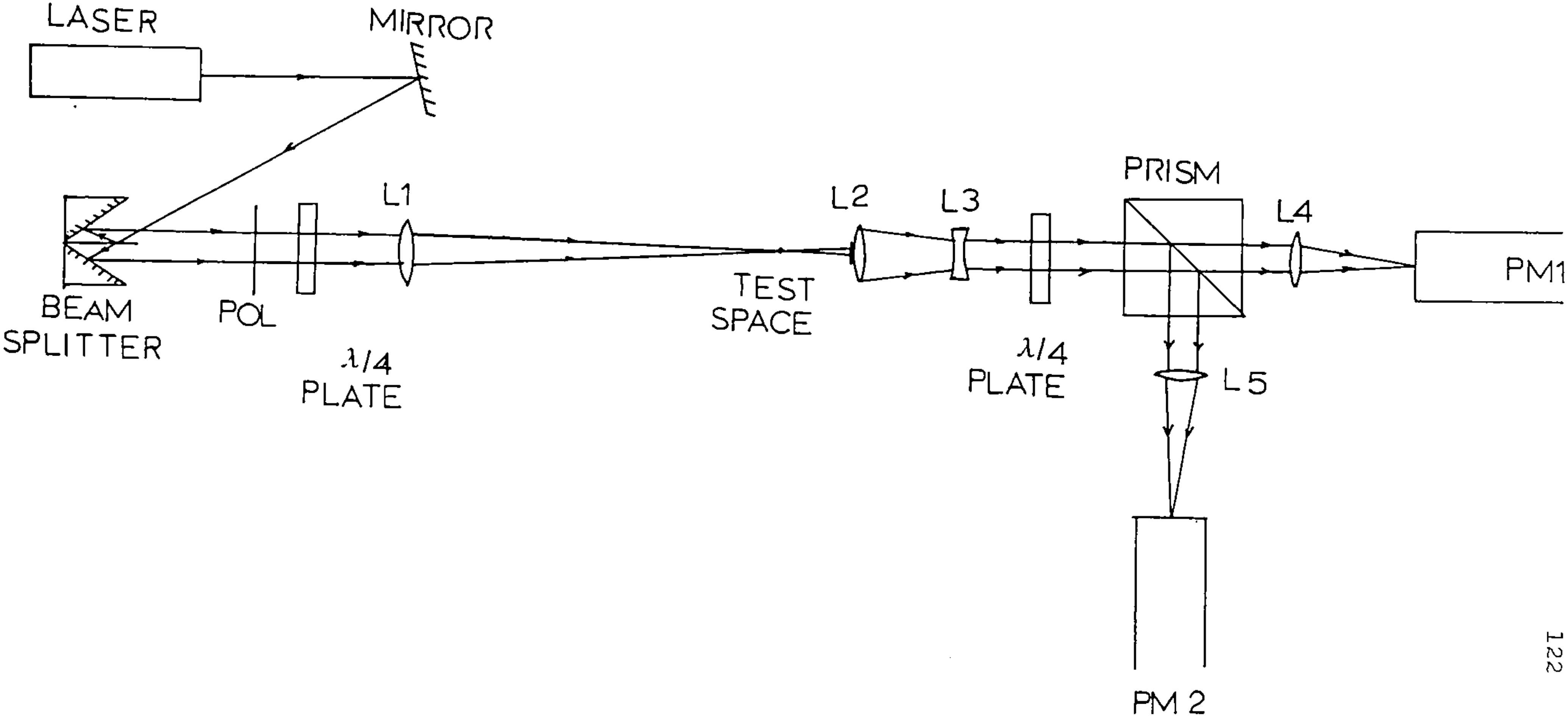

Fig.(4-3-b) Final optical system based on the laser doppler anemometer (LDA) for studying scattering in the forward direction test space.

It is possible to make a rough calculation of the test space from geometrical considerations. From Figure (4-3-c), the length D_l and the width D_w are given by

$$D_l = 2\sigma/\cos\gamma$$
$$D_w = 2\sigma/(\cos\gamma\sin\gamma) \qquad (4\text{-}3\text{-}5)$$

where σ is the beam half width at I_0/e^2 points. For example, taking $2\sigma = 1.3\text{mm}$ and $\gamma = 1^0$ gives $D_l = 1.3\text{mm}$ and $D_w = 74.5\text{mm}$.

Geometrical considerations neglect the difference in intensity of the laser beams. In fact, the intensity and the fringe contrast can vary from point to point in the test space. The contrast in the test space is affected by:

(a) The degree of coherence of light
(b) The relative intensities of the beams
(c) Mechanical vibration of system
(d) The Gaussian amplitude variation of the beams
(e) Any mismatch in geometry when the beams are focused together

All of the above conditions can be minimised by making the beam intensities equal and making sure the alignment is correct. Since the interfering beams are Gaussian, Hong (1977) has shown that the fringe contrast in the test space is given by

$$V_c = 1/(\cosh(4ZY\sin\gamma\cos\gamma/\sigma^2)) \qquad (4\text{-}3\text{-}6)$$

The highest fringe contrast is at the centre of the test space and the test volume can be defined as the sphere of radius R_s which encloses all fringes of contrast $\geqslant 0.95$ (Figure (4-3-d)). Strictly speaking the test volume is cusp shaped and its size is a function of γ.

Particles traversing the test space can follow various trajectories as shown in Figure (4-3-e). The factor which

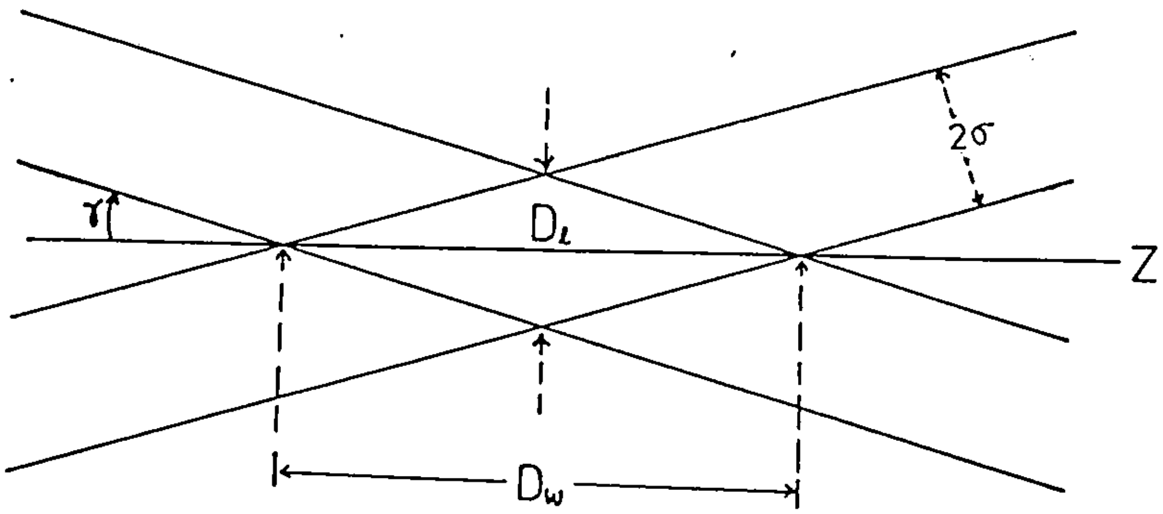

Fig.(4-3-c) Parameters for estimating the size of test space for the system of Fig.(4-3-b)

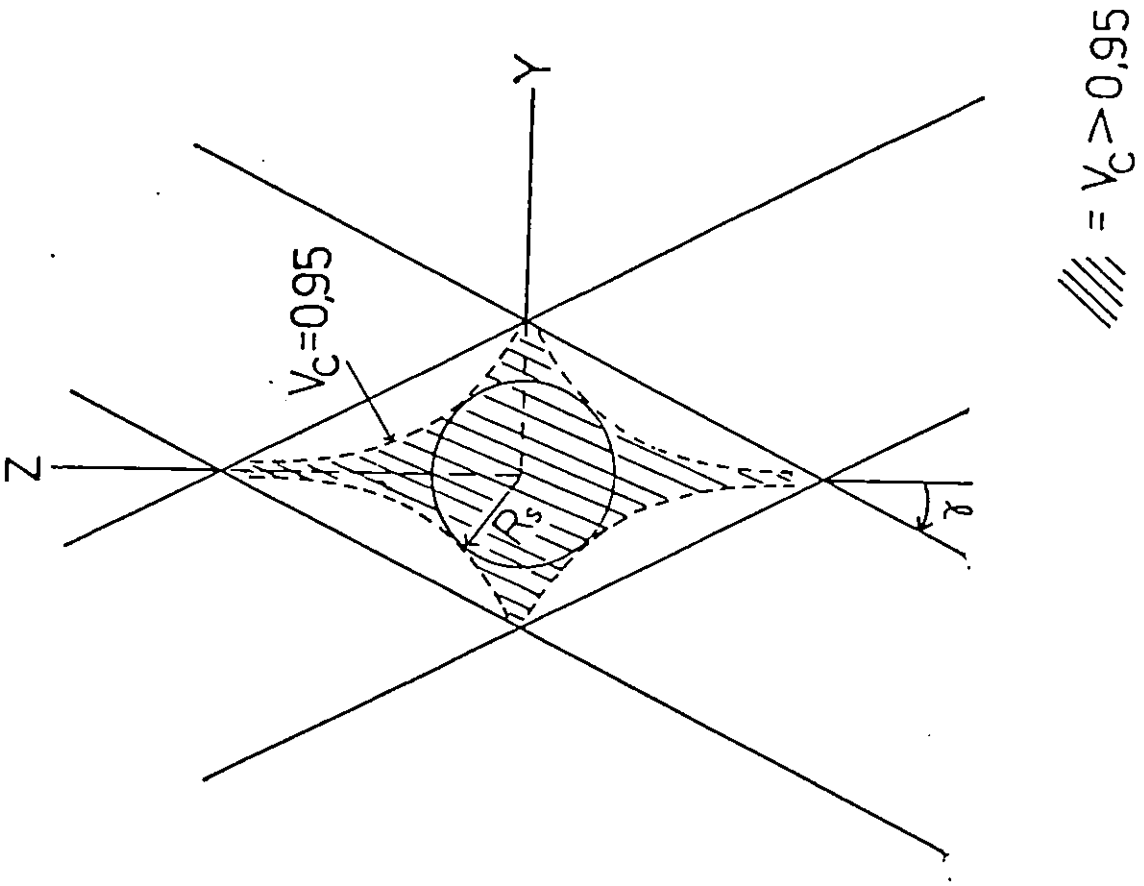

Fig.(4-3-d) Visibility of the fringes within the shaded region is >0.95 (after Hong, 1977)

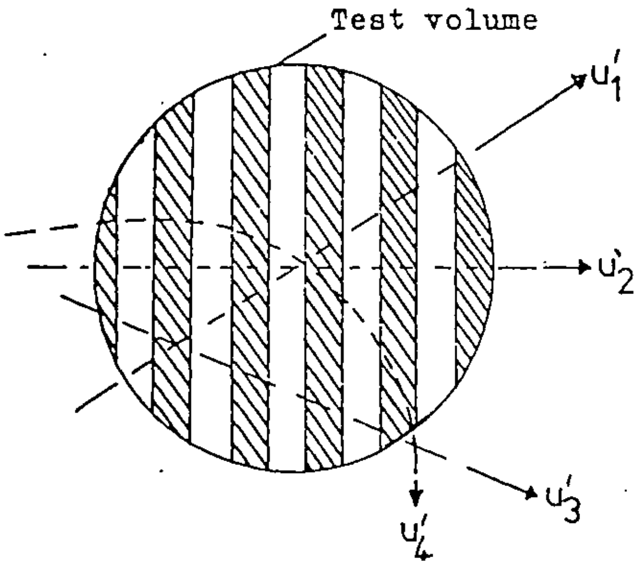

Fig.(4.3.e) Various possible trajectories for particles traversing the test space

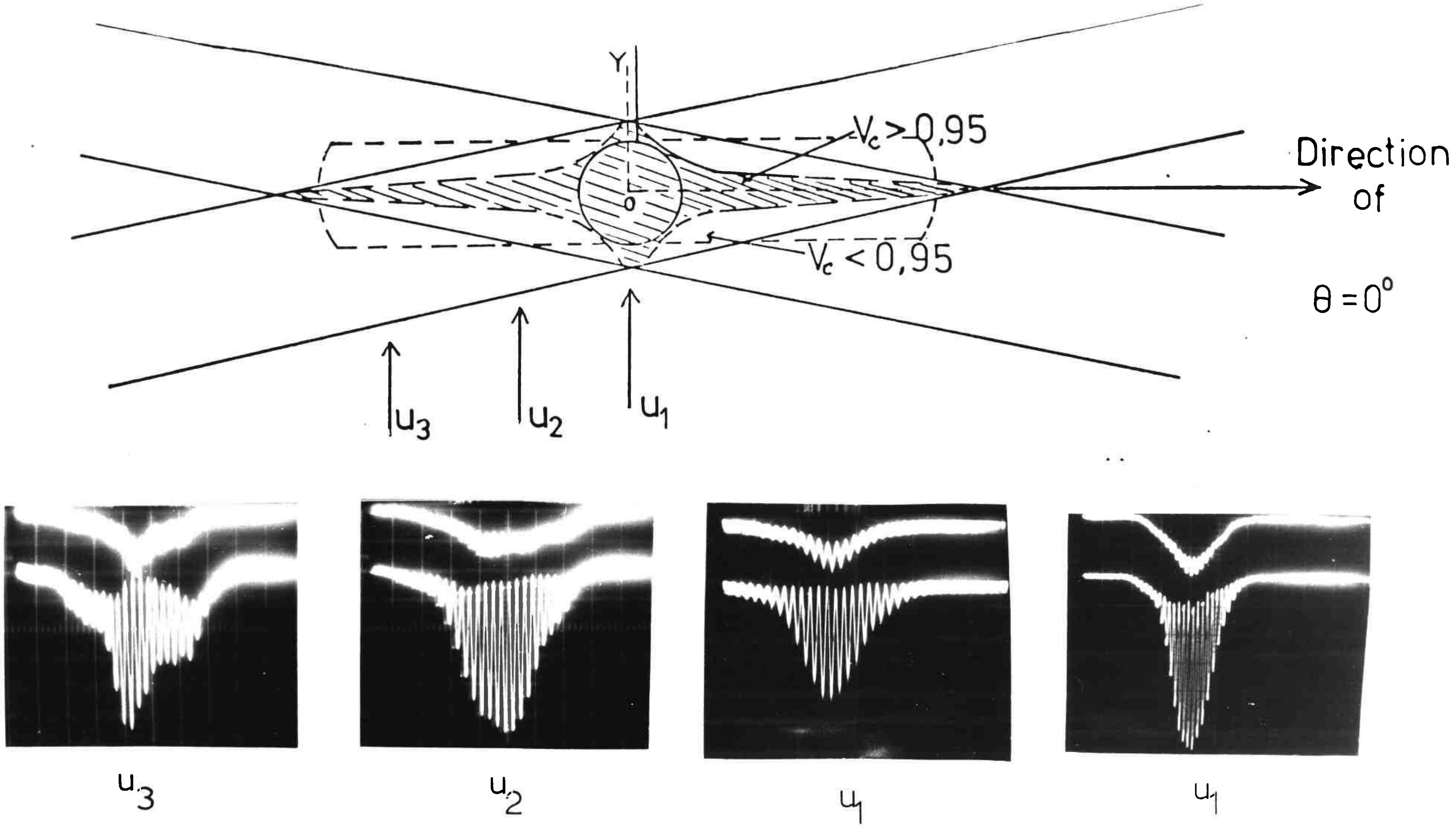

Fig.(4-4-f) Signal shapes as functions of particle trajectories for the forward direction.

distinguishes between particles travelling through various parts of the test volume is the signal shape as shown in Figure (4-3-f). For a particle travelling in the direction U_1 perfect Gaussian signals are observed from both the photomultipliers. However, for any other trajectory a distorted signal is observed. In this way only signals with Gaussian shape are measured. Apart from the obvious advantage of limiting the test space, this system has the added advantage that by counting the fringes we can find the velocity of the particle. However, confinement of the test space does not of itself eliminate the source of errors for an in-situ optical measurement system where the trajectory of the particle affects the signal observed. An approach where dependence on particle trajectory is eliminated is reported by Holve (1979).

CHAPTER FIVE

EXPERIMENTAL RESULTS AND DISCUSSION

5.1 Introduction

In this Chapter an electron micrscope study of micro-quartz fibres is presented with a summary of the experimental results for glass ballotini, water spray and quartz fibres for forward and backward scattering. Results indicate a clear distinguishability between fibres and spherical particles in the forward direction. In the back scatter mode similar distinguishability is observed but with reduced polarisation ratios.

Theoretical results are in general agreement with experiment. Results are presented for the integrated scattered intensity allowing for the finite aperture of the collecting lens. The effect of error in the phase plates, with orientation χ and scattering angle θ, is also investigated.

Results are presented of theoretical predictions of the measured polarisation ratio R given by

$$R = \left|\frac{A+B}{A-B}\right|^2 \qquad (5\text{-}1\text{-}1)$$

where A and B were defined in Chapter 2. The effect of error in the phase plates is to broaden the distribution and to change the modal value of R.

5.2 Microscope Study of Fibres

Quartz fibres generated by the Timbrell generator (see Chapter 3) were passed through the test space and deposited on electron microscope grids. These were photographed for analysis. A sample of the fibres is shown in P-5-2-1. The co-ordinates of the lengths and diameters were recorded on paper tape using a PCD image analyser unit connected to a paper tape writing machine. The analysis was carried out on the College's CDC 6600 Computer.

(i)

(ii)

P-5-2-1 (i) Electron micrograph of fibres; magnification = 2.4K
(ii) Electron micrograph of fibres; magnification = 1.8K

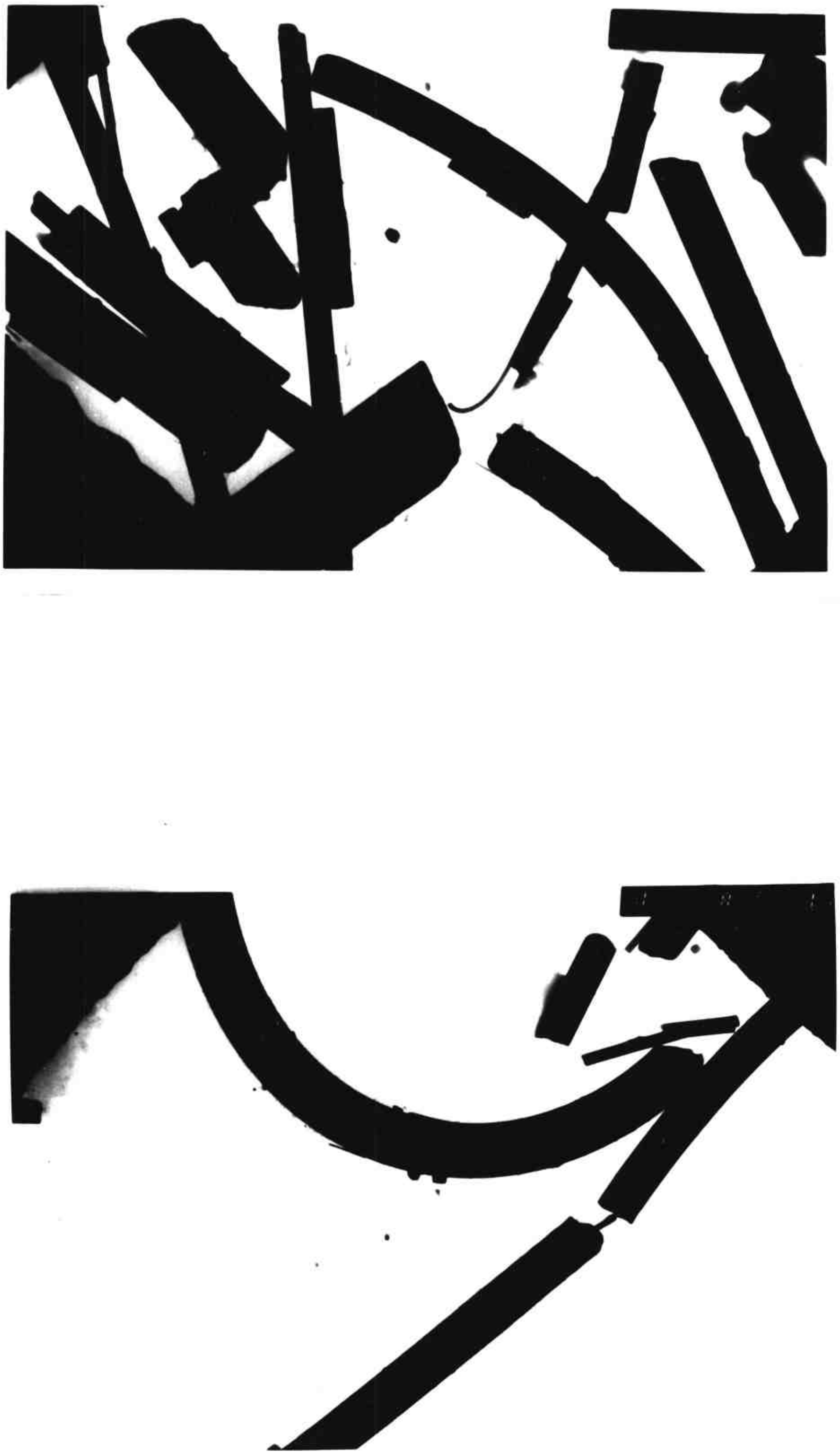

P-5-2-2 Electron micrographs of fibres showing their curved nature; magnification = 1.8k

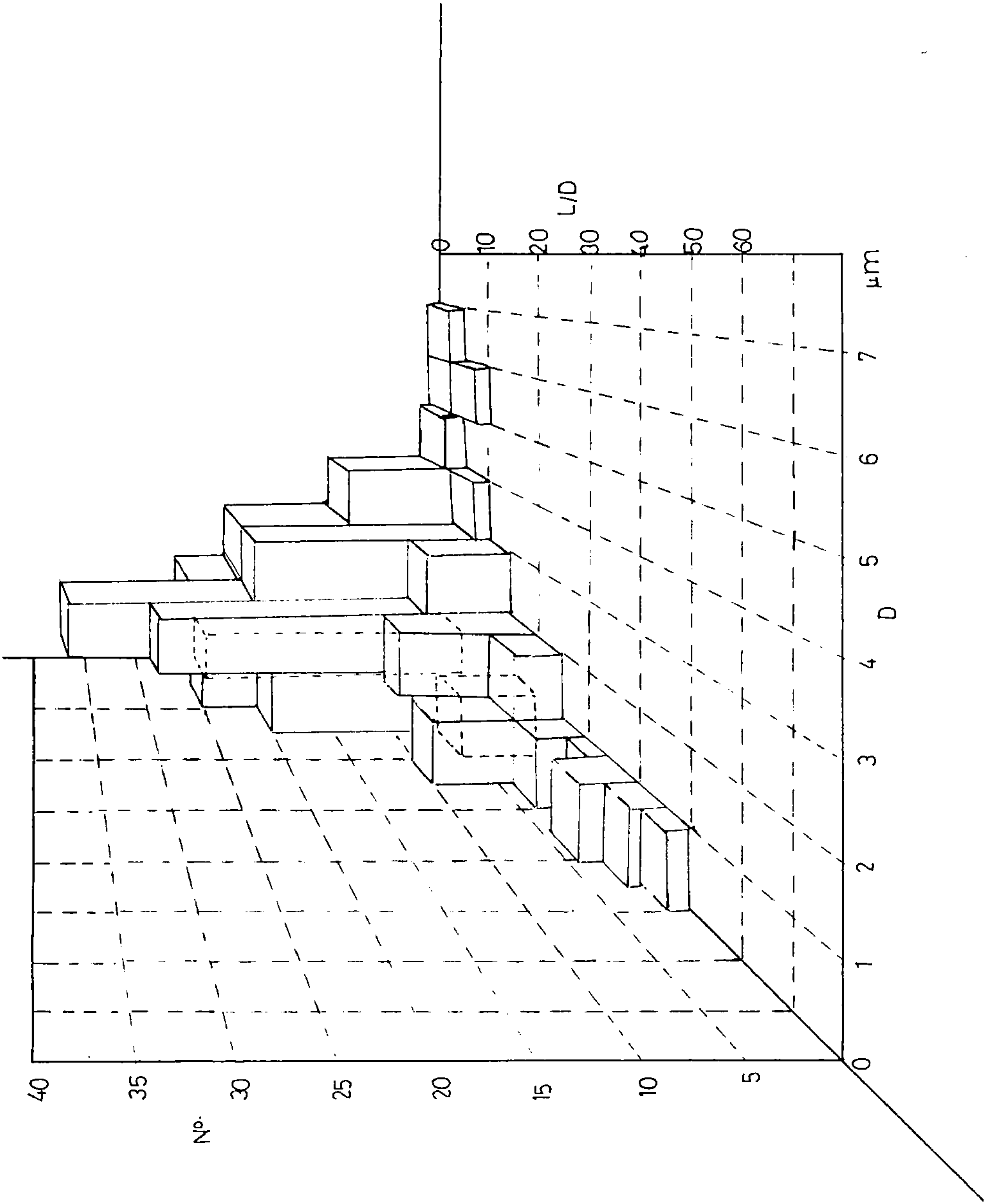

Fig.(5-2-a) 3-dimensional Number distribution for quartz fibres against diameter (D) and aspect ratio (L/D)

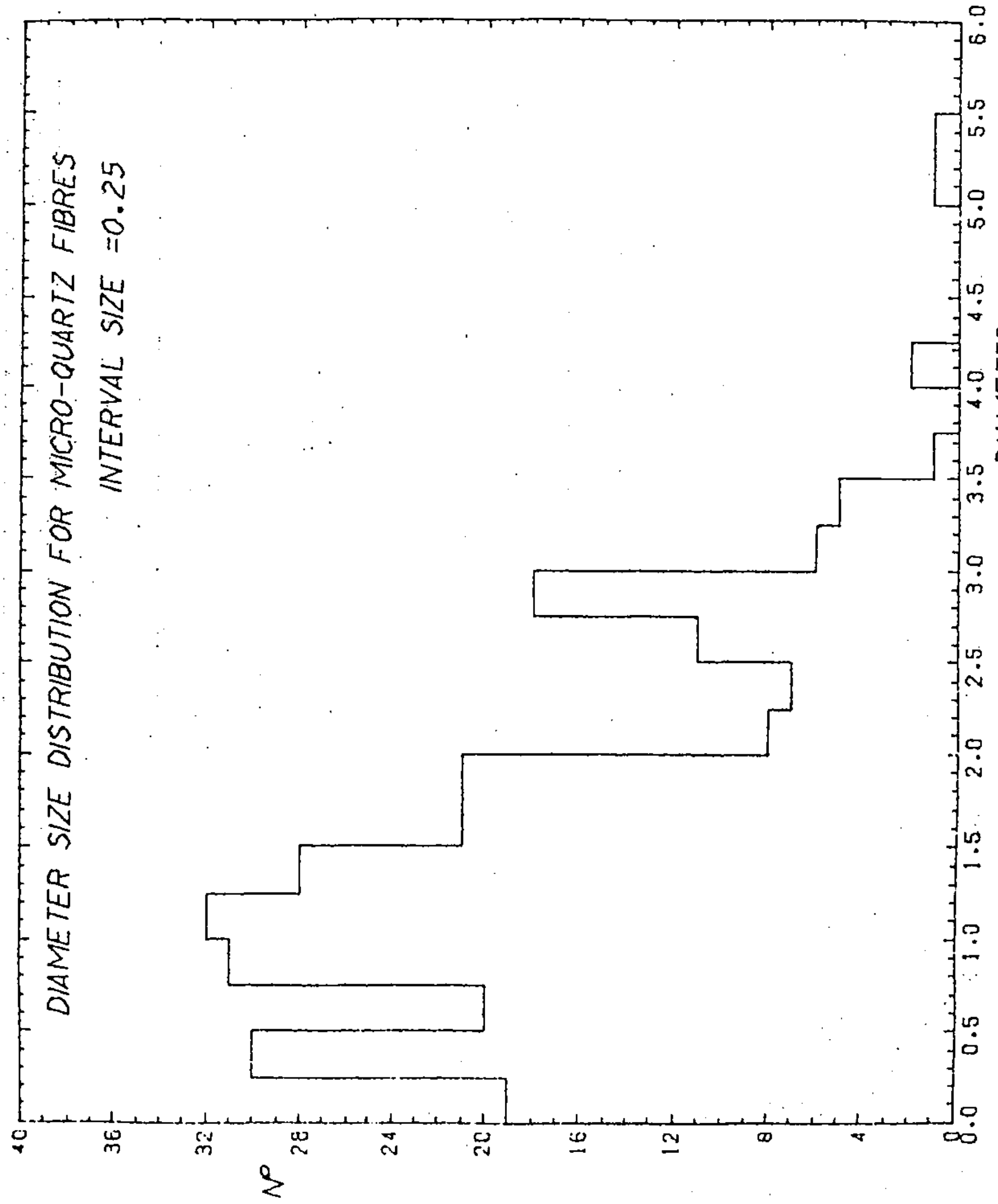

Fig.(5-2-b) Number distribution against diameter for fibres

Some fibres were curved as shown in P-5-2-2 and an approximate length had to be measured. The majority of the fibres seen were greater than 50μm in length.

A 3-dimensional distribution was plotted as shown in Figure (5-2-a), with diameter (D) in interval size of 1μm and the length to diameter ratio (L/D) in interval size of 10. The majority of the quartz fibres lie in 1-2μm diameter size range. Figure (5-2-b) shows a plot of the number of fibres against diameter in intervals of 0.25μm. It can be seen that there are three distinct peaks. This distribution is used in section (5-5) to predict theoretically the distribution of polarisation ratios for comparison with experimental results.

5.3 Results for Forward Scattering

In Chapter 2 computer results were presented for the ratio R^1 of two orthogonal intensities $I_{a_n s}$ and $I_{b_n s}$ plotted against size parameter x for various values of χ. However, the experimental set-up for forward scattering presented in Chapter 4, measures R as defined in Equation (5-1-1). In order to avoid infinities in the results, the reciprocal of R was plotted (i.e. RATIO = $1/R$).

Computations have been performed using the program for scattering from an infinite cylinder in the forward direction ($\theta=0$) for orientation angles $\chi = 90^\circ, 60^\circ$ and 30°. The results for three refractive indices are shown in Figures (5-3-a-c). It is interesting to note that the value of the RATIO increases considerably with decreasing χ, and also there are a number of resonances where RATIO is very high. Figure (5-3-d) shows that the RATIO is almost constant for $\chi = 0.01^\circ$. The effect of a complex refractive index is to dampen the

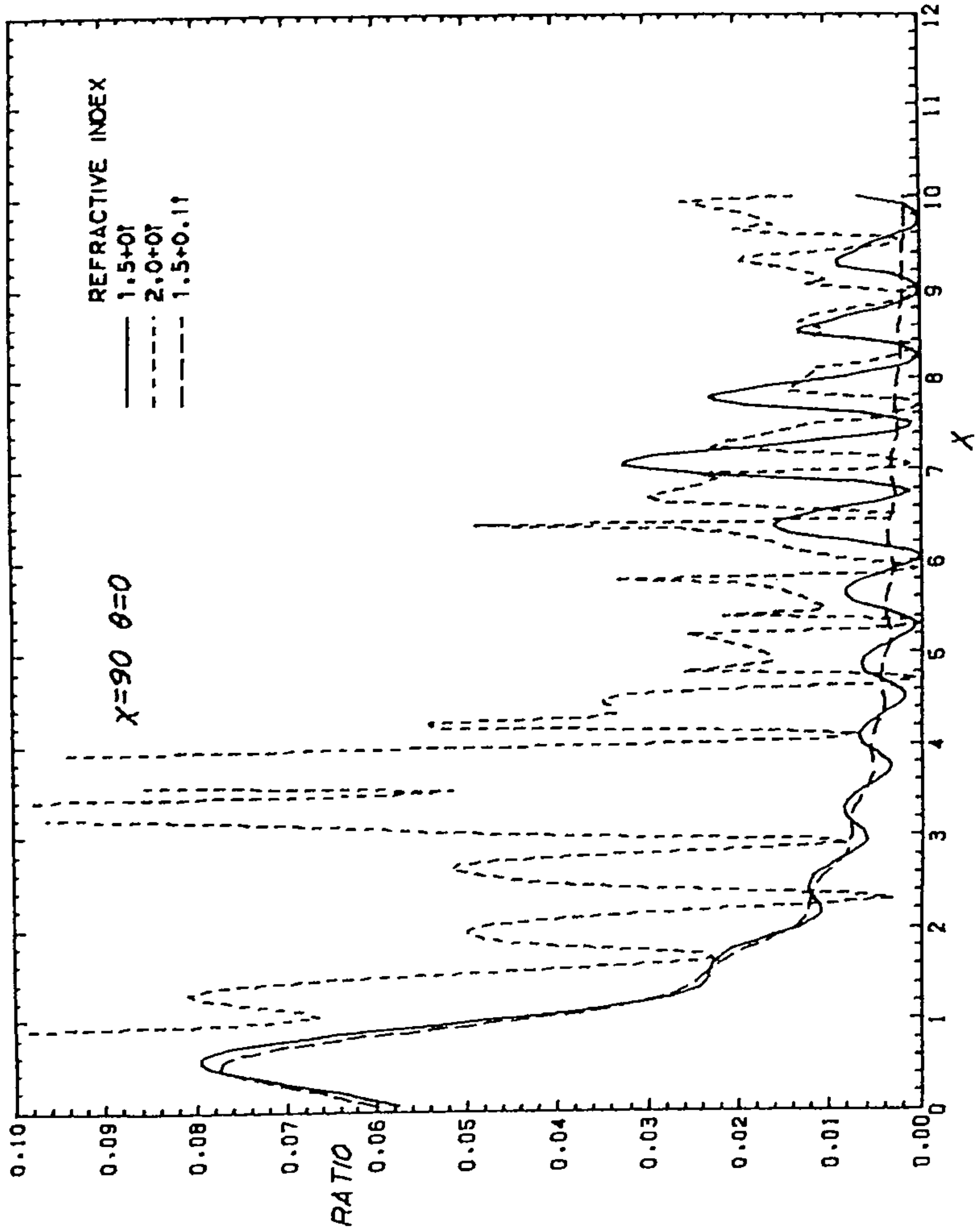

Fig.(5-3-a) Plot of RATIO against size parameter x for an upright infinite cylinder irratiated with light of λ = 632.8nm

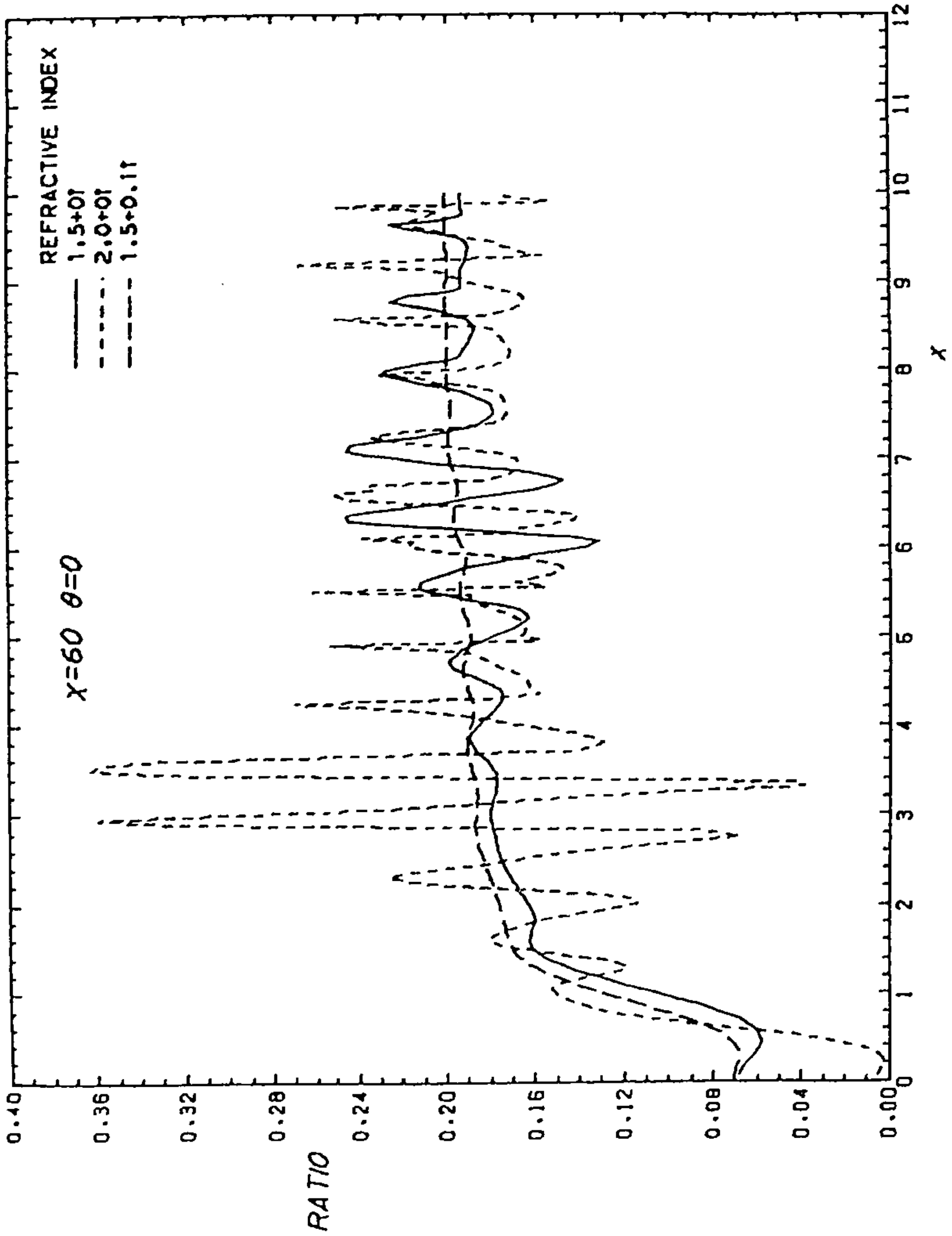

Fig.(5-3-b) Plot of RATIO verses x for an infinite cylinder

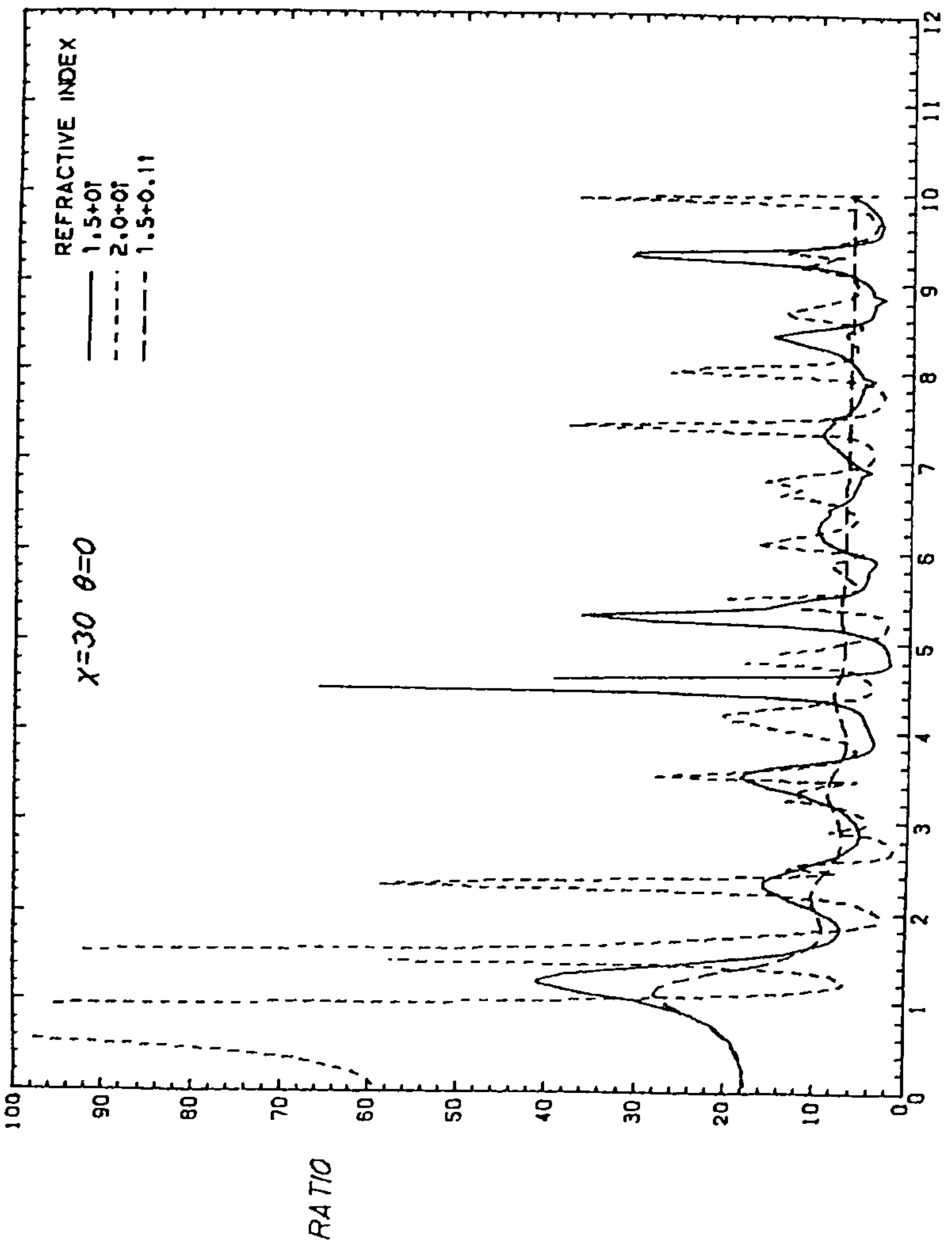

Fig.(5-3-c) Plot of RATIO against x for an infinite cylinder

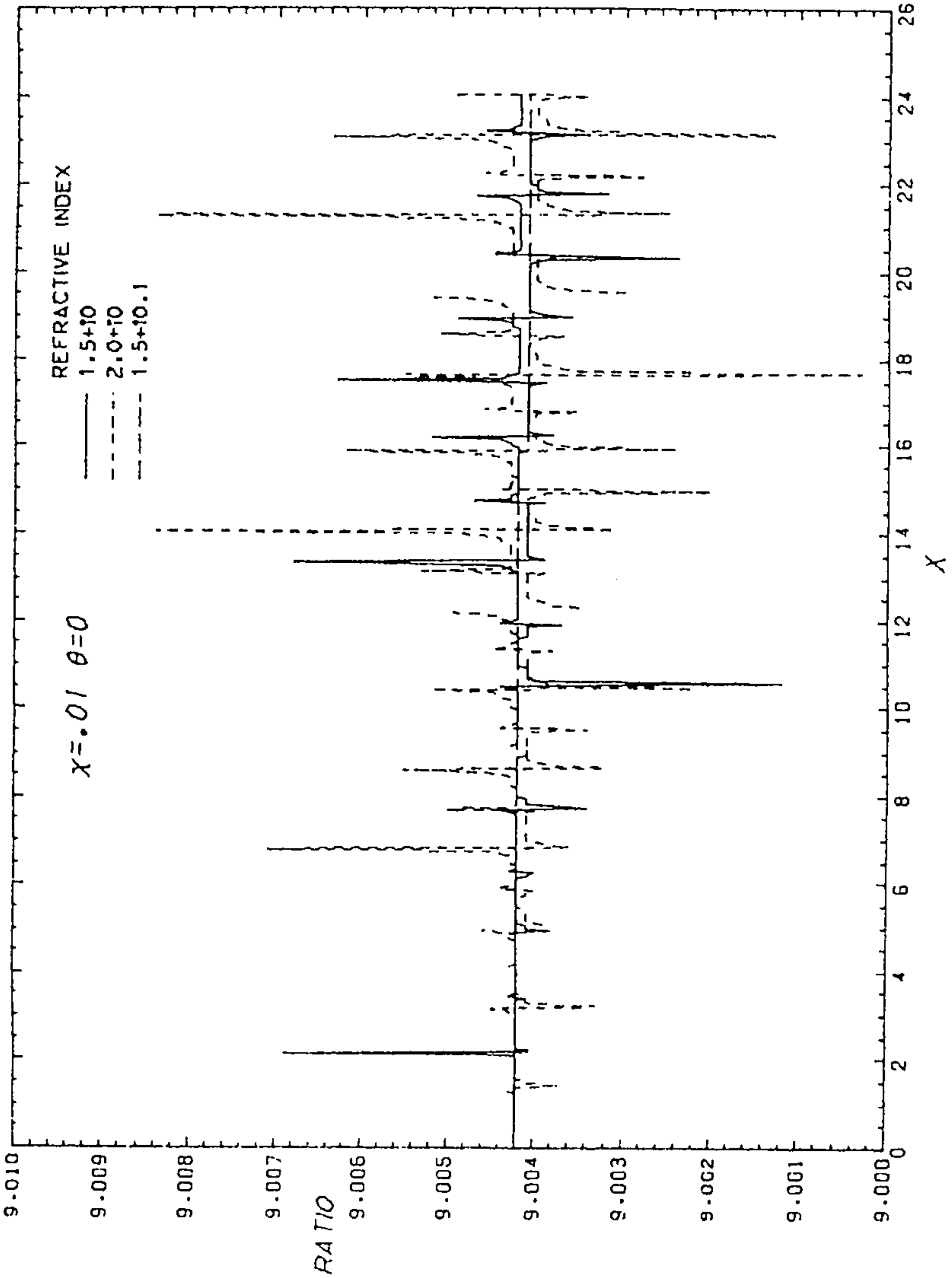

Fig.(5-3-d) Plot of RATIO against x for almost end on incidence

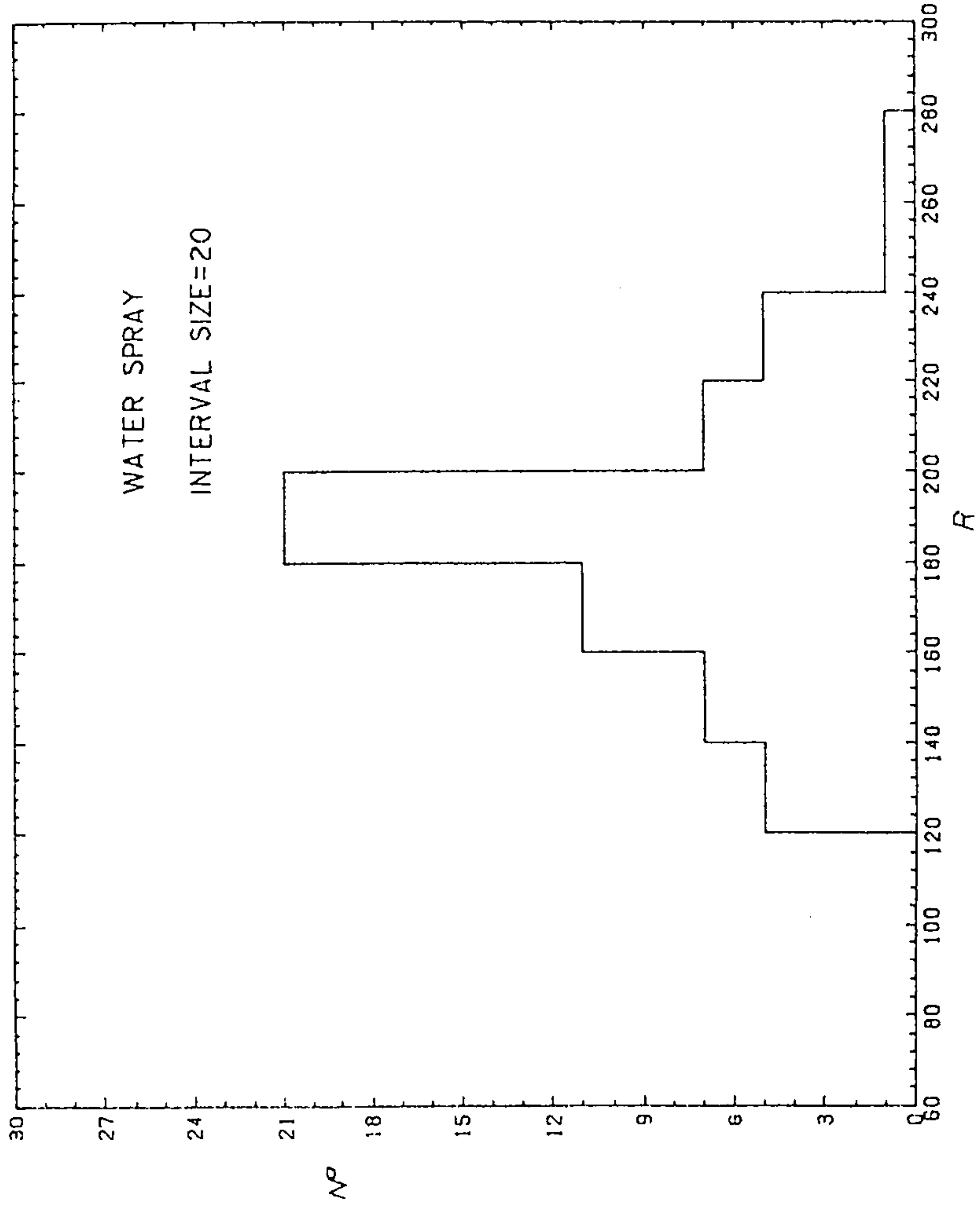

Fig.(5-3-e) Histogram of Number/R for water spray for forward scattering

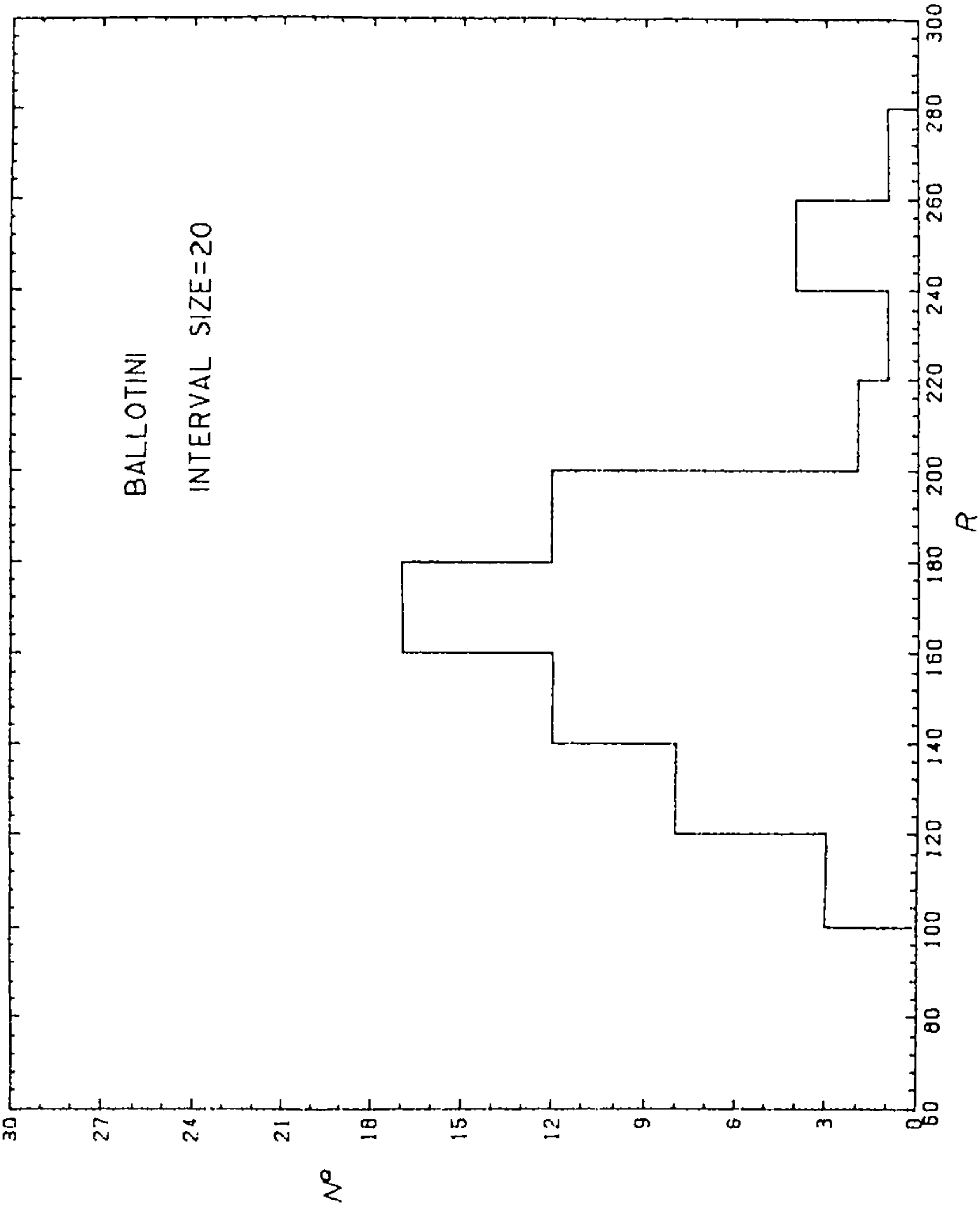

Fig.(5-3-f) Histogram of Number/R for glass ballotini for forward scatter

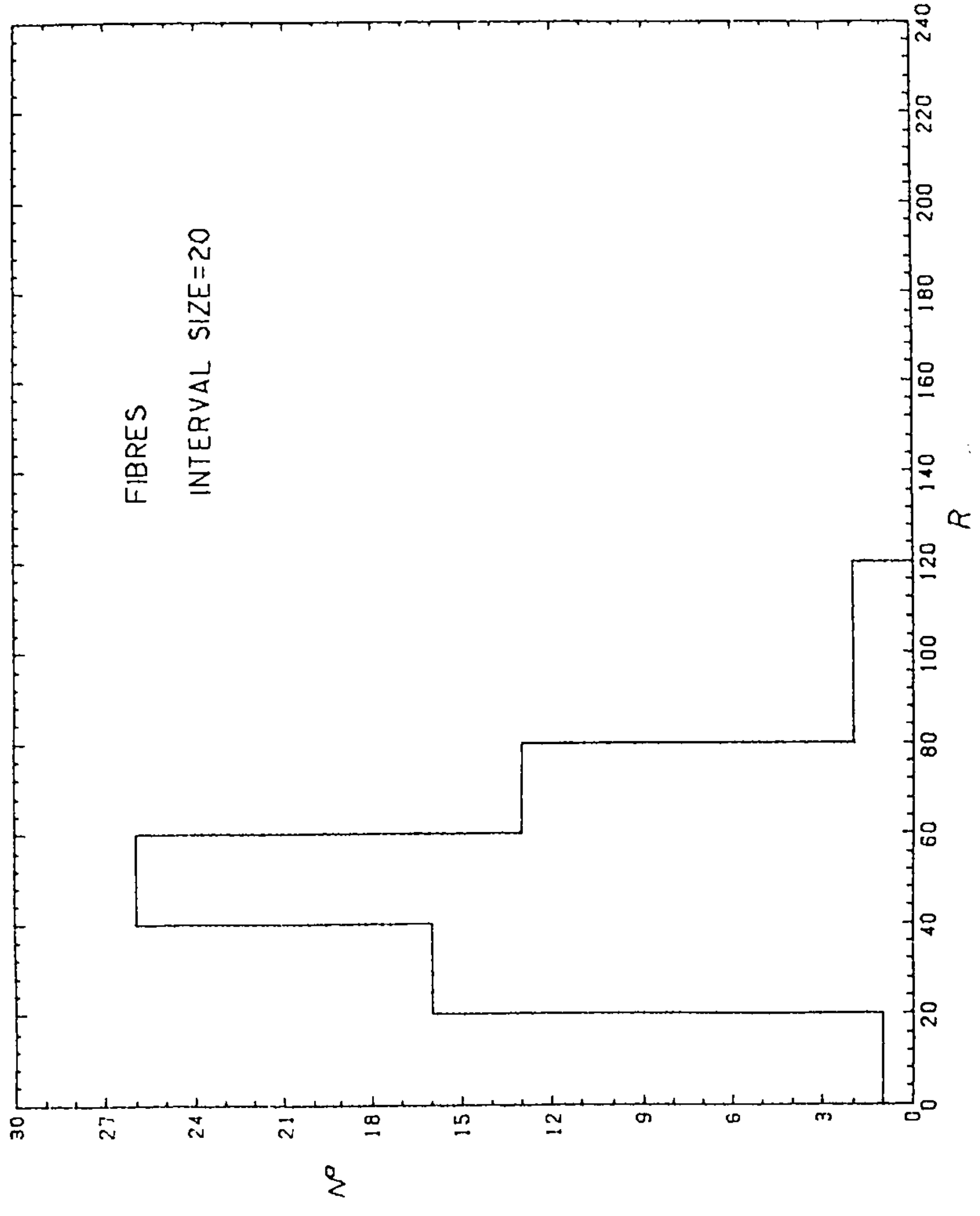

Fig.(5-3-g) Histogram of Number/R for quartz fibres for forward scattering

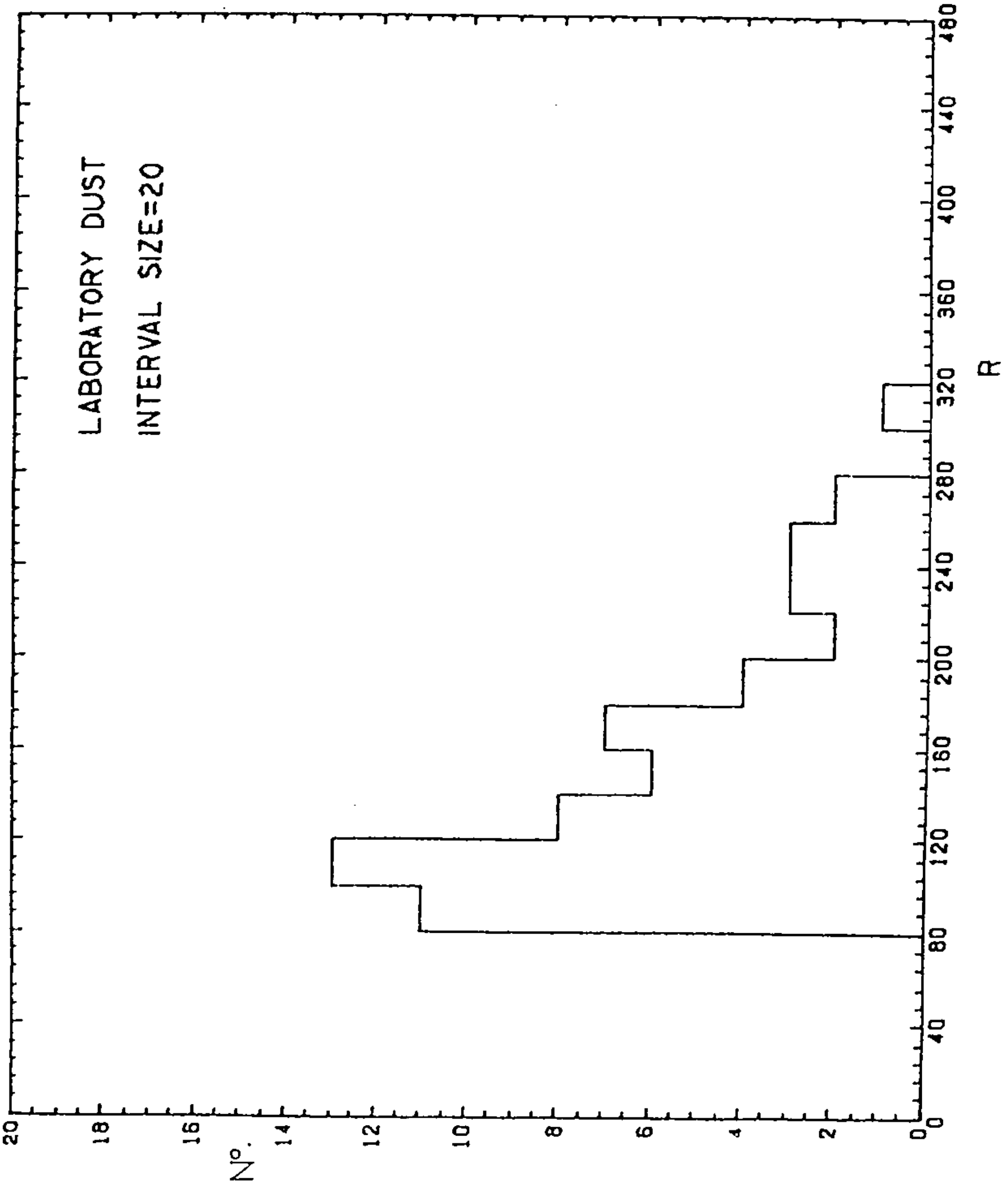

Fig.(5-3-h) Histogram of Number/R for laboratory dust for forward scattering

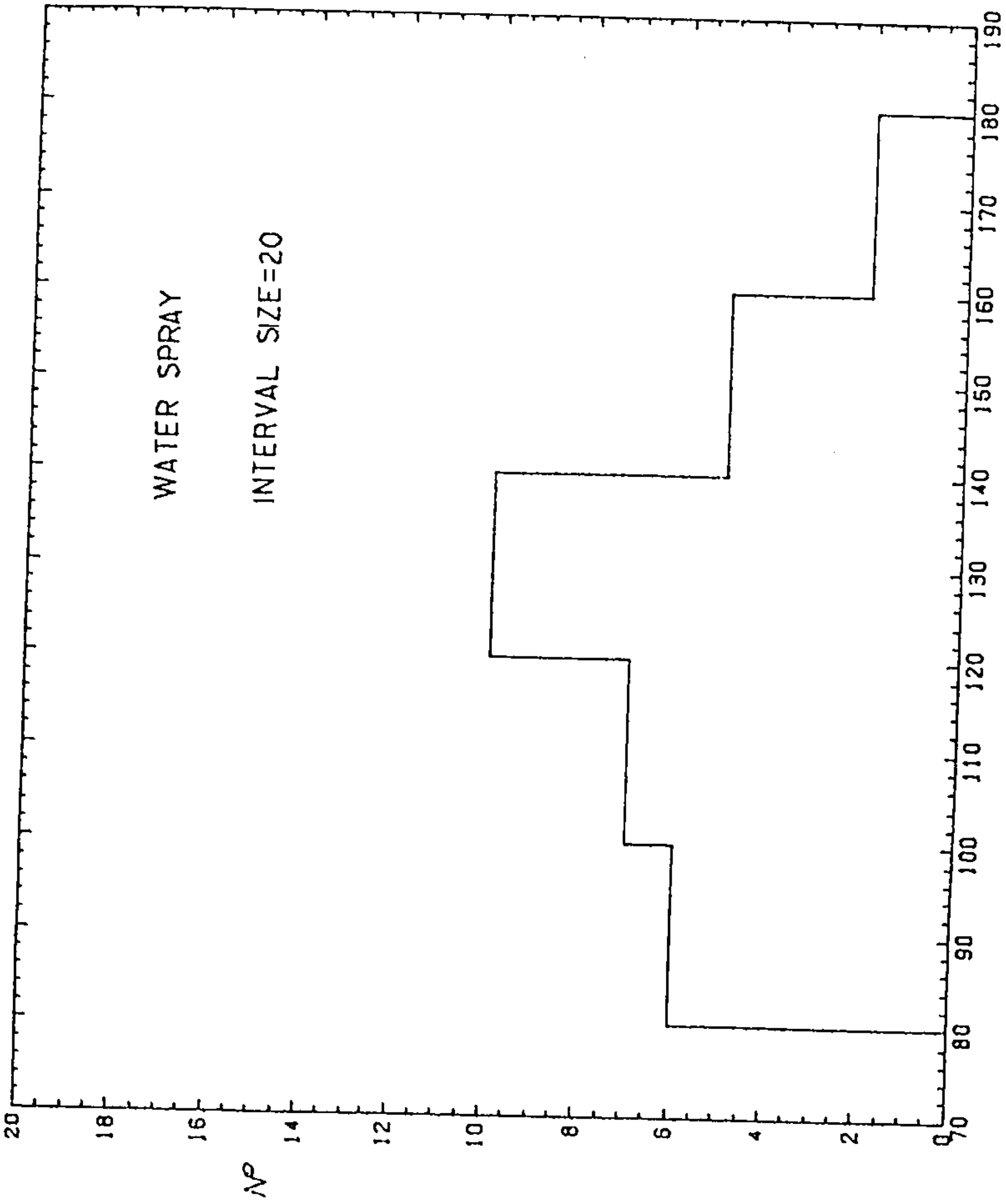

Fig.(5-3-i) Histogram of Number/R for water spray in forward scatter using LDA system

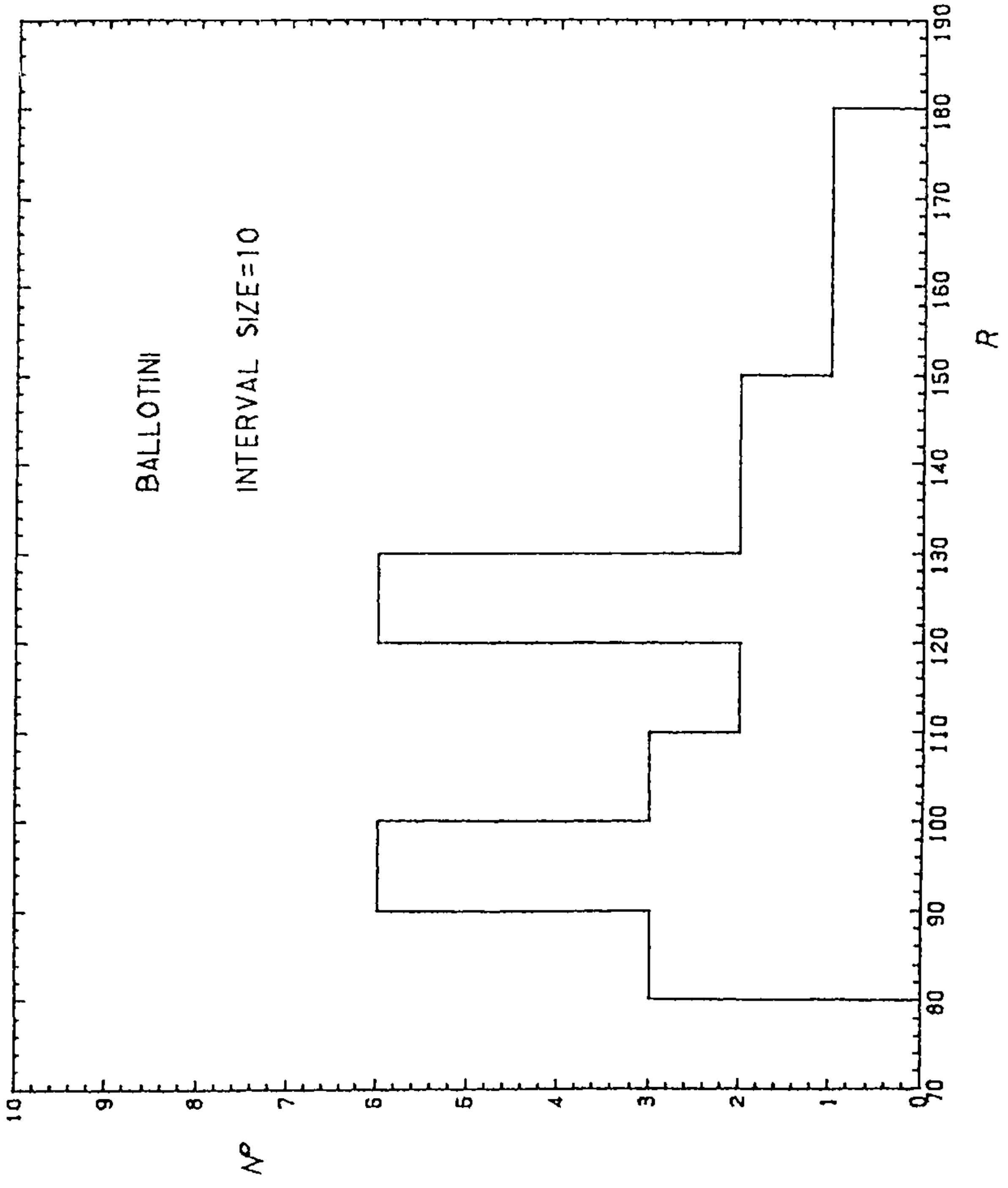

Fig.(5-3-j) Histogram of Number/R for ballotini in forward scatter using LDA system

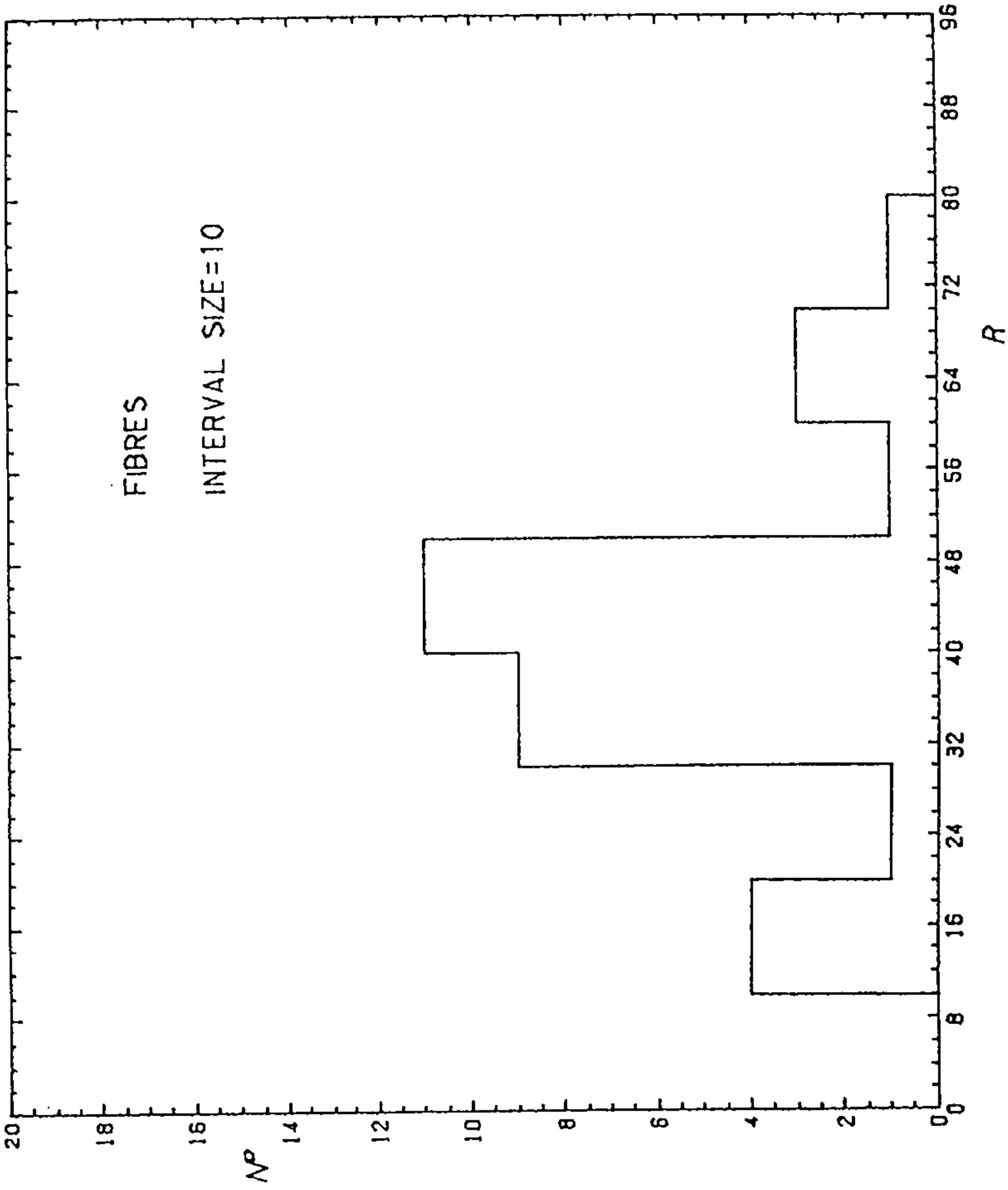

Fig.(5-3-k) Histogram of Number/R for fibres in forward scatter using LDA system oscillations.

Referring to the optical system of Figure (4-2-a) of Chapter 4 water spray, glass ballotini and quartz fibres were passed through the test space in turn and the polarisation ratios obtained for 60 readings each. The results plotted in the form of histograms are shown in Figures (5-3-e-g). It can be seen that for water spray and glass ballotini R=160-180 and for fibres the maximum occurs, with R=40-60. Figure (5-3-h) shows the result obtained for laboratory dust. Even in this case $R \geqslant 100$. Several repeats of this experiment have yielded similar results. Thus, distinguishability between fibres and non-cylindrical particles has been clearly established.

Similar results were obtained from the apparatus of Figure (4-4-b) and are shown in Figures (5-3-i-k).

5.4 Results for Back-Scattering

Figure (5-4-a) shows the RATIO plotted for back-scattering ($\theta=0$) for three values of χ and with refractive index of 1.5. Comparison between forward scattering shows that the RATIO is higher in the back scattering mode. This means that the measured ratio R in the backward direction should be lower than that in the forward direction.

Figures (5-4-b) and(5-4-c) show experimental results obtained for water spray and quartz fibres using the set-up shown in Figure (4-2-d) Of Chapter 4. The peak occurs at $R \sim 0.45$ for fibres. For water spray the value of R is about 3. The difference between the measured values of R for fibres and water spray is the basis for distinguishability between fibrous and non-fibrous materials. It is not understood

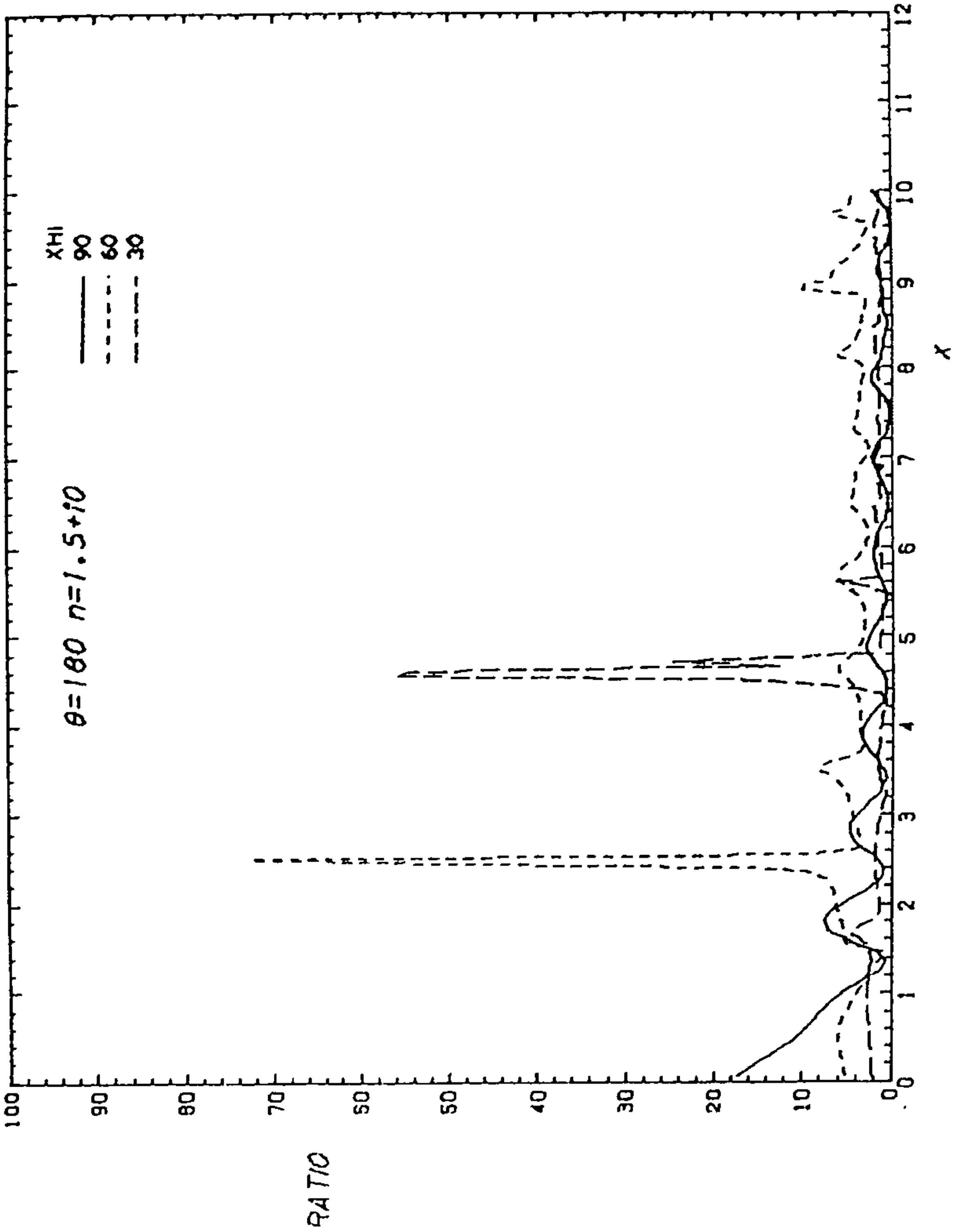

Fig.(5-4-a) Plot of RATIO against x for back scattering

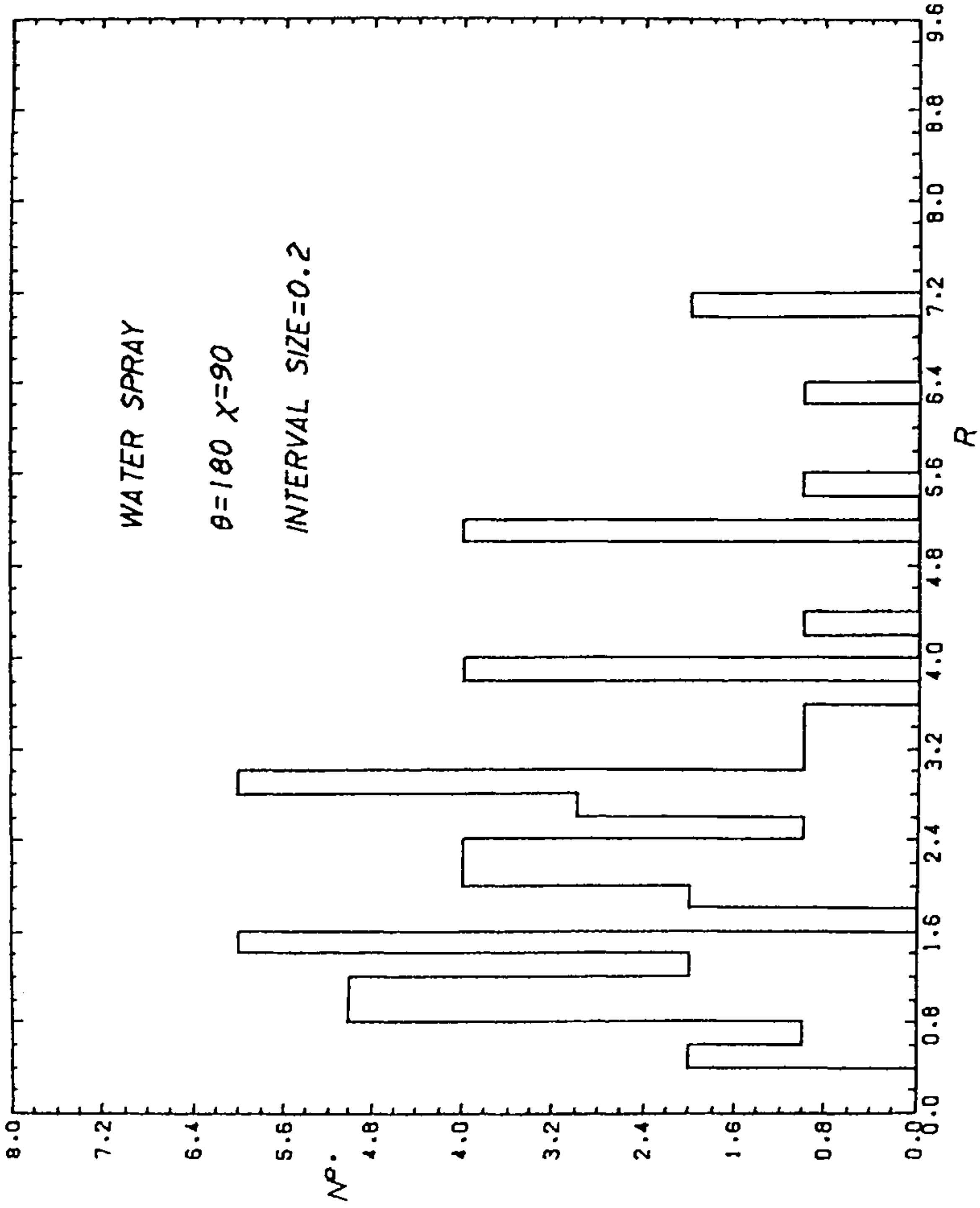

Fig.(5-4-b) Histogram of Number/R for water spray for back scatter

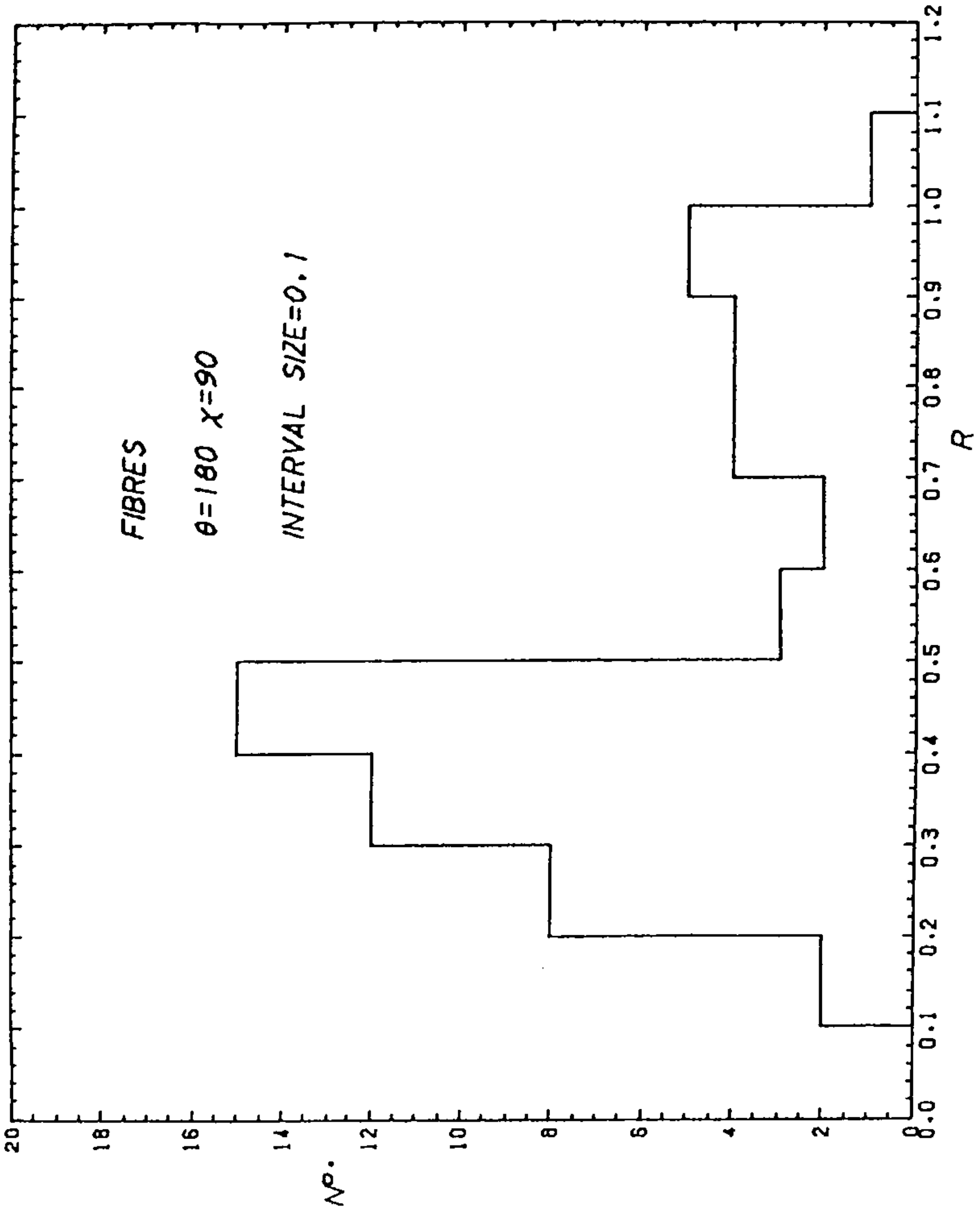

Fig.(5-4-c) Histogram of Number/R for quartz fibres for back scattering however, why we obtain such a low R for water spray when in the forward direction it is much higher. It is possible that water drops are slightly non-spherical or that the mirror introduces undesirable polarisation effects.

5.5 Investigation of Errors

(i) The phase plates.

Using the apparatus shown in Figure (5-5-a), the ratios of the maxima to the minima are found for two orientations of the half wave plate when the signals are maximum and minimum on PM1 and PM2.

Referring to Figure (5-5-b), the intensities $I_{\parallel}$ and $I_{\perp}$ are incident on the prism. $T_{\perp}$ and $R_{\perp}$ are the fractions of $I_{\parallel}$ and $I_{\perp}$ transmitted respectively. Similarly, $T_{\parallel}$ and $R_{\parallel}$ are fractions reflected by the prism.

The response of the photomultipliers, in this case, is unimportant since we are dealing with ratios. Experimentally it is found that

$$\frac{R_{\parallel}}{T_{\parallel}} = 400 \quad \text{and} \quad \frac{T_{\perp}}{R_{\perp}} = 100 \qquad (5\text{-}5\text{-}1)$$

i.e.

$$\frac{R_{\parallel}}{T_{\parallel}} = 4\,\frac{T_{\perp}}{R_{\perp}}$$

We can write, since $T \simeq 1-R$

$$\frac{R_{\parallel}}{1-R_{\parallel}} = \frac{4(1-R_{\perp})}{R_{\perp}} = 400 \qquad (5\text{-}5\text{-}2)$$

and solving Equations (5-5-1) and (5-5-2) we get,

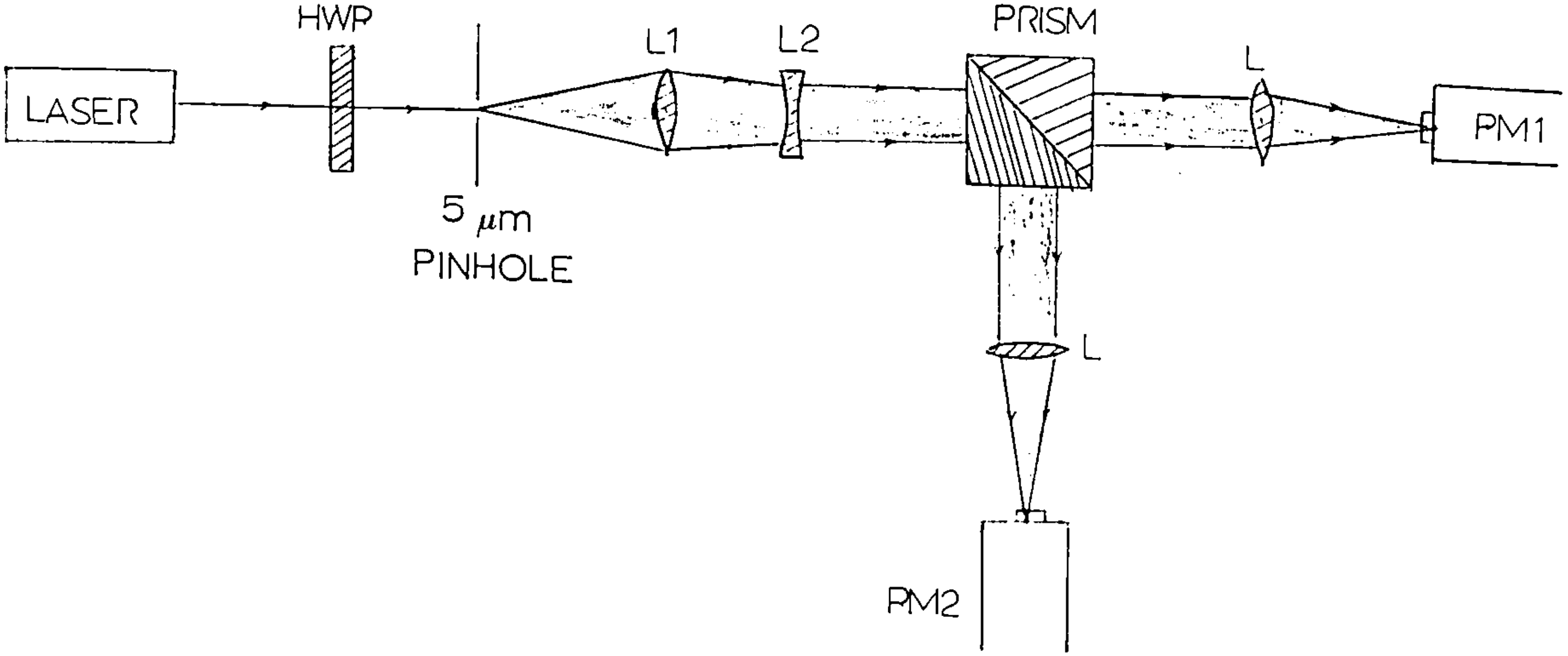

Fig.(5-5-a) Optical lay-out for investigating the variation of the polarisation ratio in the test space

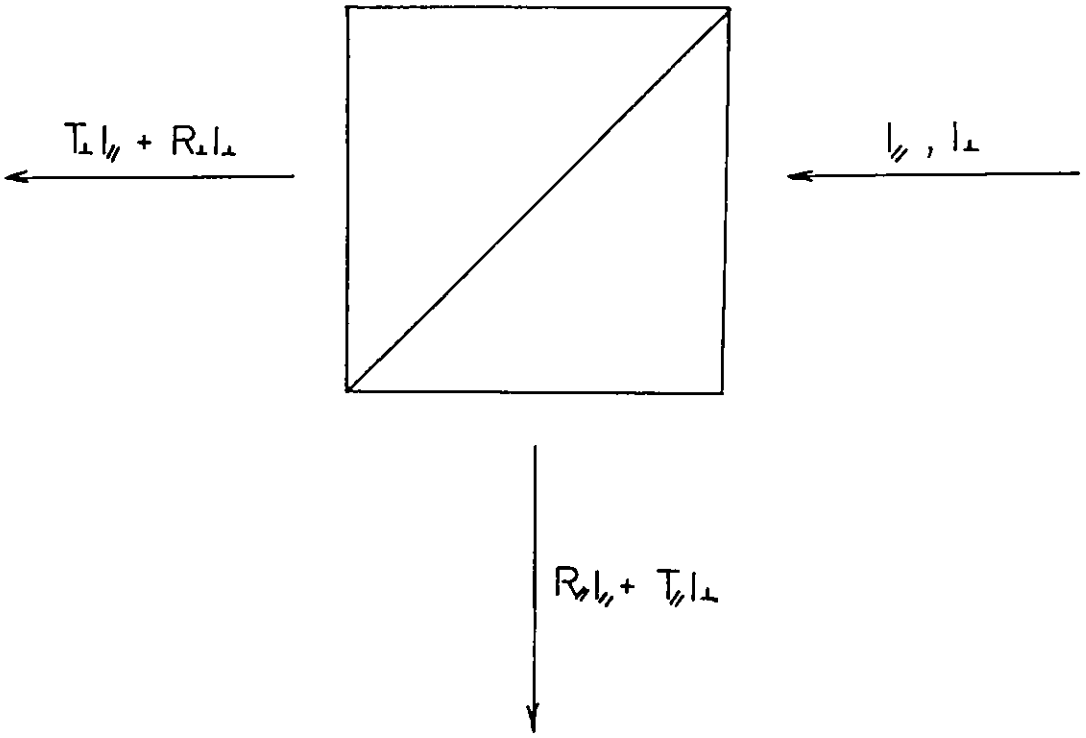

Fig.(5-5-b) Representation of optical intensities incident and emergent from the prism

$$R_{\parallel} = \frac{400}{401} \qquad T_{\parallel} = \frac{1}{401}$$

$$T_{\perp} = \frac{100}{101} \qquad R_{\perp} = \frac{1}{101} \qquad (5\text{-}5\text{-}3)$$

Thus we can write down the reflected (R) and transmitted (T) intensities as

$$\frac{400}{401} I_{\parallel} + \frac{1}{101} I_{\perp} = R$$

$$\frac{1}{401} I_{\parallel} + \frac{100}{101} I_{\perp} = T \qquad (5\text{-}5\text{-}4)$$

i.e.

$$\frac{R}{T} = \frac{\frac{400}{401}\frac{I_{\parallel}}{I_{\perp}} + \frac{1}{101}}{\frac{1}{401}\frac{I_{\parallel}}{I_{\perp}} + \frac{100}{101}} \qquad 5\text{-}5\text{-}5)$$

The half wave plate of Figure (5-5-a) is replaced by a quarter wave plate and another quarter wave plate placed between L2 and the prism. With the optic axes of the two plates having the same orientation, it can be shown that (Appendix D)

$$R_1 = \frac{I_{\perp}}{I_{\parallel}} = \frac{1 + \cos(\delta_1 + \delta_2)}{1 - \cos(\delta_1 + \delta_2)} \qquad (5\text{-}5\text{-}6)$$

where R_1 is the measured polarisation ratio and δ_1 and δ_2 are errors in the phase difference introduced by the plates (ideally $\pi/4$, but assumed to be $\pi/4 + \delta_1$ and $\pi/4 + \delta_2$). With the second quarter wave plate orthogonal to the first, we obtain

$$R_2 = \frac{II_{\parallel}}{I_{\perp}} = \frac{1 + \cos(\delta_1 - \delta_2)}{1 - \cos(\delta_1 - \delta_2)} \qquad (5\text{-}5\text{-}7)$$

Using the set-up with the quarter wave plates and 5µm pinhole, $\frac{R}{T}$ was measured to be 200 amd 83 for the two

Orthogonal positions of the second quarter wave plate. Inserting these values into Equation (5-5-5) in turn gives $\frac{I_{\parallel}}{I_{\perp}} = 400$ and $\frac{I_{\perp}}{I_{\parallel}} = 570$. If we assume that these were due entirely due to errors in the phase plates (5-5-7) then substituting these values into Equations (5-5-7) and (5-5-6) gives $\delta_1 = 5.6^\circ$ and $\delta_2 = -0.4^\circ$. If these errors were due in part to the other optical components then the overall effect would be the same.

Consider two quarter wave plates with phase errors δ_1 and δ_2.

A wave of the form

$$\underline{E}_{inc} = \hat{x}\, e^{i\omega t} \tag{5-5-8}$$

incident on the first quarter wave plate with optic axis along $\hat{y}$ as indicated below

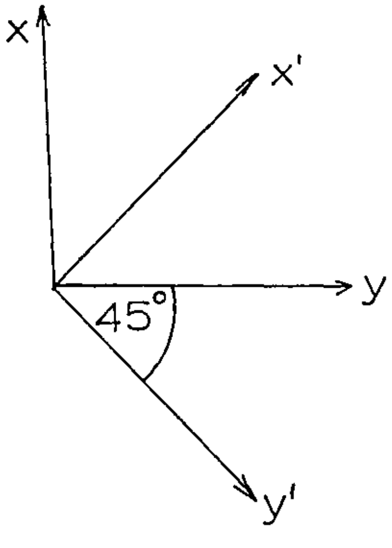

will emerge with electric field

$$\underline{E}_1 = \frac{1}{\sqrt{2}} \left(\hat{x}' - i\, \hat{y}'\, e^{i\delta_1} \right) e^{i\omega t} \tag{5-5-9}$$

For a fibre lying at angle ϕ to $\hat{y}'$ (see Figure below) the transformations are

$$\hat{x}^1 = \hat{x}_f\cos\phi + \hat{y}_f\sin\phi$$

$$\hat{y}^1 = -\hat{x}_f\sin\phi + \hat{x}_f\cos\phi$$

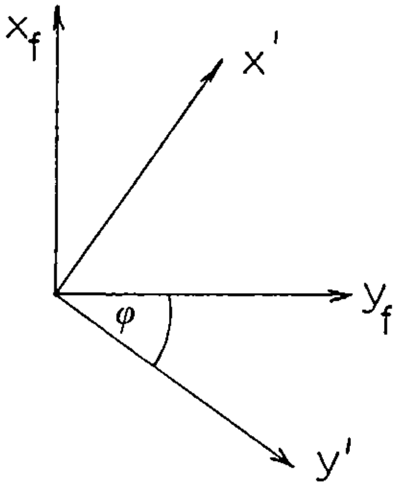

Substituting the transformations into Equation (5-5-9) gives

$$\underline{E}_1 = \frac{1}{\sqrt{2}}\left(\hat{x}_f(\cos\phi + i\sin\phi e^{i\delta_1}) + \hat{y}_f(\sin\phi - i\cos\phi e^{i\delta_1})\right)e^{i\omega t} \qquad (5\text{-}5\text{-}10)$$

The scattered field can be written as

$$\underline{E}_{sca} = \frac{1}{\sqrt{2}}\left(\hat{x}_f A(\cos\phi+i\sin\phi e^{i\delta_1}) + \hat{y}_f B(\sin\phi-i\cos\phi s^{i\delta_1})\right) e^{i\omega t} \qquad (5\text{-}5\text{-}11)$$

where A and B are the orthogonal scattering parameters defined in Chapter 2.

Transforming back to $\hat{x}^1$ and $\hat{y}^1$ using

$$\hat{x}_f = \hat{x}^1\cos\phi - \hat{y}^1\sin\phi$$

$$\hat{y}_f = \hat{x}^1\sin\phi + \hat{y}^1\cos\phi$$

gives after a little algebra

$$\underline{E}_{sca} = \frac{1}{\sqrt{2}}\Big(\hat{x}^1(A\cos^2\phi+B\sin^2\phi+i(A-B)\sin\phi\cos\phi e^{i\delta_1})$$

$$- \hat{y}^1((A-B)\sin\phi\cos\phi+i(A\sin^2\phi+B\cos^2\phi)e^{i\delta_1})\Big)$$

$$\times \quad e^{i\omega t} \qquad (5\text{-}5\text{-}12)$$

In the experimental set-up the phase plates are orthogonal i.e. the optic axis of one lies along $\hat{y}^{1}$ and that of the other along $\hat{y}^{11}$ as indicated below

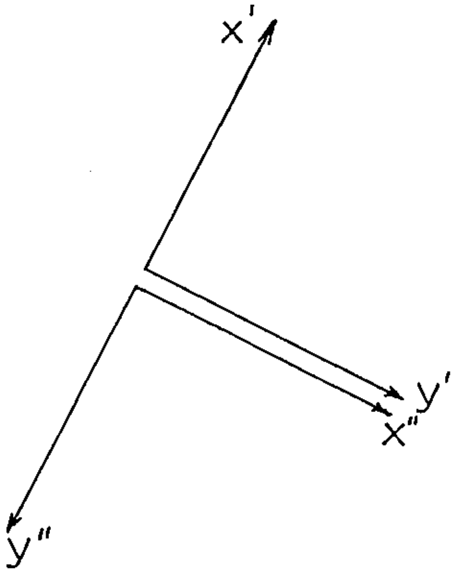

We can immediately write down that

$$\hat{x}^{1} = -\hat{y}^{11}$$

and

$$\hat{y}^{1} = \hat{x}^{11}$$

Substituting for $\hat{x}^{1}$ and $\hat{y}^{1}$ into Equation (5-5-12) gives the electric field from the second quarter wave plate as

$$\underline{E}_2 = \frac{1}{\sqrt{2}}\Big(\hat{y}^{11}\big((A-B)\sin\phi\cos\phi e^{i\delta_1} - i(A\cos^2\phi + B\sin^2\phi) \big) e^{i\delta_2} - \hat{x}^{11}\big((A-B)\sin\phi\cos\phi + i(A\sin^2\phi + B\cos^2\phi) e^{i\delta_1} \big)\Big) \times e^{i\omega t} \qquad (5\text{-}5\text{-}13)$$

Finally we have to transform back to the original x,y co-ordinates using geometry from the Figure below

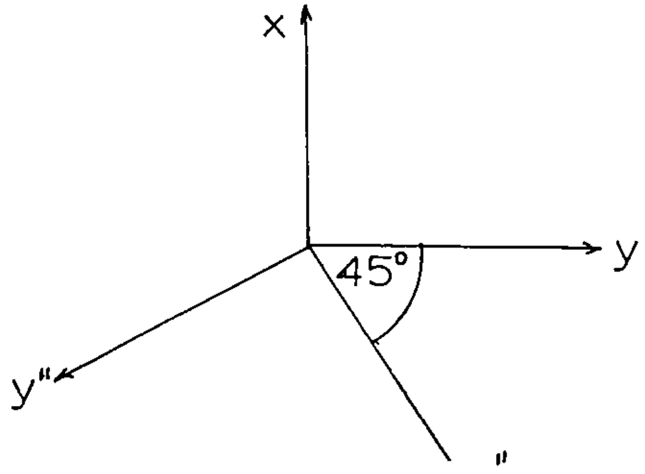

we can write down

$$\hat{x}^{11} = \frac{-\hat{x} + \hat{y}}{\surd 2}$$

$$\hat{y}^{11} = \frac{-\hat{x} - \hat{y}}{\surd 2}$$

Substituting into Equation (5-5-13) and simplifying gives the emerging field from the second phase plate. Thus

$$\begin{aligned}\underline{E}_2 = \tfrac{1}{2}\big(&\hat{x}\big((A-B)\sin\phi\cos\phi(1-e^{i(\delta_1+\delta_2)}) \\ &+ i(A\cos^2\phi e^{i\delta_2}+A\sin^2\phi e^{i\delta_1}+B\sin^2\phi e^{i\delta_2}+B\cos^2\phi e^{i\delta_1}) \\ &+ \hat{y}\big(i(A\cos^2\phi e^{i\delta_2}-A\sin^2\phi e^{i\delta_1}+B\sin^2\phi e^{i\delta_2}-B\cos^2\phi e^{i\delta_1} \\ &- (A-B)\sin\phi\cos\phi(1+e^{i(\delta_1+\delta_2)})\big)\big) \quad e^{i\omega t}\end{aligned} \qquad (5\text{-}5\text{-}14)$$

We have to examine two special cases

(a) If $A = B = 1$ (such as a sphere) then Equation (5-5-14) becomes

$$\underline{E}_2 = \tfrac{1}{2}\big(\hat{x}\, i(e^{i\delta_2}+e^{i\delta_1}) + \hat{y} i(e^{i\delta_2}-e^{i\delta_1})\big)\, e^{i\omega t}$$

giving

$$I_{11} = \tfrac{1}{2}\big(1 + \cos(\delta_1-\delta_2)\big)$$

and

$$I_{\underline{1}} = \tfrac{1}{2}\big(1 - \cos(\delta_1-\delta_2)\big)$$

This is the same as Equation (5-5-7) as expected

If (b) If there are no phase errors, i.e. $\delta_1 = \delta_2 = 0$ then,

$$\begin{aligned}\underline{E}_2 &= \tfrac{1}{2}\big(\hat{x}\, i\,(A+B) \\ &\quad + \hat{y}\big(i(A-B)\,(\cos^2\phi-\sin^2\phi) - 2(A-B)\sin\phi\cos\phi\big)\big)\, e^{i\omega t} \\ &= \tfrac{1}{2}\big(\hat{x}\, i\,(A+B) \\ &\quad - \hat{y}\big((A-B)\quad i\cos 2\phi+\sin 2\phi\big)\big)\, e^{i\omega t}\end{aligned}$$

Thus

$$I_{\parallel} = \tfrac{1}{4}\,|A + B|^2$$

$$I_{\perp} = \tfrac{1}{4}\,|A - B|^2 \qquad (5\text{-}5\text{-}15)$$

Again this is as expected.

It can be seen that Equation (5-5-15) is the same as Equation (3-4-1) and thus for no phase errors

$$\frac{I_{\perp}}{I_{\parallel}} = \left|\frac{A - B}{A + B}\right|^2 \qquad (5\text{-}5\text{-}16)$$

A computer program has been written to calculate $\frac{I_{\perp}}{I_{\parallel}}$ for the general case where $A \neq B$ and δ_1 and δ_2 are finite. Calculations have been performed using the infinite cylinder program and using Equation (5-5-12) incorporating $\delta_1 = 5.6^{\circ}$ and $\delta_2 = -0.4^{\circ}$ for three values of ϕ viz. $0^{\circ}, 45^{\circ}$ and 90°. Computations for the forward direction are shown in Figures (5-5-c-e). It can be seen that the general effect is to raise the troughs of oscillations. In fact, for $\phi = 90$ there is considerable increase in the value of the RATIO. This means that the prediction for the observed ratio R would correspondingly decrease. Figures (5-5-f-h) show the same computation for the backward direction. In this case there does not appear to be a significant change in the RATIO.

In section (5.2) a diameter size distribution for quartz fibres was presented. A smooth curve has been drawn as shown in Figure (5-5-i) and interpolated at intervals of 0.01μm. The corresponding theoretical values of R were calculated from the infinite cylinder program at intervals of $\Delta x = 2\pi \times 10^{-2}$ up to $x = 24$. Using the theoretical values of R and the interpolated number - diameter distribution, the number of fibres expected in the ratio range R to R + ΔR is found where ΔR is the interval size. In this way a

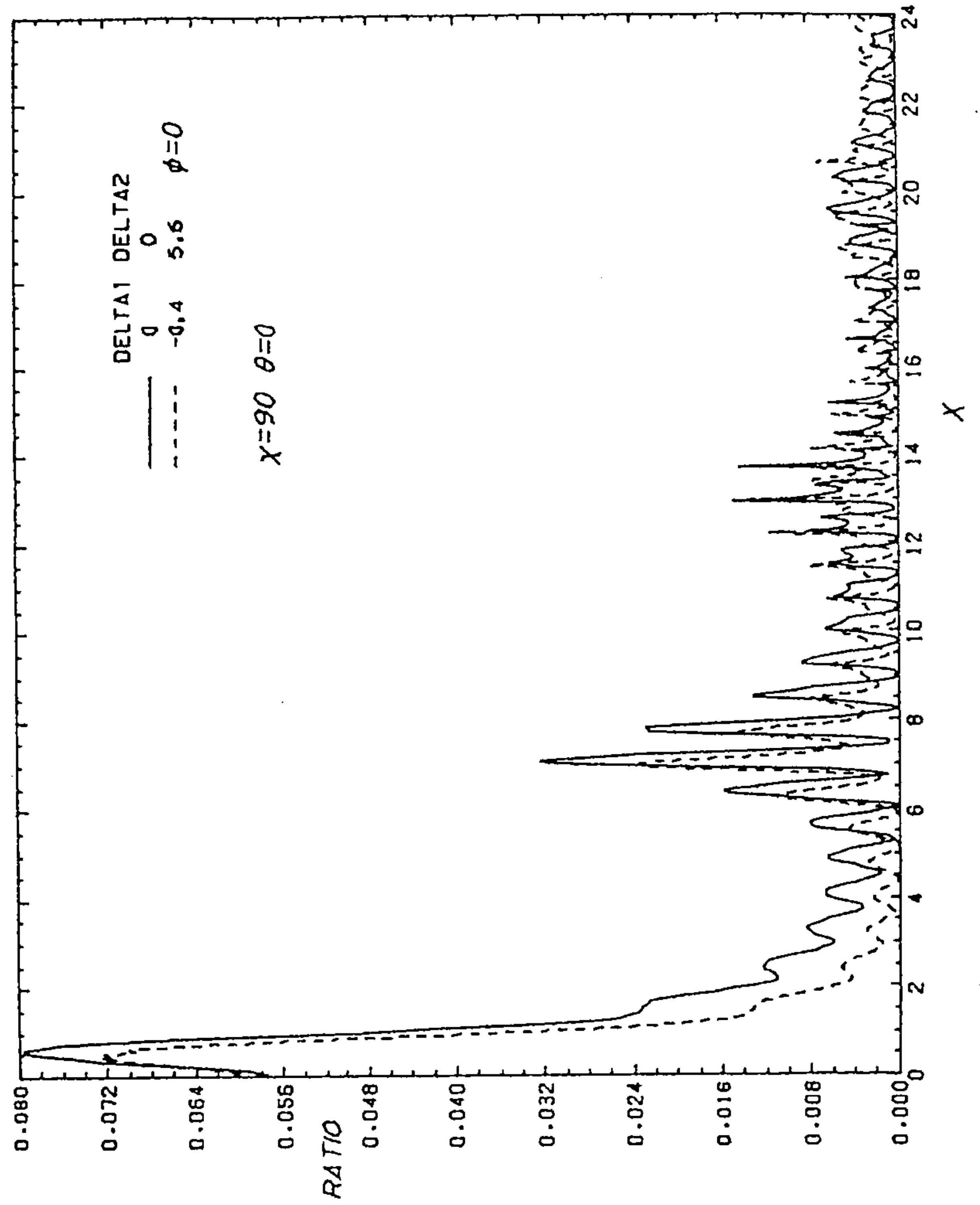

Fig.(5-5-c) Plot of RATIO against x with phase plate errors for $\phi=0$ in the forward direction

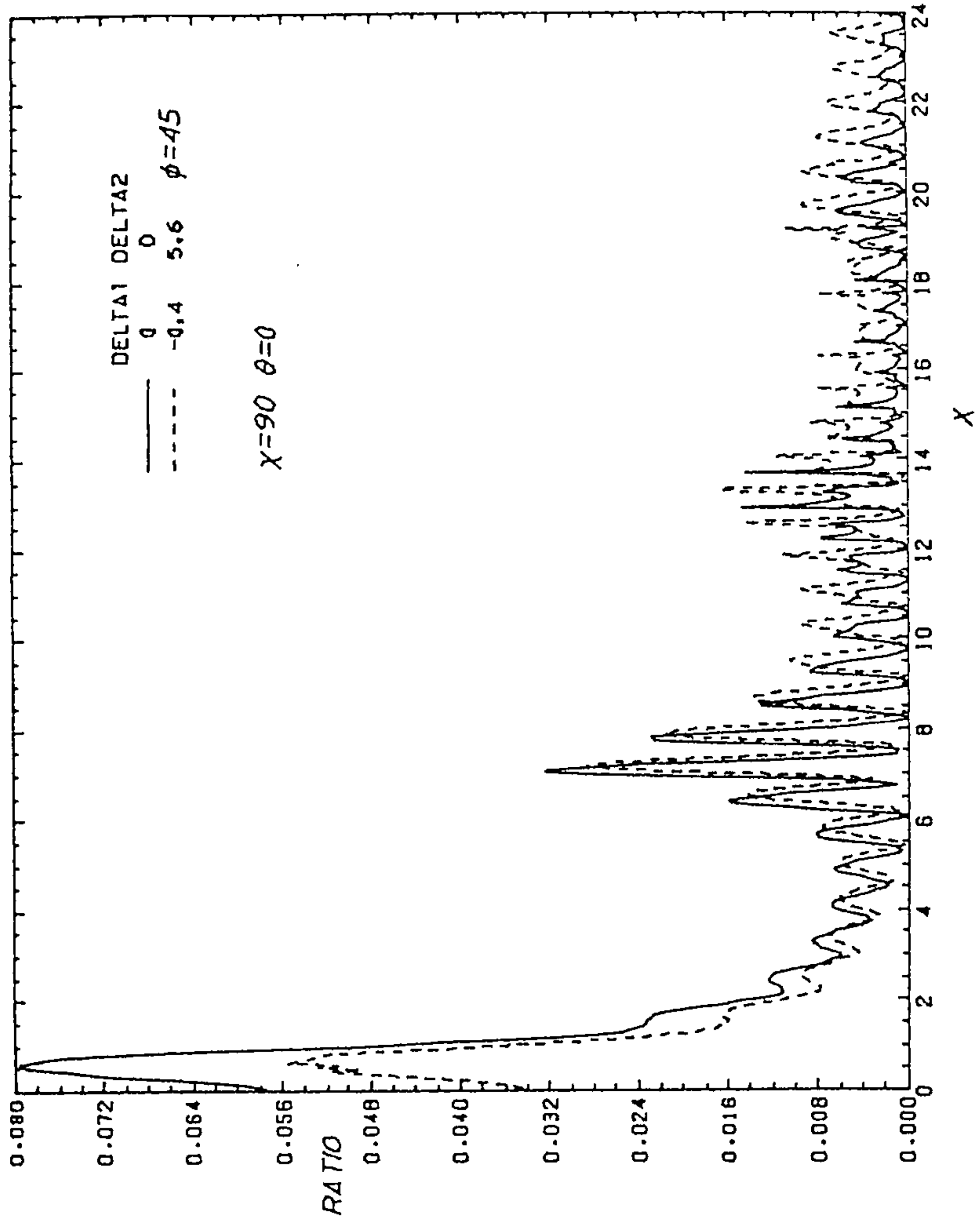

Fig.(5-5-d) Plot of RATIO against x with phase plate errors for $\phi=45$ in the forward direction

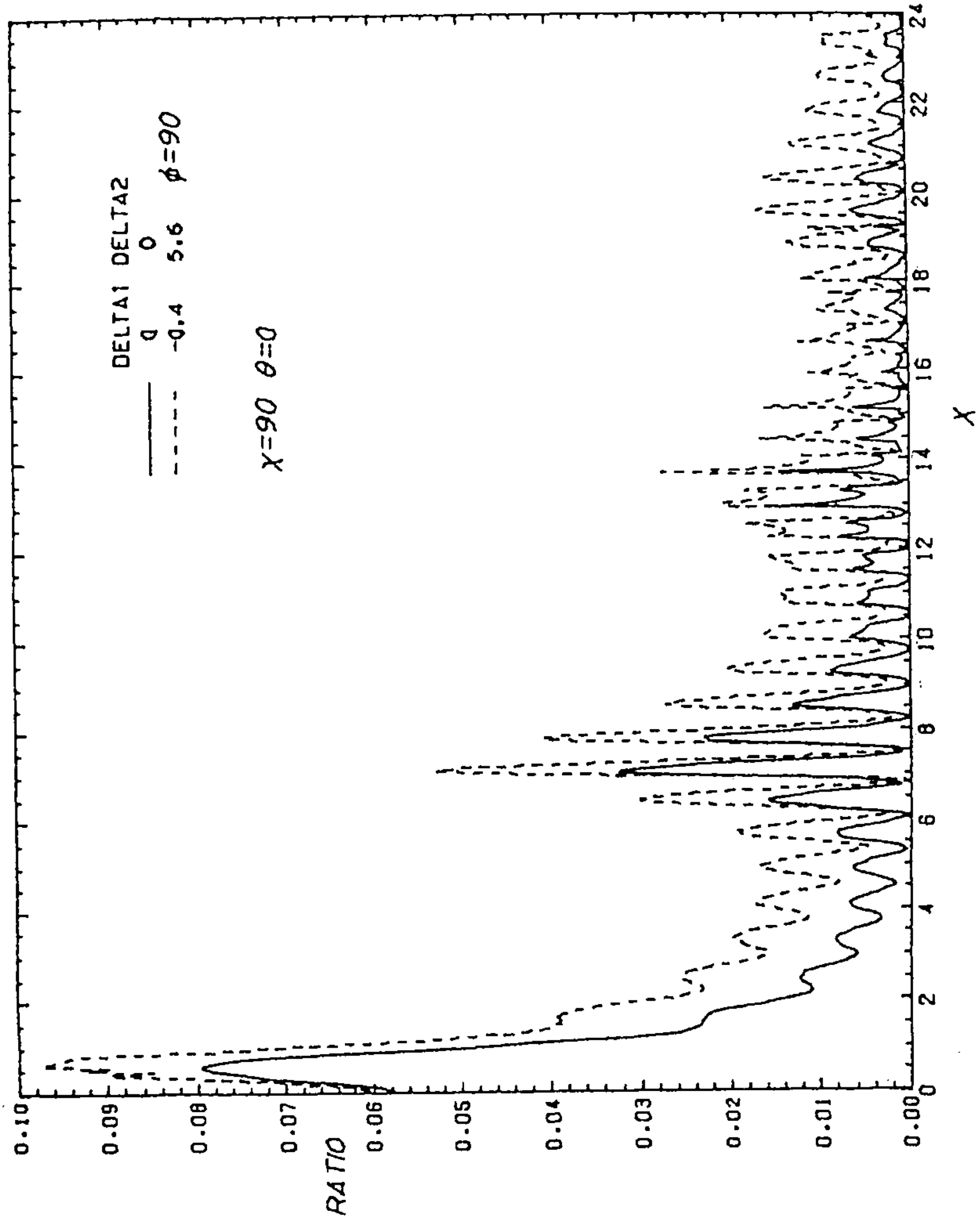

Fig.(5-5-e) Plot of RATIO against x with phase plate errors for $\phi=90$ in the forward direction

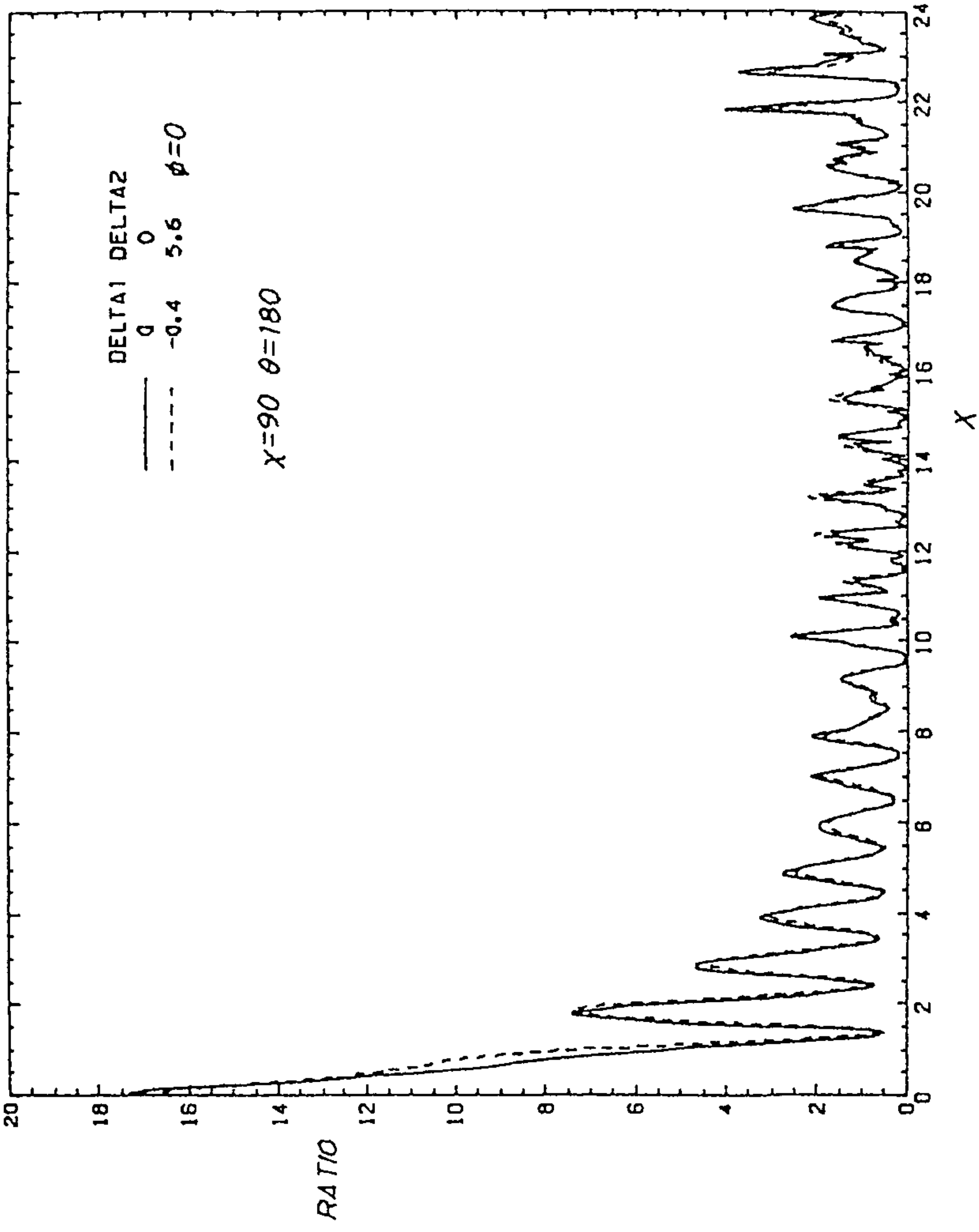

Fig.(5-5-f) Plot of RATIO against x with phase plate errors for ϕ=0 in the backward direction

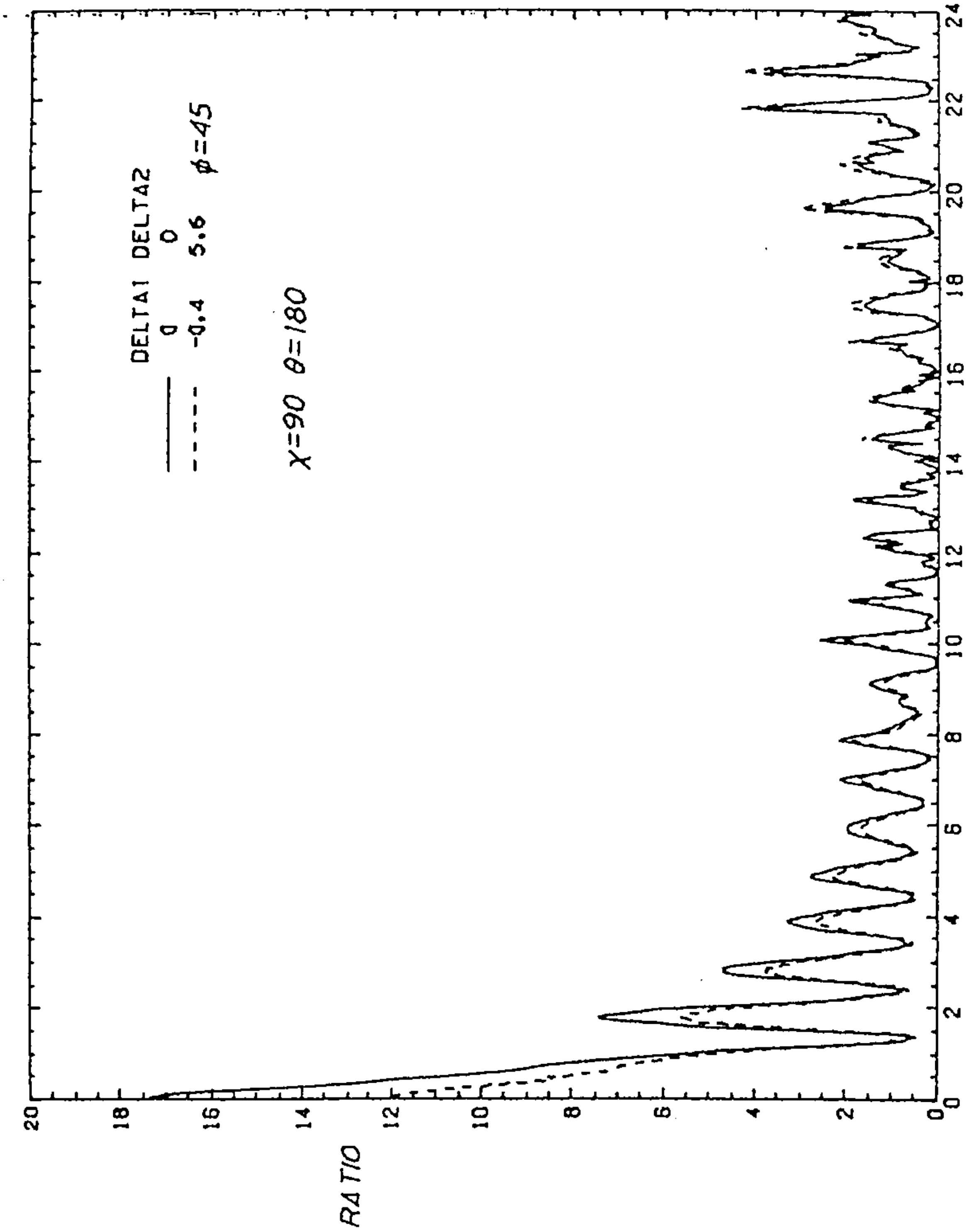

Fig.(5-5-g) Plot of RATIO against x with phase plate errors for ϕ=45 in the backward direction

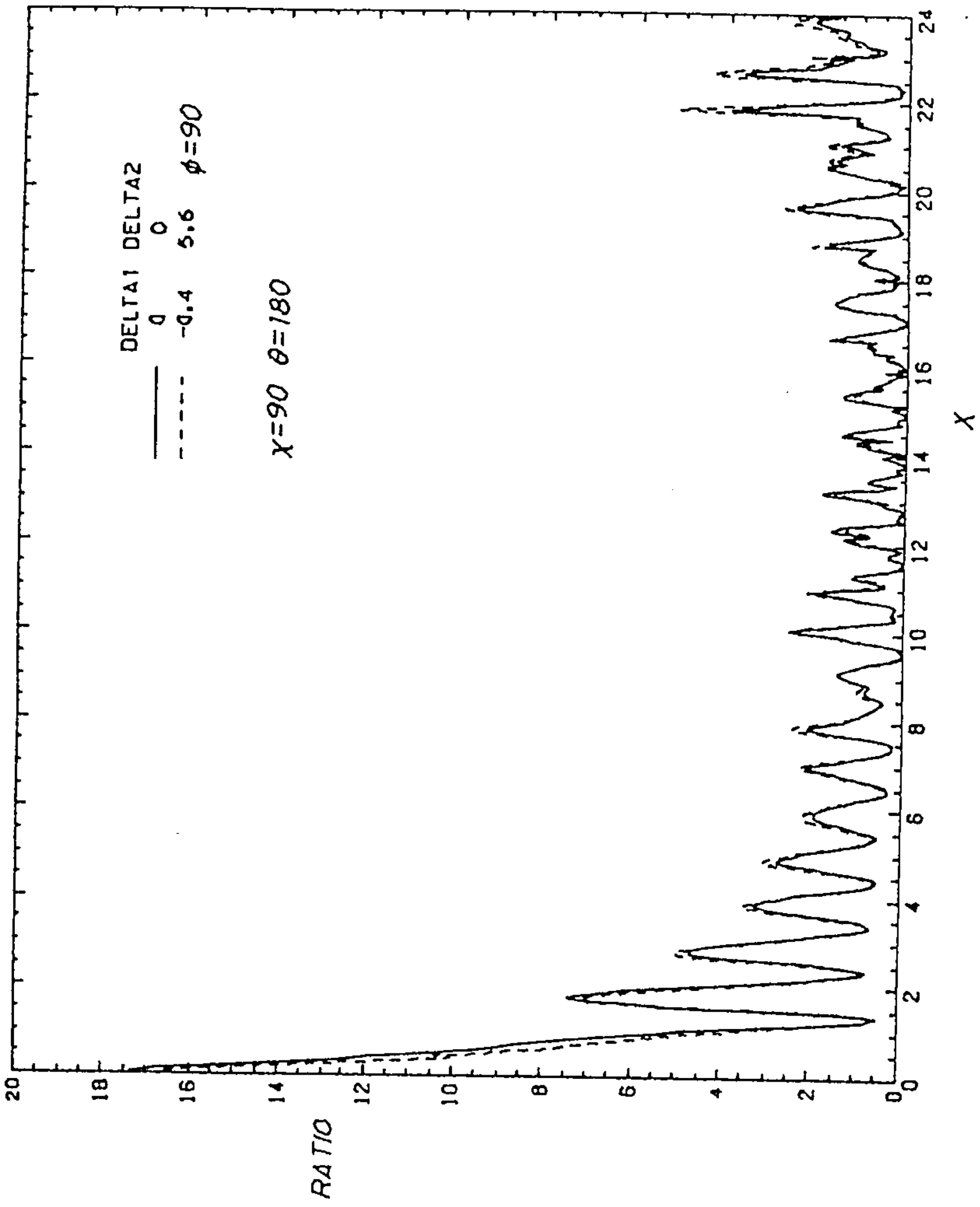

Fig.(5-5-h) Plot of RATIO against x with phase plate errors for ϕ=90 in the backward direction

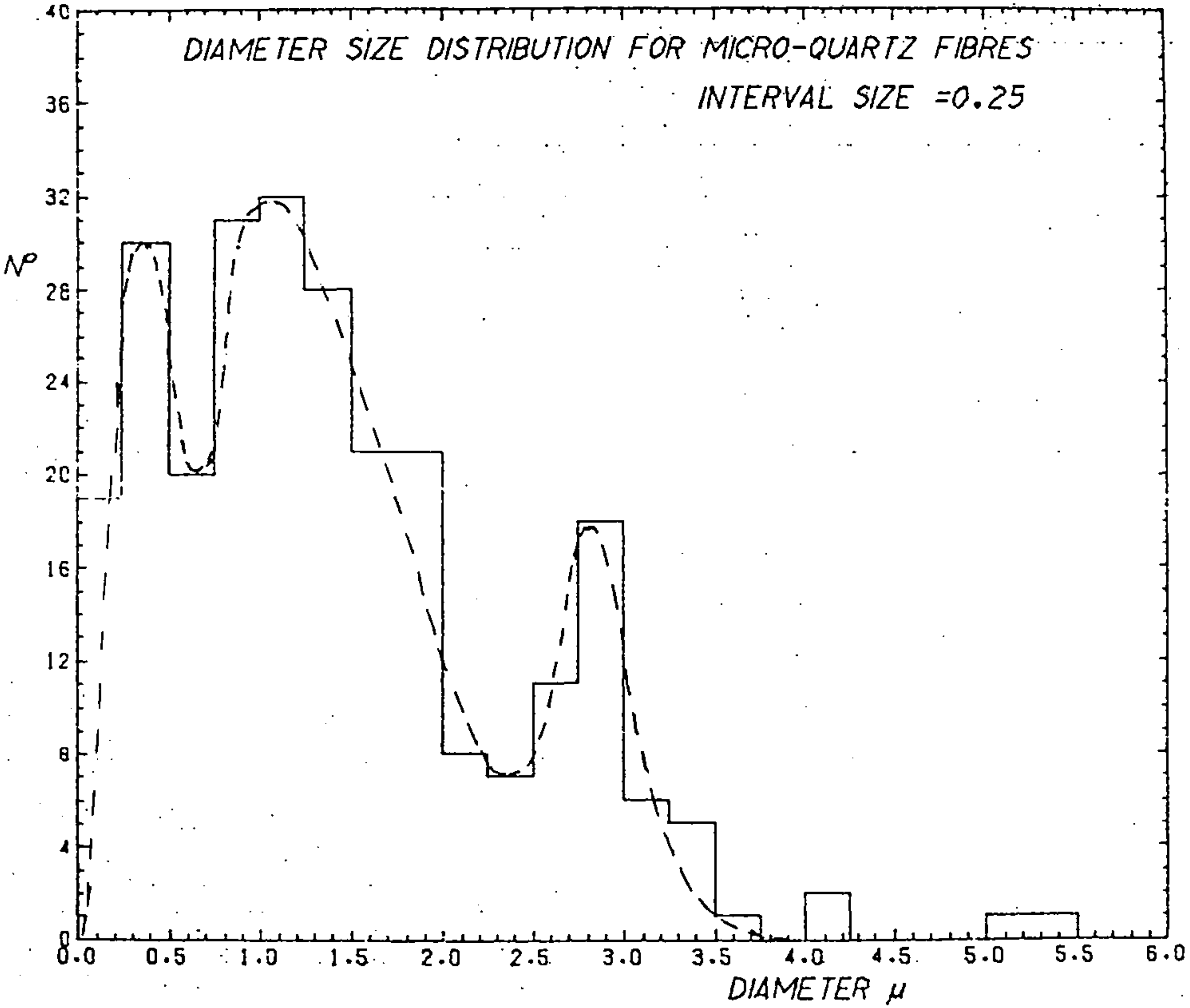

Fig.(5-5-i) Histogram plot of Number/Diameter with smooth curve drawn for interpolation theoretical prediction of the distribution of ratios was made.

Figure (5-5-j) shows this distribution for forward scatter with the cylinder at $\chi = 90^{\circ}$ and no phase error. There appear to be three dominant peaks occuring at $R \simeq 50, 80$ and 150. In Section (5.3) results indicating R=40-60 for fibres in the forward scatter mode were presented. It is envisaged that the inclusion of errors in the phase plates into the calculations would reduce the expected values of R. In fact, this is exactly what happens as can be seen in Figures (5-5-k-m). For $\phi = 45^{\circ}$ there is a considerable spread in the range of values of R. At $\phi = 90^{\circ}$ however, there is a distinct peak at $R \simeq 50$. Conseqently, the experimental and theoretical results agree well if we take into account errors in the phase plates.

Ideally, for a sphere we expect $\frac{I_{\perp}}{I_{11}} = \infty$. However, due to phase plate errors and limitation of the polarisation ratio of the prism the actual ratio obtained is around 160-180. It should be pointed out that the discrepancy for water spray can also arise from asphericity of the particles due to deformation in the air stream. Ballotini is hard and spherical, but it has been observed in clusters on filters used to collect it after its passage through the test space (see Section (5.6)). An agglomerate of spherical particles traversing the test volume would give a considerably reduced value of R due to its form anisotropy.

Figures (5-5-n-q) shows the same calculations carried out for $\theta = 180$. In this case there is a distinct peak at around $R \simeq 0.5$ and there is very little variation with ϕ. Results presented for the backward direction in Section (5.4)

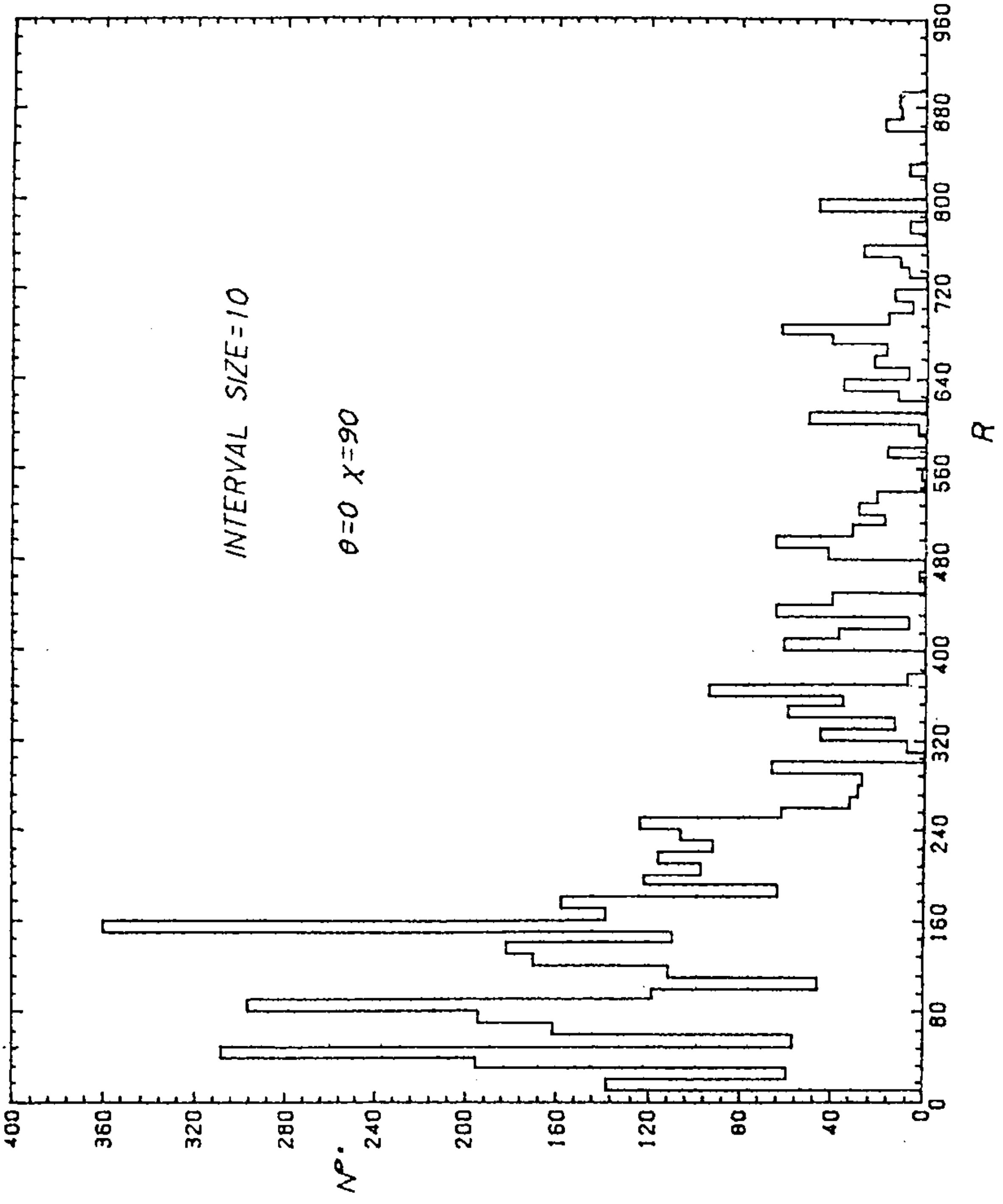

Fig.(5-5-j) Histogram of Number/R for forward scatter with no phase errors

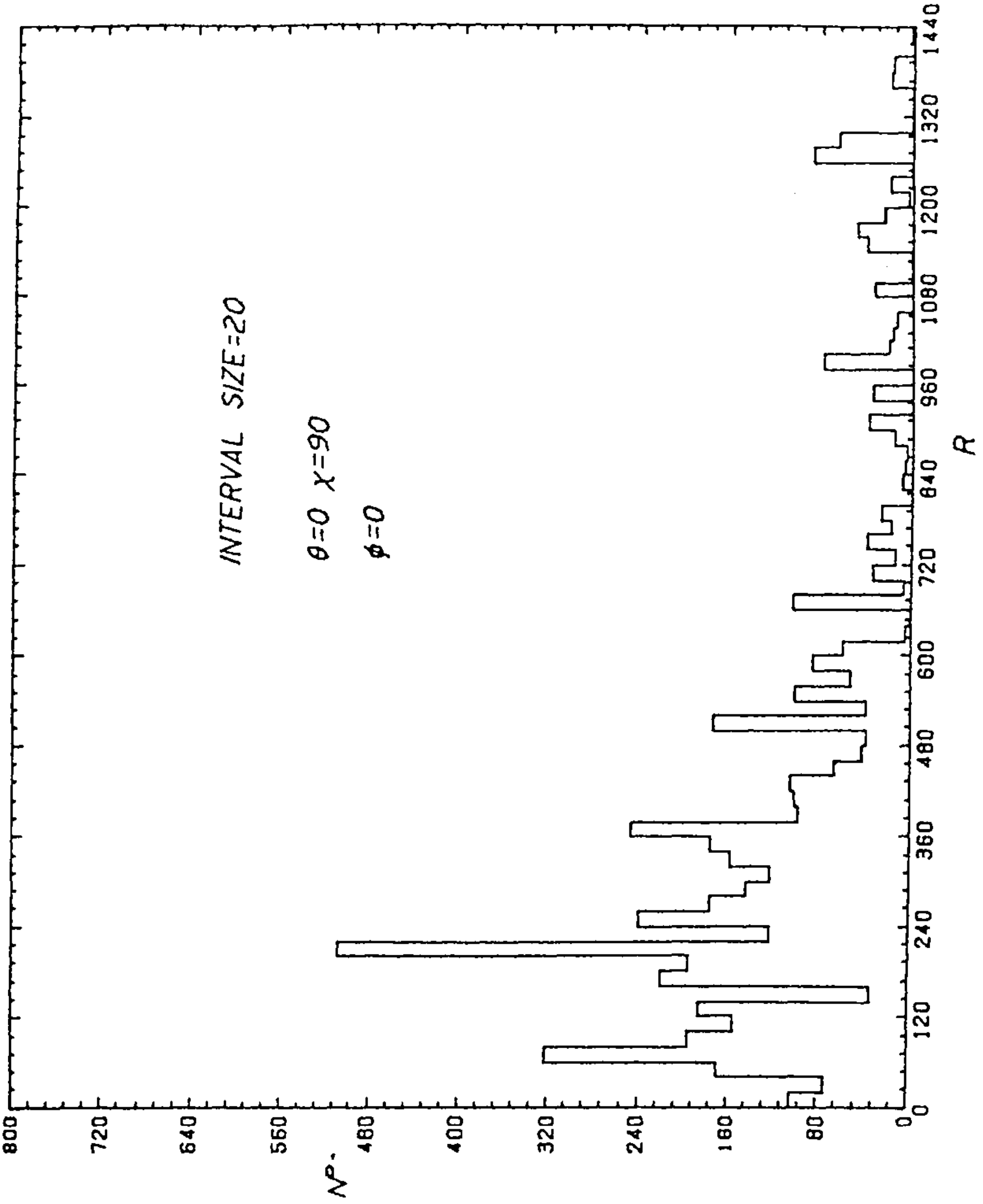

Fig.(5-5-k) Histogram of Number/R for forward scatter with phase errors (φ=0)

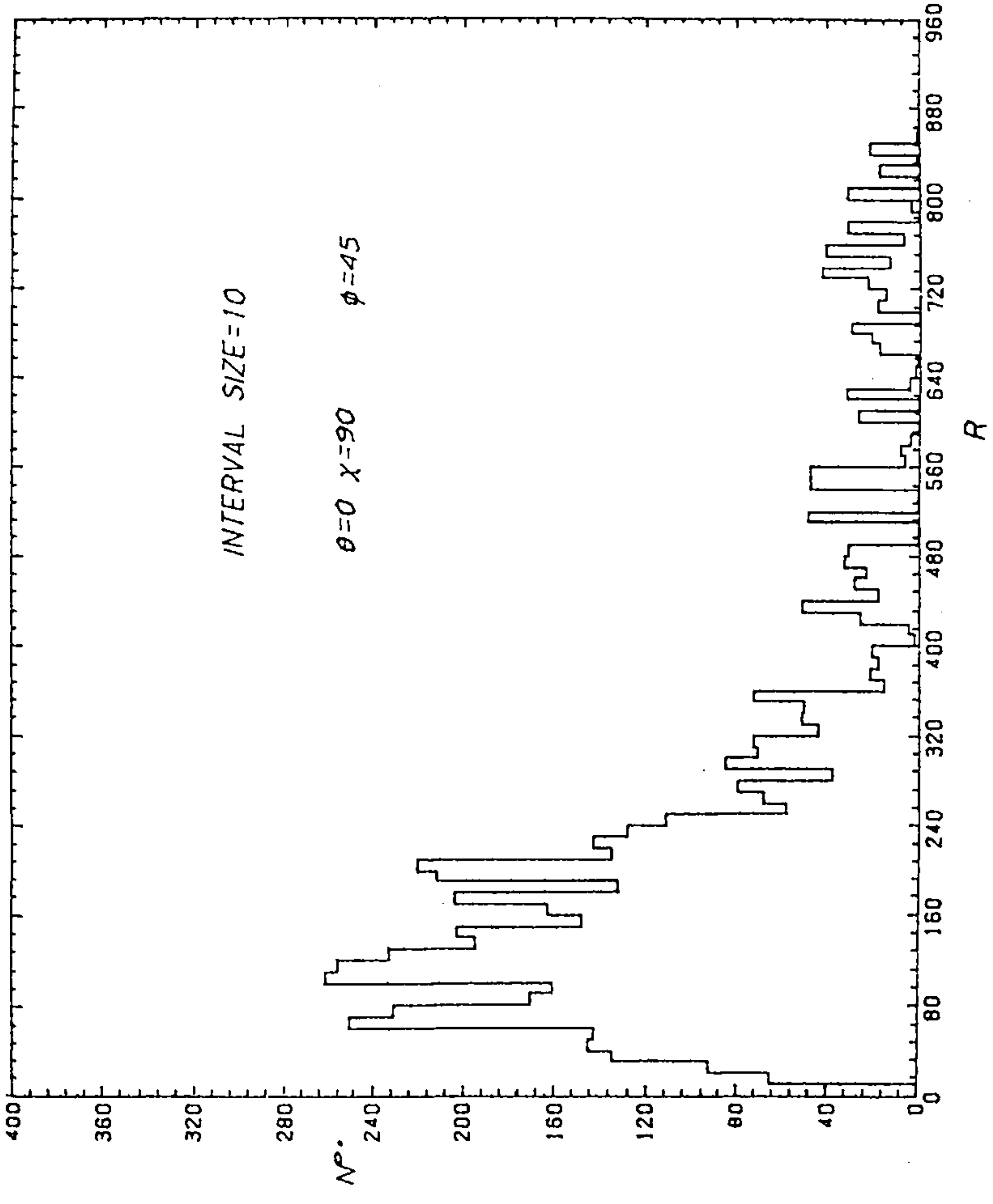

Fig.(5-5-1) Histogram of Number/R for forward scatter with phase errors (ϕ=45)

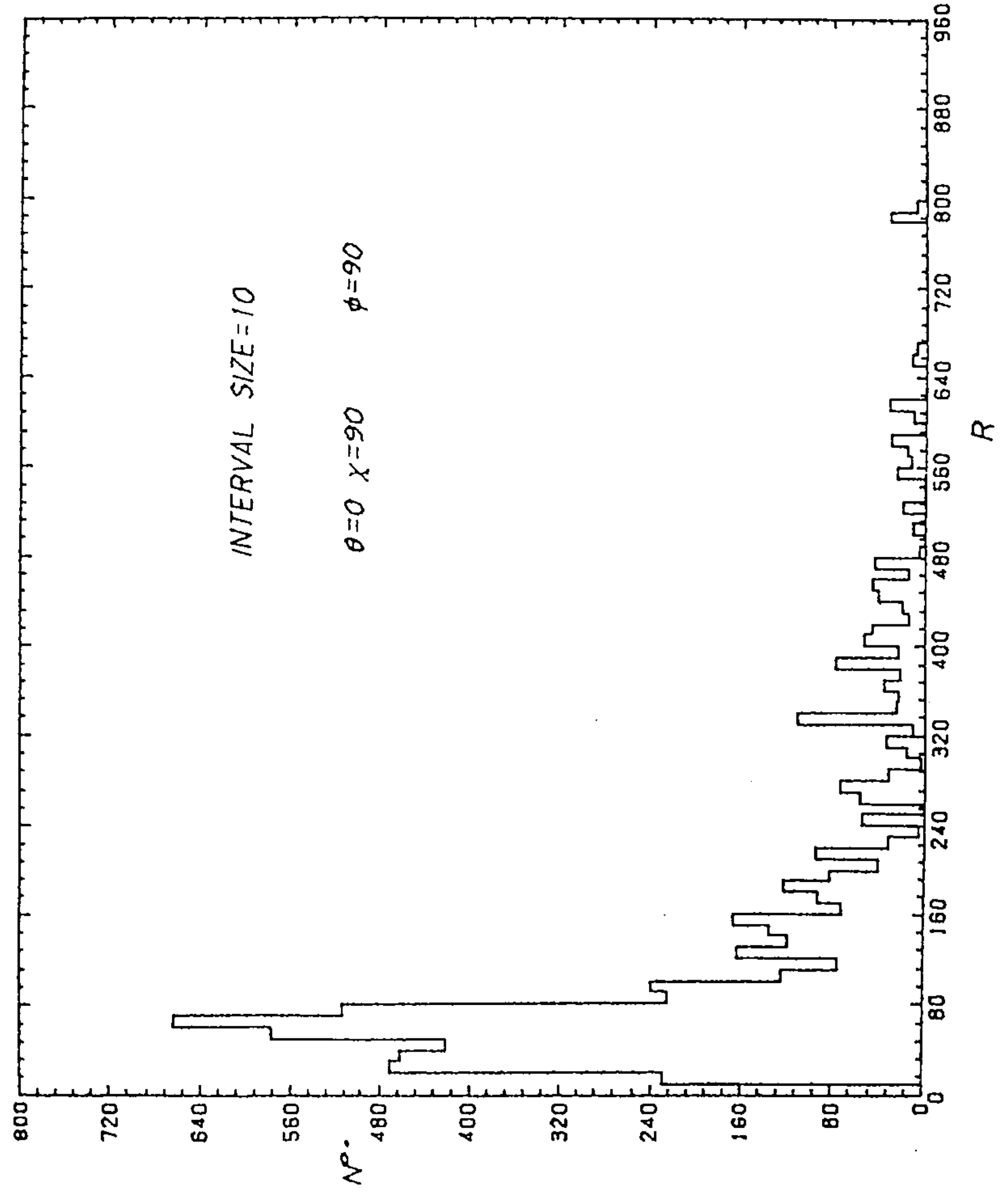

Fig.(5-5-m) Histogram of Number/R for forward scatter with phase errors (ϕ=90)

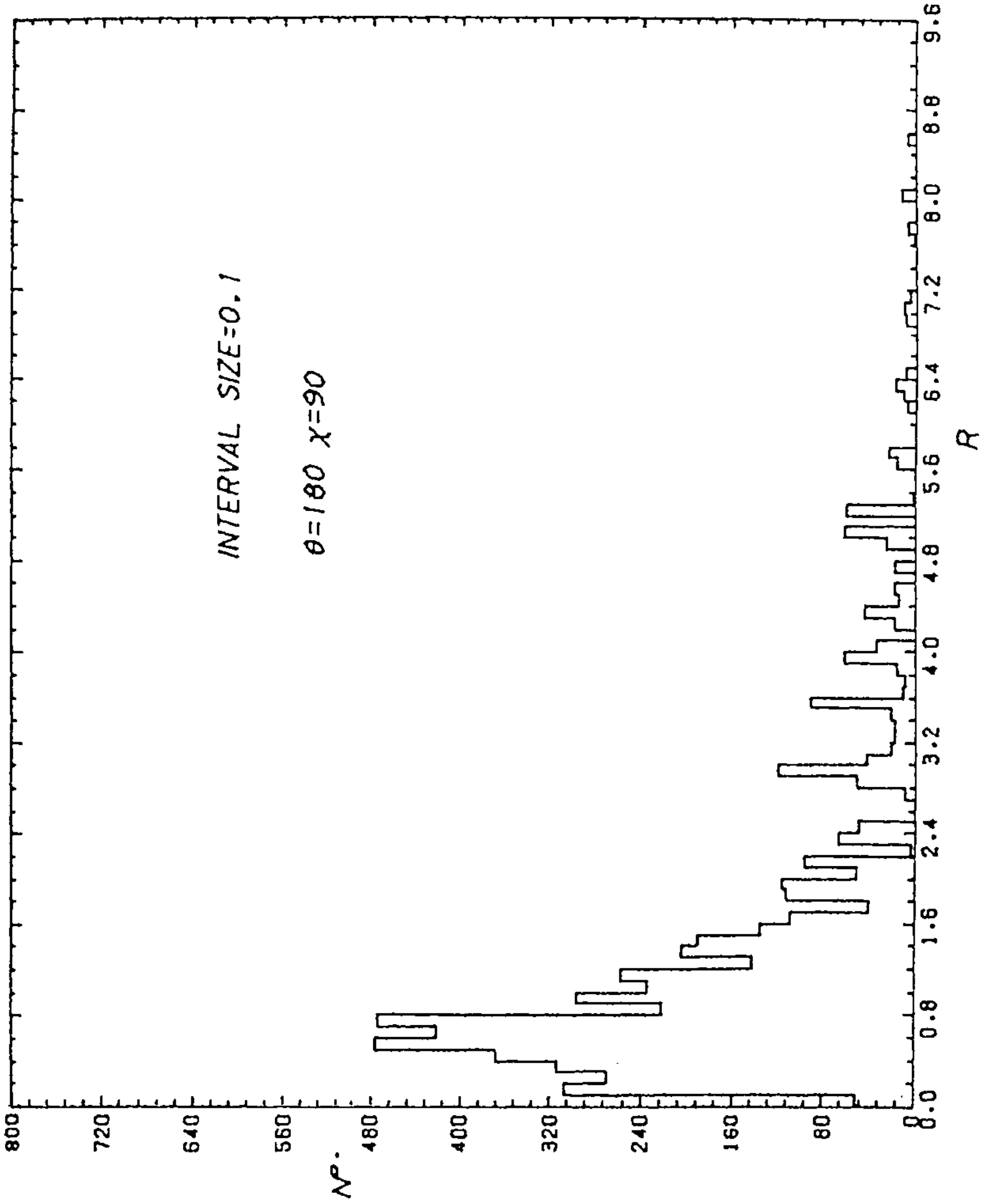

Fig.(5-5-n) Histogram of Number/R for back scatter with no phase errors

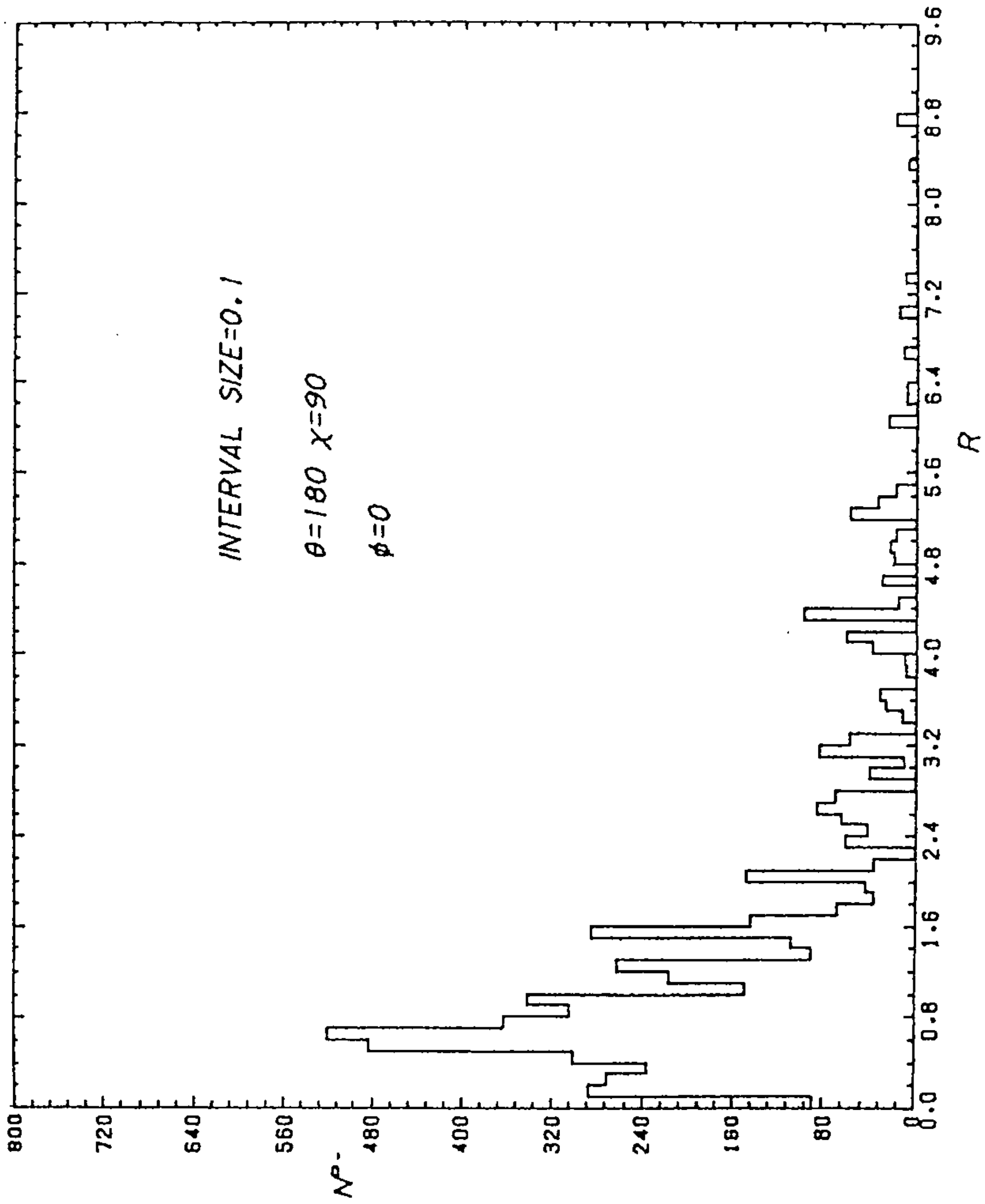

Fig.(5-5-o) Histogram of Number/R for back scatter with phase errors (φ=0)

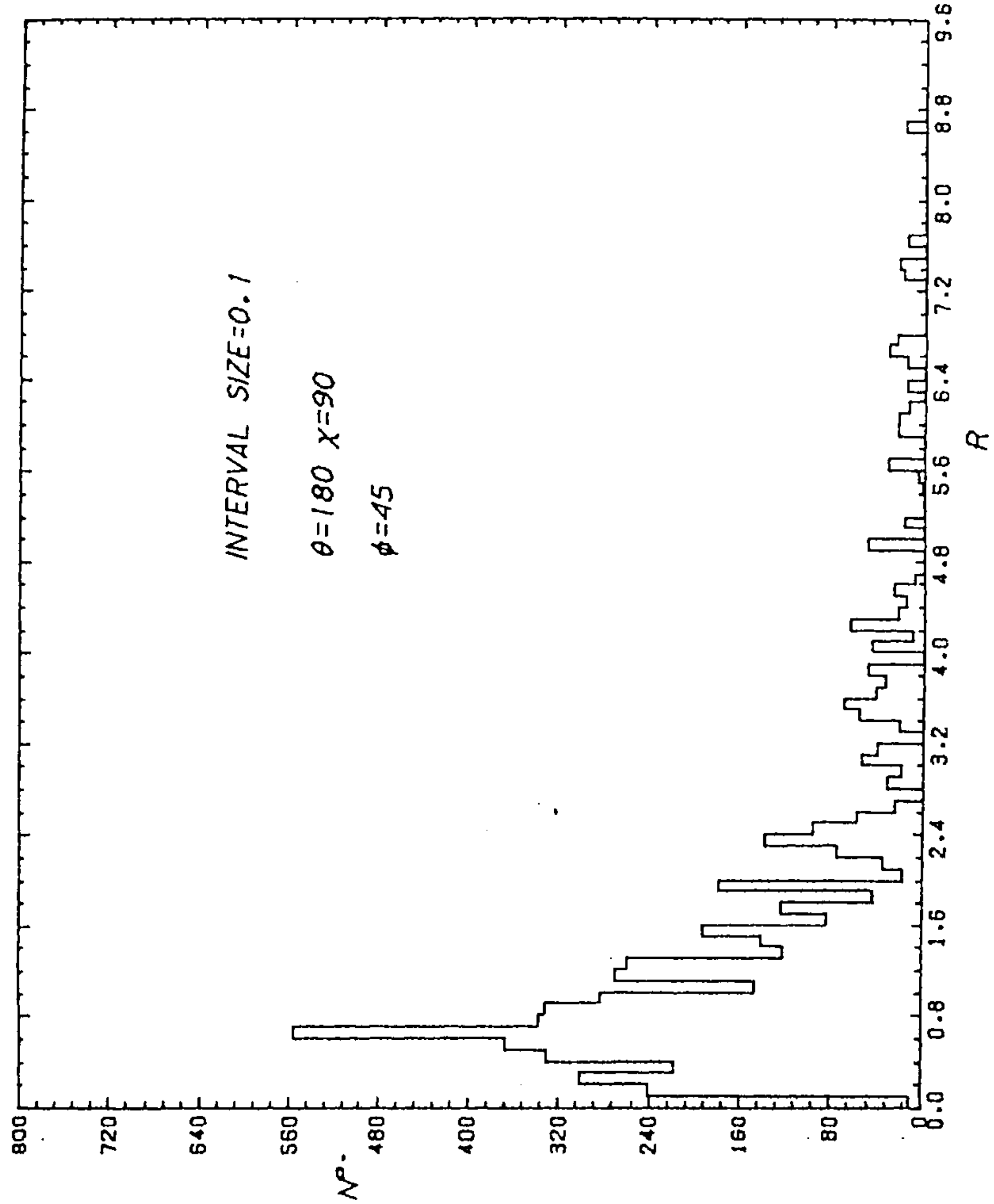

Fig.(5-5-p) Histogram of Number/R for back scatter with phase errors (φ=45)

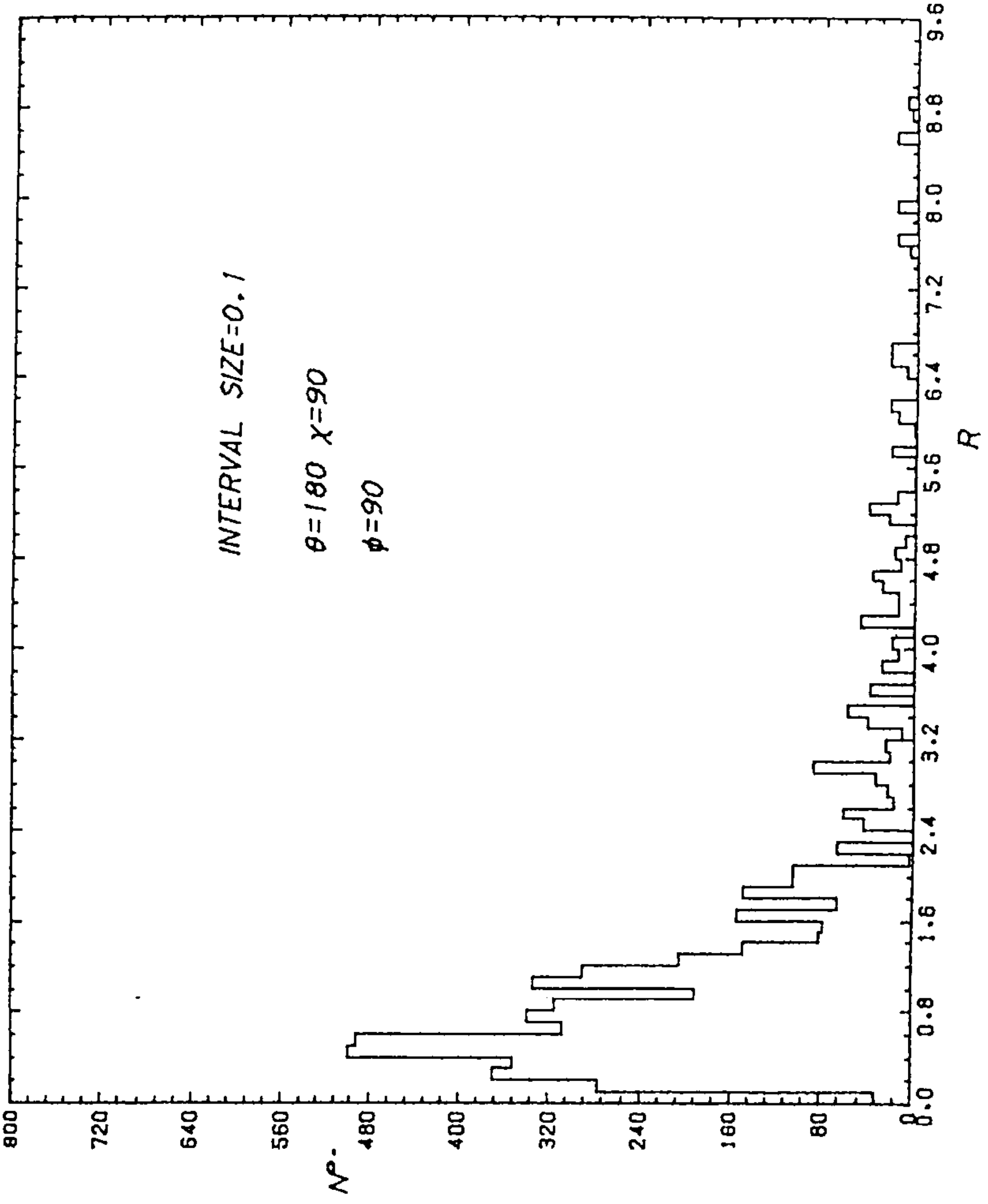

Fig.(5-5-q) Histogram of Number/R for back scatter with phase errors (φ=90) showed that in the case of fibres $R \simeq 0.45$. Thus the experiemtal result agrees very well with the predicted value.

It should be noted that we have concentrated on theoretical calculations at $\chi = 90^{\circ}$ because fibres may be expected to align themselves with the flow of air as reported by Gentry and Spurny (1978). For fibres transversing the test space at $\chi \neq 90$ even lower values of the ratios are predicted (see Sections (5.3) and (5.4)). Thus distinguishability between fibres and spheres is unimpaired by any variation of the ratio with χ.

(ii) Finite Collecting Aperture.

Theoretical calculations are usually based on light scattered to a particular scattering angle θ. However, in reality a finite aperture lens has to be used such that light is collected over a small range of angles.

Figures (5-5-r-s) show the effect of integrating the light intensity over a finite collecting lens for the forward and backward directions respectively. It can be seen that for $\theta=0$ the change in the RATIO is minimal. However, for $\theta=180$ there are noticeably higher values of the RATIO (up to three times those without the aperture) between $x=8$ and $x=20$. This partly explains the low values of R obtained in the backward direction.

5.6 Counting

Having established the distinguishability of fibrous and non-fibrous and non-fibrous particles, the system should be capable of ascertaining the concentration of fibres in the air. In order to test this the modified LDA system of

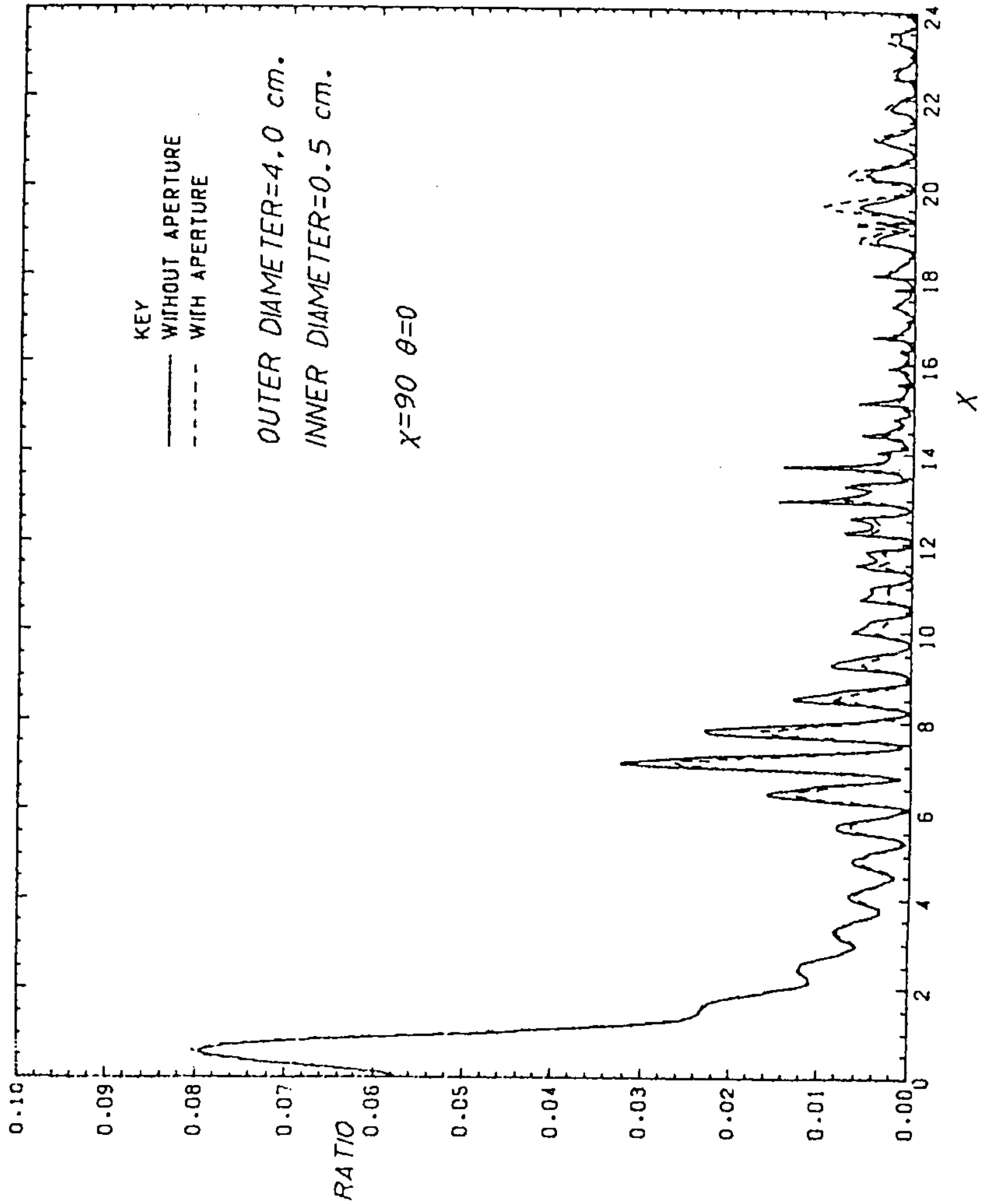

Fig.(5-5-r) Plot of RATIO against x for a finite aperture lens in the forward direction

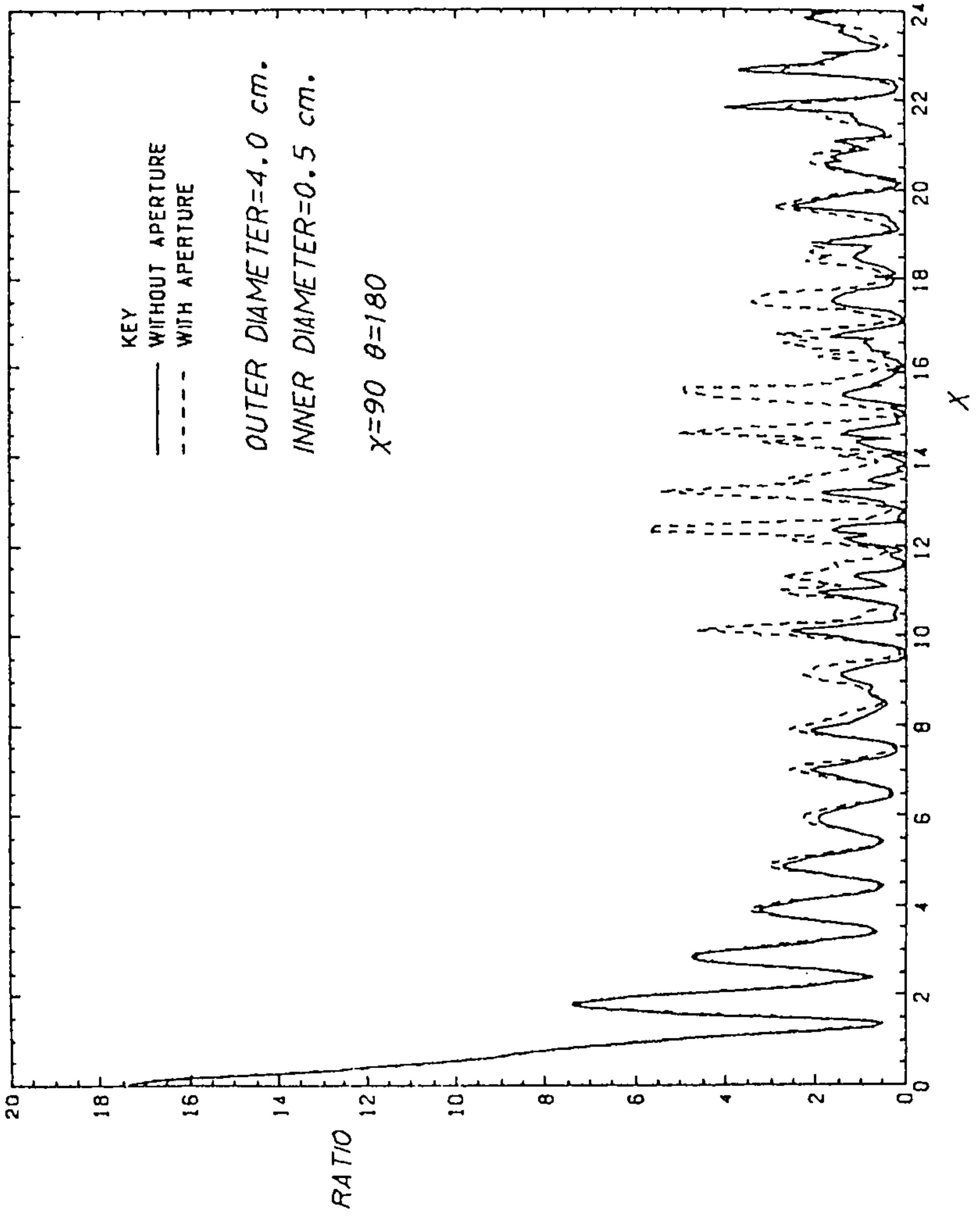

Fig.(5-5-s) Plot of RATIO against x for a finite aperture lens in the backward direction

Figure (4-4-a) was used. Instead of fibres the counting can be carried out with ballotini since the actual counting of any type of paricle is the same.

Ballotini from a fluidised bed, illustrated in Chapter 5 was passed on an air stream through the test space and deposited on three nucleopore filters situated immediately adjacent to the crossed beams as shown in Figure (5-6-a) A vacuum pump was used to provide the suction necessary for collecting the particles. The oscilloscope was adjusted to continuous trigger such that each time a signal was stored in the sampling time was the trace sweep time. The total number of particles counted was 56 in sampling time of 4s. The flow rate of air was 2.5 litres/min. By scanning the 5µm pinhole across various points of the test space in Figure (4-4-a), an estimate of the cross-sectional area of the test space was made to be 8cm.X 0.05cm. Thus the number of particles crossing per unit area per unit time can be calculated. The number of particles deposited on the filters is found from the suction rate of the vacuum pump. The area of each filter, the number of particles crossing the laser beam per unit area per unit time and the total time the experiment was running. Using the LDA system has a considerable advantage in that the velocity of the particles can be measured by simply freezing a particle trace on the oscilloscope and measuring the time taken to cross one fringe (distance = 50µm). It was calculated that approximately 10,000 particles should be observed on each filter. However, electron microscopy of the filters revealed only about 6,000 particles on each one. There can be several reasons for this discrepancy.

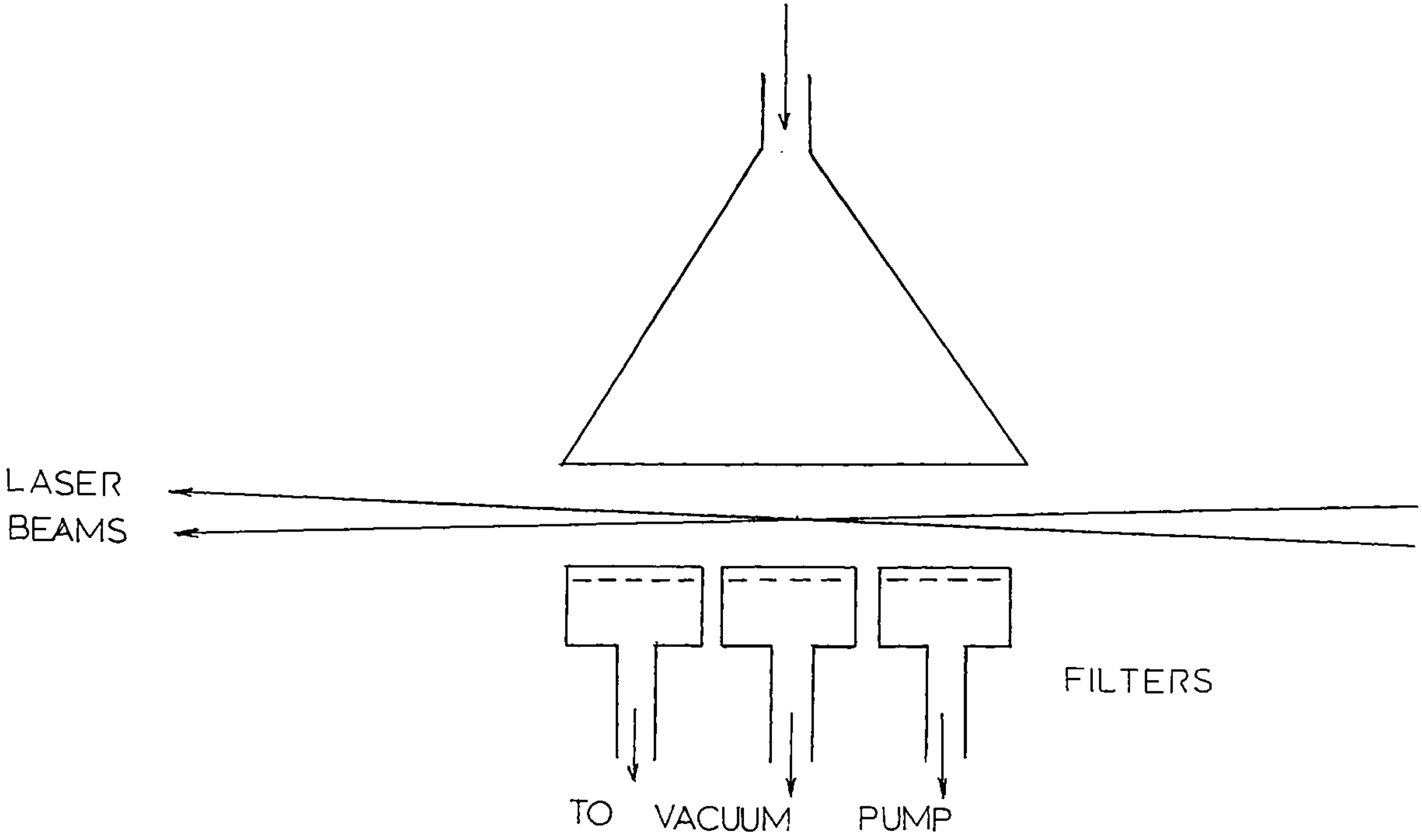

Fig.(5-6-a) Position of nucleopore filters and ballotini disperser relative to laser beams

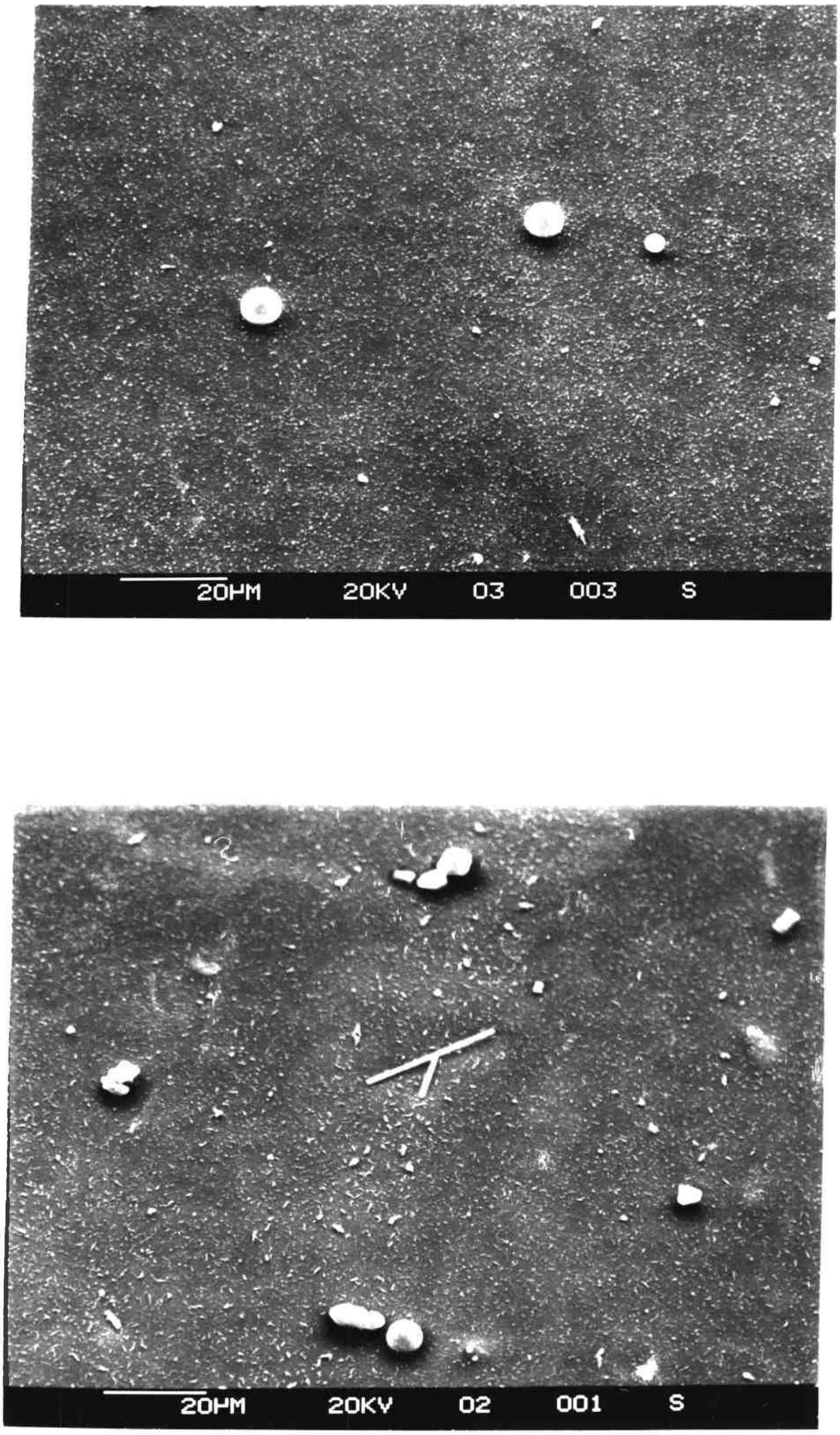

P-5-6-1 Electron micrographs of filters showing glass ballotini and extraneous particles.

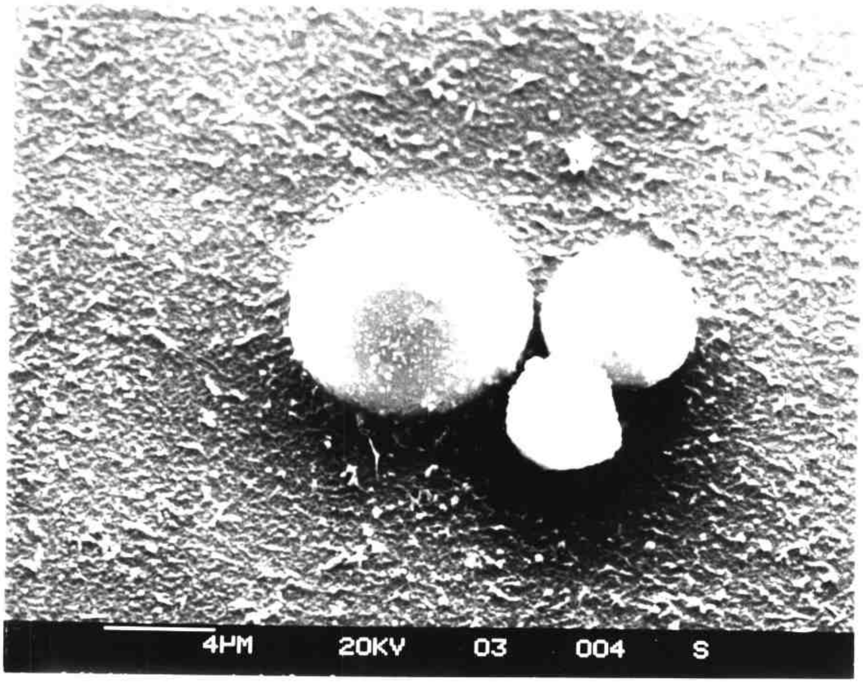

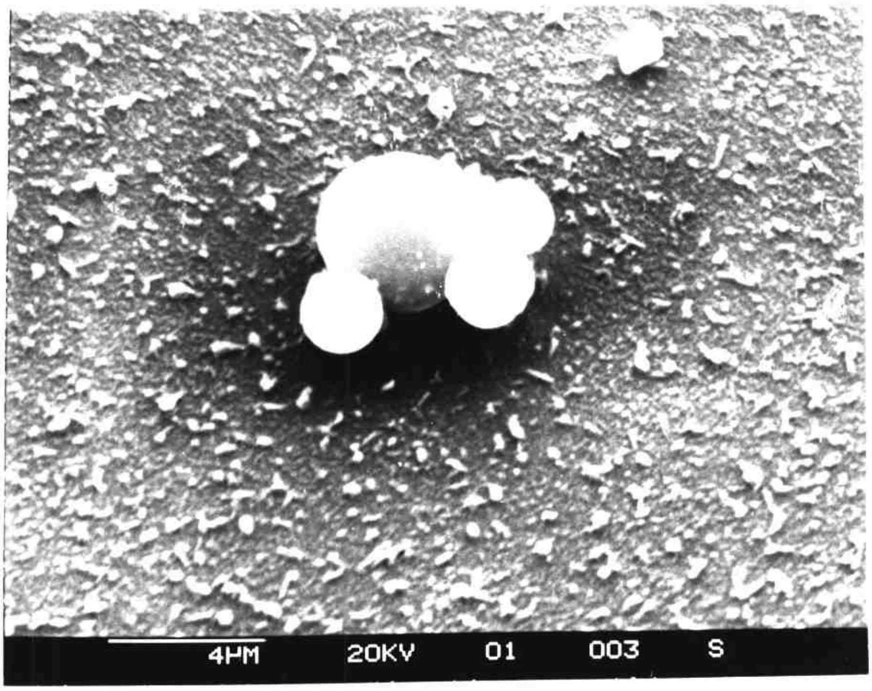

P-5-6-2 Electron micrographs showing agglomeration of ballotini particles.

(i) the suction rate is not the same as the flow rate of air carrying the particles. In fact, the suction is maximum at points very close to the filter holder. This is why the filters were placed close to the laser beams such that any particle traversing the test space should be sucked in.

(ii) electron micrographs of the filters show excessive amounts of extraneous particles including fibres as shown in P-5-6-1

(iii) ballotini is found in agglomerates as can be seen in P-5-6-2. An agglomerate would be counted as one particle but the inherent form anisotropy would give an incorrect R for ballotini.

These problems can be overcome by using a better sampling method and having a clean environment. Calibration of the test space is of the utmost significance in order to obtain consistant results. Holve (1979) has devised an inversion procedure for characterising the test space by slicing the test space into areas, through which a monodisperse size particles of known size are injected. A count distribution is obtained with a sharp cut off at the maximum signal amplitude and spreading down to lower amplitudes. If a polydisperse source was used the signal amplitude distribution of such monodisperse distributions. The technique devised unfolds the measured signal amplitude count distribution in the presence of a non-uniform test space to obtain the size distribution. With the aid of a microprocessor this inversion technique could be incorporated into our system for characterising the test space.

5.7 Conclusion

Distinguishability between spherical and cylindrical particles based on the ratio R has been clearly established in both the forward and backward scattering modes. Moreover, results obtained for dust airborne in the laboratory indicate a significantly different value of R than for fibres (see Sections (5.2) and (5.3)).

Theoretical predictions of R for fibres for forward scatter agree well with experimental values if errors in the quarter wave plates are incorporated into the calculations. However, for back scatter the influence of phase plate errors on the value of R is minimal, but experimental results correlate well with theoretical predictions.

The advantages of this method of detecting fibres are that in-situ measurement is carried out and if the system is suitably calibrated, automation with a microprocessor will ensure unsupervised monitoring of asbestos fibres. The scheme is independent of the orientation angle ψ and calculations indicate that for all values of χ the fibre should still provide distinctly low values of R. Since we measure a ratio, the result is independent of signal size and any fluctuations in laser light intensity. Accurate adjustment and measurement of phase plate errors is difficult. However, in a practical instrument this would not be a disadvantage since we only require to show that it will distinguish between fibrous and non-fibrous particles.

The method has some limitations:

(i) localisation of the test space is very difficult and is dependent on good optics and design. For a single beam system the test space is very long, but with the LDA arrangement it is limited by the interfering beams and any stops or apertures. Ideally, the test volume should be s spherical or cubical shape with a uniform illumination intensity and a uniform light collection efficiency throughout the volume.

(ii) errors in the measurement of signal. The dynamic range of the oscilloscope restricts the particle size. If sensitivity of the oscilloscope is adjusted to respond to the smallest particle then the largest signals will be outside the range. This is not a general limitation and could be overcome by coupling the signals to a microprocessor via a logarithmic amplifier.

(iii) for backscatter, polarisation effects could give unpredictable results. However, consistently different values of R for fibres and spheres indicate clear distinguishability.

(iv) errors in adjustment of the prism. These would introduce erroneous signals due to misalignment giving incorrect polarisation ratios. Improvements in the optical alignment procedure would overcome this.

(v) signal size is dependent on laser light intensity. The stability of laser output power is essential if measurement of particle size is required. However, independent monitoring could be used to allow for variations of output power.

Calibration of the instrument should be carried out with particles in the size range of interest. In the signal analysis, allowance should be made of unpredictable particle trajectories through the test space. For the LDA arrangement only one particle at a time can be present in the test space; thus measurement of the concentation is limited. However, for a test space size of ~ $1mm^3$, the maximum measureable particle concentration is ~ 10^9 particles m^{-3}. This is very large compared with the legal maximum concentration of asbestos fibres of 1 fibre cm^{-3}.

Future work should include:

(i) Pursue work in the backscattering mode. The success of this would be advantageous for the production of an instrument which incorporated all the optical components and analysis equipment in one portable box. This would require design of optics perhaps mounted on a single tubular framework. The portability would facilitate setting up and operating of the instrument.

(ii) Automate measurement of the ratio R. This is easily implemented by feeding signals directly into a microprocessor programmed for signal analysis. Holve (1979) and Holve and Self (1980) give a scheme for eliminating the dependence on particle trajectory in the test space. This has to be examined and perhaps included in the final analysis.

(iii) There may be advantages to moving to longer wavelength because the RATIO is much larger at small orders of D/λ. Also infra-red lasers are safer for workshop use. However infra-red optics are not readily available and very expensive.

(iv) Continue theoretical study of scattering from finite cylinders.

APPENDIX A

Jones (1979) used the integral formulation reviewed by Saxon (1974) to obtain the scattered electric field for chains of Reayleigh spheres where the spheres are so small that the internal field is constant. Space is divided into a number of small spherical volumes and the internal field at the centre of the jth particle is calculated.

Two Rayleigh spheres of radii R_1 and R_j, whose centres are separated by D_{1j} with common origin at O, are shown in Figure (A-1). It can be shown that the electric field at $\underline{r}_1$ is given by

$$\underline{E}(\underline{r}_1) - \frac{i}{3}\left(\frac{\varepsilon-1}{\varepsilon+2}\right)\sum_{\substack{j=1\\ j=1}}^{N}(kR_j)^3 T_{1j}\underline{E}(\underline{r}_j) = \frac{3}{\varepsilon+2}\underline{E}_{inc}(\underline{r}_1) \qquad \text{(A-1)}$$

where ε is the permittivity; K is the wave number and T_{1j} is a (3X3) matrix whose elements are given at the end of this Appendix. Equation (A-1) results in 3N linear simultaneous equations which can be solved for each of the N particles to give the Cartesian field components for each sphere.

Referring to Figure (A-2) where the spherical co_ordinates of the centre of the sphere are (r_j, θ_j, ϕ_j) it can be shown that the scattered electric field in the far field ($r >> r_j^1$ and $r >> r_j$) is

$$\underline{E}_{sca}(\underline{r}) = \frac{1}{3}(\varepsilon-1)\frac{e^{ikr}}{r}\sum_{j=1}^{N} k^2 R_j^3 e^{-ikr_j\cos\beta_j}\ \Theta_j\hat{\theta}_1 + \Phi_j\hat{\Phi}_1 \qquad \text{(A-2)}$$

where $\hat{\theta}_1$ and $\hat{\Phi}_1$ are unit vectors along θ and ϕ directions and

$$\Theta_j = \cos\theta\cos\phi E_x(\underline{r}_j) + \cos\theta\sin\phi E\ (\underline{r}_j) - \sin\theta E_z(\underline{r}_j)$$

$$\Phi_j = \sin\phi E_x(\underline{r}_j) - \cos\phi E_y(\underline{r}_j)$$

As indicated in Chapter 3 (Figure (3-2-a)) two oppositely

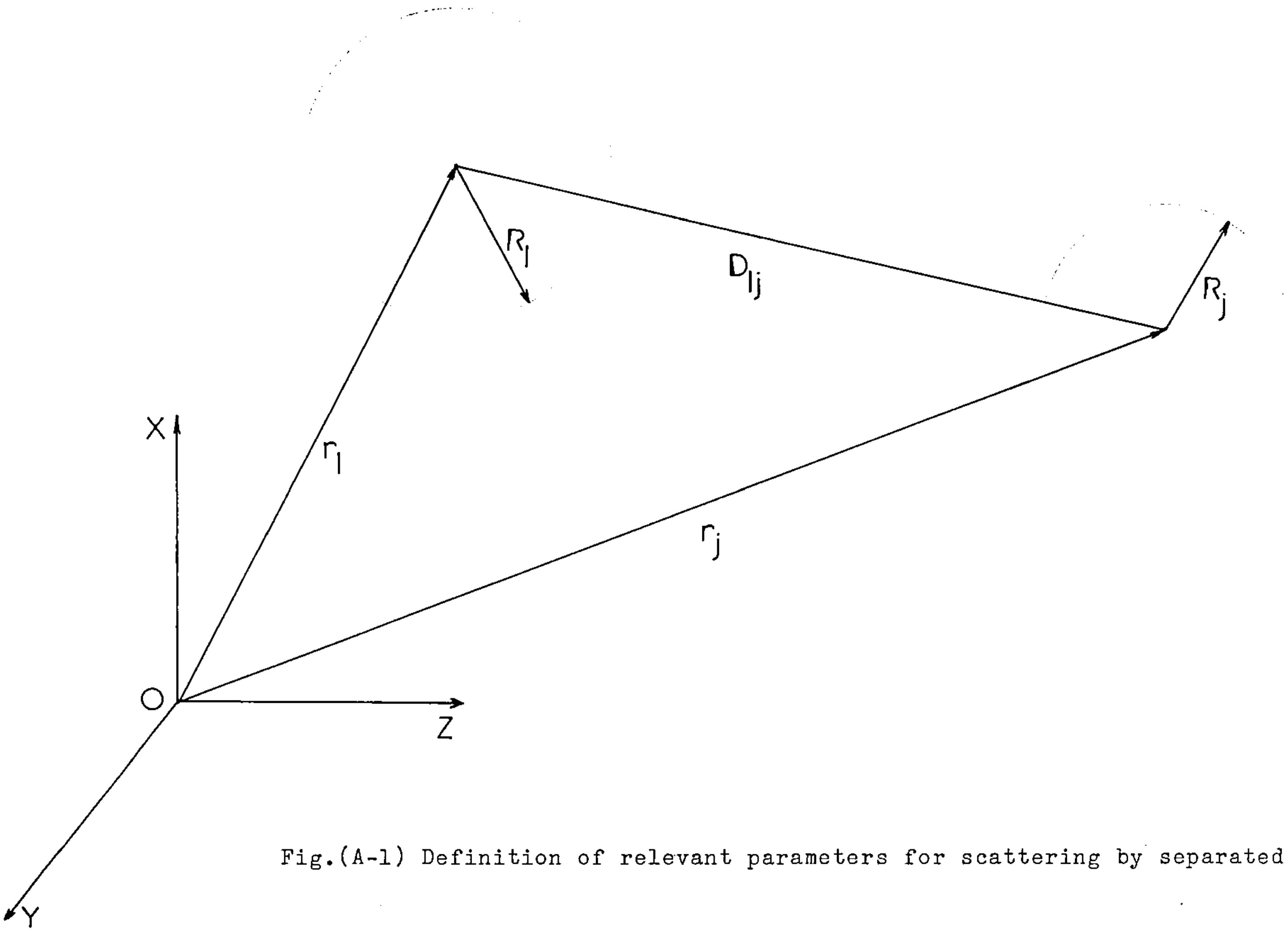

Fig.(A-1) Definition of relevant parameters for scattering by separated spheres

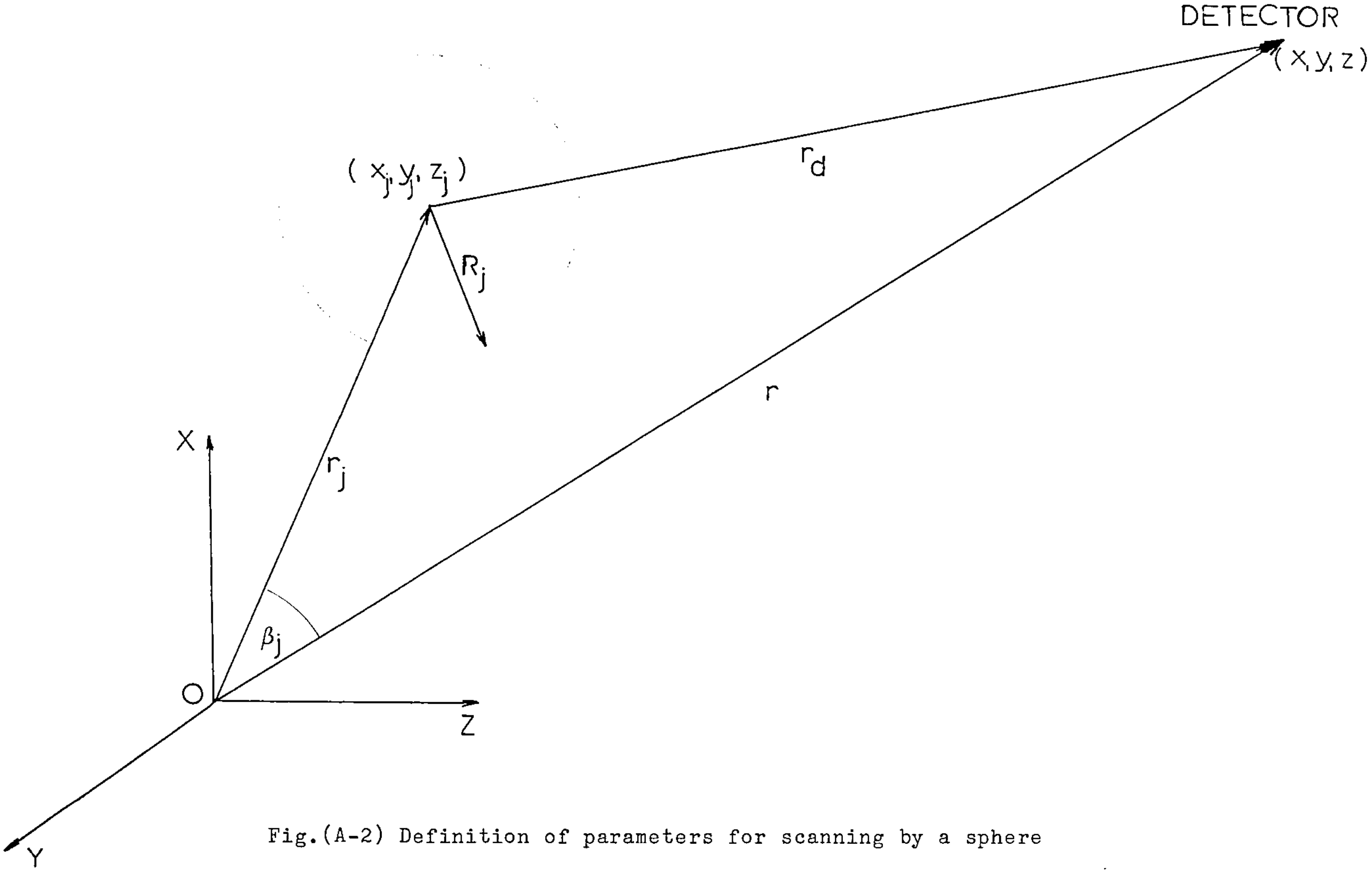

Fig.(A-2) Definition of parameters for scanning by a sphere circularly polarised waves interfere in the plane $z = 0$ to form a fringe pattern. The electric field at the j^{th} Rayleigh sphere for each of the two incident waves are given by (Equation A-1)

$$\underline{E}_j^{(1)} = \frac{3E_0}{\varepsilon+2}\left(1+\frac{i}{3}\left(\frac{\varepsilon-1}{\varepsilon+2}\right)\sum_{\substack{l=1\\ l\neq j}}^{N}(kR_l)^3 T_{lj}^{(1)} e^{ik(y_j-y_l)\sin\gamma}\right)$$

$$\times\ (\underline{W}+\underline{V})e^{i(\omega t-ky_j\sin\gamma)}$$

$$\underline{E}_j^{(2)} = \frac{3E_0}{\varepsilon+2}\left(1+\frac{i(\varepsilon-1)}{(\varepsilon+2)}\sum_{\substack{l=1\\ l\neq j}}^{N}(kR_l)^3 T_{lj}^{(2)} e^{-ik(y_j-y_l)\sin\gamma}\right)$$

$$\times\ (\underline{W}-\underline{V})e^{i(\omega t+ky_j\sin\gamma)} \qquad \text{(A-3)}$$

where $\underline{W} = \hat{x}_1 + \sin\gamma\hat{z}_1$

$\underline{V} = i\cos\gamma\hat{y}_1$

The scattered electric fields can be written as (Equation A-2)

$$\underline{E}_{sca}^{(1)} = \frac{1}{3}(\varepsilon-1)\left(\frac{kR}{kr}\right)^3\sum_{j=1}^{N} e^{-iky_j\sin\theta}\,\Gamma_{lj}^{(1)}\, e^{i(\omega t-ky_j\sin\gamma)}$$

$$\times\ e^{ikr} \qquad \text{(A-4)}$$

$$\underline{E}_{sca}^{(2)} = \frac{1}{3}(\varepsilon-1)\left(\frac{kR}{kr}\right)^3\sum_{j=1}^{N} e^{-iky_j\sin\theta}\,\Gamma_{lj}^{(2)}\, e^{i(\omega t+ky_j\sin\gamma)}$$

$$\times\ e^{ikr} \qquad \text{(A-5)}$$

Let $Z = \frac{1}{3}(\varepsilon-1)\left(\frac{kR}{kr}\right)^3$

The scattered intensity can now be found.

Thus,

$$I_{sca} = |Z|^2 \sum_{j=1}^{N} \sum_{j^1=1}^{N} \Gamma_{1j}^{(1)} \Gamma_{1j^1}^{(1)*} e^{ik(y_{j^1}-y_j)(\sin\gamma+\sin\theta)}$$

$$+ |Z|^2 \sum_{j=1}^{N} \sum_{j^1=1}^{N} \Gamma_{1j}^{(2)} \Gamma_{1j^1}^{(2)*} e^{ik(y_{j^1}-y_j)(\sin\gamma-\sin\theta)}$$

$$+ 2\mathrm{Re}\left(|Z|^2 \sum_{j=1}^{N} \sum_{j^1=1}^{N} \Gamma_{1j}^{(1)} \Gamma_{1j^1}^{(2)*} e^{ik(y_{j^1}-y_j)\sin\theta} \right) \tag{A-6}$$

Where $\Gamma_{1j} = \Theta\hat{\theta}_1 + \Phi\hat{\phi}_1$

and $\Theta_j^{(p)} = \cos\theta E_{y_j}^{(p)} - \sin\theta E_{z_j}^{(p)}$

$\Phi_j^{(p)} = -E_{x_j}^{(p)}$

P is the polarisation i.e. 1 or 2. The visibility can be calculated from

$$V = \frac{I_{AC}}{I_{DC}}$$

where I_{AC} is the last term of I_{sca} and I_{DC} is the sum of the first two terms of I_{sca}.

Isotropic particles such as spheres, produce no rotation in the plane of polarisation of the scattered light. However, anisotropic agglomerates such as a chain of Rayleigh spheres shown in Figure (A-3) would produce depolarisation. For the oriented chain $\theta_j = \chi$ and $\phi = \psi$ and is the same for all particles in the chain. Also

$$r_j^2 = x_j^2 + y_j^2 + z_j^2$$

or

$$x_j^2 = r_j \sin\chi\cos\psi$$

$$y_j = r_j \sin\chi\sin\psi$$

$$z_j = r_j \cos\chi$$

Randon orientation can be treated by calculating the mean scattered intensity defined by

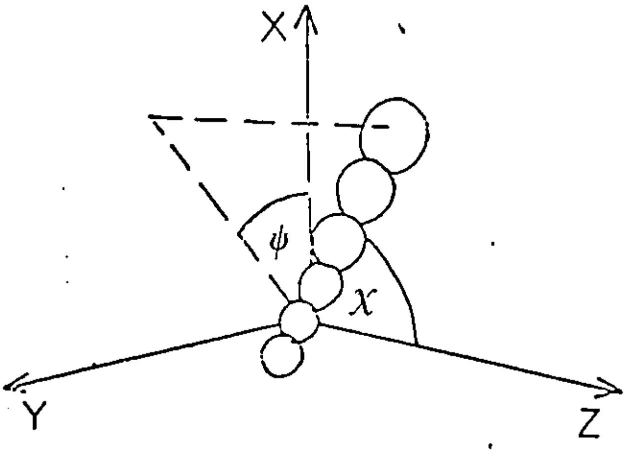

Fig.(A-3) Orientation of a chain of spheres

$$I_{sca} = \frac{1}{4\pi} \int_0^{2\pi}\int_0^{\pi} I_{sca} \sin\chi \, d\chi \, d\psi$$

using Gaussian integration

$$T_{1j}^{(p)} = \begin{pmatrix} a_{1j}^{(p)} & b_{1j}^{(p)} & c_{1j}^{(p)} \\ b_{1j}^{(p)} & a_{1j}^{(p)\prime} & d_{1j}^{(p)} \\ c_{1j}^{(p)} & d_{1j}^{(p)} & e_{1j}^{(p)} \end{pmatrix}$$

$$a_{1j}^{(p)} = h_0^{(1)}(kD_{1j}) - h_2^{(1)}(kD_{1j}) \left(P_2(\cos\chi^{(p)}) - \tfrac{1}{2}\cos 2\psi^{(p)} P_2^2(\cos\chi^{(p)}) \right)$$

$$a_{1j}^{(p)\prime} = -h_0^{(1)}(kD_{1j}) - h_2^{(1)}(kD_{1j}) \left(P_2(\cos\chi^{(p)}) + \tfrac{1}{2}\cos 2\psi^{(p)} P_2^2(\cos\chi^{(p)}) \right)$$

$$b_{1j}^{(p)} = \tfrac{1}{2} h_2^{(1)}(kD_{1j}) \sin 2\psi^{(p)} P_2^2(\cos\chi^{(p)})$$

$$c_{1j}^{(p)} = -h_2^{(1)}(kD_{1j}) \cos\psi^{(p)} P_2^1(\cos\chi^{(p)})$$

$$d_{1j}^{(p)} = -h_2^{(1)}(kD_{1j}) \sin\psi^{(p)} P_2^1(\cos\chi^{(p)})$$

$$e_{1j}^{(p)} = 2h_2^{(1)}(kD_{1j}) P_2^2(\cos\chi^{(p)})$$

with

$$P_2(x) = \tfrac{1}{2}(3x^2 - 1)$$

$$P_2^1(x) = -3x\sqrt{1-x}$$

$$P_2^2(x) = 3(1-x^2)$$

$$h_n^{(1)}(x) = j_n(x) + iy_n(x)$$

$$j_0(x) = \frac{\sin x}{x} \; ; \quad y_0(x) = -\frac{\cos x}{x}$$

$$j_2(x) = \left(\frac{3}{x} - \frac{1}{x}\right) \sin x - \frac{3}{x^2} \cos x$$

$$y_2(x) = \left(-\frac{3}{x^3} + \frac{1}{x}\right) \cos x - \frac{3}{x^2} \sin x$$

Also

$$\begin{aligned} kD_{1j} &= k(r_1-r_j) \\ &= k(y_1-y_j)/\sin\psi \\ &= k(x_1-x_j)/\cos\psi \end{aligned}$$

If $\chi=\pi/2$ then $\cos\chi^{(1)} = -\sin\psi\sin\gamma$

$$\cos\chi^{(2)} = \sin\psi\sin\gamma$$

$$\sin\psi^{(1)} = \sin\psi^{(2)} = \sin\psi\cos\gamma/\sqrt{\sin^2\psi\cos^2\gamma+\cos^2\psi}$$

$$\cos\psi^{(1)} = \cos\psi^{(2)} = \cos\psi/\sqrt{\sin^2\psi\cos^2\gamma+\cos^2\psi}$$

APPENDIX B

(i) Consider left-handed and right-handed circularly polarised waves of angular frequencies ω_1 and ω_2 incident on the plane Z = 0 at half angle γ as shown in Figure B-1. The electric fields $\underline{E}_1$ and $\underline{E}_2$ are given by

$$\underline{E}_1 = (\hat{x}_1+\hat{y}_1 i\cos\gamma+\hat{z}_1\sin\gamma)\ e^{i(\omega_1 t-k_1 y\sin\gamma)}$$

$$\underline{E}_2 = (\hat{x}_1-\hat{y}_1 i\cos\gamma+\hat{z}_1\sin\gamma)\ e^{i(\omega_2 t+k_2 y\sin\gamma)} \qquad \text{(B-1)}$$

where k_1 and k_2 are the wave numbers corresponding to ω_1 and ω_2 respectively. Superposition of $\underline{E}_1$ and $\underline{E}_2$ gives the total electric field $\underline{E}_T$ to be

$$\underline{E}_T = \underline{E}_1+\underline{E}_2 = (\hat{x}_1+\hat{z}_1\sin\gamma)\left(e^{i(\omega_1 t-k_1 y\sin\gamma)} + e^{i(\omega_2 t+k_2 y\sin\gamma)}\right)$$

$$+ \hat{y}_1 i\cos\gamma\left(e^{i(\omega_1 t-k_1 y\sin\gamma)} - e^{i(\omega_2 t+k_2 y\sin\gamma)} \right)$$

Since

$$e^{i(\omega_1 t-k_1 y\sin\gamma)} + e^{i(\omega_2 t+k_2 y\sin\gamma)}$$

$$= 2\cos\left(\omega t+\frac{\Delta k}{2}y\sin\gamma\right)\cos\left(-\frac{\Delta\cdot\omega t}{2}+ky\sin\gamma\right)$$

$$+ 2\ i\ \sin\left(\omega t+\frac{\Delta k}{2}y\sin\gamma\right)\cos\left(-\frac{\Delta\cdot\omega t}{2}+ky\sin\gamma\right)$$

$$= 2\cos\left(\frac{\Delta\cdot\omega t}{2} - ky\ \sin\gamma\right) e^{i(\omega t)\frac{\Delta k}{2}y\sin\gamma} \qquad \text{(B-3)}$$

where $\Delta\omega = \omega_2 - \omega_1$ and $\Delta k = k_2 - k_1$

Also

$$e^{i(\omega_1 t- k_1 y\sin\gamma)} - e^{i(\omega_2 t+k_2 y\sin\gamma)}$$

$$= i\ 2\ \sin\left(\frac{\Delta\omega t}{2} - ky\sin\gamma\right) e^{i\left(\omega t+\frac{\Delta k}{2}y\sin\gamma\right)}$$

$$\text{(B-4)}$$

Substituting Equations (B-3) and (B-4) into (B-2) gives

$$\underline{E} = (\hat{x}_1+\hat{z}_1\sin\gamma)2\cos\left(\frac{\Delta\omega t}{2}-ky\sin\gamma\right) e^{i\left(\omega t+\frac{\Delta k}{2}y\sin\gamma\right)}$$

$$+ i\hat{y}_1\cos\gamma 2\sin\left(\frac{\Delta\omega t}{2}-ky\sin\gamma\right) e^{i\left(\omega t+\frac{\Delta k}{2}y\sin\gamma\right)} \qquad \text{(B-5)}$$

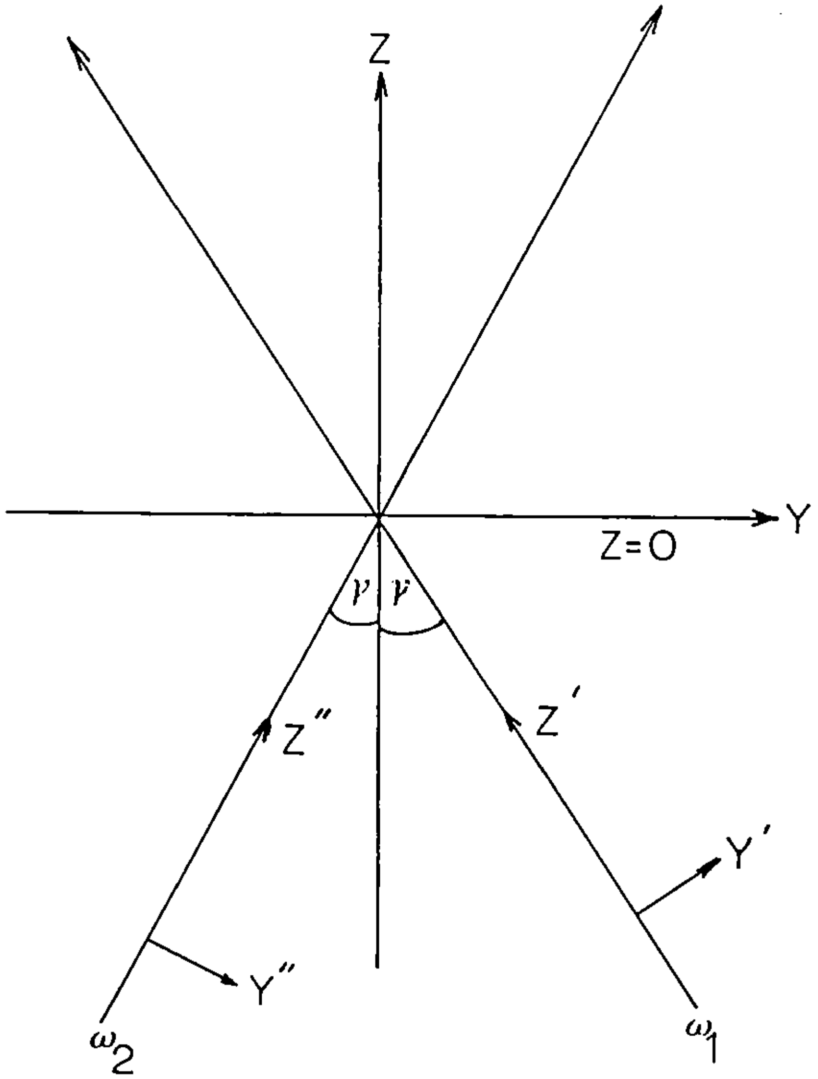

Fig.(B-1) Scattering geometry for crossed beams

The intensity in the test space is

$$\begin{aligned} I &= |\underline{E}.\underline{E}^*| \\ &= 4\cos^2F + 4\sin^2\gamma\cos^2F + 4\cos^2\gamma\sin^2F \\ &= 4(\cos^2F + \sin^2\gamma\cos^2F + \cos^2\gamma\sin^2F) \\ &= 2(1 + \cos 2F + \sin^2\gamma(1 + \cos 2F) + \cos^2\gamma(1 - \cos 2F)) \\ &= 2(2 + (1 + \sin^2\gamma - \cos^2\gamma)\cos 2F) \end{aligned} \tag{B-6}$$

where

$$F = \frac{\Delta\omega t}{2} - ky\sin\gamma$$

Finally I can be simplified to

$$I = 2(2 + (1 - \cos 2\gamma)\cos 2F) \tag{B-7}$$

The visibility of the signal is given by (Hong and Jones,1976)

$$V = \frac{I_{max} - I_{min}}{I_{max} + I_{min}} \tag{B-8}$$

From Equation (B-7)

$$I_{max} = 2 + (1 - \cos 2\gamma)$$

and

$$I_{min} = 2 - (1 - \cos 2\gamma)$$

Thus the visibility is

$$V = \tfrac{1}{2}(1 - \cos 2\gamma) \tag{B-9}$$

(ii) The total electric field incident on a particle traversing the fringe plane $Z = 0$ is given by Equation (B-2). If we associate A, B and C to represent the scattered light along three orthogonal axes, then the total scattered field can be written as

$$\underline{E}_{sca} = (\hat{x}_1 A + i\hat{z}_1 C\sin\gamma)\left(e^{i(\omega_1 t - k_1 y\sin\gamma)} + e^{i(\omega_2 t + k_2 y\sin\gamma)}\right)$$

$$+ i\hat{y}_1 B\cos\gamma\left(e^{i(\omega_1 t - k_1 y\sin\gamma)} - e^{i(\omega_2 t + k_2 y\sin\gamma)}\right) \tag{B-10}$$

The scattered intensity is

$$I_{sca} = 2\left(|A|^2 + |C|^2\sin^2\gamma + |B|^2\cos^2\gamma \right)$$

$$+ \left(|A|^2 + |C|^2\sin^2\gamma - |B|^2\cos^2\gamma\right) \cos\,(\Delta wt - 2ky\sin\gamma) \tag{B-11}$$

Thus the visibility is

$$V = \frac{|A|^2 + |C|^2\sin^2\gamma - |B|^2\cos^2\gamma}{|A|^2 + |C|^2\sin^2\gamma + |B|^2\cos^2\gamma} \tag{B-12}$$

APPENDIX C

(i) Consider rotation of the x,y co-ordinate system by ψ_1 to form a new co-ordinate system x_1y_1 as shown below

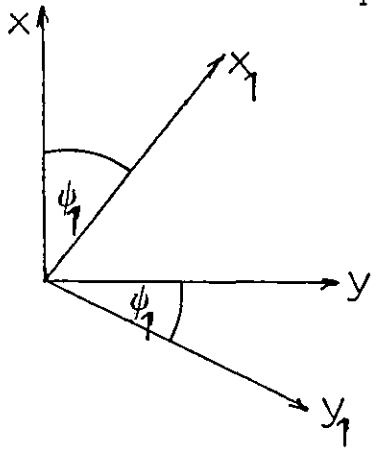

We can immediately write down the transformations

$$x = x_1\cos\psi_1 - y_1\sin\psi_1$$
$$y = x_1\sin\psi_1 + y_1\cos\psi_1 \qquad \text{(C-1)}$$

and

$$x_1 = x\cos\psi_1 + y\sin\psi_1$$
$$y_1 = -x\sin\psi_1 + y\cos\psi_1 \qquad \text{(C-2)}$$

(ii) A linearly polarised wave incident on a quarter wave plate at an angle ψ_1 produces an elliptically polarised wave. Thus, a plane wave of amplitude E_o at $t = 0$ polarised in the x direction can be written as

$$\underline{E}_{inc} = \hat{x}\, E_o\, e^{i\omega t}$$
$$= (\hat{x}_1\cos\psi_1 - \hat{y}_1\sin\psi_1)\, E_o\, e^{i\omega t} \qquad \text{(C-3)}$$

where a hat over a letter indicates a unit vector in that direction. Since the action of the quarter wave plate is to retard one component of $\underline{E}_{inc}$ by quarter of a wavelength, we can write

$$\underline{E}_1 = (\hat{x}_1\cos\psi_1 - \hat{y}_1\sin\psi_1 e^{i\frac{3\pi}{2}})E_o e^{i\omega t} \qquad \text{(C-4)}$$

since $e^{i\frac{3\pi}{2}} = -i$ and $\psi_1 = \pi/4$ for circular polarisation

$$\begin{aligned}\underline{E}_1 &= \frac{1}{\sqrt{2}}(\hat{x}_1 + i\,\hat{y}_1)\,E_o e^{i\omega t} \\ &= \frac{1}{\sqrt{2}}\left((\hat{x}\cos\psi_1+\hat{y}\sin\psi_1)+i(-\hat{x}\sin\psi_1+\hat{y}\cos\psi_1)\right)E_o e^{i\omega t} \\ &= \tfrac{1}{2}\left((1-i)\hat{x}+(1+i)\hat{y}\right)E_o e^{i\omega t}\end{aligned} \qquad \text{(C-5)}$$

(iii) If there is no scattering, the circularly polarised wave with wave vector $\underline{E}_1$ is incident on the second quarter wave plate whose optic axis is oriented at angle ψ_2 to the xy co-ordinate system as shown below

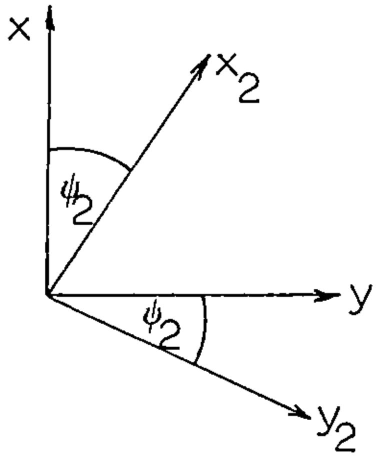

Thus the electric vector incident on the second quarter wave plate can be written using the transformations (C-1) and (C-2) as

$$\begin{aligned}\underline{E}_1 &= \tfrac{1}{2}\left((1-i)(\hat{x}_2\cos\psi_2-\hat{y}_2\sin\psi_2)+(1+i)(\hat{x}_2\sin\psi_2+\hat{y}\cos\psi_2)\right)E_o e^{i\omega t} \\ &= \tfrac{1}{2}\Big(\hat{x}_2\left((1-i)\cos\psi_2+(1+i)\sin\psi_2\right) \\ &\quad - \hat{y}_2\left((1-i)\sin\psi_2-(1+i)\cos\psi_2\right)\Big)E_o e^{i\omega t}\end{aligned} \qquad \text{(C-6)}$$

From this field emerging from the second quarter wave plate is calculated to be

$$\underline{E}_2 = \tfrac{1}{2}\Big(\hat{x}_2\big((1-i)\cos\psi_2 + (1+i)\sin\psi_2 \big)$$
$$- \hat{y}_2\big((1-i)\sin\psi_2 - (1+i)\cos\psi_2 \big) e^{i\frac{\pi}{2}}\Big) E_o e^{i\omega t}$$
$$= \tfrac{1}{2}\Big(\hat{x}_2\big((1-i)\cos\psi_2 + (1+i)\sin\psi_2\big)$$
$$-i\hat{y}_2\big((1-i)\sin\psi_2 - (1-i)\cos\psi_2\big)\Big) E_o e^{i\omega t}$$
$$= \tfrac{1}{2}\Big(\hat{x}_2\big((1-i)\cos\psi_2 + (1+i)\sin\psi_2 \big)$$
$$-\hat{y}_2 \big((1+i)\sin\psi_2 + (1-i)\cos\psi_2\big)\Big) E_o e^{i\omega t}$$

since $(1+i) = i(1-i)$

$$\underline{E}_2 = \tfrac{1}{2}\big(\hat{x}_2(1-i)e^{i\psi_2} - \hat{y}_2(1-i)e^{i\psi_2}\big) E_o e^{i\omega t}$$
$$= \tfrac{1}{2} (1-i) (\hat{x}_2 - \hat{y}_2) E_o e^{i(\omega t+\psi_2)}$$

Transforming back to $\underline{\hat{x}}$ and $\underline{\hat{y}}$ gives

$$\underline{E}_2 = \tfrac{1}{2} (1-i)\big(\hat{x}\cos\psi_2+\hat{y}\sin\psi_2+\hat{x}\sin\psi_2-\hat{y}\cos\psi_2 \big) E_o e^{i(\omega t+\psi_2)}$$
$$= \tfrac{1}{2} (1-i)\big(\hat{x}(\cos\psi_2+\sin\psi_2)+\hat{y}(\sin\psi_2-\cos\psi_2)\big) E_o e^{i(\omega t+\psi_2)}$$

For $\psi_2 = \pi/4$

$$\underline{E}_2 = \tfrac{1}{2} (1-i)\hat{x}.\frac{2}{\sqrt{2}}E_o e^{i\omega t}.e^{i\pi/4}$$
$$= \tfrac{1}{2} (1-i)\, \hat{x}\, \frac{2}{\sqrt{2}}\, E_o e^{i\omega t}.\frac{1}{\sqrt{2}}\, (1+i)$$
$$= \hat{x}\, E_o\, e^{i\omega t}$$

This is correct since circular polarisation incident on a quarter wave plate with optic axis at $\pi/4$ should produce linear polarisation.

The intensity of $\underline{E}_2$ is

$$|\underline{E_2}|^2 = \tfrac{1}{4}.2\big(\cos^2\psi_2 +\sin^2\psi_2 +2\cos\psi_2\sin\psi_2$$
$$+ \cos^2\psi_2 +\sin^2\psi_2 -2\cos\psi_2\sin\psi_2\big) E_o^2$$
$$= E_o^2$$

This is also correct assuming there are no losses.

(iv) $\underline{E}_2$ is incident on the polariser whose axis is at angle ψ_p to $\hat{\underline{x}}$. The net effect is to transmit the component along $\underline{x}_p$ only. Thus

$$\begin{aligned}
\underline{E}_p &= \tfrac{1}{2}(1-i)\big(\hat{x}_p\cos\psi_p(\cos\psi_2+\sin\psi_2) \\
&\quad + \hat{x}_p\sin\psi_p(\sin\psi_2-\cos\psi_2)\big)\; E_0e^{i(\omega t+\psi_2)} \\
&= \tfrac{1}{2}(1-i)\hat{x}_p\big(\cos\psi_p(\cos\psi_2+\sin\psi_2) \\
&\quad + \sin\psi_p(\sin\psi_2-\cos\psi_2)\big)\; E_0e^{i(\omega t+\psi_2)}
\end{aligned}$$

The intensity is

$$\begin{aligned}
|\underline{E}_p|^2 &= \tfrac{1}{4}\big(\cos^2\psi_p(1+\sin2\psi_2)+\sin^2\psi_p(1-\sin2\psi_2) \\
&\quad + 2\cos\psi_p\sin\psi_p(\cos\psi_2\sin\psi_2-\cos^2\psi_2+\sin^2\psi_2 \\
&\quad - \cos\psi_2\sin\psi_2)\big) \\
&= \tfrac{1}{4}(1+\cos2\psi_p)(1+\sin2\psi_2) \\
&\quad + \tfrac{1}{2}(1-\cos2\psi_p)(1-\sin2\psi_2) \\
&\quad + \tfrac{1}{2}\sin2\psi_p(-\cos2\psi_2)
\end{aligned}$$

This simplifies to

$$\begin{aligned}
|\underline{E}_p|^2 &= \tfrac{1}{2}(1+\cos2\psi_p\sin2\psi_2-\sin2\psi_p\cos\psi_2) \\
&= \tfrac{1}{2}(1+\sin2(\psi_p\cdot\psi_2))
\end{aligned}$$

(v) Consider the circularly polarised vector $\underline{E}_1$ is incident on a scatterer whose long axis is at angle ψ to the x axis. Thus from Equation (C-5)

$$\begin{aligned}
\underline{E}_1 &= \tfrac{1}{2}\big((1-i)\hat{x}+(1-i)\hat{y}\big)\; E_0e^{i\omega t} \\
&= \tfrac{1}{2}(1-i)(\hat{x}+i\hat{y})\; E_0e^{i\omega t} \\
&= \tfrac{1}{2}(1-i)\big(\hat{x}_s\cos\psi_s-\hat{y}_s\sin\psi_s \\
&\quad + i(\hat{x}_s\sin\psi_s+\hat{y}_s\cos\psi_s)\big)\; E_0e^{i\omega t} \\
&= \tfrac{1}{2}(1-i)\big(\hat{x}_s(\cos\psi_s+i\sin\psi_s) \\
&\quad - \hat{y}_s(\sin\psi_s-i\cos\psi_s)\big)\; E_0e^{i\omega t} \\
&= \tfrac{1}{2}(1-i)(\hat{x}_se^{i\psi_s}+i\hat{y}_se^{i\psi_s})\; E_0e^{i\omega t} \\
&= \tfrac{1}{2}(1-i)(\hat{x}_s+i\hat{y}_s)\; E_0i^{(\omega t+\psi_s)}
\end{aligned}$$

If A and B represent the scattering factors along x_s and y_s then the scattered field is

$$\begin{aligned}
\underline{E}_s &= \tfrac{1}{2}\,(1-i)\,(A\hat{x}_s+iB\hat{y}_s)\,E_o e^{i(\omega t+\psi_s)} \\
&= \tfrac{1}{2}\,(1-i)(\,A(\,\hat{x}\cos\psi_s+\hat{y}\sin\psi_s) \\
&\quad + iB(\,-\hat{x}\sin\psi_s+\hat{y}\cos\psi_s))\,E_o e^{i(\omega t+\psi_s)} \\
&= \tfrac{1}{2}\,(1-i)(\,\hat{x}(\,A\cos\psi_s-iB\sin\psi_s) \\
&\quad + \hat{y}(\,A\sin\psi_s+iB\cos\psi_s))\,E_o e^{i(\omega t+\psi_s)}
\end{aligned}$$

This passes through the second quarter wave plate at ψ_2

$$\begin{aligned}
\underline{E}_s &= \tfrac{1}{2}\,(1-i)((\,\hat{x}_2\cos\psi_2-\hat{y}_2\sin\psi_2)(\,A\cos\psi_s-iB\sin\psi_s) \\
&\quad + (\,\hat{x}_2\sin\psi_2+\hat{y}_2\cos\psi_2)(\,A\sin\psi_s+iB\cos\psi_s\,)) \\
&\quad X\ E_o e^{i(\omega t+\psi_s)}
\end{aligned}$$

Thus

$$\begin{aligned}
\underline{E}_2 &= \tfrac{1}{2}\,(1-i)(\,\hat{x}_2(\cos\psi_2(\,A\cos\psi_s-iB\sin\psi_s) \\
&\quad + \sin\psi_2(\,A\sin\psi_s+iB\cos\psi_s) \\
&\quad + i\hat{y}_2(\cos\psi_2(\,A\sin\psi_s+iB\cos\psi_s) \\
&\quad - \sin\psi_2(\,A\cos\psi_s-iB\sin\psi_s)))\quad E_o e^{i(\omega t+\psi_s)} \\
&= \tfrac{1}{2}\,(1-i)(\,\hat{x}_2(\,A\cos(\psi_2-\psi_s)+\,iB\sin(\psi_2-\psi_s)\,) \\
&\quad + i\hat{y}_2(\,-A\sin(\psi_2-\psi_s)+iB\cos(\psi_2-\psi_s)))\quad E_o e^{i(\omega t+\psi_s)} \\
&= \tfrac{1}{2}\,(1-i)(\,\hat{x}_2(\,A\cos(\psi_2-\psi_s)+iB\sin(\psi_2-\psi_s)) \\
&\quad - \hat{y}_2(\,B\cos(\psi_2-\psi_s)+iA\sin(\psi_2-\psi_s)))E_o e^{i(\omega t+\psi_s)}
\end{aligned}$$

Transforming back to xy

$$\begin{aligned}
\underline{E}_2 &= \tfrac{1}{2}\,(1-i)(\,\hat{x}\cos\psi_2+\hat{y}\sin\psi_2)\,(\,A\cos(\psi_2-\psi_s)+iB\sin(\psi_2-\psi_s)) \\
&\quad -(\,-\hat{x}\sin\psi_2+\hat{y}\cos\psi_2)(\,B\cos(\psi_2-\psi_s)+iA\sin(\psi_2-\psi_s)\,) \\
&\quad X\ E_o e^{i(\omega t+\psi_s)}
\end{aligned}$$

$$= \tfrac{1}{2}\ (1-i)\big(\ \hat{x}\big(A\big(\ \cos\psi_2\cos(\psi_2-\psi_s)+i\sin\psi_2\sin(\psi_2-\psi_s)\ \big)$$

$$+\ B\big(\ \sin\psi_2\cos(\psi_2-\psi_s)+i\cos\psi_2\sin(\psi_2-\psi_s)\big)\big)$$

$$+\ \hat{y}\ \big(A\ \big(\ \sin\psi_2\cos(\psi_2-\psi_s)-i\cos\psi_2\sin(\psi_2-\psi_s)\ \big)$$

$$-\ B\big(\ \cos\psi_2\cos(\psi_2-\psi_s)-i\sin\psi_2\sin(\psi_2-\psi_s)\big)\big)\big)$$

$$X\quad E_o e^{i(\omega t+\psi_s)}$$

For $\psi_2 = \pi/4$

$$\underline{E}_2 = \tfrac{1}{2}\ (1-i)\big(\ \hat{x}\big(\ \frac{A}{\sqrt{2}}e^{i(\psi_2-\psi_s)}+\frac{B}{\sqrt{2}}e^{i(\psi_2-\psi_s)}\ \big)$$

$$+\ \hat{y}\big(\ \frac{A}{\sqrt{2}}e^{-i(\psi_2-\psi_s)}-\ \frac{B}{\sqrt{2}}e^{i(\psi_2-\psi_s)}\ \big)\big)$$

$$X\quad E_o e^{i(\omega t+\psi_s)}$$

$$= \frac{1}{2\sqrt{2}}\ (1-i)\big(\ \hat{x}(A+B)e^{i(\psi_2-\psi_s)}\ +\ \hat{y}(A-B)e^{-i(\psi_2-\psi_s)}\big)$$

$$X\quad E_o e^{i(\omega t+\psi_s)}$$

If A = B = 1 (such as for a sphere)

$$\underline{E}_2 = \frac{1}{2\sqrt{2}}\ (1-i)\ \hat{x}\ 2E_o e^{i(\omega t+\pi/4)}$$

$$= \hat{x}\ E_o\ e^{i\omega t}$$

This is correct since there is no depolarisation for an isotropic particle.

Thus the ratio of the intensities along x and y is

$$\frac{|\underline{E}_x|}{|\underline{E}_y|} = \left|\frac{A\ +\ B}{A\ -\ B}\right|$$

APPENDIX D

Consider a plane wave of the form

$$\underline{E}_{inc} = \hat{x}\, e^{i\omega t}$$

Incident on the first quarter wave plate whose optic axis lies along $\hat{y}^1$ as shown below

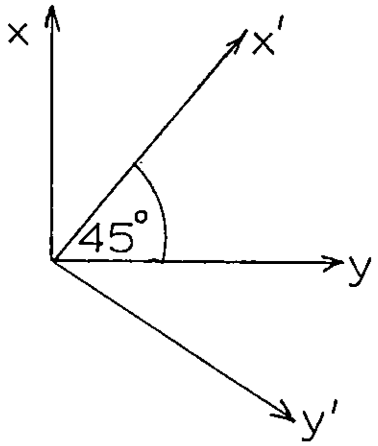

Thus we can write down

$$\hat{x} = \frac{\hat{x}^1 - \hat{y}^1}{\sqrt{2}}$$

and $\underline{E}_{inc} = (\hat{x}^1 - \hat{y}^1)\frac{1}{\sqrt{2}}\, e^{i\omega t}$

The field emerging from the first plate with error δ_1 is

$$\underline{E}_1 = \left(\hat{x}^1 - \hat{y}^1 e^{i(\frac{\pi}{2} + \delta_1)}\right)\frac{1}{\sqrt{2}}\, e^{i\omega t}$$

$$= \left(\hat{x}^1 - i\, \hat{y}^1\, e^{i\delta_1}\right) \frac{1}{\sqrt{2}}\, e^{i\omega t} \qquad \text{(D-1)}$$

There are two cases of interest:

(i) second quarter wave plate having the same orientation as the first.

The electric field emerging from the second plate with error δ_2 is

$$\underline{E}_2 = \left(\hat{x}^1 - i\, \hat{y}^1 e^{i\delta_1} .\ e^{i(\frac{\pi}{2}+\delta_2)}\right) \frac{1}{\sqrt{2}}\, e^{i\omega t}$$

$$= \left(\hat{x}^1 + \hat{y}^1\, e^{i(\delta_1+\delta_2)}\right) \frac{1}{\sqrt{2}}\, e^{i\omega t} \qquad \text{(D-2)}$$

but

$$\hat{x}' = \frac{\hat{x} + \hat{y}}{\sqrt{2}} \quad ; \quad \hat{y}' = \frac{-\hat{x} + \hat{y}}{\sqrt{2}}$$

$$\therefore \quad \underline{E}_2 = \left(\hat{x} + \hat{y} - (\hat{x} - \hat{y})\, e^{i(\delta_1+\delta_2)} \right) \tfrac{1}{2} e^{i\omega t}$$

$$= \left(\hat{x}(1 - e^{i(\delta_1+\delta_2)}) + \hat{y}\,(1 + e^{i(\delta_1+\delta_2)}) \right) \tfrac{1}{2} e^{i\omega t}$$

$$\therefore \quad I_{\parallel} = \tfrac{1}{2}\left(1 - \cos(\delta_1+\delta_2) \right)$$

and

$$I_{\perp} = \tfrac{1}{2}\left(1 + \cos(\delta_1+\delta_2) \right) \qquad \text{(D-3)}$$

(ii) Second plate at 90° to the first, i.e. its optic axis lies along $\hat{y}''$ as indicated below

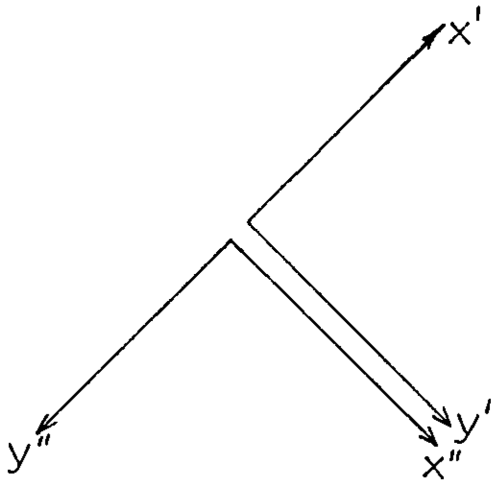

We can see that

$$\hat{x}' = -\hat{y}''$$

and

$$\hat{y}' = \hat{x}''$$

Thus Equations (D-1) and (D-2) can be written

$$\underline{E}_1 = \left(- \hat{y}^{11} - i\, \hat{x}^{11}\, e^{i\delta_1} \right) \frac{1}{\sqrt{2}}\, e^{i\omega t}$$

$$\underline{E}_2 = \left(- i\, \hat{y}^{11} e^{i\delta_2} - i\, \hat{x}^{11} e^{i\delta_1} \right) \frac{1}{\sqrt{2}}\, e^{i\omega t}$$

$$= - i \left(\hat{y}^{11} e^{i\delta_2} + \hat{x}^{11} e^{i\delta_1} \right) \frac{1}{\sqrt{2}}\, e^{i\omega t} \qquad \text{(D-4)}$$

Transforming to X and y using

$$\hat{x}^{11} = - \frac{\hat{x} + \hat{y}}{\sqrt{2}}$$

and $$\hat{y}^{11} = - \frac{\hat{x} - \hat{y}}{\sqrt{2}} \qquad \text{(D-5)}$$

since $\hat{x}^{11}$ is at 45° to $\hat{y}$ as shown below

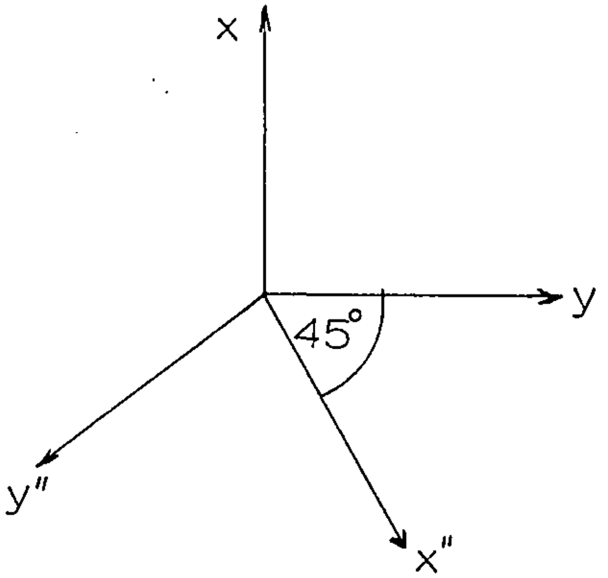

Substituting (D-5) into (D-4) gives

$$\underline{E}_2 = i \left((\hat{x} + \hat{y}) e^{i\delta_2} + (\hat{x} - \hat{y})\, e^{i\delta_1} \right) \frac{1}{2}\, e^{i\omega t}$$

$$= i \left(\hat{x}\, (e^{i\delta_2} + e^{i\delta_1}) + \hat{y}\, (e^{i\delta_2} - e^{i\delta_1}) \right) \frac{1}{2}\, e^{i\omega t}$$

Thus

$$I_{11} = \tfrac{1}{2} \left(1 + \cos\, (\delta_1 - \delta_2) \right)$$

$$I_1 = \tfrac{1}{2} \left(1 - \cos\, (\delta_1 - \delta_2) \right)$$

REFERENCES

1. Abramowitz,M and Stegun,T.A. "Handbook of Mathematical Functions" National Bureau of Standards, Washington (1964)

2. Addingley,G.G. "Asbestos Dust and its Measurement" Ann.Occup.Hyg. V.9 pp73-82 (1966)

3. Allen,T. "Particle Size Measurement" Halsted Press, New York, (1975)

4. Bayvel,L.P and Jones,A.R. "Electromagnetic Scattering and its applications", Applied Science Publishers,(1981)

5. Becklake,M.R. "Asbestos related diseases of the lung and other organs; their epidemiology and implications for clinical practice", Ann.Rev.Respir.Disease, V.114 p187 (1976)

6. Beer,J.M. and Chigier,N.A. "Combustion Aerodynamics" Applied Science Publishers, (1972)

7. Bexon,R. et.al. J.Phys.E. V.6 p245 (1973)

8. Bogovski,V.,Gilson.J.C.,Timbrell,V. and Wagner,J.C. Int.Agency for Research on Cancer, Publication n.8 (1972)

9. Born,M. and Wolf,E. "Principles of Optics" 5th ed., Pergamon Press Oxford, (1975)

10. Bruckman,L.,Rubino,R.A. and Christine,B. "Asbestos and Mesothelioma Incidence in Connecticut", Air.Pollut. Contr. Assoc.J., V.27, p121 (1977)

11. Cadle,R.D. "Measurement of Airborne Particles", Wiley, New York (1975)

12. Cerf,R. and Scheraga,H.A., Chem.Rev. V.51 pp185-261 (1952)

13. Chigier,N.A., Private Communication, (1976)

14. Chou,H.P. "A general theory of optical scattering from particles in crossed laser beams", Ph.D thesis University of Southampton (1976)

15. Chu,W.P. and Robinson,D.M., App.Opt. V.16 pp619-626 (1977)

16. Chubb,J.N. "Results of work to develop a prototype portable monitor for airborne fibres", UKAEA Culham Lab.Report n.CLM/RR/H5/6 (1977)

17. Chylek,P., J.Opt.Soc.Amer. V.66 pp285-287 (1977)

18. Cooke,D.D. and Kerker,M., J.Opt.Soc.Amer. V59 p.43 (1969)

19. Cooke,W.E., Brit.Med.J., V.2 p.147 (1924)

20. Cornillault,J., App.Opt. V.11 p.265 (1972)

21. Debye,P., Ann.Physik (4) 30,57 (1909)

22. Durst,F.,Melling,A. and Whitelaw,J.H. "Principles and Practice of Laser Doppler Anemometry", Academic Press, London (1976)

23. Durst,F. and Whitelaw,J.H., Procs.Royal Soc. A V.324 pp157-181 (1971)

24. Edwards,G.H. and Lynch,J.R. "The method used by the U.S.Public Health Source for enumeration of Asbestos dust on membrane filters", Am.Occup.Hyg. V11 pp1-6 (1968)

25. Eiden,R. App.Opt. V.5 p569 (1966)

26. Eliasson,B. and Dandliker,R. Optica Acta V.21 pp119-149 (1974)

27. Farmer,W.M. "Measurement of particle size number density and velocity using a laser interferometer", App.Opt. V.11 p2603 (1972)

28. Farone,W.A. and Kerker,M., J.Opt.Soc.Amer. V56 p.481 (1966)

29. Farone,W.A. and Querfeld,C.W. "Electromagnetic scattering from an infinite cylinder at oblique incidence" Rept.ERDA-281, U.S.Army Electron Res. and Develop. Activity, White Sands, New Mexico (1965)

30. Ferrara,R. et.al. App.Opt. V.9 p2517 (1970)

31. Fristrom,R.M., Jones,A.R.,Schwar,M.J.R. and Weinberg,F.J. "Particle sizing by interference fringes and signal coherence in Doppler velocimetry", Faraday Symposia of the Chemical Society, V.7 p183 (1973)

32. Gadsden,J.A. et.al., Atmos.Env. V4 p.667 (1970)

33. Gentry,J.W. and Spurny,K.R. "Measurement of collection efficiency of Nucleopore filters for asbestos fibres" J.Coll.Int.Sci. V.65 n.1 p.174 (1978)

34. Goodhead,K. and Martindale,R.W., Analyst V.94 p.985 (1969)

35. Greenberg,J.M., J.Coll.Int.Sci. V.39 pp513-519 (1972)

36. Henry,W.M. et.al. Batelle Columbus Labs. Rept.APTD-0965 (1972)

37. Hodkinson,J.R., App.Opt. V.5 p.839 (1966)

38. Holve,D. "In-situ particle sizing technique", J.Energy, V.4 pt.4 p.176 (1980)

39. Holve,D. and Self,S.A. "Optical particle sizing for in-situ measurements - Part 1", App.Opt. V.18 p.1632 (1979)

40. Holve,D. and Self,S.A. "Optical particle sizing for in-situ measurements - Part 2", App.Opt. V.18 p.1646 (1979)

41. Hong,N.S. "A method of particle sizing using crossed laser beams", Ph.D.thesis, University of London, (1977)

42. Hong,N.S. and Jones,A.R., J.Phys.D. V.9 p.1839 (1976)

43. Jennings,B.R. and Morris,V.J., J.Coll.Int.Sci. V.56 pp352-358 (1975)

44. Jones,A.R., J. Phys.D. V.5 pp1-4 (1972)

45. Jones,A.R., J.Phys.D. V.7 pp1369-1376 (1974)

46. Jones,A.R., Procs.Royal Soc.A V.366 pt.111 p.27 (1979)

47. Jones,A.R. and Wong,W.W.Y., Comb.Flame V.24 pp139-140 (1975)

48. Kerker,M.et.al., J.Opt.Soc.Amer. V56 p.487 (1966)

49. Kerker,M. "The scattering of light and other Electromagnetic Radiation" Academic Press (1969)

50. King,R.W.P. and Wu,T.T. "The scatter and Diffraction of Waves" Harvard Univ.Press, Cambridge (1959)

51. Larkin,B.K., Ph.D. thesis, University of Michigan, Ann Arbor (1957)

52. Larkin,B.K. and Churchill,S.W., J.Opt.Soc.Amer. V.49 p.188 (1959)

53. Lorentz,L.V., Vidensk.Selsk.Str.T. V.6 n.6 (1890)

54. Lundberg,J.L., J.Coll.Int.Sci. V.29 p.565 (1969)

55. Mentzner,J.R.,"Scattering and Diffraction of Radio Waves". Pergamon Press, Oxford (1955)

56. Mie,G., Ann.Physik, V.25 p.377 (1908)

57. Morris,V.J.et.al., J.Coll.Int.Sci., V.50 pp379-786 (1975)

58. Murray,H. "Report of the Departmental Committee on compensation for Industrial Diseases. Minutes of evidence. Appendices and Index", 127 (1907)

59. Powers,S.R.and Somerford,D.J.,Opt.Comm. V.26 n.3 p313 (1978)

60. Rajhans,and Sullivan, Ann Arbor Science (1981)

61. Ravey,J.C. and Mazeron,P., J.Coll.Int.Sci V.51 pp412-421, (1975)

62. Rayleigh,Lord, Phil.Mag. V.12 p.81 (1881)

63. Rayleigh,Lord, Phil.Mag. V.36 p.365 (1918)

64. Saxon,D.S., U.C.L.A. Conference "Radiation and Remote Probing of the Atmosphere", J.G.Kuriyan (ed.) pp227-308, (1977)

65. Seitz,W., Ann.Physik, V.16 p.746; V.19 p.554 (1905)

66. Seitz,W., Ann.Physik, V.21 p.1013 (1906)

67. Selikoff,I.J.,Chung,J.and Hammond,E.C.,"The occurance of Asbestos among insulation workers in the United States", Ann.N.Y.Acad.Sci. 132:139 (1965)

68. Selikoff,I.J.,Hammond,E.C. and Chung,J. "Carcinogenicity of amosite asbestos", Arch.Env.Health, V.25 p.183 (1972)

69. Smith,K.W., A.M.A.Archs.Ind.Health, V.22 p.198 (1955)

70. Spurny,K.R.et.al. "The sampling and Electron Microscopy of Asbestos Aerosol in ambient air by means of Nucleopore filters", J.Air Poll.Control Assoc. V.26 p.476 (1976)

71. Stratton,J. "Electromagnetic Theory", McGraw-Hill, New York, (1941)

72. Swithenbank,et.al. "Laser diagnostic Technique for the Measurement of droplet and particle size distributions" AIAA paper 76-69 (1976)

73. Timbrell,V., Ann.Occup.Hyg., V.18 p.299 (1975)

74. Timbrell,V.,Hyett,A.W. and Skidmore,J.W. Ann.Occup.Hyg., V.11 p.273 (1968)

75. Van de Hulst, "Light scattering by small particles", Wiley, New York, (1957)

76. Von Ignatowsky ,W., Ann.Physik V.18 p.495 (1905)

77. Von Schaeffer,C., Ann.Physik V.23 p.163 (1907)

78. Wait,J.R., Can J.Phys. V.33 p.189 (1955)

79. Wait,J.R.,"Electromagnetic Radiation from cylindrical Structures", Pergamon Press, Oxford (1959)

80. Wertheimer,A.L. and Wilcock,W.L., App.Opt. V.15 p.1616 (1976)

81. Wickramsinghe,N.C. "Interstellar Grains", Chapman Hall, London (1967)

82. Wyatt,P.J., App.Opt. V.7 p.1879 (1968)

83. Yeh,Y. and Cummins,H.Z., Appl.Phys.Lett. V.4 p.176 (1964)